

The University of Nottingham

UNITED KINGDOM · CHINA · MALAYSIA

Metamaterial Fabrication using combined Multiphoton polymerization and Optical Trapping

Meisam Askari, MSc

Thesis submitted to the University of Nottingham

for the degree of Doctor of Philosophy

July 2016

Abstract

Metamaterials are manmade structures with unique properties that cannot be found in nature. The metamaterial properties are structure dependent and enabled by the subwavelength periodic structure of the metamaterial. The goal of this thesis was to utilize an Additive Manufacturing (AM) technique to fabricate periodic metamaterial structures. Multi-Photon Polymerization (MPP) is a powerful AM method that has the capability to manufactures complex micro-scale 3D structures using ultra-short laser pulses. Typically, MPP has been used to manufacture micron-scale components in photopolymer materials. However, the development of sub-micron scale processes that can produce components from multiple materials within a single manufacturing step would be advantageous and open the potential to include different materials that can be manipulated and embedded within structures with sub-micron feature sizes.

A combined MPP and Optical Trapping (OT) setup was proposed to achieve the capability of fabricating periodic sub-micron structures with multiple materials. Firstly, a modular MPP system was designed, assemble and tested. Secondly, a bespoke OT setup was assembled and tested with a variety of particles. Thirdly, the single material system was combined with an optical trapping (OT) setup to independently manipulate microparticles in the x, y and z planes. An afocal lens arrangement was employed to reduce the gap produced by aberrations in the system. The assembled combined MPP and OT setup has the capability to embed trapped particles in MPP fabricated structures regardless of the trapping and polymerization wavelength and produce repeatable results for different particles and polymers. The engineering innovation in the design of the combined MPP and OT setup increase the capabilities and available materials for this system.

To test the capacity of the system particles were transported using OT, and then fixed to a well-ordered 3D matrix and encapsulated with polymer using MPP, thereby demonstrating the ability of the system as a microscale multimaterial fabrication techniques.

Acknowledgements

First and foremost, I would like to thank my supervisors Prof. Ricky Wildman and Prof. Christopher Tuck for their guidance throughout the whole process. I would also like to thank the technical and support staff of 3D printing research group and Additive manufacturing laboratory.

I would also like to thank my family for their support. I couldn't have done this without their help. Especially my wife who always supported me in everything I have done.

"Research is what I'm doing when I don't know what I'm doing."

Wernher Von Braun

Contents

ABSTRACT **2**

ACKNOWLEDGEMENTS **3**

LIST OF FIGURES: **8**

LIST OF TABLES: **19**

GLOSSARY: **19**

CHAPTER 1: INTRODUCTION **22**

1.1 RESEARCH MOTIVATION AND RATIONALE: 22

1.2 AIMS AND OBJECTIVES: 28

1.3 OUTLINE OF THE THESIS: 30

CHAPTER 2: LITERATURE REVIEW **33**

2.1 MULTI-PHOTON POLYMERIZATION 33

2.1.1 Lithographic Methods for Miniature Devices *33*

2.1.2 Review of Micro AM techniques *34*

2.1.3 Multi-photon absorption/polymerization: fundamentals *38*

2.1.4 Multi-photon absorption/polymerization: resolution *44*

2.1.5 MPP applications *47*

2.2 OPTICAL TRAPPING 52

2.2.1 Principles of Optical trapping for dielectric particles *52*

2.2.2 Principles of Optical trapping for Metallic particles *56*

2.2.3 Determining the trapping force *59*

2.2.4 Advance trapping setups *62*

2.2.5 Afocal systems *65*

2.3 METAMATERIALS 69

2.3.1 Working Principle and Structure of metamaterials *70*

2.3.2 Effective Material Approximation theories *74*

2.3.3 Photonic crystals *75*

2.4 LITERATURE REVIEW SUMMARY AND THE GAP IN KNOWLEDGE 78

2.4.1 The Gap in the knowledge *78*

2.4.2 Potential applications *80*

CHAPTER 3: METHODS AND MATERIALS **83**

3.1 MPP SETUP 84

3.1.1 SYSTEM ASSEMBLY 84

3.1.2 MPP system alignment *86*

3.1.3 MPP software development *89*

3.2 OT SETUP 94
3.3 COMBINED SETUP 105
3.4 IMAGING AND DIAGNOSTIC TECHNIQUES: 111
3.5 MATERIALS 118

CHAPTER 4: PRELIMINARY EXPERIMENTS AND RESULTS. 124

4.1 MPP SETUP FABRICATION 125
4.2 OPTICAL TRAPPING TESTING AND SIMULATION 141
4.2.1 Trapping Silica Bead suspended in deionized water 141
4.2.2 Testing Silver Nanoparticle in the OT 142
4.2.3 Trapping Gold Nanoparticle in OT 143
4.2.4 Trapping CNT in OT 143
4.2.5 Optical Trapping Simulation 144
4.2.5.1 OT simulation of Silica bead suspended in water 144
4.2.5.2 OT Simulation for silica beads suspended in PEGDA 146
4.2.5.3 Simulation of a particle suspended in the refractive index-matched medium 148
4.2.5.4 Simulation of particle suspended in a medium with higher refractive index 149
4.2.5.5 Particle monitoring 149
4.3 THE COMBINED SETUP 151
4.4 CHAPTER SUMMARY 162

CHAPTER 5: COMBINED OT-MPP SETUP SAMPLE FABRICATION & EXAMINATION 164

5.1 2D / 3D HYBRID STRUCTURES 164
5.2 PARTICLE ENCAPSULATION 170
5.3 BFM AND EDX SAMPLE EXAMINATION 172
5.4 CONFOCAL FLUORESCENT MICROSCOPY SAMPLE EXAMINATION 174
5.5 SYSTEM ACCURACY 179
5.6 TOF-SIMS ANALYSIS OF THE SAMPLES 183
5.7 SUMMARY 186

CHAPTER 6: DISCUSSION 188

6.1 THE MPP SETUP 188
6.2 OT ACHIEVEMENTS 192
6.3 FABRICATION OF COMPOSITE STRUCTURES 193
6.3.1 Combined OT-MPP Performance 196
6.3.2 Fabrication of multilayered composite structures using Combined OT-MPP 200

CHAPTER 7: FUTURE STEPS & CONCLUSIONS 208

7.1 FUTURE WORK: 208
7.2 CONCLUSION 211

REFERENCES **214**

APPENDIX A: DEVELOPED LABVIEW SOFTWARE **239**

List of Figures:

Figure 1. Representation of simultaneous two-photon absorption through a virtual state (left) and Single Photon Absorption (right) that move one electron from its ground state to an excited state with higher energy. 39

Figure 2 Two-photon (right) and single photon (left) excitation of the diluted fluorescent solution in a quartz cuvette. Image by Steve Ruzin and Holly Aaron, UC Berkeley. The integrated intensity for is constant for single photon but the integrated intensity square is peaked in the focal region [10]. 42

Figure 3. Illustration of MPP cross-section and the effect of polymerization threshold. The resin is transparent to the polymerization beam and photon absorption only occurs at the center of the focal volume of the objective lens. Therefore, true 3D structures can be fabricated inside the photoresist. 43

Figure 4. Bell shape laser intensity distribution curve vs. the distance from the optical axis and the effect of increasing the laser intensity on the minimum feature size of the setup. Polymerization only occurs above the threshold value and extremely high laser power can overheat the polymer and produce bubbles in the polymer.....43

Figure 5 The PSF generated using high NA (left) and low NA (right) objective lens. Because of the narrow separation in the wavelets available in the spherical cap for low NA objective lens pushed the first interference further from the lens. Therefore, low NA objective lens has longer working distance and broader central peak. Image by Jeff Lichtman, Harvard. 46

Figure 6. Ray-optic model of a particle in Mie region placed close to the focal volume of the objective lens. The force vectors show the net force applied to the particle by the laser beam. The thicker arrows (number 1 and F_1) represents the higher intensity areas of the beam and the thinner arrow (number 2 and F_2t) represent the low-intensity outer arrays of the trapping laser beam with TEM_{00} profile. The net force (F_{net}) is toward the centre of the focal volume of the objective lens which has the highest photon density. The scattering force ($F_{scattering}$) has firehose effect that pushes the particle in the laser propagation direction but the gradient force ($F_{gradient}$) pushes the

particle toward the centre of the beam which has higher beam intensity. The combination of forces applied to the particle through refracted, reflected and scattered beams force the particle toward the centre of the focal volume of the objective lens. 54
Figure 7. Gradient force and scattering force exerted to a particle placed close to the trapping beam waist. The particle is far smaller than the wavelength of the trapping laser and it becomes fully polarized. The generated temporary dipoles in the electromagnetic field become attracted to the areas with higher beam intensity. The scattering force F_z is proportional to the beam intensity and the gradient force F_g is proportional to the gradient of the intensity of the laser [131]. 56
Figure 8 Galilean beam expander top vs keplerian beam expander. In Keplerian beam expander, beams which are not parallel to the optical path can be blocked by placing an iris (pinhole) at the focal point between two lenses. 60
Figure 9 Basic OT system that has the capability of trapping single particle has 5 main sections. 1) The trapping laser, 2) A beam expander to fill the objective lens back aperture. The distance between two lenses are set to f_1+f_2 and appropriate lenses must be used to produce the necessary expansion. 3) An objective lens that focus the laser beam on the particle, 4) A stage to move the chamber as the trapped particle stays stationery and 5) An imaging system to observe the trapping procedure. 62
Figure 10 (a) OET tweezers setup for manipulation of nanoparticles based on optically induced electrophoresis. (b) Simulation of gradient electric field intensity [158]. 63
Figure 11. The effect of utilization of beam expander to change the divergence of the beam entering the back aperture of the objective lens. The figure demonstrated that by slightly increasing(decreasing) the distance between the lenses in the beam expander, the outgoing beam moves from parallel to diverging(converging) beams and moves the focus point of the objective lens moves closer (further) to the objective lens. 66
Figure 12 The diffraction pattern generated by an infinitely small point source at the imaging plane of a high NA objective lens. (Top) Lateral view (X-Z)

of PSF generated using high NA objective lens and its relative intensity plot (top). (Bottom) Axial view (X-Y) view of PSF and Airy disk generated with its relative intensity plot. Images by Leica Microsystem, Germany. 67
Figure 13. the only intact Lycurgus Cup that is held in the British Museum. Copyright the Trustees of the British Museum [175]. 69
Figure 14. A Bragg mirror with three dielectric layers. 76
Figure 15. The side view of a 2D photonic crystal structure with blue circles representing high dielectric constant (refractive index) areas and the dielectric well representation of the structure of work function of ε(x). ..77
Figure 16. 2D Simulation performed on spherical particles with a refractive index of 3.1, placed 5 μm apart in air. A) 2D demonstration of structure B) Photonic bandgap demonstrated by simulating the structure in part A. Analysis was done using the band solver function of the OptiFDTD software.....81
Figure 17. FTDT simulation of a 2D array of high refractive index particles with Y waveguide. The simulation demonstrates that by introducing defects in the photonic crystal structure it is possible to produce special waveguides. 82
Figure 18. The schematic diagram of the first MPP setup assembled for the experiment. The beam conditioner box controls the laser diameter and power. The Cold Mirror (CM) reflects the IR polymerization beam towards the objective lens and allows the visible light gathered by the objective lens reaches the camera. 86
Figure 19. The initial MPP setup assembled inside the laser inclusion. The stage driver, fibre coupled light, shutter control, power meter and the laser front panel is visible at the right-hand side of the image. 87
Figure 20. Laser output diagram VS. GUI amplitude control. The magnified section at the upper right corner of the diagram shows the area of interest for this project. 88
Figure 21. The front panel of the LabVIEW code developed to use an array of bitmap images to produce 3D structures. In the input section of the software step size, shutter time and the connections can be controlled. The readout

section is the feedback section and the user can control the overview of the progress. 91
Figure 22. LabVIEW code flowchart. 92
Figure 23. The initial design for the objective lens mount to increase the build volume of the MPP setup which was printed using a Connex Object 260 (A&B) and the metallic version of the design fabricated by CNC milling (C). 93
Figure 24. Schematic diagram of basic Thorlabs OT setup. The second lens in the Galilean beam expander is placed f_2-$|f_1|$ from the first lens and the objective lens is placed 200 mm (the tube length for the objective lens)| from the beam expander. The second lens of the beam expander is used as the imaging lens for the camera, Therefore, the camera is placed at the focal length ($f_{2)}$ of Lens 2. 96
Figure 25 Trapping silica beads using Optical trapping setup. 100
Figure 26. Upgraded OT setup using the GM and Keplerian beam expander. The beam expand section is longer comparing to the Gaussian beam expander and the distance between lens 1 and 2 is equal to the sum of their focal lengths. The objective lens is placed 20 cm from Lens 2 which is equal to the objective lens tube length. 101
Figure 27. The OT assembled inside the black cardboard enclosure to protect the users from potential dangers of class 3B laser used in the system. .. 101
Figure 28. The front panel of Labview code developed to control the GM and operate the imaging section of the setup. 102
Figure 29. The front panel of the LabVIEW quad detector driver. 103
Figure 30. LabVIEW VI used to extract the Sum voltage. This voltage was plotted while it was being monitored in a “while loop” and the data was plotted after finishing the operation in a 2D X-Y plot. This information was also automatically saved in a file to be used with data analysis software. 103
Figure 31. Schematic diagram of the dual objective lens combined setup. The system uses separate objective lenses for polymerization and trapping. Both objective lenses were mounted in translation mounts and it was tried to use mechanical translation mounts to overlap the polymerization and trapping

areas manually. The restricted field of view of high magnification high NA objective lenses made it impossible to accurately overlay the field of view of the objective lenses using the mechanical translation mounts. 105
Figure 32. Pictures presented in this figure were taken using the dual objective lens combined OT-MPP setup. Picture A was taken using the polymerization 10X objective lens and image B was taken using the 100x trapping objective lens. Pictures c & D were taken simultaneously using two 10X objective lenses from both sides of a graticule. 107
Figure 33. Two images demonstrate OT of a Soda-lime glass bead. The trapped particle in image A is placed above the substrate and particles on the substrate appears out of focus. As the stage moves towards the trapped particle, the immobilised beads become brighter in picture B. 109
Figure 34. Schematic diagram of the combined setup that yielded the highest performance. This setup was the setup used to produce majority of the results in this work. The single objective lens inverted configuration of the setup made it the most stable setup. The trapping section of the setup remained unchanged comparing the upgraded OT setup presented in Figure 26. 110
Figure 35 The electron beam penetration in a sample with different emitting signals and their sites. 113
Figure 36 schematic diagrams of an atom and Elastic scattering of an electron with a high angle of reflection. The nucleus is placed at the centre, and different electron band is labelled M, L and K. 113
Figure 37 Schematic diagram of characteristic X-rays generation from the incident electron beam. The inelastic scattering of the electron (solid line) and possible Auger scattering (dotted line) is shown. 115
Figure 38. molecular structures of (a) PEGDA (Mn 575 g/mol), (b) melamine resin and (c) 2-benzyl-2-2(dimethylamino)-4-morpholinobutyrophenone (photoinitiator). 120
Figure 39. Pictures taken from the combined setup imaging camera. The photoresist produced using Soda-lime glass beads suspended in the photoresist. The particle aggregation and small contaminations produced by particle breakage are visible in the image. 122

Figure 40. The viscosity of the equal mixture of PEGDA Mn575 g/mol and Mn250 g/mol at 20^{o}c over 20 minutes. After few minutes the system becomes stable, and the viscosity of the mixture becomes constant as the shear rate increases. 123
Figure 41. Different stages of sample preparation are shown in this figure. (A) Marked coverslip, (B) A droplet of the photoresist placed on the marked coverslip, (C) The spacer was placed on the coverslip, and (D) the polymer is sandwiched with a second coverslip. 126
Figure 42. High magnification images of voxels fabricated using an exposure time of 300 ms and laser power of 33.5 mW.....129
Figure 43. An array of voxels fabricated using different exposure time. All voxels fabricated using identical laser power and voxels in each row had similar exposure time. By increasing the exposure time the voxel length increases faster than the voxel diameter. The fallen voxels in the lower left corner can be used to measure the voxel length. The voxels measured was 0.96 µm and 1.26 µm.....130
Figure 44. Zigzag structures fabricated using the piezoelectric stage driver software with different step size in X and Y (0.5 μm and 2 μm). The stage speed, step size and the laser power defines the feature sizes produced by the system. 131
Figure 45. Two complex structures fabricated using the developed Labview code by importing bitmap files from the user-defined locations. The lower structure was fabricated to test the capabilities of the system to fabricate voxels close to each other. 133
Figure 46**.** The effect of vibration on fabricating microstructure using MPP setup. 133
Figure 47. High magnification image of a structure fabricated using a bitmap file for a negative Printed Circuit Board (PCB). The metallic connections are left empty. 134
Figure 48. The sawtooth structure on the surface of the structure presented in Figure 49. Due to the point by point fabrication of the samples and the elliptical shape of the voxels this saw-tooth profile is produced. 135
Figure 49. First 3D structures fabricated using the MPP rig. 136

Figure 50. Multilayer structures fabricated with a laser wavelength of 800 nm and laser power of 14.55 mW and exposure time of 100 ms. (Left) the image shows the structure from the top. (Right) illustrates the structure with 37° tilt to demonstrate the layers stacked on top of each other. 137
Figure 51. Nottingham design fabricated using different laser powers and step sizes. A) The structure in this figure fabricated with laser power of 9.62 mW and step size of 0.3 μm. Low laser power decreases the voxel length and the voxels was partially outside the substrate. B) This structure is fabricated using laser power of 14.55 mW and step size of 0.3 μm. The increase in the laser power improved the surface adhesion but the step size was smaller than the voxel dimension. Therefore, the small feature sizes were covered. C) The upper structures in figure C is fabricated with laser power of 14.55 mW and step size of 0.5 μm. Increasing the laser power and step size produced good structures but the saw-tooth surface profile is visible. The lower structure in figure C is fabricated with laser power of 11.65 mW and step size of 0.4 μm. 139
Figure 52 Single particle trapped using the laser beam. The particles outside the trap appear darker out of focus. 142
Figure 53. Forces applied to a particle placed close to the focal volume of the objective lens by the laser beam. The net force (orange arrow) is pointing towards the centre of the beam, and stable trapping is possible if the gradient force is larger than the scattering force. 145
Figure 54. Trapping force excreted to 10 μm beads suspended in water. a) Illustration of the particle in the trap gray lines simulate the laser beam converges into the red particle using the objective lens. b) Force field diagram with the position of trap at the center of the field. C & D) forces applied to the particle in Z and X direction. The Orange line shows the net force; Blue is gradient force and red the scattering force. 146
Figure 55. Trapping force excreted to 10 μm beads suspended in PEGDA. a) Illustration of the particle in the trap lines simulate the laser beam converges into the red particle using the objective lens. b) Force field diagram with the position of trap at the centre of the field. C & D) forces

applied to the particle in Z and X direction. Orange line shows the net force; Blue gradient force and red scattering force. 147
Figure 56. Force excreted to a particle suspended in the refractive index-matched medium by the trapping laser beam. The maximum applied force is 0.18 pN. The direction of the force is toward the center but the gradient force is very small and stable trapping cannot be achieved. 148
Figure 57. Force excreted to a high refractive index particle in a medium with lower refractive index. The direction of the force is toward the edge of the field and stable trapping cannot be achieved. 149
Figure 58. Demonstration of the QPD output voltage as the particles move in and out of the trap. The light level that reaches the QPD fluctuates as the number of particles in the trap changes. Therefore, the output voltage of the QPD changes abruptly. The numbers on the graph represent the events that a particle entered or exited the trap. Due to different arrangement that multiple particles can have in the trap, the light level can increase or decrease as the particle particles enter the trap. 150
Figure 59. Trapping events for a combination of silica beads and metallic particles. As the metallic particle enters the trap the amount of light that reaches the QPD is reduced sharply. The 300 nm gold nanoparticle absorbs and reflects almost all the trapping beam and the QPD voltage reduces to zero. 150
Figure 60. Laser power vs the attenuator level graph before the objective lens. As the attenuation level increases the laser power should decrease. Due to misalignment in the beam conditioner box, after 780, the laser power increases. This graph also presents loses in the optical chain. 152
Figure 61. An array of voxels fabricated close to the focus mark on a coverslip using a fixed exposure time and varying laser power. The exposure time for this experiment was set to 100 ms and the laser power increased from top to bottom. No fabrication was achieved using laser power of 5.78 mW. 153
Figure 62. Left image: Array of voxels fabricated with different exposure times using the prepared photoresist. The voxels in each column fabricated with

identical fabrication parameters. The exposure times increased from left to right (30 ms, 70 ms, 100 ms, 150 ms, 200 ms, 250 ms and 300 ms).....154
Figure 63. 50 μm square Fishnet structure fabricated using the MPP section of the combined setup. Change in the substrate thickens and tilt in the stage pushes the focal volume of the objective lens inside the substrate.....157
Figure 64. Single High refractive index soda lime particle immobilised by the polymer solidified using the MPP laser pulse. The minimum feature size of the MPP system is comparable with the particles and problems in particle suspension reduces the quality of the produced samples. 158
Figure 65. The fabricated structure using the soda-lime glass beads suspended in the photoresist. The combined setup was used to demonstrate the capability of the system to control the position particles and produce defined structures. Unwanted particles are scattered around the actual structure and contaminated the sample.....160
Figure 66. Using the combined setup the particles were placed one after another and arranged into a line. The particle breakage contaminated the combine setup photoresist and reduced the quality of fabricated structures. 161
Figure 67. A cluster of particles left on the substrate after washing the sample with deionized water. The photoresist trapped between the particles solidifies with ambient UV radiation.....161
Figure 68. Bright field microscope image of 5 by 6 array of particles immobilised using the MPP laser. The distance between particles and the position of each particle was controlled using the piezoelectric stage. Drift in the stage and vibration in the system introduces inaccuracies in the particle array. 165
Figure 69. Soda-lime particles with different sizes arrange inside the fishnet structure fabricated using MPP laser. 166
Figure 70. Fishnet structure fabricated using the MPP section of the combined MPP-OT setup to house particles. Openings are set to be 4 μm each. The structure was fabricated using the laser power of 14.55 mW and fabrication speed of 30 μm/s.....167
Figure 71. Image of 3 μm melamine resin based particles placed inside the fishnet structure fabricated with PEGDA. The fabrication speed of this

sample was 20 μm/s with laser power of 14.55 mW. The solidified polymers that glue the particles on the substrate can be seen in this image. 167
Figure 72. A structure fabricated using the MPP studio software. The bitmap file shows 3 particles inside a Y channel. But a portion of the structure has been washed away during the development process. 169
Figure 73. Step like structure with 3 particles adhered to each step. This picture demonstrates the ability of the structure to embed particles in deferent elevations and into 3D structures. 170
Figure 74. Multilayered structures fabricated using the combined setup. The arrow points out the position of a particle in the lower layer of the structure. The particles in the lower layer were partially covered with polymer and second set of particles embedded on top of the structure. 171
Figure 75. Multilayered structures fabricated in the combined setup. The first layer of structure has 9 particles in it. While immobilizing the particles in the second layer, the laser overheated the structure and damaged the particles. 172
Figure 76. A multi-layered structure fabricated in the combined setup. Using a piezoelectric stage and the imaging section of the combined setup the structure is sliced into two layers. Left, the objective lens focus is close to the particles in the upper layer of the structure. Right, the imaging plane of the objective lens is placed close to the bottom layer of the structure and particles in the lower layer of the structure are in focus. 173
Figure 77. EDX elemental mapping of the structure fabricated using the combined setup. The high nitrogen content of the particles makes them distinguishable from the photoresist. In this picture the nitrogen content is demonstrated by accumulation of blue dots. 174
Figure 78. A structure fabricated using the combined setup with 12 particles in the first tier and 4 particles in the second tier. The Confocal fluorescent microscope was used to excite the particles with specific frequency and image them in their excitation wavelength. pictures clearly show the particle arrangements in both layers. 176

Figure 79. 3D reconstruction of the structure demonstrated in figure 67. By stacking the images taken from each layer, it is possible to produce 3D representation of the structure. 177
Figure 80. Confocal fluorescent image of the multilayered structure with fluorescent beads embedded in it.....178
Figure 81. 20μm by 20μm structure fabricated that contains 23 particles in two layers and the 3D representation of particle arrangement. 179
Figure 82. The first picture is an SEM image of a 2 by 4 array of particles immobilised using the MPP laser (exposure time of 150 ms and laser power GUI 700). The SEM image was processed using ImageJ 1.49v software, to define the particles borders and the coordinates for the centre of each particle are demonstrated in the picture.....181
Figure 83. The first picture shows a SEM picture of an array of particles immobilised on the substrate using reduced laser power and exposure time. (b) Particle edge and the position of the centre of particles defined in the ImageJ 1.49 software. 183
Figure 84. TOF-SIMS image of a structure fabricated using the combined MPP-OT setup. Images a / b demonstrate different layers of the structure. The bright spots show regions with higher Nitrogen content. Image c shows the cross-section view of the structure. The shift produced by the system in the position of the particles can be seen in image c.....185
Figure 85 Longitudinal view of a focused beam with (top) negative, (center) zero and (bottom) positive spherical aberration. The lens is placed at the left hand side. 190
Figure 86 The polymerization laser is focused on a reflective surface. The focused light can be considered as a point source. The light collected by the objective lens produces diffraction patterns that can be seen by removing the IR filter from the imaging section of the system. Using the piezoelectric stage the reflective sample was moves in Z direction and a stack of images were captured. (left)Diffraction pattern produced by the focused laser beam in X-Y plane (right) Z projection of the stacked images produced using ImageJ v1.49.....191

Figure 87. Fishnet structure fabricated using the stage scanning speed of 30 μm/s. Freestanding walls fabricated in this experiment collapsed under their own weight. 199
Figure 88. Multimaterial 3D printed cube printed using Objet 260 multimaterial printer. A 3D array of flexible black spheres was placed inside the rigid transparent plastic cube.....200
Figure 89. A composite structure fabricated on top of a fishnet structure. The fishnet structure was built to increase the surface adhesion of the samples. 202
Figure 90. A 4 by 4 array of melamine resin based particles encapsulated in polymer cube. 206

List of Tables:

Table 1. Micro AM classification graph.....35
Table 2. Summary of different methods for improvement of MPP processing accuracy. 51
Table 3 Shells and subshells of atom.....115
Table 4 Comparison table of PEGDA Mn 575 g/mol and ORMOCOMP. 120
Table 5. Flowchart of sample fabrication steps. 127
Table 6. Flowchart of sample fabrication steps using the combined setup. ...159

Glossary:

Abbreviations	Explanation
3DDW	3 Dimensional
3DDW	3 Dimensional Direct Writing
ACS	Alignment Checking System
AJ	Aerosol Jetting
AM	Additive Manufacturing
CAD	Computer-Aided Design
CIJ	Continuous jetting
CM	Cold Mirror
CNT	Carbon Nano Tube

CW	Continuous Wave
DAQ	Data Acquisition device
DBS	Dichroic Beam Splitter
DM	Dichroic Mirror
DMD	Digital Micromirror Device
EBL	Electron Beam Lithography
EFAB	Electrochemical Fabrication
EM	Electro-Magnetic
ESLM	Electrically addressed Spatial Light Modulator
FDM	Fused Deposition Modelling
FDTD	Finite Difference Time Domain
FIBDW	Focused Ion Beam Direct Writing
GLMT	Generalized Lorenz-Mie Theory
GM	Galvo Mirrors
GUI	Graphics User Interface
HM	Hot Mirror
HOT	Holographic Optical tweezers
IC	Integrated Circuits
IR	Infra-Red
ITO	Indium Tin Oxide
LC	Liquid Crystal
LCVD	Laser Chemical Vapor Deposition
LIFT	Laser-Induced Forward Transfer
LS	Laser Sintering
MAPLE	Matrix Assisted Pulsed-Laser Etching
MEMS	Micro Electro Mechanical System
MMAM	Multi Material Additive Manufacturing
MPA	Multi-Photon Absorption
MPP	Multi-Photon Polymerization
MSL	Micro Stereolithography
MSOT	Minimum Shutter Open Time
NI	National Instruments
NIR	Near Infra-Red

OET	Opto-Electro Tweezers
OSLM	Optically addressed Spatial Light Modulator
OT	Optical Trapping
PCM	Photo Conductive Material
PEGDA	Poly(ethylene glycol) diacrylate
PI	Photo Initiator
PSF	Point Spread Function
QPD	Quad Photodiode Detector
SDM	Shape Deposition modelling
SEM	Scanning Electron Microscope
SLA	Stereolithography
SLM	Spatial light modulator
SOP	Safe Operation Procedure
SPA	Single Photon Absorption
STED	Stimulated Emission Depletion
TOF-SIMS	Time of Flight Secondary Ion Mass spectrometer
TPA	Two-Photon Absorption
UV	Ultra Violet
VI	Virtual Instrument

CHAPTER 1: INTRODUCTION

This thesis reports on a study to additively manufacture complex multi-material constructs through a combination of multiphoton polymerization and optical trapping resulting in a versatile technique for the fabrication of microscale composite structures and metamaterials.

1.1 Research motivation and rationale:

Additive Manufacturing (AM) or three-dimensional (3D) printing is the technology of building 3D objects layer-by-layer using computer-aided designs (CAD) [1]. Layer-by-layer manufacturing in AM is in contrast to conventional subtractive and formative manufacturing. AM starts with a CAD software that sends the digital objects (the design) to the printer. The design is then sliced into a predefined number of layers and fabricated sequentially [1].

Currently, there are more than 20 different recognised AM technologies [2]. R.F. Housholder patented the first AM technology in 1979 with the U.S. patent office [3] but his work was not commercialised. Thirty-six years after the Householder patent, AM is still in relative infancy when compared to traditional manufacturing techniques and there are many issues to be solved. Similar to conventional manufacturing techniques the process accuracy, production cost and material availability are some of the main challenges that AM researchers are facing. However, it has been shown that it is possible to reduce the overall AM cost by decreasing the energy usage, material waste and raw material cost of an AM processes [4]. Recent technological advancements in AM are happening in both high-end and low-end applications. High-powered, sophisticated systems are being developed for the autonomous fabrication of complex structures. At the same time, affordable desktop AM devices are available to the general public [4]. The progress in inkjet printing is a good example of scientists' effort to reduce the manufacturing cost while increasing the process accuracy and material availability [5]. The printhead performance, which is measured by the number of droplets per second (number of nozzles times the maximum operating frequency of the printhead), is steadily increasing [5]. Another example of researchers effort in advancing AM materials is the

‘carbomorph’ which is a low-cost, conductive thermoplastic that can be used in the fabrication of active devices using low-end desktop printers [6].

AM has yet to make a significant impact on the sub-mm length scale parts and components. There is a growing need for miniaturisation and new Nano/Microfabrication techniques [7], [8]. One of the most promising AM techniques for high-resolution manufacturing is called Multi-Photon polymerization (MPP), which is capable of fabricating structures with sub-micron resolution using femtosecond Infra-Red (IR) laser pulses [8]. MPP uses photoresists which are transparent to the IR laser, therefore the laser beam can focus deep inside the oligomeric vat and fabricate true 3D structures [9]. The nonlinearity of Multi-Photon Absorption (MPA) only allows the photon absorption in the centre of the objective lens focal volume, which permits the MPP system to achieve sub-diffraction-limit resolution [10]. MPPs’ unique properties make it a suitable candidate to replace conventional nano/micropatterning techniques [11]. Unlike conventional lithography techniques, which are generally 2D patterning techniques, MPP is a true 3D manufacturing technique. MPP can be used in an interlocked box in the normal laboratory environment. Although Ti-Sapphire femtosecond lasers are costly, there is no need for sophisticated vacuum chambers or clean rooms, which reduce the operation and maintenance cost of the MPP setup. As an AM method, MPP is a maskless manufacturing technique and there is no need to prefabricate a mask for each layer. Therefore, the fabrication steps are simplified, and the time-consuming and error-prone steps such as mask fabrication and alignment are removed.

Currently, most of the AM systems have been designed to produce parts using a single material [12]. There is a growing interest in fabrication of functional structures using more than one material. The ability to produce multifunctional parts using different materials, which is one of the challenges for the AM community, can increase the possible applications of AM [13][6]. Using different materials, it is possible to fine-tune the material properties and optimise the mechanical, electrical or optical properties of the printed structure[13].

Multi-Material AM (MMAM) systems in mm scale have been realized by introduction of multi-print head Inkjet printers [14][15]. Inkjet printers with multiple printheads can printing conductive ink alongside different polymers [5][13]. Different research groups have also demonstrated multimaterial Stereolithography (SLA) with mm resolution. SLA is one of the vat polymerization techniques that use a UV beam to polymerise the liquid monomer. To produce composite structures using SLA, more than one polymer vat is needed. The fabrication process starts by placing the platform in the first photoresist and building the object using the first polymer. For incorporation of the second material, the platform is transported to the second polymer vat through a cleaning process [16][17].

Moving toward sub-micron resolution, MPP has been used to fabricate structures with 2 or 3 different polymers [18][19]. Currently, using MPP with more than one material is very similar to conventional lithography techniques, and it needs multiple rounds of sample preparation, fabrications and developments [18] [19]. Fabrication of hybrid structures using MPP is composed of the following steps.

1) A droplet of the first photoresist is placed on the substrate.
2) Mounting the sample to the stage.
3) Aligning the laser beam with the substrate.
4) Fabrication of structures using polymer one.
5) Removing the sample from the setup and developing the solidified polymer.
6) Placing a droplet of the second photoresist on the substrate
7) Aligning the polymerization laser beam with the structure fabricated in step 4 and repeating steps 4 to 8 for each material.

There has been a considerable effort in the fabrication of conductive structures using MPP [20]. Fabrication of metallic structures using MPP is divided into

two major categories, direct deposition and post-functionalization [8]. There are three main strategies for direct deposition of metallic microstructures:

1) Direct metallic salt reduction,
2) Photoreduction of metallic salt in the polymer matrix, and
3) Simultaneous photopolymerization and photoreduction of metallic salt [20].

Kawata and co-workers demonstrated the fabrication of 3D silver structures using photoreduction of silver salt [21][22]. Fourkas and co-workers demonstrated solution phase deposition of Iron and Gold [23]. In general solution phase deposition has been shown to produce isolated metallic structures with generally poor conductivity [8].

By using electroless plating or other metal coating techniques, it is possible to produce 3D periodic conductive structures using MPP fabricated structures. Such hybrid techniques have been used for fabrication of periodic woodpile structures [24]. In electroless plating, the deposited metal conductivity is comparable to the bulk material. Using metal coating techniques, a thin metallic layer is deposited on the substrate as well as the polymer structure that limits the functionality of the sample. Hossain and Gu suggested an intermediary step to mechanically remove the fabricated microstructure from the coated substrate and place it on a new substrate [24].

The complicated and error-prone steps involved in multi-material MPP demonstrate the need for a technique that can fabricate structures with tailored properties in one process.

Fabricating structures with sub-micron resolution and fine-tuning the properties of various sections of the design, while being fabricated, has many benefits. Firstly, the fabrications steps are reduced, which can potentially increase the fabrication speed of the system. Secondly, by reducing the sample handling and development steps, there is a lower probability of sample contamination.

Thirdly, fabricating microstructures is a delicate process and steps such as mechanically removing the structures from the substrate or realigning the prefabricated microstructure with the polymerization area make the process less repeatable. Therefore, using a single process to construct the composite structures will have more accurate and repeatable results when compared to the multi-stage fabrication methods. The possible applications of a multimaterial fabrication technique with sub-diffraction limit resolution are considerable. Manufacturing metamaterials, Microelectromechanical Systems (MEMS), microsensors and biosensors are some of these applications.

The host material properties can be modified by incorporating particles with specific properties in the host material. Bruggeman's and Maxwell-Garnett's effective material approximation are two effective technique to mathematically predict the effective properties of the composite materials [25][26][27]. One of the methods that enable fabrication of composite structures by incorporation of particles with different properties and length scale into the MPP fabricated structures is to utilise Optical Trapping (OT) to transport particles into the MPP vat.

Two seminal papers demonstrated the simultaneous use of OT and MPP. Dawood *et al.* demonstrated successful transportation of particles using OT and immobilisation of these particles using MPP [28]. Tsai *et al.* placed a microbead (held in place using OT) in front of the polymerization beam and used the near-field focusing effect of the spherical microbead to increase the MPP resolution. They demonstrated that by using bigger particles than their primary 3 μm particles, it is possible to increase the distance between the particle and the polymerization area. Therefore reducing the risk of the particle being adhered to the substrate [29]. By comparing the structures fabricated in [29] and [28] it is clear that the position of the trapped particle in relation to the polymerization area defines the mode of operation of the combined setup. In the paper published by Dawood *et al.* the trapping laser wavelength was close to the polymerization wavelength. Hence the trapped particle was placed close to the polymerization area, and it enabled them to glue the particles to the substrate using the MPP

laser [28]. However, in Tsai *et al.* they used widely different laser wavelengths for trapping and polymerization and the gap between the trap position and the polymerization area helped them to perform OT assisted nanopatterning and avoid particle immobilisation by the MPP laser [29]. In a follow-up paper published by the Tsai group, they studied the effect of particle position in relation to the substrate on the polymerization resolution. They found out that by placing the particle too close to the substrate, the polymerization will not occur [30].

The research presented in this thesis is aimed at bridging the gap between the works of Dawood *et al.* and Tsai *et al.* and produce a more versatile technique that is not limited by the polymerization and the trapping wavelengths. Being freed from wavelength limitations can potentially increase the application of a combined setup by enabling the users to use different polymerization wavelengths for various photoresists without changing the trapping laser wavelength. The new system also enables the researchers to fix the polymerization wavelength and choose the most suitable trapping wavelength for the particle used in the system to increase the trapping force applied to the particle and avoid optical damage to the particles.

This technique can potentially address the need for a multi-material MPP technique, by enabling in-situ tailoring of material properties by embedding and manipulating the placement of particles with desired properties inside the host material. One example of the application of the combined setup is in the fabrication of microbead-based biosensors in microfluidic devices. Microbeads are commonly used as a support for target analytes of interest. The lab-on-chip sensors are designed based on immobilisation of functionalized particles in microfluidic chambers [31]. MPP has been used for fabrication of microfluidic systems [32], but using the combined MPP and OT setup, it is possible to immobilise a variety of functionalized particles while fabricating the microchannels. Therefore, it is feasible to fabricate the sensor in one system and reduce the fabrication steps.

Utilisation of high refractive index spherical particles for production of 3D photonic crystals has been demonstrated [33][34]. The combined setup described in this thesis can be used in the fabrication of 3D photonic crystals by producing a well-defined 3D array of particles embedded in the polymer matrix or on top of each other. Using OT, the researchers can have control over the arrangement and placement of every single particle. Therefore, highly tailorable structures can be realised.

Single high refractive index dielectric particles have been used as a functional element in optical devices [35]. The ability of the combined setup to manipulate and transport high refractive index dielectric microbeads enables this system to have potential applications in fabrication and assembly of the optical circuits for ultrafast optical switches, which are based on high refractive index particles.

1.2 Aims and objectives:

The aim of this PhD was to produce metamaterial structures using a combined approach of optical trapping and multi-photon polymerization. To achieve the project goal, a set of objectives were defined to break down the project goal into measurable phases to be completed.

1) Gaining the ability to fabricate micro/nanostructures with high resolution and repeatability. A modular MPP setup with sub-diffraction limit resolution was designed, assembled and tested.
2) To achieve the capacity to manipulate and transport particles suspended in different mediums. An OT setup, which is a versatile technique to transport a variety of particles with high precision, was designed, assembled and tested.
3) To combine the assembled OT with the modular MPP setup. The new combined setup utilises the OT section to transport particles into the MPP vat to be immobilised or encapsulated by the host polymer.
4) Fabricate hybrid structures using the combined setup. In this step, the built samples were characterised and studied to demonstrate the capabilities of the setup. The techniques were used to examine

samples fabricated with this system include Scanning Electron Microscopy (SEM), fluorescent/confocal microscopy, Time Of Flight Secondary Ion Mass Spectroscopy (TOF-SIMS) and focus ion beam SEM.

1.3 Outline of the thesis:

This thesis is composed of 7 chapters. A brief description of each chapter is presented below.

Chapter 1 presents an introduction to the thesis area and the motivation for the PhD.

Chapter 2 presents a comprehensive literature review, which is divided into five main sections.

- The first part of chapter two introduces MPP as a high-resolution AM technique and covers all aspects of multiphoton polymerization. In this section, the history and recent advancements in MPP are reviewed.
- The second section of the literature review chapter explains the optical trapping principles for metallic and dielectric particles with different sizes. Different arrangements used for trapping particles and their advantages, for a specific range of particles, are explained in this section.
- The third section of the second chapter is dedicated to studying metamaterials and photonic crystals.
- The last part of the literature review section summarises the relevant technical information, which is useful throughout the thesis. In this section, the most relevant works were compared to identify the gap in the literature and highlight the engineering advancements needed to bridge this gap. Potential applications of the setup are discussed in this section and Finite-Difference Time-Domain (FDTD) simulation results for two possible structures that can be built using the combined MPP-OT setup is presented.

Chapter 3 presents the methods and materials used to complete the project's objectives. This chapter is divided into four major subsections.

- Firstly, the MPP setup design and its components are explained in detail. The setup assembly, alignment and benchmarking processes, which were

essential to the seamless operation of the setup, are explained in this section. The developed MPP studio software that enables the users to fabricate complex multi-layered objects using the assembled setup is also explained in this chapter. Few early examples of the fabricated samples are also demonstrated in this section.

- The second section of this chapter is focused on the OT setup. Different OT setups assembled and used during this project are discussed. The Labview software that was developed to utilise the capabilities of the Galvo Mirrors (GM) system is thoroughly explained in this part.
- The third section of the methodology chapter is based on the process of combining the individual OT and MPP setups into one functional combined system. Different designs that were used during the project and shortcomings of each setup will be examined. The final arrangement that yielded the best possible outcome is explained in this section.
- The materials employed in the MPP and OT setups are explained in the last part of this chapter. The combined setup photoresist preparation and particle suspension processes are rationalised in this segment.

Chapter 4 presents some of the earliest results achieved using the assembled setups.

- In the first section of this chapter, the fabrication procedure for the MPP setup is explained. In this section, some of the structures fabricated for benchmarking the MPP setup are presented. The sample preparation, fabrication procedure, and post-fabrication processing of samples are explained in this section.
- The operation procedure of OT is discussed in the second part of the fourth chapter. The OT experimental results were collaborated by performing a number of simulations. The simulation results and force measurement graphs are presented in this chapter.
- In the final section of chapter four explains the operation procedure for the combined setup, which involved testing each part of the combined setup independently and performing basic tasks by utilising both OT and MPP simultaneously. In this section, the preliminary experiments

performed using the combined setup are presented alongside their fabrication procedure.

Chapter five presents advanced structures fabricated using the combined setup. In this chapter, Different 3D structures fabricated using the combined setup are presented. These structures are examined using various diagnostic tools, and the results are shown in the second section of chapter five.

Chapter six is the discussion chapter. In this chapter, the project results are examined and compared with the literature to demonstrate different aspects of the project that bridge the gaps in the literature.

Chapter seven is the conclusion chapter that presents the major achievements of the project and points out the shortcomings of the approach for fabrication of metamaterial structures. Future steps that can increase the capabilities and functionalities of the setup are also presented in this chapter.

Appendix one shows different layers of the developed LabVIEW software. The screenshots provide detail information about the working principle of the software.

CHAPTER 2: LITERATURE REVIEW

2.1 Multi-Photon Polymerization

MPP is one of many AM techniques, and it is classified as a vat photopolymerization process [13]. To be able to highlight the advantages of MPP and the need for a 3D fabrication technique with high resolution, the established microfabrication methods are explained before introducing MPP.

2.1.1 Lithographic Methods for Miniature Devices

There is a need for miniaturisation to produce novel devices [36]. Gordon E. Moore envisioned that the number of transistors in the Integrated Circuits (IC) would double every two years [37], commonly known as Moore's law. Moore's law is known as the golden rule of miniaturisation, and it drives researchers to develop novel fabrication techniques to achieve ever higher resolution. Currently, a collection of well-established techniques used in the fabrication of micro/nanostructures is called lithography. One of the limiting factors of lithographic methods is the radiation source and its wavelength. UV lithography is a conventional technique in the micro/nanofabrication industry. In an attempt to increase the resolution of UV lithography the wavelength used in this method has reduced from g-line (436 nm) to i-line (365 nm) and using Deep UV lithography transistors with 90 nm gate lengths have been realised [38]. To keep up with Moore's law, new techniques were established based on the use of immersion oil between the microscope objective lens (the final optic) and the samples. Using immersion oils with high refractive index reduced the minimum feature size to 45 nm [39]. Going towards shorter wavelengths (deep-UV lithography), the output power of the radiation source becomes severely limited, and an alternative radiation source is needed [9].

X-ray lithography [40] and Electron Beam Lithography (EBL) [41][42] were developed to achieve higher resolution. Replacing the light source with an electron gun with sub 100 nm wavelengths increased the resolution of the lithography technique to 30 nm [43]. The highest resolution achieved using lithographic techniques is by using Extreme UV source with an exposure wavelength of 13.5 nm to reduce the feature size to 11 nm [44]. All the

mentioned lithographic techniques have drawbacks that limit their application. Expensive and time-consuming mask manufacturing, complicated radiation generation, small fabrication area and high installation price are some of these limitations. It is also important to understand that all the lithographic techniques mentioned here are 2D patterning techniques [9].

There is a need for a true 3D manufacturing technique with high resolution for fabrication of complex freestanding structures with high aspect ratio. MPP or femtosecond laser writing is an emerging technique that can solve these issues and delivers high-resolution 3D structures [7] [45].

2.1.2 Review of Micro AM techniques

MPP is not the only additive manufacturing technique with sub-millimetre resolution. There are a number of additive techniques that can potentially achieve sub-millimetre resolution and have promising applications [7]. Vaezi et al. categorised the micro AM processes into 3 main classes. In this section, this classification will be presented alongside a brief explanation of some of the key techniques.

The first group of micro AM processes is Scalable AM techniques. AM processes like Laser Sintering (LS), Stereolithography (SLA), inkjet printing and Fused Deposition Modelling (FDM) can be modified, and under the right circumstances, they can be used to fabricate microstructures [7].

The second group of AM technologies with sub-millimetre resolution are 3D Direct Writing technologies (3DDW). Direct writing processes are mainly developed for 2D patterning, but some of these techniques can achieve 3D fabrication capabilities. Processes like Laser Chemical Vapor Deposition (LCVD), Focused Ion Beam Direct Writing (FIBDW), aerosol-jet, Laser-induced forward transfer (LIFT), Matrix-Assisted Pulsed-Laser etching (MAPLE), and nozzle dispensing processes can be utilised to fabricate free-standing 3D structures [7].

Hybrid processes like Electrochemical Fabrication (EFAB) and Shape Deposition Modeling (SDM) are the last groups of micro AM technologies.

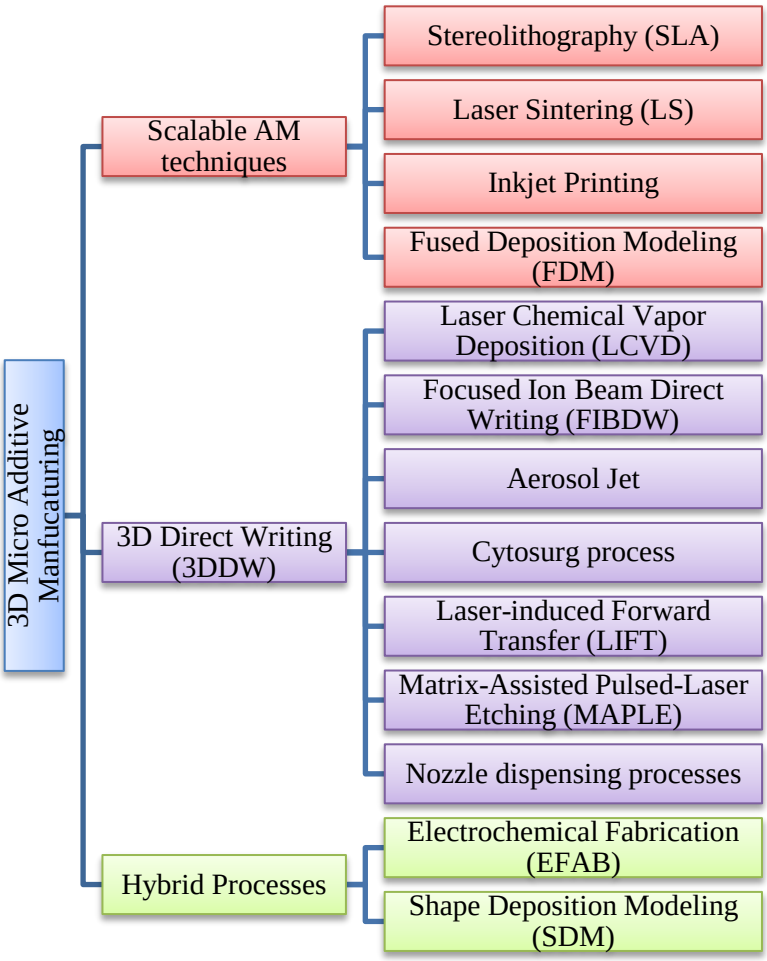


Table 1. Micro AM classification graph

1) Stereolithography (SLA) is a commercial term for SPP. In this technique, a UV source solidifies the photoresist near the moving platform and build 3D structures layer-by-layer. Ikuta and Hirowatari first introduced Micro Stereolithography (MSL) with a resolution of 1-10 μm [46]. MSL has smaller laser spot size, and the platform has a sub-micron resolution in x, y and z. MSL has been used in the fabrication of micromachines and microsensors [47], microfluidic systems [48], optical waveguides [48], 3D photonic band gap structures [49], fluid chips for protein synthesis [50] and bio-analysis [51][52].

   Depending on the beam delivery system the MSL systems are divided into two categories.

A) Scanning MSL system, which uses Galvo mirrors to move the laser spot and fabricate layers point-by-point [53].

B) Projection MSL, which can polymerise the entire layer of a structure. Project MSLs can use liquid crystal displays [51][52] and Digital Micro-mirror Device (DMD) [54] to produce the dynamic masks for each layer. Structures with a minimum pixel size of 30 μm and layer thickness of 15 μm have been fabricated using commercial MSL setups. The minimum feature size of MSL is limited by the polymer viscosity and surface tension [7].

2) Laser sintering (LS) is a powder bed fusion process uses a laser to sinter a layer of metal or polymer powder and form structures layer-by-layer. After completion of each layer, a roller spread fresh powder on the bed and the process is repeated for each layer [55]. The minimum layer thickness for commercial SLS machines is few hundred microns. The main limitations of SLS for achieving higher resolution are the laser spot size, powder grain size and powder feeding mechanism. Using fine powder increases the reactivity of the particles with humidity and the oxygen in the air. It also increases the interparticle forces that increase agglomeration in the powder bed [7]. Regenfuss et al. for the first time demonstrated Micro SLS technique by fabricating parts with a structural resolution of <30 μm and aspect ratio of >10. In this experiment the used a vacuum chamber and shielding gases to enable them to use powder with submicron grain size [56].
3) Inkjet printing is one of the most well established AM techniques that have the potential to be a micro AM process. Inkjet technology is based on the ejection of the liquid ink from the printhead reservoir and subsequent solidification of the droplet via cooling (crystallization), heat (evaporation of the solvent) or chemical reaction (photocrosslinking) [7][5]. Inkjet printers are either Drop On Demand (DOD) or continuous inkjet (CIJ) in mode and the droplet size for both techniques can be as small as 0.5 pL.
4) LCVD is a direct writing technique that uses the laser beam to convert the gaseous reactant to a thin solid layer. In this technique, the reactive

gas pumped into the build chamber and the laser beam is used to heat the specific areas of the substrate selectively. Subsequently, the reactant solidifies on the heated areas of the substrate. Complex 3D structures can be fabricated by repeatedly scanning the substrate. Laser beam diameter, laser wavelength, process parameters (scanning speed and laser power), and substrate thermal properties are some of the factors that define the resolution of this technique [57]. It is also possible to have multi-material LCVD by feeding different gases or use jets of gas to have a local gaseous atmosphere [58].

5) FIBDW is a similar technique to LCVD but utilizes an ion beam instead of laser beam decreases the fabrication speed of this system. Structures with minimum feature size of 80 nm and layer thickness of 10 nm have been demonstrated using this technique.
6) Aerosol jetting (AJ) uses aerodynamic focusing for accurate deposition of ink onto the substrate. The AJ process has 3 major steps. 1) Atomiser produces a dense mist from the printing liquid with a droplet size of 1 to 5 μm. 2) The droplets are transported to the deposition head. 3) The sheath gas was used to focus and deliver the droplets to the substrate [59]. AJ can be used to deposit a wide variety of materials (Metal, semiconductor and polymer) on virtually any substrate [60]. AJ has been utilised in the fabrication of solar cells, fuel cells, fully printed thin film transistors, embedded resistors, sensors, flexible displays and high-density assays for drug discovery [61].
7) The cytosurge process is one of the newest micro AM techniques and has the capability to direct fabricate partially overhanging metal microstructures [62]. This technique works based on deposition of metal salt from the atomic force microscope cantilevers tip in an electrochemical cell. The pressure regulator used in the setup precisely controls the localised deposition of the metal salt. If the cantilever has sufficient cathodic potential, the deposited metal salt reduces and confined electroplating occurs under the atomic force microscope tip [62].

2.1.3 Multi-photon absorption/polymerization: fundamentals

Multi-photon polymerization is developed from the stereolithography technique and shares same principles, however MPP is a process by which a Photo Initiator (PI) molecule absorbs more than one photons to move an electron from its ground state to an excited state [63]. Maria G. Mayer first explained TPA in her PhD thesis in 1931. She predicted that if two photons can be simultaneously absorbed through a virtual state, the electronic state of the atom or molecule will change [63]. 30 years after her numerical prediction, Kaiser and Garret observed Multi-photon luminescence produced by a europium-doped crystal illuminated using a ruby optical maser [64]. TPA is the fundamental process of MPP, and it is one of the multiphoton processes [45]. Development of monochromatic laser sources with high power density enabled the researchers to fabricate microstructures using TPA in 1997 [65][66]. Excitation of electrons from their ground state to an excited state has two mechanisms, sequential and simultaneous excitation [67]. In the sequential excitation, the PI absorbs a single photon, and an electron moves from its ground state to a real intermediate state with the lifetime of 10^{-4} to 10^{-9} s. If a secondary photon gets absorbed during this time frame, the electron will move from the intermediate state to the excited state. Simultaneous excitation works through a virtual intermediate state with a much shorter lifetime (10^{-15} s). Figure 1 (right) demonstrates that single Ultra Violet (UV) photon absorption provides enough energy to move a single electron from its ground state to the excited state. Figure 1 (left) shows simultaneous absorption of two infrared photons to move a single electron from its ground state to the excited state through a virtual state.

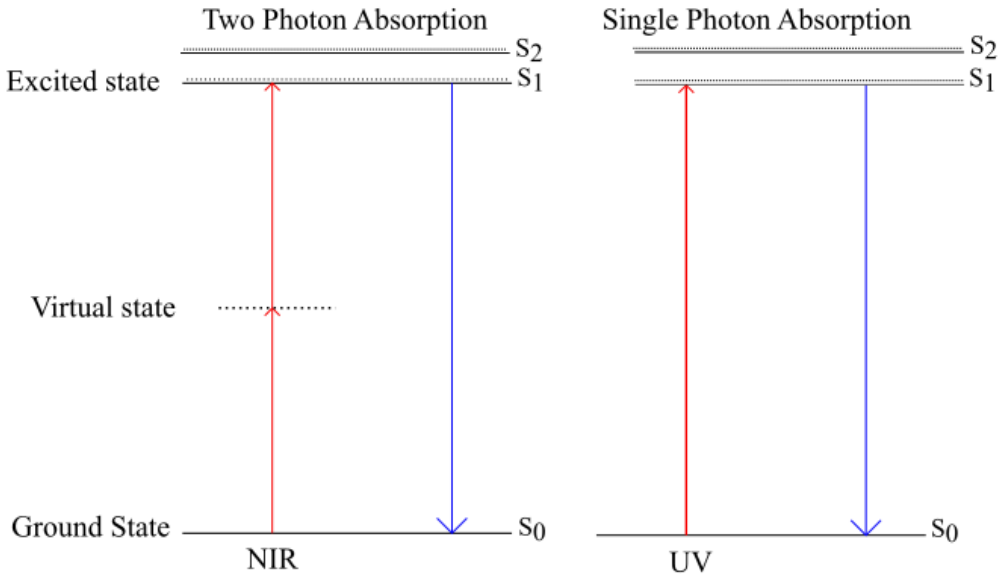


Figure 1. Representation of simultaneous two-photon absorption through a virtual state (left) and Single Photon Absorption (right) that move one electron from its ground state to an excited state with higher energy.

Different selection rules apply to TPA in comparison to SPA. The angular momentum of the electrons in the excited state must be similar to the one in their ground state. Since each photon presents the spin change of ±1, in SPA the angular momentum of the electrons differs by ±1 or 0 but in TPA angular momentum difference of ±2 or 0 is needed [68]. Therefore the angular momentum conservation rules impose different limitations for TPA in comparison to SPA and using linear spectroscopy techniques it is not possible to observe multiphoton states [68].

Due to the low probability of TPA, extremely high photon density is needed for simultaneous absorption of two photons (Multi-photon coincidence in time and space) [67], [68]. Using a Continuous Wave (CW) laser to provide such a high photon density can potentially damage the photoresist. Ultra-short femtosecond pulses are being used to deliver high photon density and avoid thermal damage to the photoresist [9], [69].

The TPA coefficient (β) can be calculated using Equation 1. In this equation δ is the molecular absorption cross-section, which is usually given in units of Goeppert-Mayer (GM):

$$\beta = \frac{\delta N}{h\upsilon}$$ Equation 1

where N is the number of absorbers per unit volume, h is the Planck constant ($6.62607004 \times 10^{-34}$ m^2 kg / s) and ν is the frequency of light [68]. Similar to SPA in UV lithography, TPA can lead to polymerization of the photoresist. Two main components of photoresists are the required monomers/oligomers and the Photo-Initiators (PI). The PI molecule absorbs two/multiple photons and transforms into a free radical. Monomer radicals are produced by combination of the radicals ($\dot{R}$) and monomers (M). If two monomer radicals react with each other, a longer chain molecule will be generated. These long chain molecules can propagate in the photoresist to form longer molecules with other radical monomers. If a long chain molecule reacts with another long chain molecule, the propagation will terminate. Equations 2 to 5 demonstrate the polymerization process [70].

Initiation	1) $PI \xrightarrow{h\upsilon h\upsilon} 2R^{\cdot}$	Equation 2
	2) $\dot{R} + M \rightarrow R - M$	Equation 3
Propagation	3) $R - M_{\dot{n}} + M \rightarrow \mathrm{R} - M_{\dot{n}+1}$	Equation 4
Termination	4) $2\dot{R} - M_n \rightarrow M_{2n} - R$	Equation 5

To better understand the advantages of the MPP process, this process is explained in comparison to UV lithography. In SPA, UV radiation gets absorbed as it goes through the photoresist and large area polymerization occurs on the monomer surface. Beam intensity and the single photon polymerization threshold affects the resolution of Single Photon Polymerization (SPP) technique. The rate of SPA is linearly dependent on the radiation intensity and by increasing the beam intensity larger minimum feature sizes will be achieved. It is possible to utilize optical lenses to focus the UV light into a tight spot and increase the resolution of SPP technique. The optical diffraction limit of the lens system is one of the main factors that defines the minimum spot size achieved by the for this technique. The diffraction limit is the theoretical maximum

resolution that an optical system can achieve [71]. Equation 6 [72] shows the radius of the smallest lateral light spot (r) that a light source with a wavelength of λ going through an objective lens with numerical aperture of NA can generate.

$$r = \frac{k\lambda}{NA} \qquad \text{Equation 6}$$

Equation 7 [73] shows the relationship between the objective lens numerical aperture (NA) and the convergence angle (α) of the beam after the objective lens for an oil immersion objective that uses and immersion oil with refractive index of n.

$$NA = nsin\,(\alpha) \qquad \text{Equation 7}$$

In high NA objective lenses, the light converges rapidly after the objective lens and reduces the working distance and the spot size of the objective lens. Higher resolution is attainable using high NA oil immersion objective lenses. Equation 6 calculates the objective lens spot size for a light source with uniform intensity profile. It is possible to decrease the effective spot size by using aTEM_{00} laser beam, the bell-shaped intensity profile of the TEM_{00} beam reduces the effective spot size and the new spot size is known as beam waist (w_0). The beam waist can be calculated using Equation 8 [68].

$$w_0 = \frac{\lambda}{\pi NA} \qquad \text{Equation 8}$$

Theoretically, SPP can fabricate structures with feature sizes close to the diffraction limit by setting the beam intensity slightly above the single photon polymerization threshold. But in SPA, the absorption rate scales linearly with the light intensity [74] and fluctuations in the beam intensity stop the polymerization if the beam intensity is very close to the polymerization threshold. Therefore, it is not practical to operate the SPP with beam intensity close to the polymerization threshold.

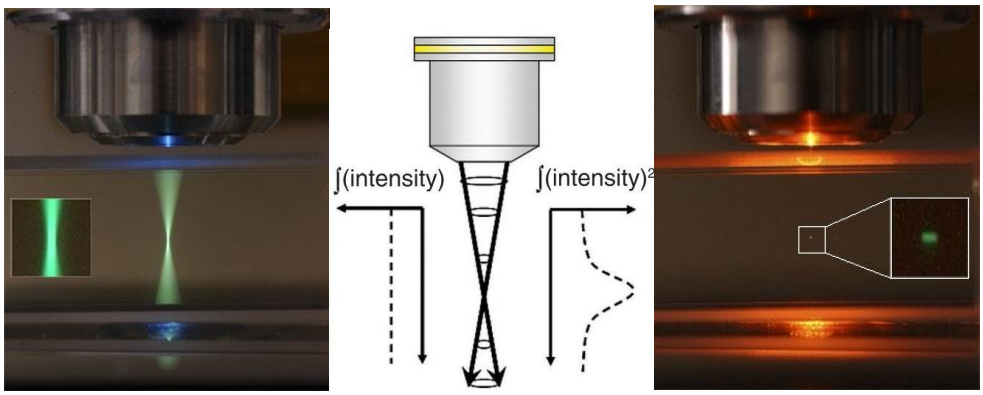


Figure 2 Two-photon (right) and single photon (left) excitation of the diluted fluorescent solution in a quartz cuvette. Image by Steve Ruzin and Holly Aaron, UC Berkeley. The integrated intensity for is constant for single photon but the integrated intensity square is peaked in the focal region [10].

Using more than one photon to initiate the polymerization has a number of benefits. MPP uses Near Infra-Red (NIR) laser and the photoresists used in MPP are transparent to the laser beam. Therefore, freestanding 3D structures can be fabricated within the photoresist [75].

The second main benefit of MPP is the sub-diffraction limit resolution of this technique. Because two or more photons must reach the photoresist and the same time and place, the probability of MPP depend on the intensity of the light to the power of number of photons. Therefore, the dependency between the absorption rate and beam intensity is not linear.

MPP photoresists have a high polymerization threshold, if the photon density is below the threshold, enough radicals cannot be produced in the photoresist. The excitation beam intensity should be in the order of ~1 $TW/cm^2$to surpass the polymerization threshold for multiphoton polymerization [76]. The restrictions imposed by the combination of the polymerization threshold and MPA probability, makes MPP a third order non-linear effect that can break the diffraction limit of the optical instrument [8], [77], [78]. Using a microscope objective lens to focus the laser beam, it is possible to create a situation that efficient MPP occurs at the centre of the focal volume of the objective lens (in a volume as small as a few attoliters) and produce sub-diffraction limit feature sizes [10]. Figure 3 illustrates the NIR laser focused in the photoresist. The diagram also shows the effect of the polymerization threshold value that further limit the polymerization area to the centre of the focal volume of the objective

lens. Figure 4 shows the effect of the laser power and polymerization threshold on the voxel size.

The nonlinearity of MPP that enables this process to achieve sub-diffraction resolution has two different sources. A) The Polymerization efficiency which depends nonlinearly upon the beam intensity. B) The chemical nonlinearity which is produced by the photoresist polymerization threshold and radical quenching that stops the generated radical to propagate in the photoresist [10].

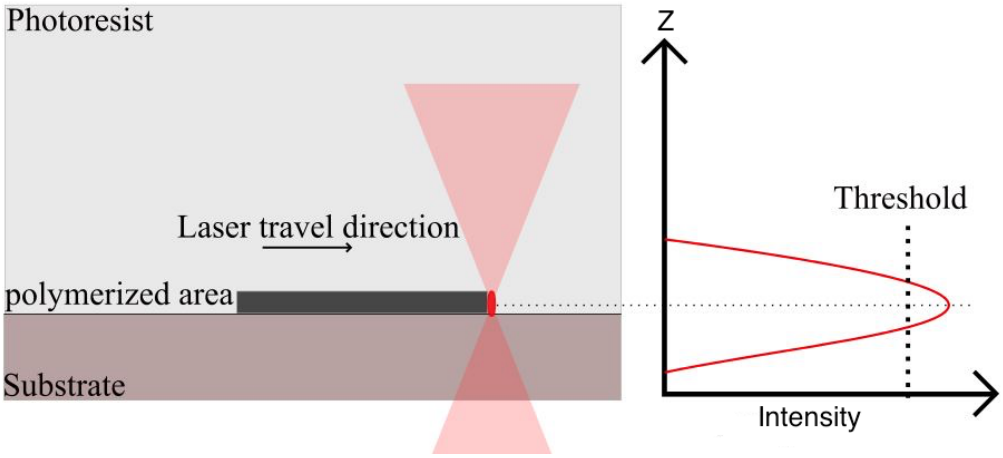


Figure 3. Illustration of MPP cross-section and the effect of polymerization threshold. The resin is transparent to the polymerization beam and photon absorption only occurs at the center of the focal volume of the objective lens. Therefore, true 3D structures can be fabricated inside the photoresist.

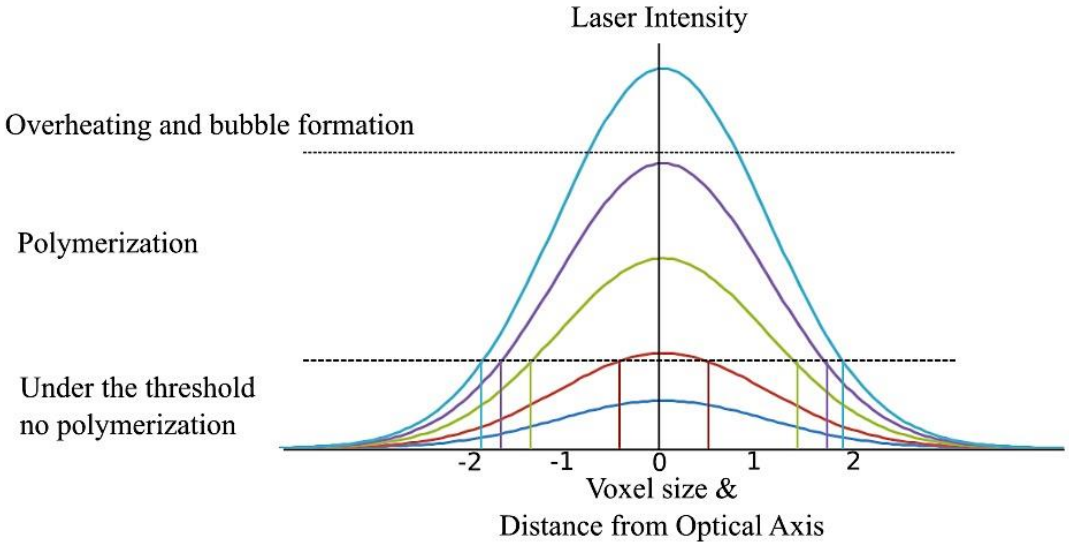


Figure 4. Bell shape laser intensity distribution curve vs. the distance from the optical axis and the effect of increasing the laser intensity on the minimum feature size of the

setup. Polymerization only occurs above the threshold value and extremely high laser power can overheat the polymer and produce bubbles in the polymer.

2.1.4 Multi-photon absorption/polymerization: resolution

In MPP the resolution and minimum feature size of a setup are easily confused. Resolution is the minimum distance between two adjacent yet separate features [45], but the minimum feature size is the smallest feature fabricated using the setup. The MPP minimum feature size is also referred as the voxel (volumetric pixel) size of the setup.

Calculating the actual minimum feature size of the MPP setup is a challenging task. There are a number of parameters that affect the resolution of the setup, but their effects cannot be factored in the resolution formulas. Optical alignment, non-ideal optical components and aberration in the system are some of the most important factors that produce the gap, between the calculated and experimentally measured resolution of an MPP setup. The voxel diameter (*d*) is closely related to the volume in which the photon flux density is high enough to exceed the polymerization threshold. Therefore, only at the centre of the objective lens focal volume, enough radicals will be generated to start the crosslinking process (the initiation step) [79]

$$d(N_0, t) = r_0[ln(\frac{\sigma_2 N_0^2 \tau_L}{c})]^{0.5} \qquad \text{Equation 9}$$

Where τ_L is the laser pulse duration, σ_2 is the coefficient of Multi-photon cross section, r_0 is the distance from the optical axis, N_0 is the photon flux, and c can be calculated by following equation:

$$c = ln[\rho_0(\rho_0 - \rho_{th})] \qquad \text{Equation 10}$$

In Equation 10 [79], ρ is the radical's particle density and ρ_0 is primary initiator particle density. ρ_{th} is the threshold value radical density. To estimate the

minimum feature size along the beam axis we use Gaussian distribution for axial light distribution.

$$N_{(z)} = N_0/(1 + z^2/z_{R^2}) \qquad \text{Equation 11}$$

Using above distribution, the pixel length will be:

$$l(N_0, t) = 2z_r[(\sigma_2 N_0^2 n\tau_L/c)^{1/2} - 1]^{1/2} \qquad \text{Equation 12}$$

Here Z_r is the Rayleigh length. Based on Equations 9 to 12, laser intensity, exposure time and the threshold value of the polymer are among the most important factors in defining the voxel size and the resolution of the system [76], [79]. It is also worth mentioning that the voxels' length is more sensitive to the laser power than the exposure time [67]. Figure 5 demonstrates the Point Spread Function (PSF) generated using a high NA (left) and a low NA (right) objective lens. The PSF is broader in the low NA objective lens and laser power is distributed in the larger area.

There are hardware related parameters that also affect the minimum feature size attainable for a setup. The operation speed of the shutter (beam blocker) defines the minimum exposure time for the system and the type of objective lens used for the experiment defines how tightly the laser beam can be focused.

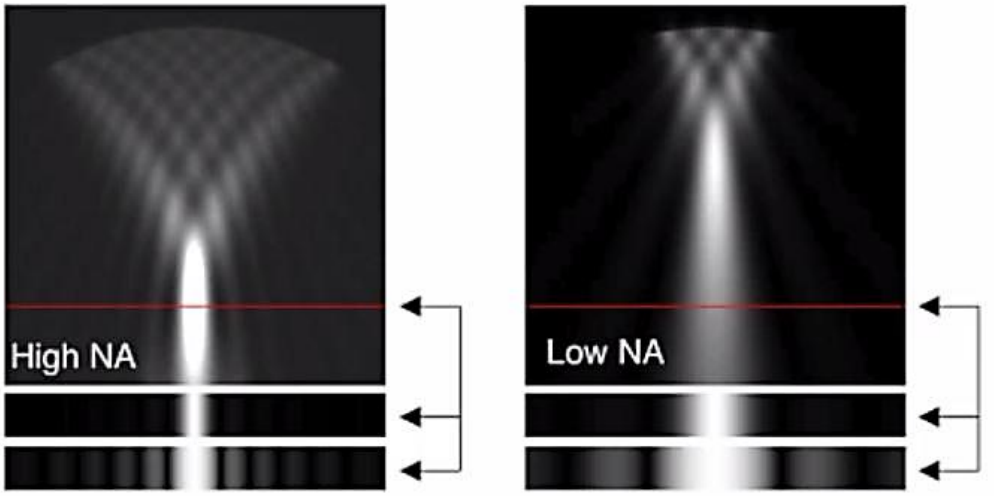


Figure 5 The PSF generated using high NA (left) and low NA (right) objective lens. Because of the narrow separation in the wavelets available in the spherical cap for low NA objective lens pushed the first interference further from the lens. Therefore, low NA objective lens has longer working distance and broader central peak. Image by Jeff Lichtman, Harvard.

Also, the spherical aberrations in the optical system change the PSF of the beam and changes the shape of the focal volume of the objective lens. Therefore, the laser power spreads in a larger area and makes the voxel sizes unpredictable.
The femtosecond pulse duration changes as it travels through the optics. The light in ultrashort pulses consist of a range of frequencies and each frequency travels at different speed. Therefore, due to group velocity dispersion that occurs in the optical elements the pulse width increases [80]. Pulse width has great influence on the polymerization process. Tan et al. tested the effect of pulse width by fabricating free-standing walls while changing the pulse width of the laser [81]. Free standing walls fabricated using longer pulses were thicker but shorter. They concluded that the volume of polymerized voxels and the polymerization threshold is linearly proportional to the pulse width. Subsequently, due to pulse width dependent two photon cross section, voxel sizes increases by increasing the pulse width and due to the temperature dependent radical diffusion uneven growth occurs in axial and lateral directions[81]. Therefore, shorter pulses are advantageous in improving the resolution of the MPP system.

By decreasing the laser intensity and exposure time and using an efficient multi-photon PI, it is possible to fabricate smaller structures, but there is a lower limit for the laser intensity that is defined by the threshold value of the photoresist and laser intensity fluctuation [45]. Smaller feature sizes can be achieved by introducing the radical quenchers to the photoresist [76][70]. Radical Quenchers are oxygen-rich materials that oxidise the radicals and prevent them from spreading in the polymer and efficiently stop the propagation step of the polymerization [82]. Gan et al. reported the smallest feature size fabricated using the MPP [83]. In their work, they achieved 9 nm feature sizes and 52 nm Multi-line resolution. They demonstrated that the main limitation of their setup was the mechanical properties of the photoresist and developed a new photoresist

with high mechanical strength and broad Multi-photon cross-section. By utilising a new photoresist in a Multi-beam MPP setup, they achieved a resolution comparable to electron beam lithography. The Multi-beam MPP system works based on utilisation of a second doughnut-shaped CW laser to reduce the propagation of radicals produced by the femtosecond laser beam [83].

Polymer shrinkage also affects the minimum feature size of MPP. Asymmetric shrinkage can also deform the fabricated structure and invalidate the results in case of photonic crystals. The shrinkage that occurs during polymerization is due to a reduction in the intermolecular distance during polymerization [84]. Monomer molecules typical intermolecular distance is 3-4 Å that reduces to 1.5 Å during polymerization [84]. Shrinkage can be reduced by utilization of low shrinkage polymers or it can be compensated in the design stage [85].

2.1.5 MPP applications

The demand from Nanotechnology communication and the information industry has increased the effort in the development of new nano/micro fabrication technologies [67]. After Maruo et al. utilised MPP for fabrication of 3D structures [65], it was suggested that MPP could be instrumental in manufacturing MEMS, Photonic crystals, optical memory storage, microelectronic and optoelectronic systems [8]. MEMS Fabrication is one of the most attractive applications of MPP. Micro tweezers [86] and microturbines [87] are two examples of MEMS fabricated using the MPP method. Microfluidic systems and optically driven pumps fabricated using MPP by S. Maruo and H. Inoue are other examples of MPP fabricated structures [88].

High resolution and 3D capabilities of MPP have made this an attractive technique for fabrication of photonic crystal structures. Numerous geometries have been fabricated and tested including woodpile structure [89][90], diamond lattice [91] spiral lattice [92] and complex mixture of different types of lattices. However, there are two shortcomings in utilising MPP in the fabrication of photonic crystals. First of all, the refractive index of polymers employed in MPP is not high enough to produce effective bandgaps in the air. The contrast between

the refractive index of the solid material and air should be two [93][8]. The second shortcoming is in the fine structural parameters [45]. The shrinkage and surface morphology of the structures can invalidate the photonic crystal structure and prevent the generation of stop bands in the photonic crystals [45].

There are a number of approaches to increase the refractive index of the structures fabricated using MPP, developing high refractive index monomers to be used in MPP [94] or incorporating high refractive index particles in the low refractive index photoresists [95] are two of these approaches. Structures fabricated using MPP can be used to produce a negative mould for fabrication of photonic crystals with high refractive index materials. It is possible to generate structures with sufficient contrast by backfilling the structure fabricated using MPP with a high refractive index material and removing the MPP structure using calcination or other methods [8]. MPP fabricated structures have been employed in the fabrication of silicon photonic bandgap structures using double negative method [96]. In this technique, the polymerised structure was removed after being backfilled by SiO_2 and the produced mould was filled using silicon. In the last step of this process, the silica mould was removed using hydrofluoric acid.

Creating conductive structures is another interesting application of MPP. Direct deposition and post-functionalization have been used in the fabrication of 3D metallic structures through multiphoton processes [8]. Direct deposition techniques rely on photoreduction of a metal salt or photo aggregation of metal nanoparticles. Metallic structures fabricated using direct deposition technique are composed of isolated metallic particles and have poor conductivity [21]. To improve the efficiency of the fabrication process and the conductivity of the fabricated structures Kawata et al. used Multi-photon sensitive dyes to assist with the metal reduction process [21]. In their experiments, they excited the Multi-photon sensitive dyes using a mode-locked femtosecond laser. Consequently, the electron transfer between the excited dyes and the metal ion started the reduction process. Through this process, they achieved sub-diffraction structures with superior conductivity (400 nm thick conductive

wires) [21]. To produce an array of metallic structures Formanek et al. utilised a microlens array to fabricate periodic structures and used electroless plating to deposit a thin layer of metal on top of the structures [97]. To protect the substrate and restrict the metal coating to the polymer structures a layer of hydrophobic coating was applied to the glass substrate before coating.

Post-functionalization is another promising method for selective metal coating of specific areas of design. Using photoresists coupled with metal receptive functional groups enable selective metal coating of polymer structures [98]. Kawata and his co-workers demonstrated the fabrication of polymer structures with the non-activated and activated polymer (amide-containing polymer). They illustrated that by completing the plating process, the non-activated polymer structures stayed transparent but the structures fabricated with activated polymer changed colour and accepted the silver coating [98].

The other development in multiphoton polymerization is combining this technique with other scientific instruments such as optical trapping. Optical trapping assisted multiphoton polymerization has been reported by Tsai et al. [29]. They used a 3.5 μm polystyrene bead as a microlens to further increase the resolution of their MPP setup. In their setup by utilisation of the near-field focusing effect of the microspherical beads held by OT above the glass substrate minimum feature size of $\lambda/_{10}$ was achieved. They reported that using larger particles the polymerization will occur further from the particle surface and there was lower probability of particles getting glued to the substrate [29].

Dawood et al. used a similar setup for adhering microbeads to a substrate [28]. In this work, they manipulated 5 μm carboxyl functionalized silica beads using OT and ‘glue’ the particles onto the substrate using MPP. The polymerization and trapping laser wavelength used in this experiment were close to one another, and they manage to place the particle close to the substrate and polymerise between the particle and the glass substrate. Comparing the results in the Tsai et al. paper and their far-field simulation with the work by Dawood et al. shows the effect of trapping and polymerization wavelength in the generation of a gap

between the trap position and the polymerization area. Due to chromatic aberration, the working distance of the objective lens depends on the laser wavelength. Using trapping lasers with a wavelength close to polymerization laser wavelength reduces the gap between the trap position and the polymerization area. Using two laser beams with largely different wavelengths for trapping and polymerization, places the trap further from the polymerization area and enable the usage of the particle as a microlens. In a follow-up paper published Tsai et al. they demonstrated that by placing the particle close to the substrate, no polymerization could occur [30].

It is also worth mentioning that by utilizing two different wavelengths, it is possible to produce sub-diffraction feature sizes using single photon polymerization. Scott et al. demonstrated that co-irradiation of single spot using two different wavelength and precise overlapping of these two beam spots can produce sub-diffraction features [99].

Different techniques have been used to increase the capabilities of the MPP setup and increase the processing accuracy of the MPP. Some of the key papers published in this area and their proposed methods are summaries in Table 1.

Improvement	**Method**	**Reference**
Voxel size	Changing processing Parameters	S. Kawata et al.[100]
		D. Tan et al.[101]
		Dong et al.[102]
	Radical Quenchers	K.Takada et al. [103]
		S.H. Park et al.[82]
	Efficient photoinitiator	J.f. Xing et al.[104]
	Stimulated emission depletion (STED)	L.Li et al.[71]
		J.Fischer et al.[105]
		Y.Coa et al.[106]
		R.Wollhofen et al.[107]
Shrinkage	Shape pre-compensation	H.B.Sun et al[108]

Deformation	Multipath scanning method	J.F.Xing et al.[104]
Shape distortion	Multi-dimensional slicing method	C.Y.Liao et al. [109]
Step effect	Increase the overlapping size	K.Takada et al.[110]
	Sub-regional slicing method	S.H.Park et al.[82]

Table 2. Summary of different methods for improvement of MPP processing accuracy.

2.2 Optical trapping

Optical Trapping (OT) is a precise non-contact technique to manipulate and transport a variety of particles [111]–[114]. It is a technique that can produce a force in the range of hundreds of piconewtons to move biological samples [115], [116] measure forces as fine as 100 ÅN [117]–[120] or moves objects as small as 5 nm [121], [122]. Ashkin pioneered the optical manipulation field with single-beam levitation of dielectric microparticles in air and water [123]. 3D trapping of particles using counter-propagating beams was the next big step in the development of efficient OT [124]. To make OT a practical tool to be used in diverse scientific fields, single beam OT was developed in the Bell Laboratory in 1985 [125]. It was a significant step in confirming the existence of negative optical pressure due to the gradient force [125]. Askin and his colleagues employed OT in experimenting with Neutral atoms and live bacteria [126] and [127]. After the introduction of single beam OT, many scientists experimenting with a highly focused laser beam to transport different particles and formulate sophisticated theories that explain the trapping phenomena for these particles. To date, none of these theories completely explain the optical trapping of particles with various sizes.

Capabilities of OT such as the precise force and displacement measurement and the ability to apply pico-newton-level forces to organic samples makes it a useful tool in different disciplines [112], [122], [127]–[129]. Recent technological advancements in piezoelectric stages, capacitive sensors and lasers resulted in improvements in the trapping capability and control of OT. These advancements pushed the boundaries for OT towards particles, which were not considered trappable like metallic nanoparticles. Hajizadeh and Reihani demonstrated trapping of 9.5-254 nm gold particles suspended in deionized water [130].

2.2.1 Principles of Optical trapping for dielectric particles

The radiation pressure of light was first deducted by James C. Maxwell in 1873. The force applied by a 1 W of light to a mirror is about 7 nN which is very small. The inception of laser enabled the researchers to strongly focus the beam into a tight spot and produce considerable forces to move micron scale particles [131].

The forces involved in optical trapping can be calculated using Generalized Lorenz-Mie Theory (GLMT) [114]. To explain the trapping phenomena, the particles are classified into metallic and dielectric particles. For dielectric particles with dimensions much larger than the wavelength of the trapping laser ($a \gg \lambda$), the Mie approximation provides accurate information about the trapping force and reduces the complexity of GLMT theory. In Mie regime the optical forces on the particles can be calculated using ray optics [114].

Large dielectric particles exhibit lens like behaviour. Therefore, it reflects, refracts and absorbs the light. The momentum transfer between the reflected, refracted and absorbed photons produces the scattering and gradient forces that moves the particle [128][116]. Since the momentum of each photon is very small, microscope objective lens is needed to increase the photon density and produce required force to move the particles. By focusing a Gaussian laser beam which has higher intensity at the center of the beam, the net force (F_{net}) to the particle will be toward the center of the objective lens focal volume and stable trapping can be achieved at the center of the focal volume of the objective lens. Figure 6 is a simplified diagram for momentum force transfer from a beam with Gaussian intensity profile to a dielectric particle placed off center. The net force applied to the particle force the sphere toward the center of the beam that has a higher intensity.

The scattering and gradient forces produced by the momentum transfer between the photons and the particle are the result of absorbed, reflected and refracted photons. The generated scattering force pushes the particle along the laser propagation direction and the gradient force produced in the direction of light spatial gradient stabilizes the particle in the trap [112], [114], [128], [132], [133].

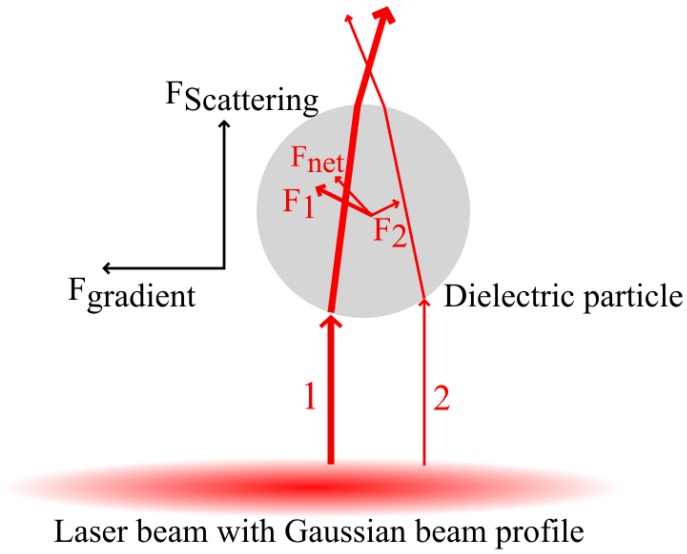


Figure 6. Ray-optic model of a particle in Mie region placed close to the focal volume of the objective lens. The force vectors show the net force applied to the particle by the laser beam. The thicker arrows (number 1 and F_1) represents the higher intensity areas of the beam and the thinner arrow (number 2 and F_2t) represent the low-intensity outer arrays of the trapping laser beam with TEM_{00} profile. The net force (F_{net}) is toward the centre of the focal volume of the objective lens which has the highest photon density. The scattering force ($F_{scattering}$) has firehose effect that pushes the particle in the laser propagation direction but the gradient force ($F_{gradient}$) pushes the particle toward the centre of the beam which has higher beam intensity. The combination of forces applied to the particle through refracted, reflected and scattered beams force the particle toward the centre of the focal volume of the objective lens.

To achieve stable trapping the gradient force must exceed the scattering force [113][133]. Utilising a high NA objective lens to focus the laser beam into a very tight spot generates a steep intensity gradient and produce large enough gradient force to suppress the scattering force [133].

The scattering force pushes the particle in the laser propagation direction, and its magnitude is dependent on the angle in which the photons reach the particle. Photons reaching the particle perpendicular to the surface have higher contribution to the scattering force. Using a high NA objective lens, the beam converges sharply after the lens and reduces the number of photons that reach the particle in near normal to the surface [133]. Photons reflected from the surface of the particle contribute greatly to the scattering force generation.

To increase the gradient force when compared to the scattering force, Simpson et al. suggested to overfill the objective lens back aperture using the beam expander [134]. By overfilling the back aperture, the outer portion of the laser

beam that has lower intensity will be truncated by the objective lens retainer ring and the light going into the objective lens has higher intensity at the edge of the beam. Therefore, the edge of the beam that converges with steeper angel has higher intensity and produces larger gradient force.

Particles much smaller than the wavelength of the trapping laser ($a \ll \lambda$) are classified in the Rayleigh scattering regime [112][135]. In the Rayleigh regime, the gradient force is generated because of the electromagnetic nature of light [136]. Based on the light intensity and the polarizability of the dielectric particle, the trapping laser polarises the molecules and produces temporary dipoles. By placing these dipoles in a non-uniform electric field, particles are pushed towards the field gradient [137].

In this regime, it is possible to simulate the optical force exerted on the particle by replacing the particle with a point dipole in the inhomogeneous field. In a Rayleigh approximation, the scattering force is generated by light absorption and re-radiation by the particles [112]. The scattering force can be calculated using Equation 13 [112]. In this equation I_0 is the light intensity, σ is the scattering cross section $n_m$is the index of refraction of the medium

$$F_{scatt} = \frac{I_0 \sigma n_m}{c} \qquad \text{Equation 13}$$

The scattering cross section can be calculated based on the particle radius *a*, the ratio of index of refraction of the particle to the medium (*m*) and the wavelength of the trapping laser (λ).

$$\sigma = \frac{128\,\pi^2 a^6}{3\lambda^4}\left(\frac{m^2-1}{m^2+2}\right)^2 \qquad \text{Equation 14}$$

The gradient force generated by the trapping laser beam is proportional to the polarizability of the particle (α) that can be calculated using Equation 15 [112].

$$\alpha = n_m^2 a^3 \left(\frac{m^2-1}{m^2+2}\right) \qquad \text{Equation 15}$$

Using α from Equation 15, the gradient force generated by the polarized particle in the inhomogeneous electric field can be calculated as follow:

$$F_{\text{grad}} = \frac{2\pi\alpha}{cn_m^2}\nabla I_0$$ Equation 16

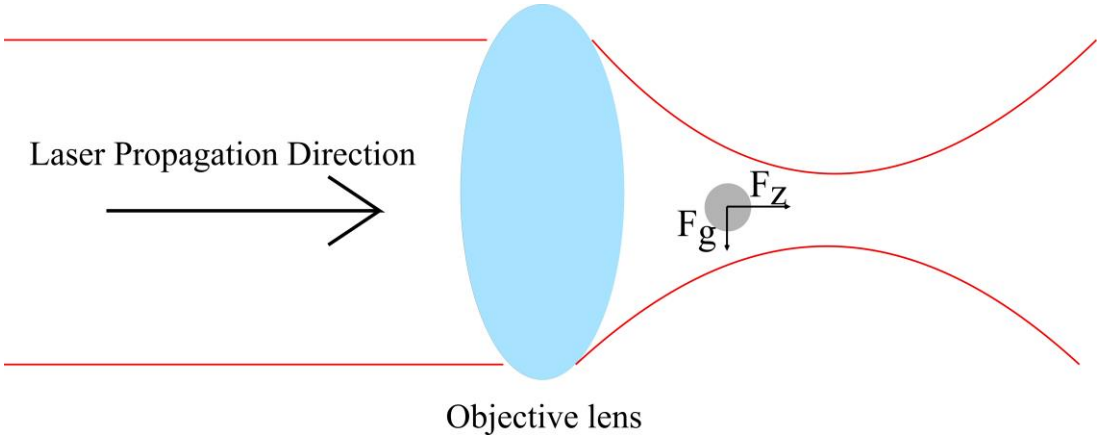


Figure 7. Gradient force and scattering force exerted to a particle placed close to the trapping beam waist. The particle is far smaller than the wavelength of the trapping laser and it becomes fully polarized. The generated temporary dipoles in the electromagnetic field become attracted to the areas with higher beam intensity. The scattering force F_z is proportional to the beam intensity and the gradient force F_g is proportional to the gradient of the intensity of the laser [131].

Particles comparable to the trapping laser wavelength ($a \sim \lambda$) have the most applications in physical science and biology. Unfortunately for these particles the ray optic model and Rayleigh approximation is not valid and more complicated electromagnetic theories must be employed to simulate the interaction of laser light with these particles [112].

2.2.2 Principles of Optical trapping for Metallic particles

Metallic particles are useful tools for probing biological samples, and because of their unique properties, researchers are interested in the precise handling of these particles [138]. Metallic particles have a complex dielectric constant, the real part of the complex dielectric constant describes the stored energy and the imaginary part describes dissipation or losses in the particle [139]. Due to their high scattering and absorption rate, metallic particles were not considered trappable [140]–[142].

K. Svoboda and S.M. Block demonstrated 3D trapping of 36 nm gold with a TEM_{00} beam for the first time [122]. In their experiment, they used a Wollaston prism to divide the trapping beam into two linearly polarised laser beams. The separated laser beams entering the back aperture of the objective lens produce two diffraction-limited spots that centred 250 nm apart in the sample plane.

These two beams produce single trap with a local minima place asymmetrically in the middle of these beams [122]. Svoboda and Block demonstrated that the trapping force for metallic particles in Rayleigh regime is almost seven times larger than dielectric particles with the same size, and this ratio is directly proportional to the ratio of polarizability of the particles [122].

The physics behind trapping metallic particles are not as well understood as dielectric particles. The interaction of the trapping laser with a particle in Rayleigh regime is divided into absorption, gradient and scattering components [122][139].

$$F_{grad} = \frac{|\alpha|}{2}\nabla < E^2 >$$ Equation 17 [122]

$$F_{scat} = \frac{n}{c}\nabla < p > c_{scat}$$ Equation 18 [122]

$$F_{abs} = \frac{n}{c}\nabla < p > c_{abs}$$ Equation 19 [122]

In this equation E is the Electric field, n is the index of refraction of the surrounding medium, p is the averaged axial component of the Poynting vector, $c_{scat}$is the scattering cross section and c_{abs} is the absorption cross section.

For stable trapping, the gradient force must exceed the sum of other forces ($R = F_{grad}/[F_{scat} + F_{abs}] \geq 1$) [143]. In contrast to dielectric particles for the metallic particles, there is no refraction and the trapping laser penetrates and polarizes the particle to the depth of few tens of nanometers. The depth that the laser beam can penetrates and polarizes a material, is defined by the skin depth of the material. The skin depth (δ) of a material with resitivity of ρ and absolute magnetic permeability of μ for the trapping beam with frequency of F can be calculated using the Equation 20.

$$\delta = \sqrt{\frac{\rho}{\pi F \mu}}$$ Equation 20 [130]

Optical trapping of metallic particles greatly depends on the particle size and the trapping beam. Based on these two factors different principals can explain the trapping of metal particles. For example, the skin depth of gold for an incident laser beam with the wavelength of 975 nm is about 43 nm. Usually, particles in

the Rayleigh regime are smaller than their skin depth, and they become uniformly polarised. Therefore, gradient force is directly proportional to the particle size [139]. For these particles, the gradient force increases faster than the scattering. Therefore, stable trapping of these particles can be achieved with low laser intensity when compared to the dielectric particles of same size [122].

Larger metallic particles become partially polarised, and the gradient force increases slower than the scattering force as the particle size increases. However, for large particles, other forces stabilise/destabilize the trap. As an example, Inhomogeneous heating of the large particle produces radiometric forces that push the particle from the focal plane of the trapping system [144].

One of the first techniques that were used for trapping metallic particles was using counter propagation laser beams to utilise the scattering force for stabilising the trapped particle [145], [146]. Another technique used for trapping metallic particles is based on the usage of TEM_{01} mode lasers [147]. Using a TEM_{01} mode laser decreases the centre rays that destabilises the trap and increases the gradient force [148].

Furukawa and Yamaguchi suggested that it is possible to trap metallic particles using the surface diffraction (creeping wave) [142]. Larger metallic particles, Silver (2 to 3 μm), gold (2 to 5 μm) and bronze (2 to 15 μm) was trapped using a Gaussian laser beam by placing the focal volume of the objective lens after the particles and gradually approaching the particle from underneath [147].

The wavelength of the trapping laser is critical for metal particles. According to Bosanac et al., if the trapping laser wavelength is close to the particles plasmon resonance frequency the laser absorption component increases faster than the gradient force. Therefore, the scattering and absorption forces exceed the gradient force, and stable trapping is not possible [139].

The trapping beam polarisation is also an important factor for trapping metallic particles. Mathematical calculation done using a radially polarised laser beam proves that 3D trapping of metallic particles is possible. The strong axial component of the tightly focused radially polarised laser beam can provide enough gradient force to overcome the scattering force and produce stable 3D trap for metallic particles [143].

Physical principles governing the optical trapping of metallic particles are not well understood. Different groups have attempted trapping and manipulation of metallic particles using dissimilar techniques, and in some cases their findings are contradictory. Hansen et al. demonstrated optical trapping of metallic particles ranging from 18 nm to 254 nm. They suggested that the technique to significantly increase the capabilities of the OT is to expand the laser beam to slightly overfill the objective lens, so the Gaussian beam tail is not cut off by any optics [144]. However, others suggested that the centre rays mainly contribute to the scattering force and by largely overfilling the objective lens back aperture, it is possible to increase the intensity of the outer rays entering the objective lens. By overfilling the objective lens back aperture, the intensity gap between the centre rays that reach the particle in near perpendicular angle and the outer rays decreases. Therefore, the gradient force produced by outer rays will increase [112], [139], [149].

2.2.3 Determining the trapping force

The strength of the optical trap depends on the particle, its surrounding medium, trapping laser and the optical apparatus used for trapping. Using equation 21 [113] the maximum trapping force applied to a particle with a refractive index of n_1 trapped by the laser power P can be calculated [113]. Q is the scaling factor that depends on the particle size and the ratio of the refractive index of the particle over its surrounding medium.

$$F = Q\left(\frac{n_1 P}{C}\right) \qquad \text{Equation 21}$$

The intensity gradient (∇I) must be maximized to increase the trapping efficiency. High NA objective lenses focus the laser beam into a tight spot and the beam's intensity gradient increases sharply as it reaches the objective lens

focal point [150]. Equation 22 shows the effect of the objective lens aperture size (D) and its working distance on the OT beam waist.

$$w_{trap} = \frac{1.22\lambda}{2D}\sqrt{\left(\frac{n}{NA}\right)^2 - 1} \qquad \text{Equation 22 [113]}$$

In building an OT setup, the trap waist is the limiting factor for the trapping efficiency and it is crucial to get the most out of the high NA objective lens by filling the objective lens back aperture [112]. Different beam expanders can be used to expand the laser beam. Galilean beam expanders (Figure 8) are one of the most popular choices to be employed in an OT setup. A Galilean beam expander's simple design, low manufacturing cost and small package size has made it a popular choice for the optical systems. The Galilean beam expander consists of a negative input lens and a positive output lens that can have high expansion ratio. There are other types of beam expanders like the Keplerian beam expander. Keplerian beam expanders (Figure 8) can achieve larger expansion ratio, and spatial filtering is possible by placing a pinhole at the focus of the first lens. Keplerian telescope uses positive input and output lenses.

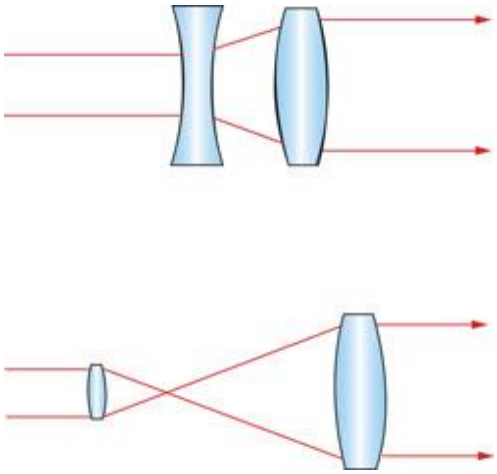


Figure 8 Galilean beam expander top vs keplerian beam expander. In Keplerian beam expander, beams which are not parallel to the optical path can be blocked by placing an iris (pinhole) at the focal point between two lenses.

Another factor that can decrease the trapping quality is the spherical aberration in the system. Spherical aberration distorts the Gaussian intensity profile of the beam and deforms the PSF produced by the objective lens. Therefore, it spreads the laser power over a larger spot and decreases the trapping efficiency[151].

Multiple dielectric particles can be trapped using a single trapping beam and the trapping force changes by increasing the number of particles in the trap. The trapping force is generated by the refraction of light and by increasing the refraction the trapping force increases [152]. Depending on the size, number and arrangement of particles, the trapping force may increases or decreases. Bhatt et al. studied the effect of particle number on the trapping force, with particles ranging from 330 nm to 2.47 μm, the trapping force increases by trapping the second particle and it reduces after trapping the third particle [152].

The trapping force can be calculated experimentally by considering the balance between the Stokes' drag force and the restoring force that keeps the particle in the trap while being transported [153] [154]. The Stokes' drag force can be calculated using Equation 23. In this equation a is the particle radius in meter, v is the particle travel speed, and η is the viscosity of the medium in Pa.S.

$F = 6\pi a v \eta$ Equation 23 [113]

Transporting the particles in its surrounding liquid produces the drag force that acts against the trapping force. By increasing the transportation speed the Stokes' drag force generated by the liquid increases to the point that suppress the trapping force and dislocate the particle from the trap. Based on the transportation speed and the viscosity of the surrounding liquid (i.e. a photoresist), the Stokes' drag force needed for removing the particle from the trap can be calculated [116].

While the particle is being manipulated by the optical trap, it can moves inside the trap. The optical trapping force is proportional to the distance between the particle and the beam waist [155]. Video-based position detection is the simplest technique to detect particle position. This technique relays on the camera and the light source. The position of the particle can be monitored with sub-pixel accuracy with the help of image recognition software. Video acquisition rate is the limiting factor of this technique.

Using a quad photodiode is one of the most popular laser-based techniques to monitor the position of the particle. This technique uses the interference between

the light that was scattered by the bead and the unscattered light to identify the position of the particle [112].

2.2.4 Advance trapping setups

A basic single beam OT setup which is demonstrated in Figure 9 consists of 5 main sections: a trapping laser, beam expander, an objective lens, imaging system and the stage. There are many variations of OT setups with additional components to enhance the performance of the OT. To be able to control the position of the trap, 2D Galvanometer Mirrors (GM) can be used. The GM changes the angle that the laser beam enters the objective lens back aperture. Therefore, the position of the objective lens focal point moves in its field of view.

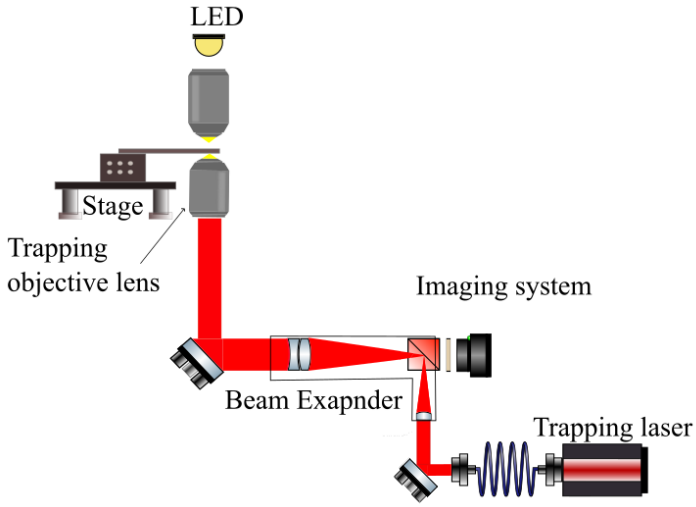


Figure 9 Basic OT system that has the capability of trapping single particle has 5 main sections. 1) The trapping laser, 2) A beam expander to fill the objective lens back aperture. The distance between two lenses are set to f_1+f_2 and appropriate lenses must be used to produce the necessary expansion. 3) An objective lens that focus the laser beam on the particle, 4) A stage to move the chamber as the trapped particle stays stationery and 5) An imaging system to observe the trapping procedure.

Complex OT setups have been developed to expand the OT capabilities and applications. Trapping metallic nanoparticles is one of the applications, which is challenging to perform using the basic OT setups. To be able to trap metallic nanoparticles, evanescent waves generated by micrometer-sized gold disks can be used. In this configuration, the laser beam is coupled into the gold microdisks using a prism and the surface evanescent wave generated on the front side of the microdisks enable the trapping of dielectric nanoparticles [156].

Another creative innovation to increase the capabilities of OT is producing nano-tweezers by focusing the trapping beam into a sub-diffraction limit double-nano holes created in a gold film [157]. Jamshidi et al. managed to trap 60 to 250 nm metallic particles using Opto-Electronic Tweezers (OET) shown in Figure 10. Due to very low laser power (20 µW) used in trapping particles, they reported temperature increases of less than 0.1°C [158]. OET functions based on optically induced electrophoresis and consists of two Indium-Tin-Oxide electrodes sandwiching a thin layer of Photoconductive Material (PCM) and the particles suspended in the liquid. The combination of the AC power supply connected to the ITO electrodes and the laser source that excites the PCM enables trapping of metallic nanoparticles. When the laser is off, the AC voltage drops across the PCM, but by focusing the laser beams on the PCM layer, its local impedance decreases below the liquid impedance. Therefore, the voltage drops occurs in the fluid. The inhomogeneous electric field (Figure 10a) inside the liquid polarises the metallic particle and attract them to areas that the laser beam is focused [158].

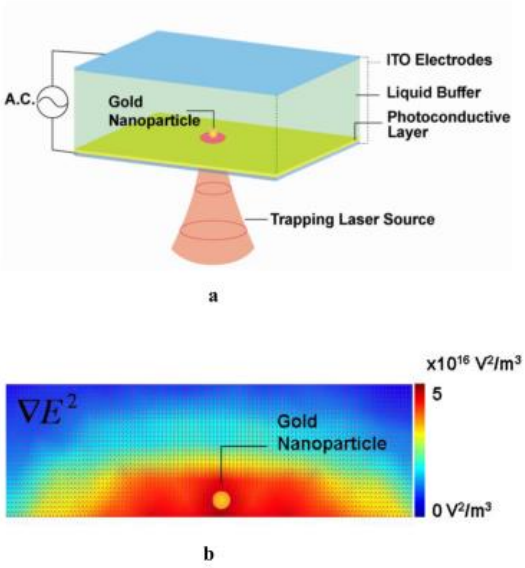


Figure 10 (a) OET tweezers setup for manipulation of nanoparticles based on optically induced electrophoresis. (b) Simulation of gradient electric field intensity [158].

Combining OT with other fabrication technique is one of the avenues that can greatly increase the application of OT. Linnenberger et al. integrated a commercial OT setup with a maskless lithography setup (SLA) to control the

position of cells in a hydrogel microstructure. In their experiment, they managed to align live cells in a line and encapsulate them in a hydrogel using UV light [159].

Holographic Optical Trapping (HOT) is also another example of new OT setups, which are designed to answer the growing need to control micron size particles with high precision and manoeuvrability. Using HOT a single laser beam can be divided into an array of traps that can be controlled independently [135], [160]–[162]. Because of the potential application of HOT in the future of this work this section is dedicated to explaining different types of HOT, their capabilities and drawbacks of each setup.

In the past few years Holographic Optical Tweezers (HOT) and optical trapping have been studied by several research groups [64], [129], [148], [163], [164]. HOT systems tend to be more complicated than the basic OT setups. Curtis et al. demonstrated the generation of 400 traps (an array of 20 by 20) using a single laser beam reflected from a Spatial Light Modulator (SLM) device. Here, each trap could be controlled independently using computer-generated holograms [148]. The main component that allows a single laser beam to divide into a number of controllable traps is a light modulator [165]–[167]. The SLM is a device that changes the phase, intensity or polarisation of the light [135]. The SLM uses a liquid crystal layer to reflect the expanded laser beam. Based on the technique that changes the position of the molecules in the liquid crystal it can be classified as an Electrically addressed SLM (ESLM), and Optically addressed SLM (OSLM). The ESLM devices use electrodes that are etched on a silicon substrate to modulate the liquid crystal molecules. The ESLM has very high refresh rate and high resolution. However, poor phase modulation and surface flatness make them undesirable for some applications but not OT [168].

The OSLM uses a layer of photosensitive material sandwiched between 2 electrodes to modulate the refractivity of the liquid crystal. The external light source employed in OSLM project an intensity pattern to produce a spatially

varying electric field in the photosensitive layer and respectively produce the patterns generated by the applied voltage [135].

Light modulators can be classified as electrical or mechanical. Digital Mirror Device (DMD) uses an array of micromirrors to reflect the laser beam and each of the mirrors can be controlled independently. DMD works based on changing the beam trajectory. Different types of DMD is available and being used in different commercial Day Light Projection (DPL) stereolithography machines like Autodesk Ember DLP printer.

Using each system, SLM or DMD, to produce multiple traps using a single laser beam has its advantages and drawbacks. Typically, SLM that utilizes a Liquid Crystal (LC) display has higher modulation speed and pattern refresh rate when compared to DMD but recently high refresh rate DMD devices has been introduced by Texas Instrument. The main disadvantage of SLM is the low damage threshold of the LC display [150]. Using a dielectric coating has been shown to increase the SLM damage threshold to 10 W/cm^2 (Peter Brunt, personal communication, September 9, 2013) which is an acceptable range for most applications.

2.2.5 Afocal systems

An afocal system is a system that produces no net divergence or convergence, therefore it has no focus point [169]. The parallel beams entering the beam expander exits the system parallel to the system optical axis and the net divergence or convergence is zero. Therefore, the beam expander can be considered as afocal system [154].

It is possible to change the convergence or divergence of the beam expander exiting beam By changing the distance between the first and second lens in the beam expander. by increasing (decreasing) the gap between the first and second lens, the beam going into the objective lens back aperture converges(diverges) accordingly. The reference focal distance of objective lenses is calculated using parallel beams entering the back aperture of the objective lens. Having a convergent beam going into the objective lens decreases the focal distance of

the objective lens. If the beam entering the objective lens is divergent then the beam focus point will be further from the objective lens tip than its original focal distance (Figure 7).

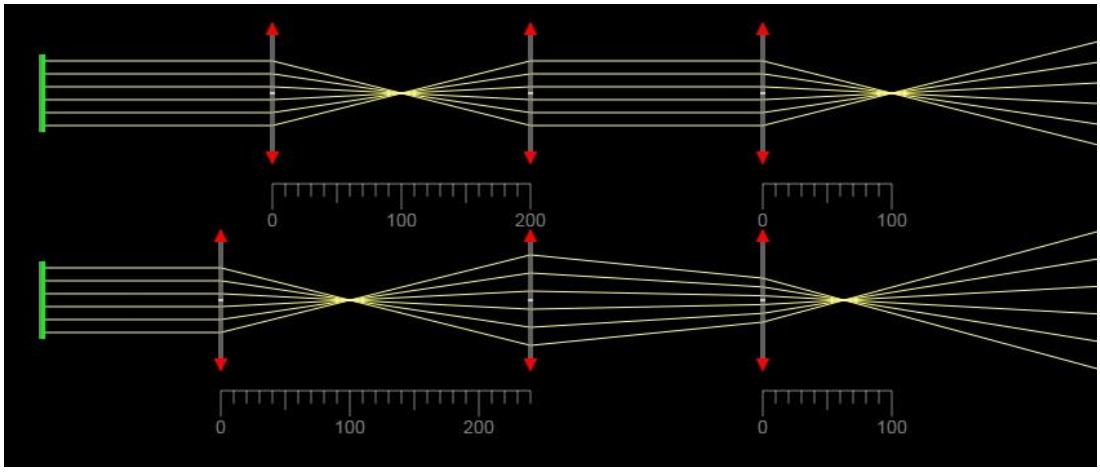


Figure 11. The effect of utilization of beam expander to change the divergence of the beam entering the back aperture of the objective lens. The figure demonstrated that by slightly increasing(decreasing) the distance between the lenses in the beam expander, the outgoing beam moves from parallel to diverging(converging) beams and moves the focus point of the objective lens moves closer (further) to the objective lens.

The focal distance of the objective lens is also affected by the laser wavelength. The refractive index of materials is wavelength dependent therefore, beams with different wavelengths converge onto various focal planes. Using an afocal beam expander is particularly important in systems that utilizes multiple laser sources with widely different wavelengths. An afocal beam expander can be used to change the working distance of the objective lens for one or a number of lasers to enable the system to have similar working distances regardless of the radiation source.

Changing the distance between the two lenses in the beam expander distort the PSF produced by the objective lens. The PSF for a perfect optical system with circular elements would be an Airy pattern. Equation 24 shows the radius of first dark ring around the Airy disk. The centre disk has the highest laser intensity and the polymerization/trapping occurs within the centre disk. In the z-axis the dimension of the high-intensity pattern is calculated using Equation 25.

Equation 24 $$D_{X,Y}\frac{0.61\lambda}{NA}$$

Equation 25 $$D_z = \frac{2n\lambda}{NA^2}$$

As it was mentioned in section 2.1.4, the distortion in PSF increases the minimum feature size attainable for the MPP system. For optical trapping distorted PSF reduces the gradient force generated by the trapping beam and destabilized the trap. Figure 12 shows the ideal PSF generated using a high NA objective lens in X-Z and X-Y planes. **Error! Reference source not found.** shows the diffraction pattern generated by focusing the polymerization laser beam on a reflective sample using a 50X objective lens.

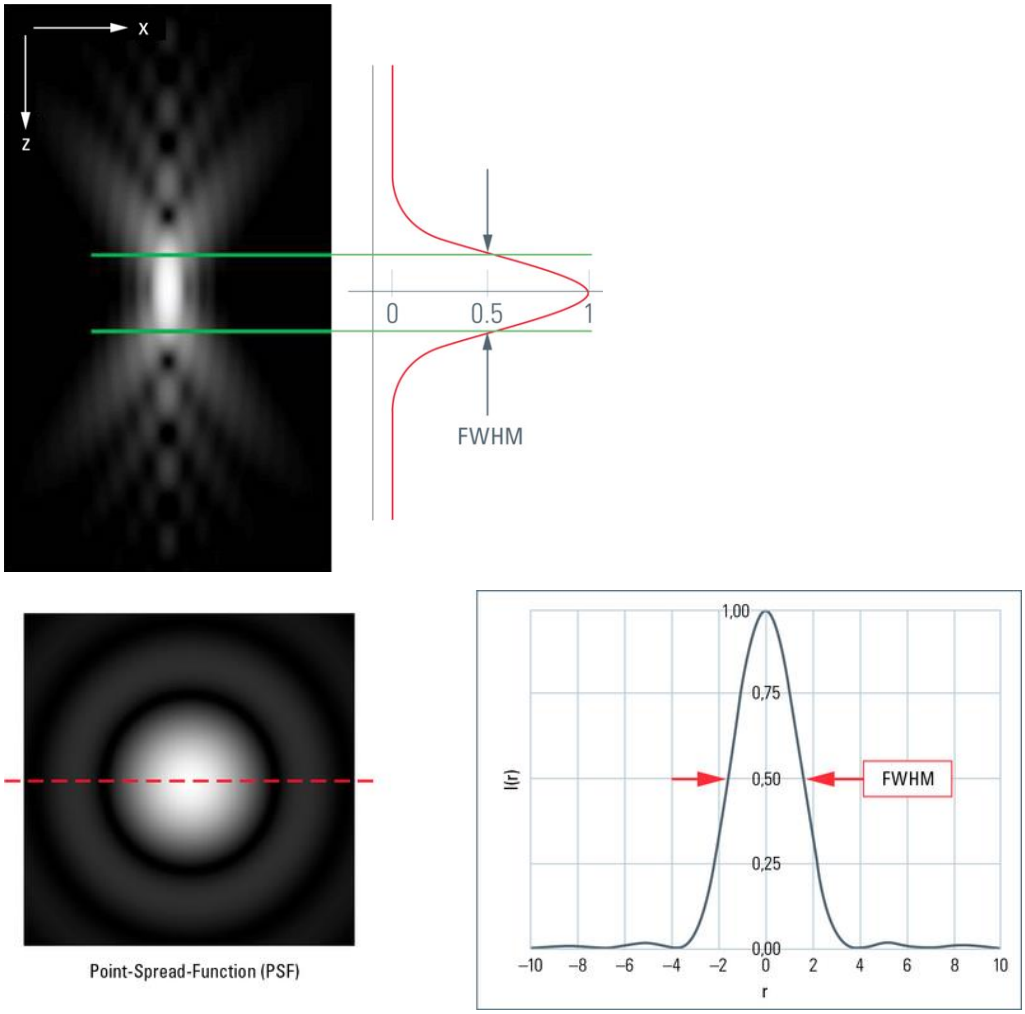


Figure 12 The diffraction pattern generated by an infinitely small point source at the imaging plane of a high NA objective lens. (Top) Lateral view (X-Z) of PSF generated using high NA objective lens and its relative intensity plot (top). (Bottom) Axial view

(X-Y) view of PSF and Airy disk generated with its relative intensity plot. Images by Leica Microsystem, Germany.

2.3 Metamaterials

The prefix “meta” in Greek means “beyond” and metamaterials are materials designed to have novel electromagnetic properties that are beyond the normal interaction of light with matter. The presented definition is not the only definition, and the term metamaterial had been defined by the European’s Union Metamorphose network as “an arrangement of artificial structural elements, designed to achieve advantageous and unusual electromagnetic properties” [170]. In this definition, it is pointed out that: Metamaterials are human-made materials, and their properties are not found in nature. The building block of the metamaterial is called a meta-atom, which is far smaller than the metamaterial functioning wavelength [171]. Therefore, the inhomogeneous microstructure could be considered as a uniform material [172][173]. The interaction of light (electromagnetic wave with intended wavelength) with a metamaterial structure is governed by the structure of the metamaterial rather than an individual material’s properties [174]. Effective material permeability and permittivity must be calculated for metamaterials that depend on the geometry of structures. One of the oldest metamaterial structures built is the Lycurgus Cup. In this ancient cup, gold and silver particles were embedded in a glass matrix. The cup’s colour changes based on the lighting in the room [171].



Figure 13. the only intact Lycurgus Cup that is held in the British Museum. Copyright the Trustees of the British Museum [175].

In the study of metamaterials and their application, there were three major steps. It started with the mathematical prediction of the negative refractive index by Veselago at 1968 [176] followed by the seminal paper published by Smith et al.,

that experimentally proved the existence of negative index materials [177]. The third major advancement in metamaterials was the work done by Pendry et al., who theorized the possibility of building a perfect lens using left-handed material [178].

Currently, optical metamaterials are one of the most exciting and challenging topics, and due to the advancements in nanofabrication and imaging technologies, there is an increase in the optical metamaterial research [179]. Due to their unique ability to manipulate and control light in ways that were not possible before a wide variety of applications has been proposed for metamaterials. Researchers have had some progress in applications like metamaterial antennas [180][181], photonic crystals [96][182], waveguides and perfect lenses [178], but they are in their early development stages [171].

2.3.1 Working Principle and Structure of metamaterials

Maxwell's equations describe the interaction of light (electromagnetic waves) with materials [27]. These equations are based on the interrelationship of the field, sources, and the material properties [171]. Two parameters that describe the effective electromagnetic properties of a material as a whole are permittivity (ε) and permeability (μ).

The basic building block of the crystalline structure is called the unit cell. In the unit cell atoms are fashioned into different geometrical shapes, a few angstroms apart from each other. The electromagnetic (EM) wave polarises the atoms and produces periodic inhomogeneous fields inside the crystal. On a macroscopic scale, the incident light sees the crystal structure as a uniform structure and by averaging the effect of each dipole macroscopic parameters like permittivity and permeability can be calculated.

In metamaterials, meta-atoms behave similarly to the crystal unit cells. By artificially tailoring the meta-atoms size and design the optical properties of the metamaterial can be changed.

The refractive index of the materials can be calculated using the relative permittivity and permeability of the material [183].

$n = \sqrt{\mu_r \varepsilon_r}$ Equation 26

For all non-magnetic materials (most natural materials), the permeability of materials (μ) in the visible region is nearly 1, and the refractive index is only dependent on the relative permeability or the dielectric constant. The dielectric constant (ε) can have a complex form and the imaginary part of the dielectric constant represent the energy absorption inside the material [184].

The refractive index of materials (n) can be represented by two parameters of ε and μ that produces 4 possible sets of materials [173]. The majority of materials have positive permittivity and permeability. In these materials the direction of the induced electric / magnetic field is in the incident wave direction. Nobel metals in optical frequencies exhibit negative permittivity and ferromagnetic materials near their resonance frequency have negative permeability [185] & [186]. One of the most significant properties of an optical metamaterial is the negative refractive index, which is not available in nature. Veselago described that an EM wave that propagates into a double negative metamaterial from a standard environment becomes refracted between the first and second mediums but there is no reflection [176].

In metamaterials with unit cells much smaller than the wavelength of light, the refractive index n can be calculated using Equation 25 [174].

$n = n' + in'' = \sqrt{\mu\varepsilon}$ Equation 27

$$\boldsymbol{\varepsilon = \varepsilon' + i\varepsilon''}$$

$$\boldsymbol{\mu = \mu' + i\mu''}$$

It is sufficient to have to $\varepsilon' < 0$ and $\mu' < 0$ to achieve negative refractive index, but it is not necessary [174]. Metamaterials with negative refractivity can be used in optical antennas, super lenses and hyper lenses with very high resolution [181].

The ultimate metamaterial is a coating that can make an object invisible to naked eye. To make an object invisible, the metamaterial must work in a broad range of frequencies and wavelengths starting from 390 to 790 nm. The unit-cell of such a metamaterial must be far smaller than 390 nm and it should be very efficient. Gold and silver and other metals have a negative dielectric constant at all frequencies but materials with negative magnetic permeability in the visible frequency are not available [185].

Different structures have been proposed by scientists to fabricate efficient metamaterial structures. Split Ring Resonators (SRR) is one of the most well-known structures for metamaterials [177]. The metallic layer has negative dielectric constant. The SRR structure acts like an inductor-capacitor tank (L-C tank) with the resonant frequency of f_c [187]. The resonant frequency can be calculated using Equation 26 [188], the inductance (L) and capacitance (C) of the SRR can be calculated using equations 27 & 28 [188]. In these equations D is the distance between parallel plates of a capacitor, A is the electrode area, ε dielectric constant, $\mu_o$is permeability, *l is* wire length, *d* distance from wire and *a* wire radius. Y is a constant equal to 0.5 for uniform current in cross-section of the wire and Y=0 for uniform current on surface of the wire.

$$f_c = \frac{1}{\sqrt{LC}} \qquad \text{Equation 28}$$

$$L = \frac{\mu_{ol}}{\pi}\left(ln\left(\frac{d}{a}\right) + Y\right) \qquad \text{Equation 29}$$

$$C = \frac{\varepsilon A}{d} \qquad \text{Equation 30}$$

These equations show the relationship between the operating frequency of the metamaterial and the SRR design. From equation 26, it's clear that by decreasing the capacitance and inductance values the operation frequency of the structure increases. By decreasing the SRR dimensions (*A*, *l* and *d*), it is possible to increase the operation frequency of the structure. Therefore, the SRR structures functioning in the visible frequency must be far smaller than ones operating in the microwave region. Using SRR different research groups have achieved negative refractive indices up to 200 THz [189]–[191]. One of the limiting factors above 200 THz is the metal conductivity at high frequencies. Metals can

be considered as an ideal conductor with infinite carrier density and zero kinetic energy below 200 THz but above 200 THz ($\lambda = 1.5\,\mu m$) the required miniaturization leads to a non-ideal conductor behavior in the metal (finite velocity and kinetic energy). Because of the miniaturization and fabrication problem new structures and methods have been proposed for THz region that their active frequency is independent of SRR size [11].

The proposed structure for higher frequencies and shorter wavelengths is based on parallel metallic strips spaced by a dielectric layer. The parallel metallic strips with a dielectric layer in between act as a capacitor and each rod can function as an inductor [174]. In the design process for a new metamaterial structure, Shalaev et al. faced a critical issue to overlap regions with negative permittivity and permeability. They proposed a metallic mesh structure that provides $\varepsilon<0$ in a broad range of frequencies and solves the overlapping problem. The metallic mesh structure consists of 2 metallic layers (50 nm Au) with a spacer layer (50 nm SiO_2) between the metallic layers [11].

The standard fabrication method for fabricating structures that were described earlier is Electron-Beam Lithography (EBL). In EBL, a highly focused electron beam is used to pattern the surface. Etching, deposition, and lift-off processes are essential to fabricate multi-material structures using EBL. A group at Karlsruhe Institute of Technology achieved $n' = -2$ at $\lambda \sim 1.5$ μm using fishnet structures [192]. Going towards shorter wavelengths $n' = -0.9$ and -1.1 at 780 and 810 nm achieved by a group at Purdue University [185][193].

Fabrication of optical metamaterials with sub-diffraction resolution is an integral part of metamaterial research. In past two decades, the advancements in nanofabrication technologies boosted the metamaterial research. Currently, focused ion beam milling, electron beam lithography, nanoimprinting and direct laser writing are the main techniques used in the fabrication of metamaterial structures. All these techniques are 2D patterning techniques and building functional 3D metamaterial structures remains a daunting task [171].

2.3.2 Effective Material Approximation theories

Composite structures fabricated with a combination of two materials exhibit properties different from both materials. The effective properties of the composite material depend on properties of the materials used and their filling factor. There are two widely used approximation theories governing the effective medium parameters, Maxwell-Garnett [27] and Bruggeman [26] theories, either one of them can be used to approximate the effective parameters of composite structures [25]. The mathematical fabric of these two theories is different, but both theories work based on random unit cells. These unit cells are not detectable by the intended electromagnetic wave and consist of both materials with the same ratio as the composite material. Maxwell-Garnett effective material approximation is more accurate while the filling factor is low (limited to $f \leq 0.7$) since the separate grain structure could not be maintained in high filling factor [25], [194].

The effective dielectric constant of a composite (ε_e) can be calculated using Equation 29 [25]. The effective dielectric constant depends of the dielectric constant of the medium (ε_m), the dielectric constant of the inclusions(ε_i) and the filling factor of the inclusions.

$$\frac{\varepsilon_e-\varepsilon_i}{\varepsilon_e+2\varepsilon_i} = f\frac{\varepsilon_m-\varepsilon_i}{\varepsilon_m+2\varepsilon_i} \qquad \text{Equation 31}$$

In Bruggeman's approach the composites are characterised based on the materials properties (A_{I} & A_{II}) and their filling factors (φ_{I} & φ_{II}). For convenience $\varphi_{\mathrm{II}} = \varphi$ and $\varphi_{\mathrm{I}} = 1 - \varphi$. When the filling factor for the second material is small ($\varphi_{\mathrm{I}} = 1$), the effective material parameter of A_{eff} can be written as Equation 30 [195].

$$A_{eff} = A_I(1 + f(A_I, A_{II})\varphi) \qquad \text{Equation 32}$$

The function $f(A_{\mathrm{I}}, A_{\mathrm{II}})$ has been calculated for variety of specific systems. The function f can be written as $f(A_{\mathrm{I}}, A_{\mathrm{II}}) = (\alpha A_{\mathrm{I}} + \beta A_{\mathrm{II}})/(\gamma A_{\mathrm{I}} + \delta A_{\mathrm{II}})$[195], so the equation 30 will transform to equation 31 [195].

$$A_{eff} = A_I \left(1 + \frac{\alpha A_{II} + \beta A_I}{\gamma A_{II} + \delta A_I} \varphi\right) \qquad \text{Equation 33}$$

For spherical inclusions, the effective dielectric constant of the composite material is calculated using α=3, β=-3, γ=1 and δ=2. Therefore, the equation 31 is transformed to:

$$\varepsilon_{eff} = \varepsilon_I \left(1 + \frac{3(\varepsilon_{II} - \varepsilon_I)}{\varepsilon_{II} + 2\varepsilon_I} \varphi\right). \qquad \text{Equation 34}$$

2.3.3 Photonic crystals

Photonic crystals are a class metamaterials that are designed to slow down light propagation. Dielectric materials with high refractive index slow the light as it propagates through it and the slow light produces structure dependent functionalities [196]. The nonlinear effects scale with the square of the slowdown factor but linear effects such as electro-optic and thermo-optic interactions scale with the slowdown factor [197]. Photonic crystals play an indispensable role in the utilisation of light waves for light storage and computation [198]. An analogy between semiconductors and photonic crystals can be beneficial for understanding the working principles of the photonic crystals. Electrons and photons have a dual nature; they can behave like a particle or a wave. Electrons propagate through a crystal structure as a wave. The arrangement of atoms in the semiconductor lattice structure produces periodic potentials that affect the electron waves while propagating through the crystal. Residing atoms in the lattice and the lattice geometry are the two governing factors that affect the electrons propagation. The semiconductor crystal structure stops electrons with specific energy from propagating through the crystal. Blocking electrons with specific energy produces the semiconductor bandgap. The semiconductor bandgap is a range of forbidden electron energies that can't be occupied by the electrons. The same principle applies for photons travelling through the periodic structure of photonic crystals. The photonic crystal microstructure constructed using materials with different dielectric

constant (refractive index). The periodic change in the dielectric constant of the structure produces local potentials that can block some of the photons and produce an optical bandgap [199]. The existence of a photonic bandgap was proposed in the early 1980s [200]. Development of lasers in the 20th century was an important milestone to increase the applications of photonic bandgap crystals.

A Bragg mirror (Reflector) can be a 1D photonic crystal. The reflection of an EM wave from the first and second layer of a dielectric material produces constructive interference and total light reflection can be realised.

$$2n_{average}dcos(\theta) = m\lambda \qquad \text{Equation 35}$$

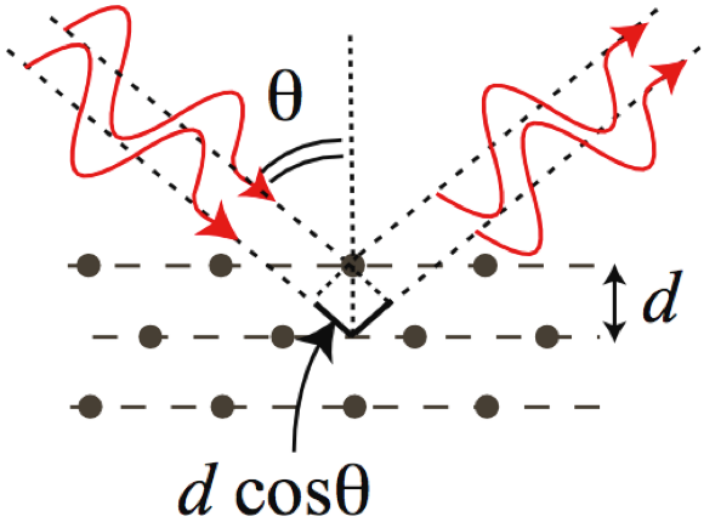


Figure 14. A Bragg mirror with three dielectric layers.

Designing Photonic crystals with an extended band gap is a complicated task. To produce wide bandgap high refractive index materials are needed. This material must have very low losses in the wavelength of interest (less than 1 dB/cm).

There are two distinct resonance scattering mechanisms in the photonic crystals. These two mechanisms should occur at precisely the same wavelength To have an effective bandgap. The primal resonance scattering mechanism is macroscopic Bragg resonance, demonstrated in Figure 14. The light reflects at the air-glass boundary. To have a strong scattering signal, the integer number m

= 1,2,3 of half wavelength ($\lambda/2$) must be equal to the photonic crystal unit cell length L ($m\lambda/2 = L$).

The second resonance scattering mechanism is the microscopic scattering within a single particle (dielectric element) in the photonic crystal. To increase the microscopic scattering rate, a quarter of a wavelength must be equal to the size of single dielectric element ($\lambda/4 = 2a$). Figure 15 represents a section of a photonic crystal structure and an illustration of dielectric wells with potential of *ε(x)*.

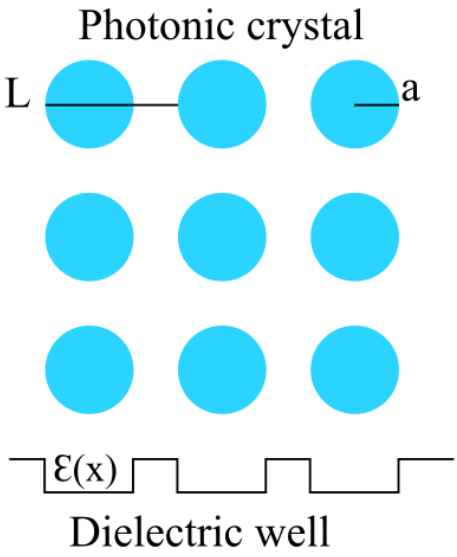


Figure 15. The side view of a 2D photonic crystal structure with blue circles representing high dielectric constant (refractive index) areas and the dielectric well representation of the structure of work function of ε(x).

Photonic crystal fibres are new class of optical fibres that operates based on the properties of photonic crystal and its ability to confine light in the core of the fibre. 3D Photonic crystals can be employed in the fabrication of efficient light-emitting diodes, radio frequency antennas, optical filters, waveguides [201] and lasers [202].

2.4 Literature review summary and the gap in knowledge

Multi-photon polymerization is a third-order nonlinear technique with a sub-diffraction limit resolution that can fabricate freestanding 3D structures [8], [83], [197]. MPP is not limited to polymer structures, and some progress has been made in the fabrication of metallic structures with submicron features using direct and indirect deposition [21]. This process is not efficient and generates isolated metallic particles with poor conductivity [203].

OT is a noninvasive precise method for transportation of a wide variety of particles [127]. OT of dielectric particles in Mie regime occurs due to the momentum transfer between the photons and the particle. The dielectric particles behave similar to a negative lens, and the refracted/reflected light pushes the particle toward the area with higher photon density, which is the focal volume of the objective lens [114].

Metamaterial structures are manmade structures that exhibit properties dependent on both their structure and building material [204]. The building block of the metamaterial is called a meta-atom, which is far smaller than the metamaterial interested wavelength [171]. Therefore, the inhomogeneous microstructure could be considered as a uniform material in the operational frequency of the metamaterial [172][173].

2.4.1 The Gap in the knowledge

The micro-fabrication processes for metamaterials with high operation frequency are costly and time-consuming [11]. Therefore, it is favourable to find a new technique for fabrication of metamaterial structures. A MMAM technique with sub-diffraction limit resolution is a good candidate to replace conventional manufacturing techniques.

MPP is a promising AM technique that has sub-diffraction limit resolution and multi-material MPP structures have been demonstrated in a number of research papers [18] [19]. These papers demonstrated the advantages of multimaterial MPP systems, but the structures fabricated in these papers were built by

repeating the fabrication/development steps for all the materials involved. Therefore, they failed to deliver a true MMAM technique.

The approach taken by Dawood et al., which demonstrated local immobilisation of microbeads using simultaneous utilisation of OT and MPP, was the stepping-stone for a new generation of hybrid MPP systems [28]. Although they didn't embed particles inside the polymer matrix to produce composite structures, they showed the potential of the hybrid MPP-OT system for immobilization of trapped particles in a specific arrangement. Other papers that used OT assisted MPP, achieved widely different results and the trapped particle behaved as a microlens placed before the polymerization area. Consequently, particle immobilisation was not achieved and the polymerization occurred further from the particle surface [29][30].

By comparing the papers that demonstrated simultaneous utilization of OT and MPP, it was understood that the position of the trapped particle when compared to the polymerization area is the critical factor in the system functionality and limitations. The gap between the polymerizing and trapping areas is produced by:

1) Chromatic aberration in the system. Due to the chromatic aberration, the objective lens has longer working distance for the laser beam with a longer wavelength. Therefore, by not using similar wavelengths for the OT and MPP section of the combined OT-MPP setup the system suffers from the gap between the polymerization and trapping area. To overcome the effect of chromatic aberration it is possible to choose the trapping laser wavelength close to the polymerization wavelength but it limits the available wavelengths for trapping and polymerization. Not being able to freely choose the polymerization wavelength hinders the ability of the system to use different photoresists and limits the capabilities of the setup. The trapping force is also wavelength dependent, and the laser wavelength is an especially important factor in trapping metallic particles and biological samples [205].

b) The equilibrium position for the trapped particle may occur further from the objective lens focal volume. Non-spherical particles are often trapped outside the focal volume of the objective lens [200], which can broaden the gap between the trapping and polymerization areas.

To be able to use a combined OT-MPP setup to fabricate hybrid structures (metamaterial structures), the system must be able to overlay the polymerization and trapping areas regardless of the laser wavelengths or the particles used in the system. The new versatile combined OT-MPP setup can increase the potential applications of the combined OT-MPP system and reduce the limitations of the system. The system that can compensate for the gap between the trapping and the polymerization areas can be used for encapsulation a variety of particles in different photoresists. Yet, such a system is not available, and particle encapsulation using combined OT-MPP has not been demonstrated. Current systems cannot produce similar results for different photoresists, and by changing the polymerization/trapping wavelength or the particle size/shape, the results may change.

2.4.2 Potential applications

Opti FDTD software was used to perform a 2D simulation of an array of particles embedded in the photoresist. The refractive index of the photoresist used in this experiment was 1.47, which increased slightly after polymerization [76]. The refractive index of melamine beads utilised in the experiment was 1.68. The contrast between the refractive indices of the polymer and particles are not enough to produce complete stop bands. In the FDTD simulation of structures with melamine beads, effective bandgap was not realised. By increasing the refractive index of the particles, complete bandgap was generated in the photonic crystal with particle refractive index of 3.1. The calculated bandgap is presented in Figure 16. In this simulation array of 3 μm particles (blue circles) was placed 5 μm apart from each other to mimic the particle size and arrangement of fabricated structures. Two observation points (small green

circles were placed through the structure, and the red line at the left-hand side of the figure shows the excitation source.

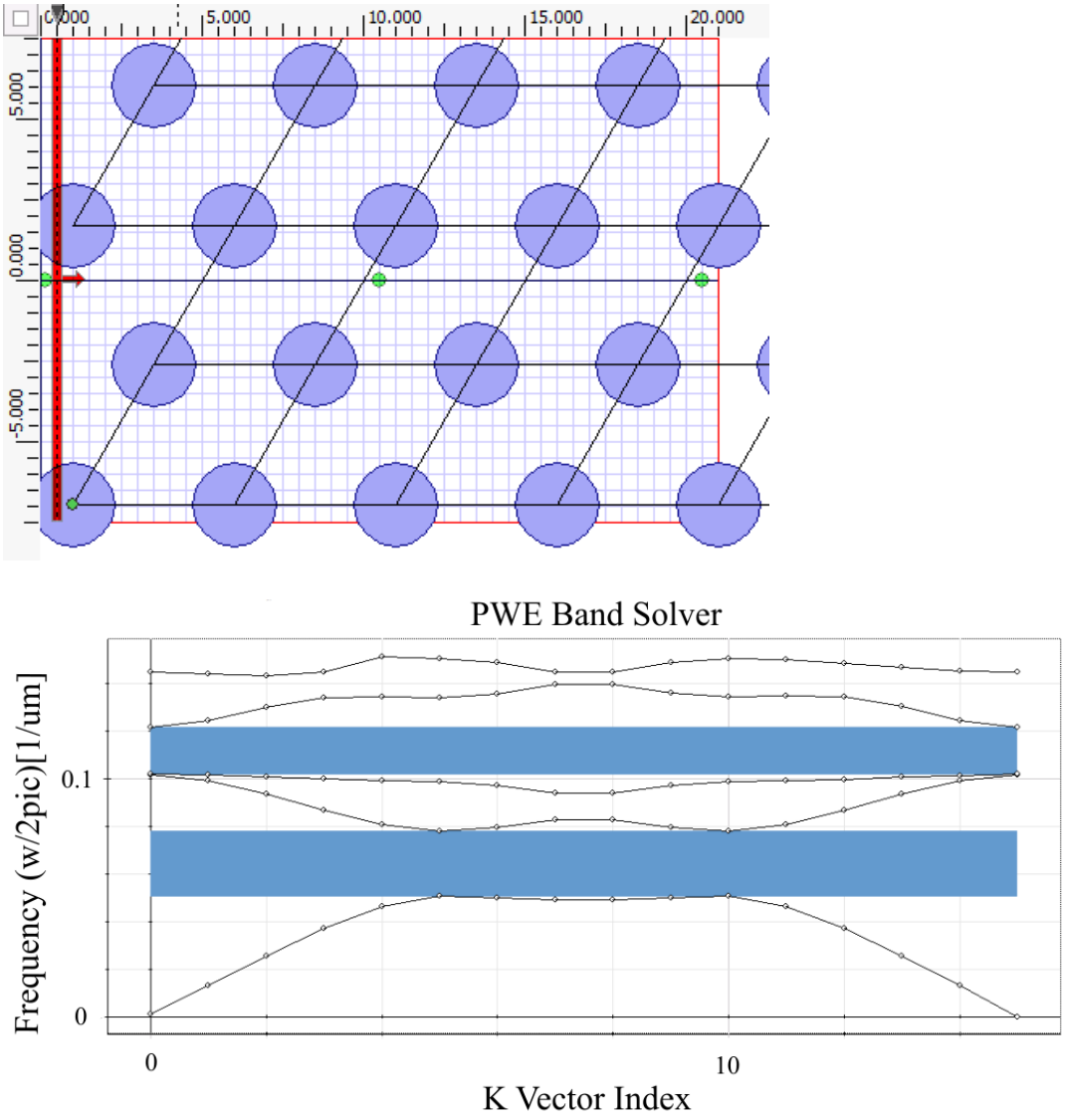


Figure 16. 2D Simulation performed on spherical particles with a refractive index of 3.1, placed 5 μm apart in air. A) 2D demonstration of structure B) Photonic bandgap demonstrated by simulating the structure in part A. Analysis was done using the band solver function of the OptiFDTD software.

Optical tweezers can be used to produce defects with specific pattern. These defects be used to produce waveguides that bends the light in tight radii. Figure 17 shows results of a 2D FDTD simulation of high refractive spherical particles in a polymer structure. The wave propagates in the Y-waveguide produced by displacement of particles.

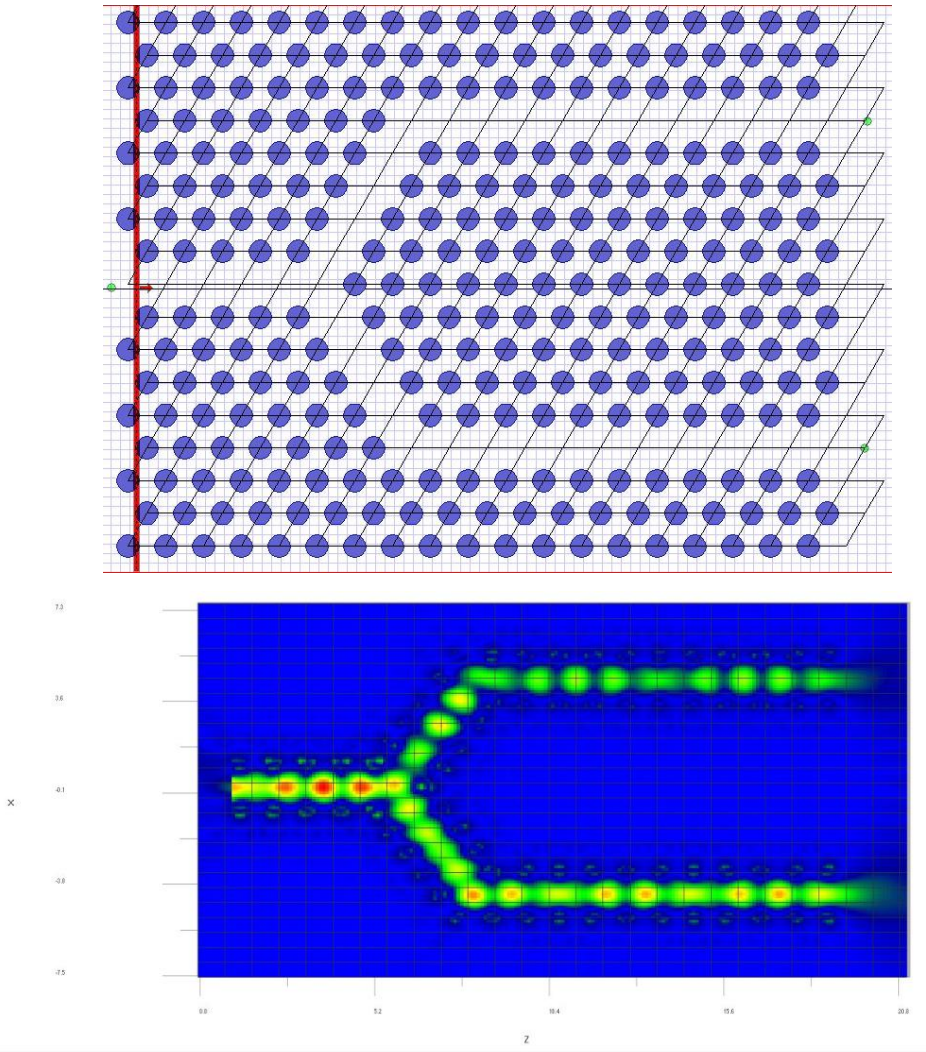


Figure 17. FTDT simulation of a 2D array of high refractive index particles with Y waveguide. The simulation demonstrates that by introducing defects in the photonic crystal structure it is possible to produce special waveguides.

CHAPTER 3: METHODS AND MATERIALS

To be able to combine materials with different length scale and properties in a polymer matrix, a combined OT and MPP system was envisioned and assembled. Before assembling and utilising the combined setup, OT and MPP setups were designed, constructed and tested independently. This chapter is divided into four sections, with each section dedicated to one of the PhD's objectives.

The first objective of this project was to design and assemble a modular MPP setup. In this chapter, the basic design of the MPP setup is explained alongside its assembly and alignment process. The MPP studio software which was developed using Labview will also be presented. This software enables the user to fabricate true 3D objects using .STL files exported from commercial 3D design software.

The second section of this chapter is dedicated to the OT module design, assembly, and alignment. An OT setup was assembled and upgraded in two steps. Components used in building the OT setup and the alignment processes are explained in detail. A Labview coded software was developed to enable the GM to control the XY position of a trapped particle. The development process of the software is discussed to complete the introduction to the OT rig that was developed.

In the third section of this chapter, the design process of the combined setup is presented. Different designs were tested before reaching the final layout. In this section, the configurations of three combined setups including the final setup that yielded the best outcome are explained.

In the last part of this chapter, different materials used in the MPP and OT setups are discussed. In this section, various attempts to produce a suitable combined setup photoresist with low refractive index and viscosity are demonstrated.

3.1 MPP setup

Designing a modular MPP setup that could be coupled with an OT rig was the first milestone of this work. Modular setups enable users to have access to different parts of the setup, and the users can replace components in the setup to add new functionalities to the system. In contrast to modular setups, commercial rigs are closed devices (black box) and the user cannot change the functionality of rig. Therefore, it limits the researchers to specific functionalities that the system was designed for.

3.1.1 System Assembly

The first component of the MPP setup was a Nexus optical table with active isolator legs (Thorlabs T1020CK). The optical table produced a stable base for the MPP setup to be built on, and it reduced the ambient vibration to the system. The most sophisticated component of the MPP setup was a femtosecond laser, which was the polymerization light source of the setup. The femtosecond laser beam produces high photon density to suppress the multiphoton polymerization threshold without overheating the polymer. In this project, a Ti-Sapphire femtosecond laser (Coherent Chameleon Ultra II) was used as the polymerization light source. The Chameleon Ultra II was a TEM_{00} mode-locked broadband laser with 80 MHz repetition rate and 140 fs pulse width. The maximum output power of this laser was 4.1 W at 780 nm, and peak power of 300 kW. The $1/e^2$ beam diameter of this laser was 1.2 mm, and a beam expander should be used to expand the beam to fill the objective lens back aperture. A multi-photon beam conditioner box (Thorlabs MPM-BCU) was used to expand and attenuate the laser beam. This conditioner was designed for multiphoton imaging applications, and all the components in the box were designed to have optimal output in the IR range. The beam conditioner box Graphic User Interface (GUI) enabled the user to control the beam diameter and the power output remotely. The GUI operates the motors inside the beam conditioner box to change the distance between the beam expanders' lenses and hence the beam diameter. Power attenuation in the beam conditioner box was achieved by rotating a $\lambda/4$ wave plate against a polarising beam splitter. In this system, a

motor controls the rotation of the wave plate. A full rotation of the wave plate is divided into 1000 steps that could be selected using the GUI.

The beam conditioner box was equipped with an SM1 threaded output port, and the Thorlabs SH05 mechanical shutter was attached to the output port of the beam conditioner box. The mechanical shutter used in this experiment employs a solenoid to control the shutter blade and block the laser beam. This mechanical shutter was used to control the laser exposure time. The Minimum Shutter Open Time (MSOT) for the SH05 shutter with an SC10 shutter driver was 27 ms [85].

The expanded laser beam was guided toward an oil immersion objective lens (Olympus RMS100X-PFO, NA 1.30 and working distance 0.2 mm) using three 30 mm cage cube-mounted turning mirrors (Thorlabs CM1-E03). The 45° mounted fixed mirrors were the first set of optical elements after the beam conditioner box. The mirrors were fixed in place using a 30 mm cage system. Different cage rods (ER05, ER8 and ER10) were used to guide the laser beam toward the microscope body, and steel posts were used to stabilise the optical train.

The objective lens was mounted on a microscope body (Thorlabs TSCOPE) with manual focusing and five objectives turret. The imaging section of the MPP setup was fitted to the microscope body using a flexible accordion mount. A Cold Mirror (CM) was used to pass the visible light collected by the objective lens towards a high-speed CCD camera (Thorlabs DCC1240M). An IR filter was placed between the CM and the camera to protect the camera from stray laser reflection. A fibre coupled broad-spectrum light source was used to illuminate the sample area.

Another crucial component of the MPP setup was the stage. The experimental setup was designed based on a fixed beam MPP rig and a piezoelectric stage (PI P-615 NanoCube XYZ Piezo System) was used to move the sample and build complex structures layer-by-layer. The travel range of the piezoelectric stage was 400 μm in X/Y directions and 300 μm in Z direction with ± 7.5 nm

repeatability and 1 nm resolution. The Ø10 mm clear aperture in the middle of the stage enabled back illumination of the sample. To increase the travel distance of the stage, the piezoelectric stage was mounted on a 3-axis roller block stage with differential micrometers (Thorlabs RB13M/M). The preassembled differential micrometers enabled the stage to have 13 mm travel range with 50 μ/rev resolution. Figure 18 shows the schematic diagram of the experimental setup.

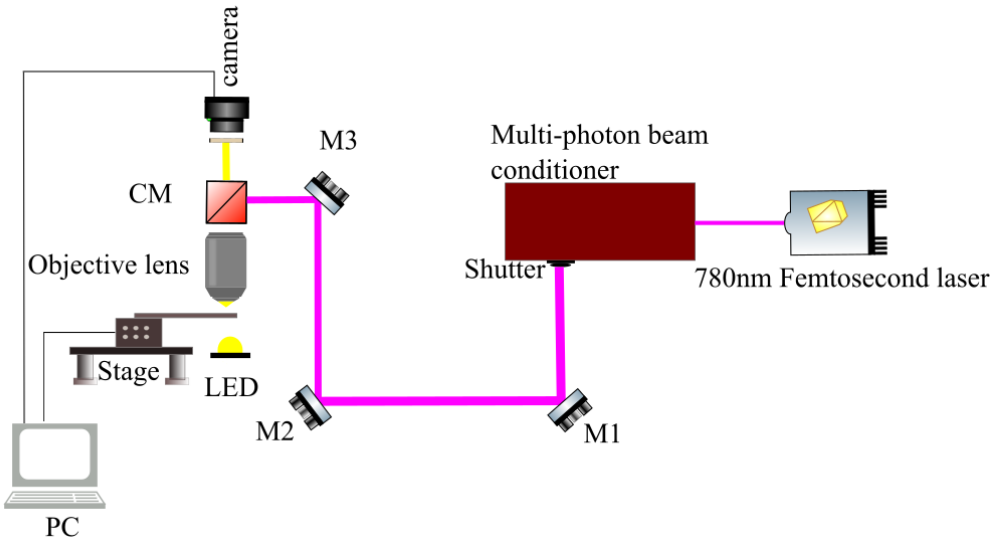


Figure 18. The schematic diagram of the first MPP setup assembled for the experiment. The beam conditioner box controls the laser diameter and power. The Cold Mirror (CM) reflects the IR polymerization beam towards the objective lens and allows the visible light gathered by the objective lens reaches the camera.

3.1.2 MPP system alignment

After completing the system assembly, the MPP setup alignment was tested. The femtosecond laser was set to the alignment mode during the alignment procedure. In the alignment mode, the mode-locked portion of the beam was blocked, and the laser output was limited to a visible CW alignment laser beam.

The alignment process had to be done for all the mirrors to make sure that the laser was propagating in the middle and parallel to the cage system. An Alignment Checking System (ACS) was assembled using two cage plates and four ER6 cage rods to help with the detection of the laser position and direction. To align the mirrors, the ACS was mounted after each mirror and by placing the cage alignment target (Thorlabs CPA1) inside the ACS and moving it further

from the mirror (laser source) the position and the direction of the laser beam was monitored and corrected. To increase the accuracy of the ACS two irises (Thorlabs SM1D) were mounted into the ACS cage plates. By closing the first iris, it blocks the outer rays of the beam, and the position of the centre of the beam can be observed. It is possible to refine the alignment process further by utilising a second iris. By closing both irises and only leaving small openings at the centre of the irises, only the centre rays that propagate through the centre of the ACS can reach the target. Having a strong signal with a circular diameter at the target shows good alignment in the system. This alignment process is particularly important for platform mounts that have more freedom to control the position of the mirror.

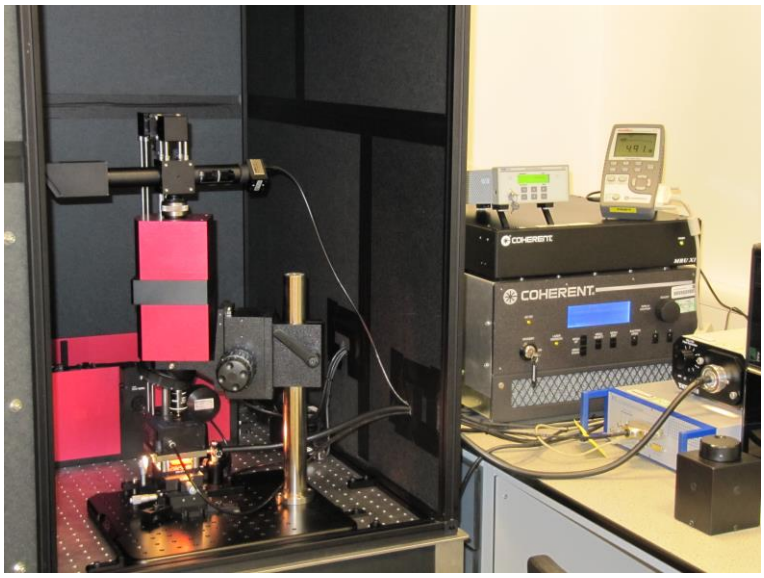


Figure 19. The initial MPP setup assembled inside the laser inclusion. The stage driver, fibre coupled light, shutter control, power meter and the laser front panel is visible at the right-hand side of the image.

Upon completion of the alignment process, a good quality circular beam reached the objective lens. The laser output power after the beam conditioner box and the objective lens were monitored to estimate the losses in the optical chain. Figure 20 shows the laser output power versus the power control GUI amplitudes. The expanded section on the upper right corner of the graph indicates the area of interest for polymerization using the commercial photoresists. By increasing the power control GUI amplitude, the laser power decreased till it reached its minimum power at 850. After 850 due to the

misalignments between the $\lambda/4$ plate and the beam splitter the laser power increased. The difference between the laser power after the beam conditioner box and the objective lens shows the laser power losses in the optical train and the objective lens. The IR mirrors used in this experiment reduced laser power by 2% each and the objective lens transmission for IR the laser was 95%. In total 11% of the light was lost due to non-ideal optics and the rest of the power loss was due to the misalignments in the system.

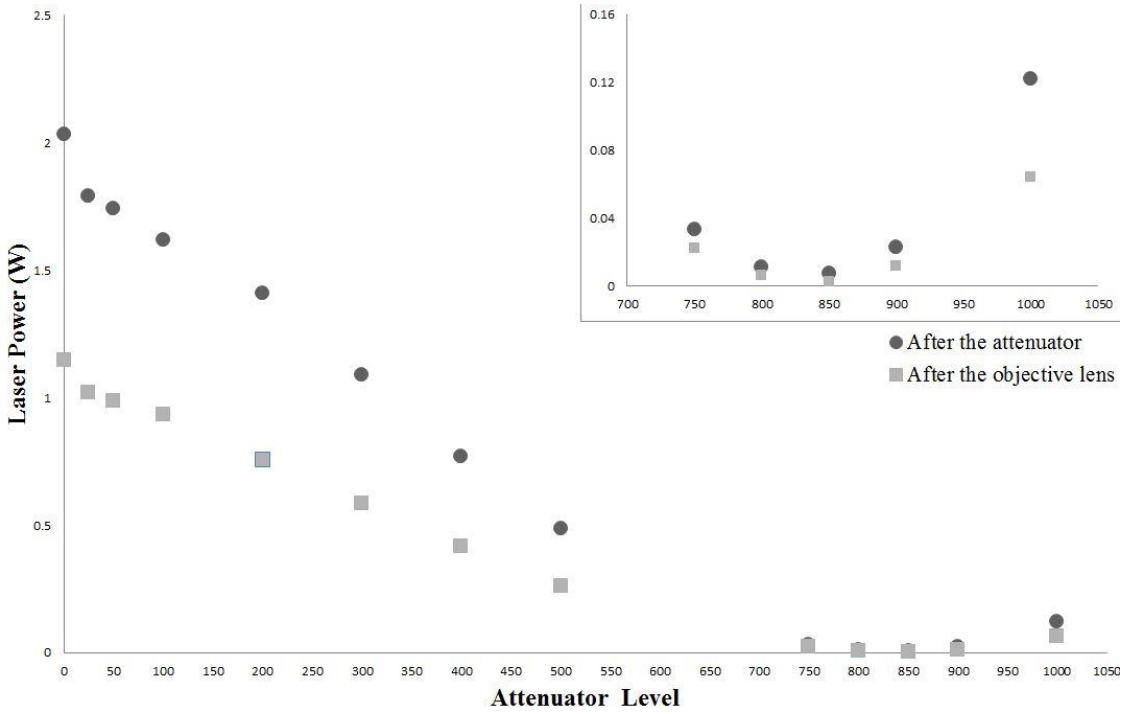


Figure 20. Laser output diagram VS. GUI amplitude control. The magnified section at the upper right corner of the diagram shows the area of interest for this project.

To optimise the operational values of the MPP setup, a commercial photoresist ORMOCOMP by Microresist Gmbh, was used to build test structures. The fabrication process, sample preparation and development process of this photoresist will be discussed in section 4.1.

The optical elements that guide the polymerization beam toward the sample reduces the laser intensity at the sample. Optical dispersion produced by optical elements also increases the pulse duration of the femtosecond laser and reduces the pick intensity of the laser beam at the sample. Therefore, the laser power

should be well above the polymerization threshold value, to compensate for the optical dispersion in the system.

3.1.3 MPP software development

Driver software was needed to automate the fabrication process of the MPP setup and enable the system to fabricate complex structures. Commonly, commercial 3D printers use .STL files to fabricate complex, multilayered structures. For the MPP driver software, a MATLAB code was developed to transfer the .STL files to a user-defined number of bitmap pictures and number them consecutively. After producing an array of images, a Labview code was developed to import the bitmap files one-by-one and fabricate complex structures layer-by-layer. The Labview code was written based on a stacked sequence code. First, the Labview software establishes a connection between the PC, stage and E-725 piezoelectric stage driver unit to initialize the stage. After checking the position of the stage, it performs auto zero correction to calibrate the stage with its new load. By completing the stage initialization, the stage ID will be held in a local variable and the software moves to the second layer of the code. The image was imported in the second layer of the software. In this layer, the image (2-bit bitmap file) was converted to a 2D array of pixels and the image size (number of pixels in X and Y) was saved in a local variable. In this step, the software also converts the 2D array of pixels into a string of 1s and 0s (0 representing white areas of the bitmap file) and sends the string to the next stage one bit at the time.

The software uses the string generated in the previous step to operate the shutter. If the first bit is one, the software operates the shutter and moves the stage one step in the X direction. The user can control the step size in the software front panel. Using the image size and the step size defined by the user the software controlled the position of the stage by raster scanning of the built area. The Labview code used relative movement commands to scan each pixel in a row (X direction). When the pixel number becomes equal to the image size in the X direction or any integer multiple of this number, the software moves the stage in the Y direction. The software uses the absolute move commands to go back to the starting point of the next row. Using a combination of absolute and relative

movements in the system prevents the accumulation of errors in the system and increases the accuracy of the system.

The exposure time can be controlled using the shutter driver (SC10) and the Labview code at the same time. Using the shutter driver to control the exposure time made it harder to synchronise different components of the software, but its alternative increased the fabrication time.

Figure 21 shows the front panel of the LabVIEW code. The left-hand side of the front panel is the input section of the software. Variables like the step size in X and Y, File location and a number of layers should be entered before fabrication. The middle section of the front plane is the feedback section that shows the stage ID, file path, image size and the current position of the stage for the user. On the right-hand side of the figure, a portion of the imported image will be displayed. Figure 22 shows the Labview software flow chart that explains the dependencies between different layers of the code.

Optimising the fabrication parameters is critical. The step size chosen in the software must be equal to the system voxel size. Having step sizes smaller than the voxel size produces overlapping voxels and deforms the fabricated structure. Using step sizes bigger than the system minimum feature size produces disconnected parts.

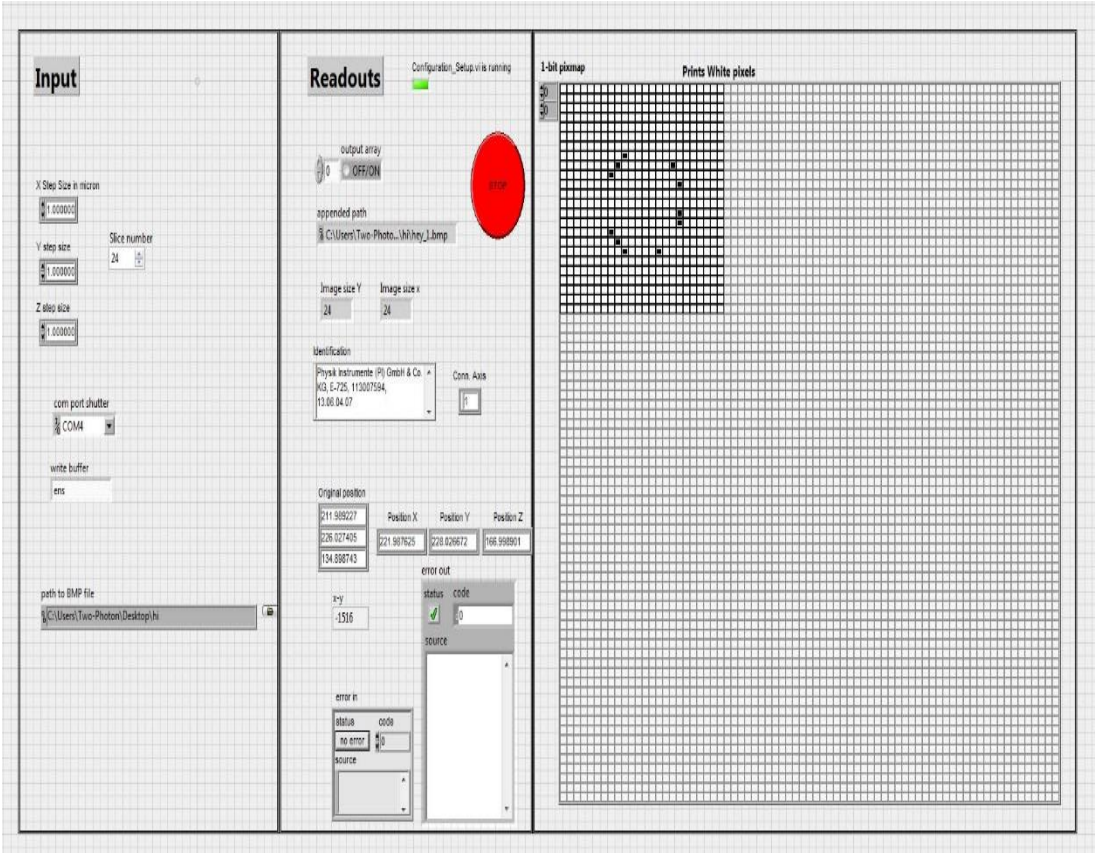


Figure 21. The front panel of the LabVIEW code developed to use an array of bitmap images to produce 3D structures. In the input section of the software step size, shutter

time and the connections can be controlled. The readout section is the feedback section and the user can control the overview of the progress.

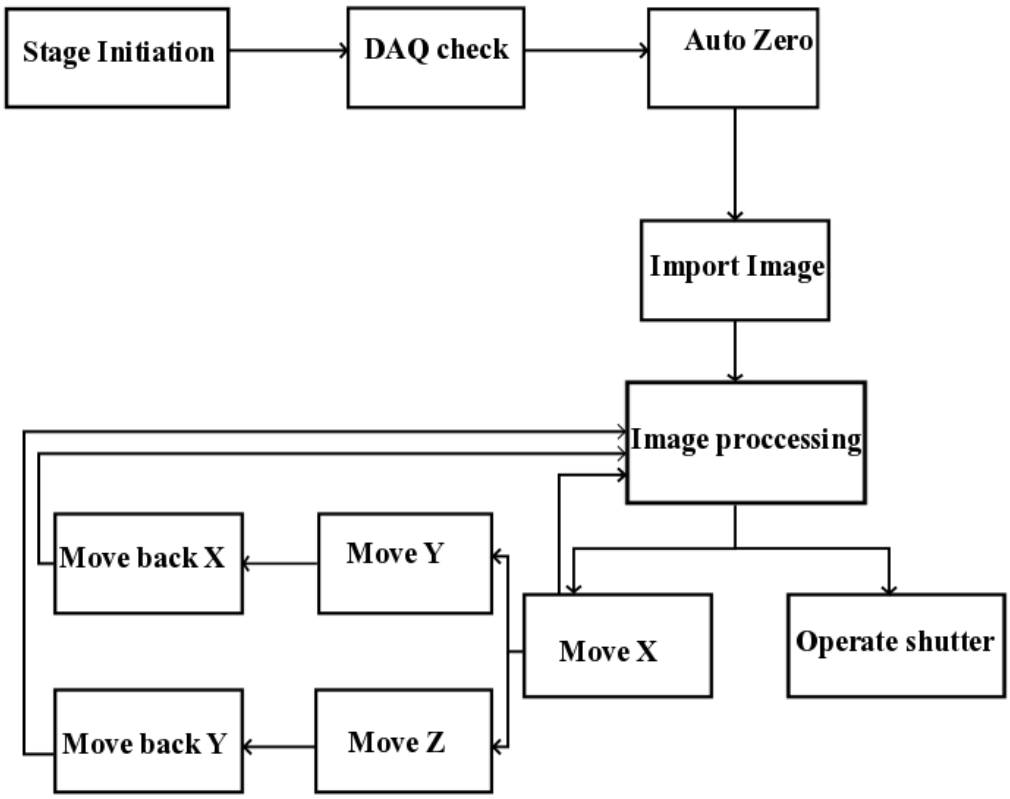


Figure 22. LabVIEW code flowchart.

The high NA objective lens used in this setup had a limited working distance (200 μm). To increase the possible build volume of the system an objective lens cover was designed to enable the objective lens to dip into the polymer without damaging the lens or reducing the objective lens NA. The objective lens-mount accommodated the high refractive index immersion oil and the coverslip. It also separated the objective lens from the polymer. Figure 23 shows one of the designs for the objective lens cover. The most challenging part of using this mount was placing the coverslip as close as possible to the objective lens tip and fixing it to the lens body.

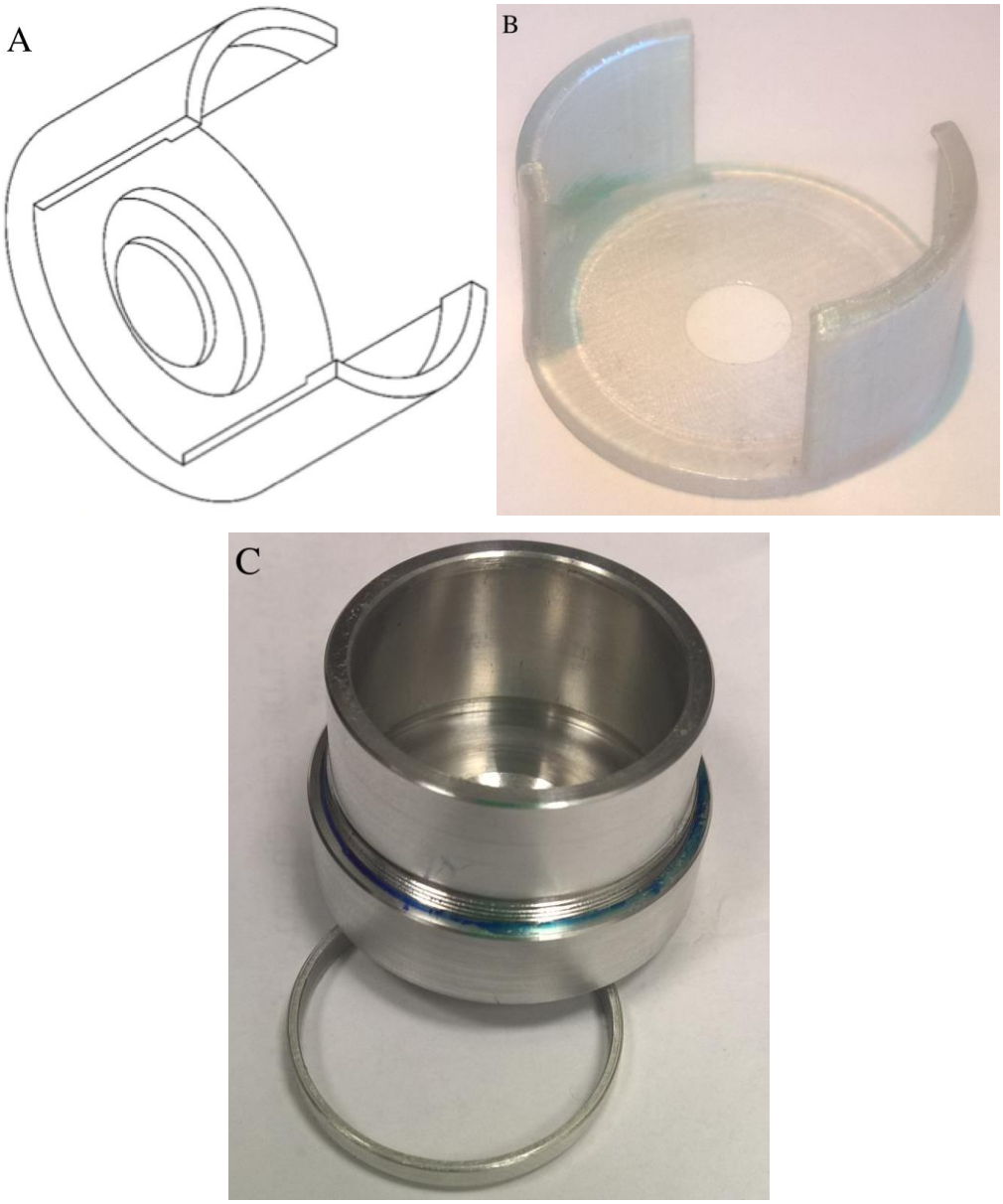


Figure 23. The initial design for the objective lens mount to increase the build volume of the MPP setup which was printed using a Connex Object 260 (A&B) and the metallic version of the design fabricated by CNC milling (C).

3.2 OT setup

The optical trapping system used in this experiment was based on a Thorlabs optical trapping setup (Thorlabs OTKB/M). In this section, the OT setup and components used in assembling the setup will be explained. OT commissioning, which includes system alignment, calibration and software development is also described.

The OT setup used a 975 nm butterfly laser diode with a maximum output power of 340 mW (Thorlabs PL975p350J). A touchscreen laser driver unit with integrated temperature control module to monitor the output power and the temperature of the diode, controlled the laser diode. The laser diode output was coupled into a single mode optical fibre (Thorlabs P3-980A-FC-1) using a beam collimator (Thorlabs TC06APC-980). The optical fibre connected the laser driver to the OT optical chain through a combined fibre port and beam collimator unit (Thorlabs PAF-X-2-B) mounted in a 30 mm cage plate. The cage system enclosed the laser beam before the objective lens and provided support for the components used in the system. Broadband dielectric mirrors (Thorlabs BB1-E03) mounted in the right angle kinetic mirror mount (Thorlabs KCB1/M) reflects the collimated laser beam towards the beam expander section of the OT setup. The beam expander section of the setup is based on a Galilean beam expander that enables up to 3X expansion of the beam diameter in a moderately confined distance. The beam expander uses two achromatic doublet lenses (Thorlabs ACN254-050-B and AC254-150-B) to expand the laser beam. These lenses are designed for IR light, and they were coated with an anti-reflection coating to increase the efficiency of the setup.

The expanded laser beam reflects towards the vertical section of the OT setup using a Hot Mirror (HM). The HM reflected the expanded laser beam towards the second broadband mirror (M2) that is mounted at the base of the vertical section of the OT setup. The HM passes the visible light collected by the objective lens and reflected by M2 toward the camera (Thorlabs DCC1240C) mounted behind an IR filter (Thorlabs FES0700). The M2 mirror reflects the

expanded laser beam towards the objective lens and sent the visible light collected by the objective lens towards the camera.

The objective lens used in the OT setup was an Olympus 100X oil immersion objective lens with N.A=1.3 and a working distance of 0.16 mm (N100X-PFO). The objective lens focuses the laser beam into a tight space that produces the gradient force needed for trapping dielectric particles. This system uses a 10X condenser lens to ensure uniform illumination of the sample using the white light LED, which is mounted at the top of the vertical section. The condenser lens can be used to collect the refracted laser light after the sample to be used with the quad detector unit (Thorlabs OTKBFM).

The OT system was a fixed beam system and by moving the stage, particles trapped in the OT stay stationary as the rest of the particles in the sample move with the stage. A nanomax stage (Thorlabs Max313D/M) was used in the OT system. The nanomax stage had 4 mm travel range in all three axes. Three differential micrometres (Thorlabs DRV3) were used to adjust the stage position manually. The stage was mounted on a broadband translation board (Thorlabs TBB1515/M); that enabled the stage to slide in between the objective and the condenser lenses. The sample was mounted on a microscope slide holder (Thorlabs MAX3SLH) for easy installation and removal.

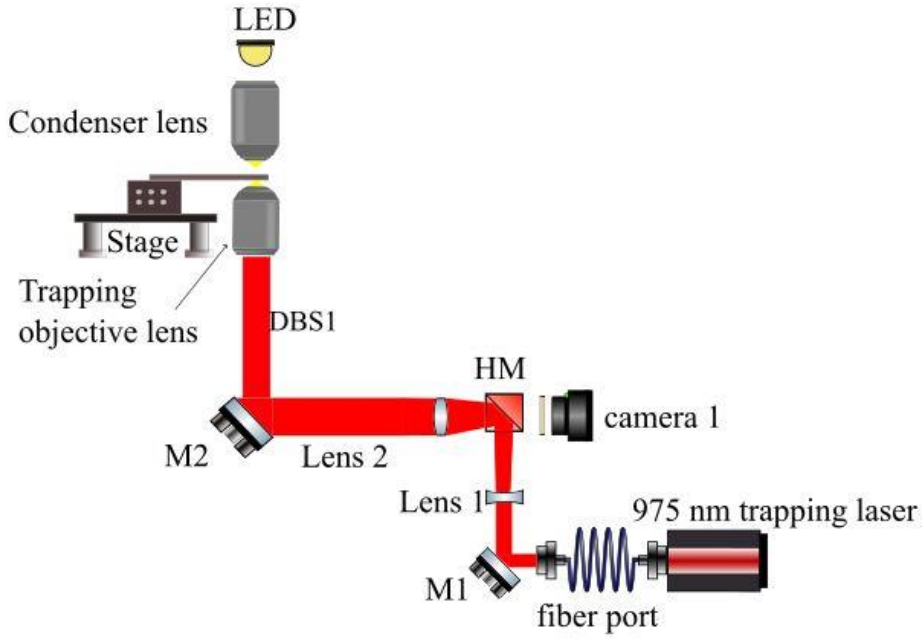


Figure 24. Schematic diagram of basic Thorlabs OT setup. The second lens in the Galilean beam expander is placed f_2-$|f_1|$ from the first lens and the objective lens is placed 200 mm (the tube length for the objective lens)| from the beam expander. The second lens of the beam expander is used as the imaging lens for the camera, Therefore, the camera is placed at the focal length ($f_{2)}$ of Lens 2.

Figure 24 shows the schematic diagram of the OT setup. The first step in assembling the OT rig was mounting the laser diode into the driver unit and connecting the output port of the diode to the single mode optical fibre. The optical fibre then connected to a fibre port. The fibre port mounted to a 30 mm cage plate (Thorlabs CP08) was fixed to the optical table using a table base mounts for 30 mm cage system (Thorlabs CPB1). Two cage rods (Thorlabs ER8) inserted into the top two holes of the cage plate and an IR Fluorescing Alignment target (VRC4D05) with cage plate mount (Thorlabs VRC4CPT) placed at the end of the rods. The IR target was placed 20 cm from the fibre port to show the beam diameter and profile. The beam spot must be uniform, circular and at the centre of the IR fluorescent target. If the beam position was off centre, it must be adjusted using the fibre port alignment screws. The fibre port utilised in the setup had 5 degrees of freedom to control the beam profile and trajectory. It is also critical to check the beam divergence. If the beam is converging or diverging as it travels, it must be corrected. The beam should travel directly without any change in its size for up to 3 m. The spot size was checked at 3 m

from the fibre port using the IR detector. After correcting the fibre port exiting-beam, the cage rods were removed and the M1 mirror attached to the cage plate. The same alignment procedure was followed for the first mirror (M1), and the beam trajectory was checked using the IR detector and the cage rods. Attaching the ACS to the kinetic mirror mount increased the accuracy of the alignment procedure. The first iris was almost closed, and the IR detector placed after the second iris. Closing the first iris blocks a significant portion of the laser beam and allows a very narrow light from the centre of the beam to travel toward the detector. The position of the centre of the beam can be checked on the detector. If the centre of the laser beam is not at the midpoint of the detector, using the controls on the M1 kinetic mount, the laser spot can be moved to the centre of the detector. Having a second iris and nearly closing the second iris can demonstrate the beam's trajectory. If the beam is travelling parallel to the cage system, it passes both irises and reaches the detector. If the laser is travelling at an angle, the second iris will block the beam, and it will not reach the detector. It is also possible to check the beam trajectory by moving the detector away from the laser source. If the laser trajectory is not parallel to the cage system (perpendicular to the detector), as the detector moves away from the laser source the spot size / position changes. This technique must be used after each element in the optical train.

After aligning the first mirror, the beam expander section was built. The beam expander section of the OT setup was constructed by fixing both lenses into the lens tubes using the retainer rings. The beam tubes screwed to cage plates, and the lenses placed 12.5 cm apart from each other to produce 3X expansion. An iris was mounted at the end of the beam expander section to help with the alignment process of the next section.

After completing the beam expander section, an HM was mounted into a 30 mm cage cube platform (Thorlabs B4C/M). This platform can control the beam trajectory using pitch, roll, and X/Y/Z translation. The platform was mounted into a cage cube (Thorlabs C4W). The cage cube gave access to the beam from four directions and featured four SM1 threaded openings to be used with the

beam tubes and holes for inserting the cage rods. By mounting the HM in the cage cube and attaching the cube to the beam expander section of the OT rig, the alignment process of the HM started.

The first element in the vertical section of OT rig was the second IR mirror (M2). Using the knobs on the M2 kinetic-mount the laser beam trajectory corrected to be perpendicular to the optical table. Four cage rods attached to the M2 kinetic-mount connected the mirror to the objective lens. In this system, the objective lens was mounted in a cage XY translator mount (Thorlabs CXY1). A second XY translator mount was used to mount the condenser lens and the white light LED. To reinforce the vertical section of the OT system, a 25 mm steel post was used to hold the objective lens and the condenser lens. Two post clamps (Thorlabs C1510/M) were attached to 30 mm to 60 mm cage plate adaptors (Thorlabs LCP06/M) and connected to the XY translation mounts using cage plate adaptors (Thorlabs LCP02).

The imaging section of the OT setup was the last part that was attached to the system. The imaging section consists of a mirror that reflected the light collected by the objective lens toward the camera and the CCD camera. The imaging section was attached to the HM using cage rods (Thorlabs ER01). The last part of system alignment was done using the imaging section. The CCD camera software enables precise monitoring of the light level that reaches the camera. Using the XY translation mounts the position of condenser lens was moved to maximise the amount of light that reaches the camera.

After completing the system assembly and alignment, sample preparation started. An optical trapping sample preparation kit (Thorlabs OTKBTK) was supplied with the OT setup. The sample kit contained 100 μl sample chambers (Ibidi µ-Slide I 0.1 Luer Uncoated) and 2 µm silica particles suspended in deionized water. To test the OT setup, a sample chamber was filled with diluted solution of silica beads and placed in the sample mount. A droplet of immersion oil was placed on the objective lens and the rolling stage was used to move the sample in between the objective and condenser lens. The suspended particles are

brought into the focus of objective lens using the Z stage translation. By focusing on the particles, the laser beam waist was placed close to the particles and the gradient force generated attracted particles toward the beam.

The next step in completing the OT rig was upgrading the setup and incorporating the 2D Galvo mirrors (GM) in the system. As explained in chapter 2, GM can be used to control the XY position of the trap by changing the beam trajectory. The GM system consisted of 8 components and their connecting cables. The first IR mirror (M1) was replaced with a Thorlabs GCM001 cage cube to incorporate the GM in the system. The GM motorised mirrors were mounted in the cube afterwards. Mirrors used in the GM unit changes the angle that the laser beam enters the objective lens back aperture and using both mirrors the objective lens field of view can be scanned. The stepper motors that rotate the mirrors were connected to two driver units that controlled the position of the mirror using a National Instruments Data Acquisition (DAQ) device. A separate power source was needed to power the GM unit and the drivers. The Galilean beam expander in the OT setup was replaced with a Keplerian beam expander to use with the GM system. By changing the beam expander and installing the Keplerian beam expander and realigning the system, the OT rig was ready to be used with silica beads.

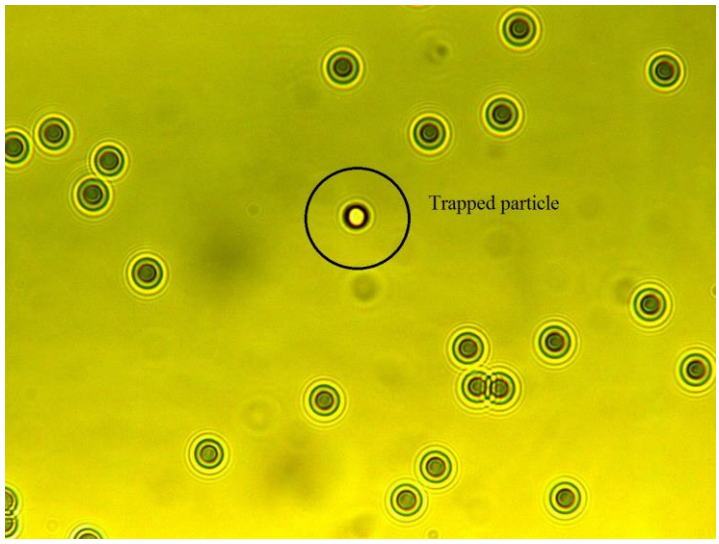


Figure 25 Trapping silica beads using Optical trapping setup.

A Labview code was developed to control the position of the trapping laser beam (trap) using the computer mouse pointer. The Labview code used the imaging camera live video feed and the mouse pointer position on the camera feed to control the NI DAQ device output. By moving the mouse pointer on the camera feed, the coordinates of the mouse pointer were translated into voltages that could change the GM mirrors angle and the laser trajectory. At this stage, it was crucial to calibrate the system to find the exact conversion formula that could convert the mouse pointer movements to a similar amount of particle manipulation in the imaging field of view.

To calibrate the system and enable accurate translation of mouse movement to particle movement, the video feed frame size was measured and using a simulation software the output voltage of the DAQ was monitored as the mouse pointer moved to all four corners of the frame. The mouse coordinates for all four corners and at the centre of the camera feed (white box in Figure 28) were recorded to calibrate the system for the first time. To test the calibration another software program was developed that enabled particle movement by directly inputting coordinates or voltages. A mathematical formula was devised to convert the mouse coordinate at all four corners to the recorded DAQ output voltage for the respected corner. Because of the linear relationship between the DAQ output voltage and change in the position of the trap, it was possible to produce a linear equation between the mouse coordinates and the DAQ voltage. Figure 26 shows the schematic diagram of the upgraded OT setup. In comparison to Figure 24, the GM unit has been added to the setup, and the Galilean beam expander section has changed to the Keplerian beam expander. In

Figure 27 shows the assembled OT setup with GM unit and quad-detector are assembled on a Nexus optical table. Figure 28 shows the Labview code front panel. The CCD camera control variables are placed on the left-hand side of the front panel, and the camera feed is positioned on the right-hand side of the front panel. The information section on the front panel enables the user to observe the camera ID, mouse coordinates and the output voltage of the NI DAQ device.

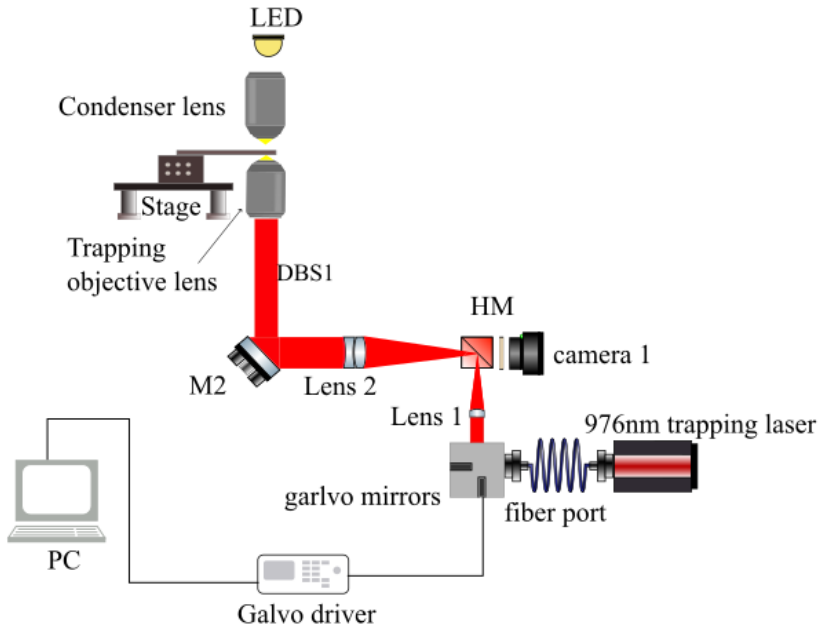


Figure 26. Upgraded OT setup using the GM and Keplerian beam expander. The beam expand section is longer comparing to the Gaussian beam expander and the distance between lens 1 and 2 is equal to the sum of their focal lengths. The objective lens is placed 20 cm from Lens 2 which is equal to the objective lens tube length.

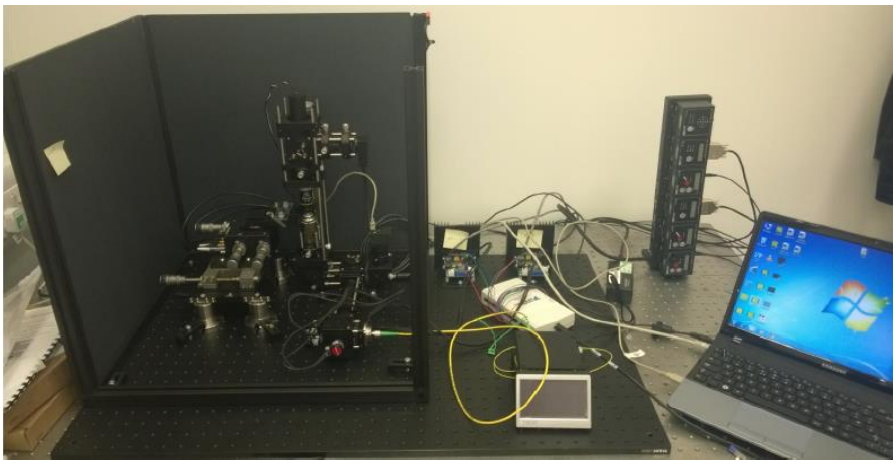


Figure 27. The OT assembled inside the black cardboard enclosure to protect the users from potential dangers of class 3B laser used in the system.

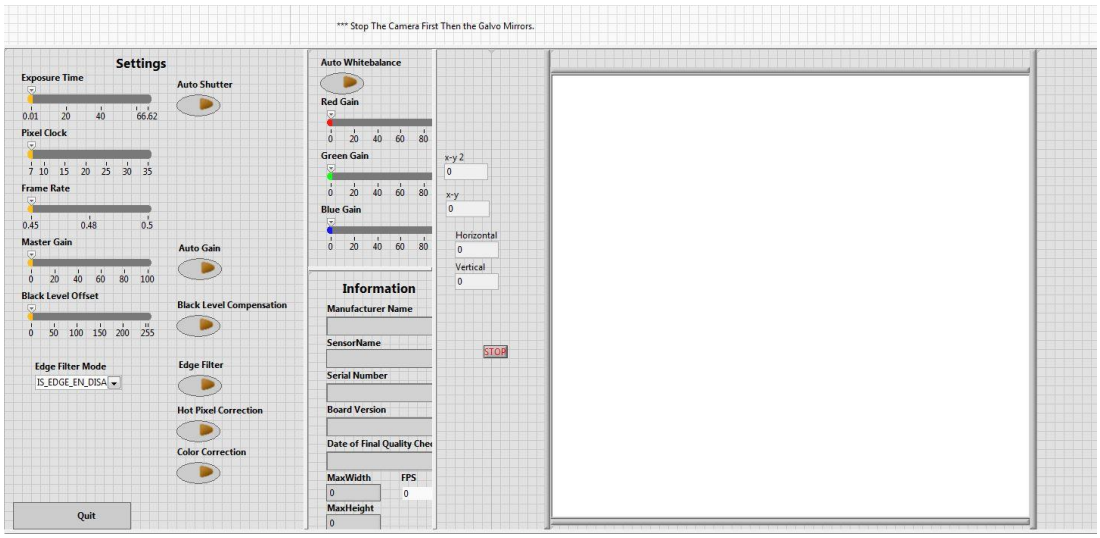


Figure 28. The front panel of Labview code developed to control the GM and operate the imaging section of the setup.

The force measurement unit (Thorlabs OTKBFM) was the last part of the OT setup. This section starts with a Dichroic Mirror (DM) mounted in a cage cube. The DM placed in front of the white light LED passes the visible light towards the condenser lens and reflects the refracted laser gathered by the condenser lens towards the quad detector. The laser light collected by the condenser lens reaches a biconvex lens (LB1027-B) with a focal length of 40mm. This lens focuses the laser light on the quad detector surface. An absorptive neutral density filter (NE06B) was placed before the quad detector to protect the detector and avoid detector saturation. This filter absorbs 75% of the laser beam in the operation frequency of the setup and passes 25% of the light toward the detector. PQ80A quad detector is the sensory element in the OTKBFM unit. This quad detector was placed 40mm from the lens and mounted to the section using an XY translation mount (CXY1). The XY translation mount can be used to move the detector and place the laser spot in the middle of the detector. The detector unit was connected to a control cube (TPA101) that was connected to the PC. Using the LabVIEW software the laser position and amount of light that reaches the detector can be monitored. Figure 28 shows the front panel of the LabVIEW software. The Sum voltage represents the amount of light that reaches the detector. Using the XY translation mounts and moving the condenser lens in regards to the objective lens can maximise the Sum value. X diff and Y diff values represented the position of the laser beam on the detector and by adjusting

the quad detectors' position using the XY translation mount these numbers are reduced, and the laser spot (represented by a blue circle in Figure 29) is transferred to the centre of the graph.

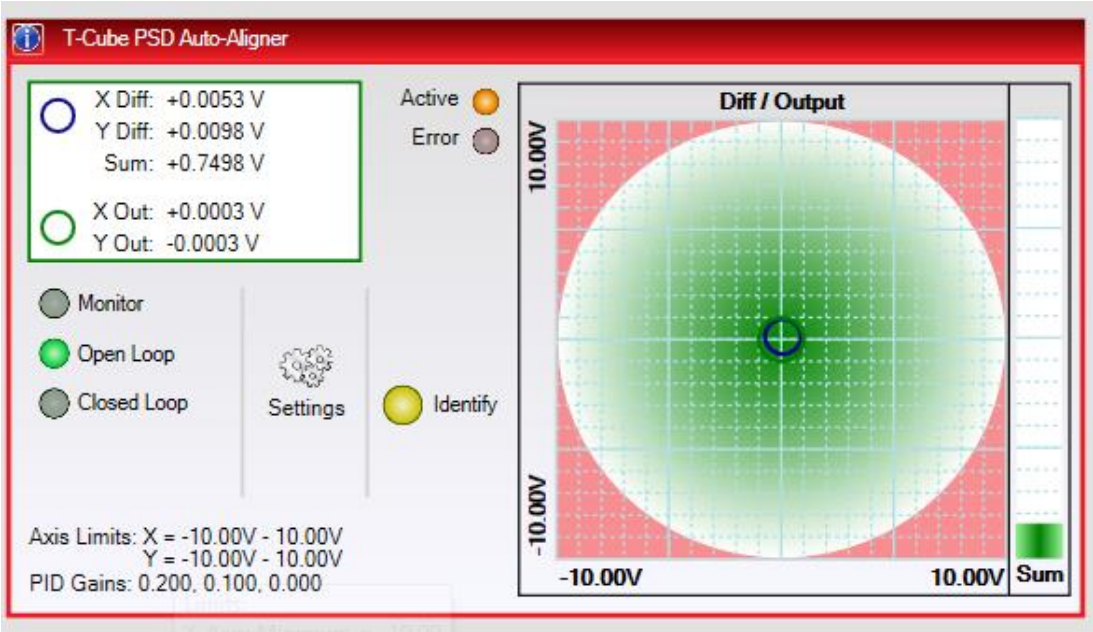


Figure 29. The front panel of the LabVIEW quad detector driver.

In Figure 29, the sum voltage is +0.7498 V with the laser driving current of 100 mA. The laser is positioned at the centre of the detector, and difference values in X and Y directions are minimised.

The LabVIEW driver did not allow users to extract the real-time data regarding the position of the particle. A separate LabVIEW code was developed to extract this information and plot it in a time graph to demonstrate the change in the trapping condition over an extended period. Figure 30 shows a Virtual Instrument (VI) developed to extract the Sum voltage from the LabVIEW driver and plot it in different conditions.

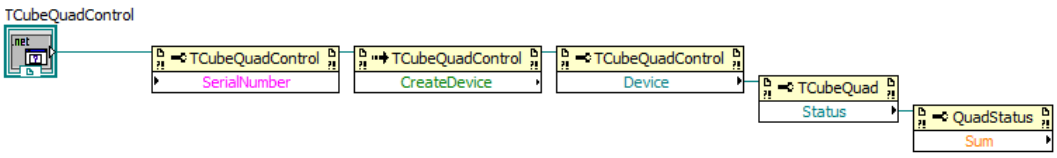


Figure 30. LabVIEW VI used to extract the Sum voltage. This voltage was plotted while it was being monitored in a "while loop" and the data was plotted after finishing the

operation in a 2D X-Y plot. This information was also automatically saved in a file to be used with data analysis software.

3.3 Combined setup

After testing the MPP and OT setup independently, the design procedure for the combined setup started. Different design parameters were taken into consideration for constructing the combined setup with the ability to trap particles and polymerise around them in a single rig. 3 Different designs were considered before reaching the final layout that was the most stable system. In this section, different designs will be explained and their shortcoming will be highlighted.

The first design for the combined OT and MPP was assembled based on separate polymerization and trapping objective lenses. At this stage, it was believed that the difference between the polymerization and trapping wavelengths affected the capabilities of the combined setup. Using two separate objective lenses simplified the alignment process of the combined setup by making each section independent of the other. Figure 31 shows the schematic diagram of the double objective lens combined setup.

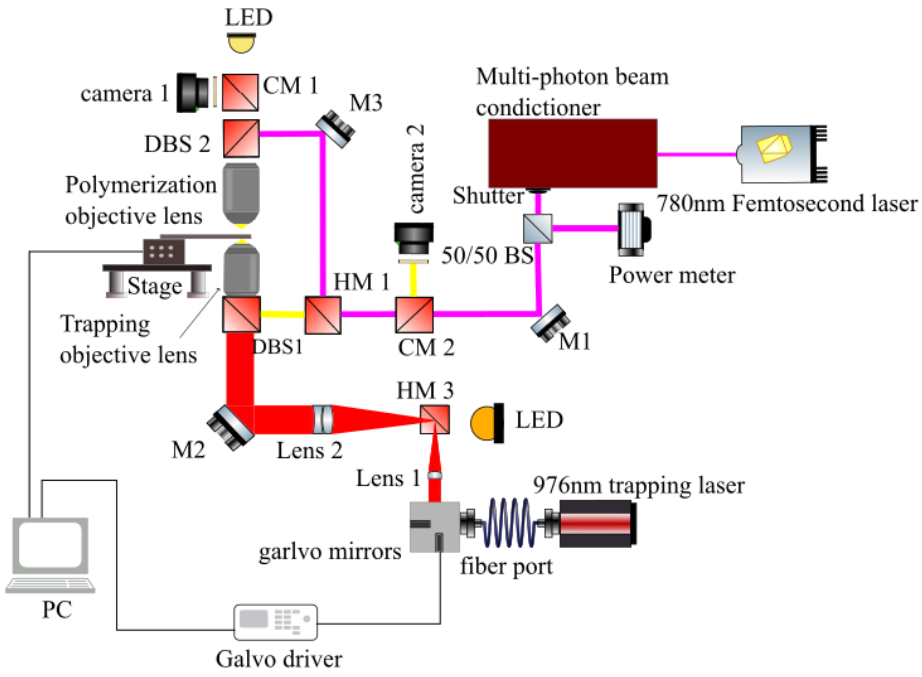


Figure 31. Schematic diagram of the dual objective lens combined setup. The system uses separate objective lenses for polymerization and trapping. Both objective lenses were mounted in translation mounts and it was tried to use mechanical translation mounts to overlap the polymerization and trapping areas manually. The restricted field

of view of high magnification high NA objective lenses made it impossible to accurately overlay the field of view of the objective lenses using the mechanical translation mounts.

To assemble the combined setup without interfering with the functionality of the previously assembled MPP setup, a 50/50 beam splitter placed in front of the multiphoton beam conditioner box. The beam splitter divided the polymerization laser beam and sent half of the beam toward the MPP setup and the other half toward the combined setup. An IR mirror mounted in a kinetic mirror mount (M1) reflected the polymerization beam parallel to the optical table towards the vertical section of the combined setup. The vertical part of this setup consisted of two, 3.8 cm damped steel posts (Thorlabs DP12A/M) that supported the components in a vertical section of the setup and reduced the vibration in the system.

In this setup both trapping and polymerization objective lenses were used as imaging lenses too. To be able to guide the IR laser to the objective lens and collect visible light to it a combination of CM and HM were used. Before the MPP beam reaches the vertical section of the combined setup, the beam goes through CM2. The last optical element behind the polymerization objective lens is the Dichroic Beam Splitter (DBS2), which reflects the IR beam toward the objective lens and enables illumination and imaging using the single objective lens.

The OT section of the combined setup was based on the OT setup assembled and explained in the previous section. Three major changes were applied to the OT setup to be integrated with the MPP setup. A Dichroic Beam Splitter was inserted behind the objective lens that reflects the visible light gathered by the trapping objective lens towards the second camera. This camera is mounted after CM2 that passes the polymerization laser beam and reflects the visible light toward the camera 2. The second major change in the OT setup was the camera position. The OT setup camera, which was mounted after the beam expander, was replaced with a white light LED to illuminate the sample using the trapping objective lens. The light gathered using the polymerization objective lens travel

towards the first camera and reflected toward it using CM1. The third major change to the OT setup was mounting the trapping objective lens in a cage translation mount (Thorlabs CT1) that moved the lens toward the polymerization objective lens. The translation mount was used to overlay the trapping and polymerization point in the Z direction. XY translation mounts were used to overlay the spots in X and Y-axes.

Using two high NA objective lenses decreased the field of view of the system to a few hundreds of μm, and the resolution of the mechanical translation mounts was not high enough to enable precise alignment of the polymerization and trapping objective lens. To be able to use this system one of the objective lenses must be replaced with lower magnification objective lens. Figure 32A shows pictures taken by replacing one of the 100X objective lenses with a 10X objective lens. These pictures were taken using both CCD cameras simultaneously.

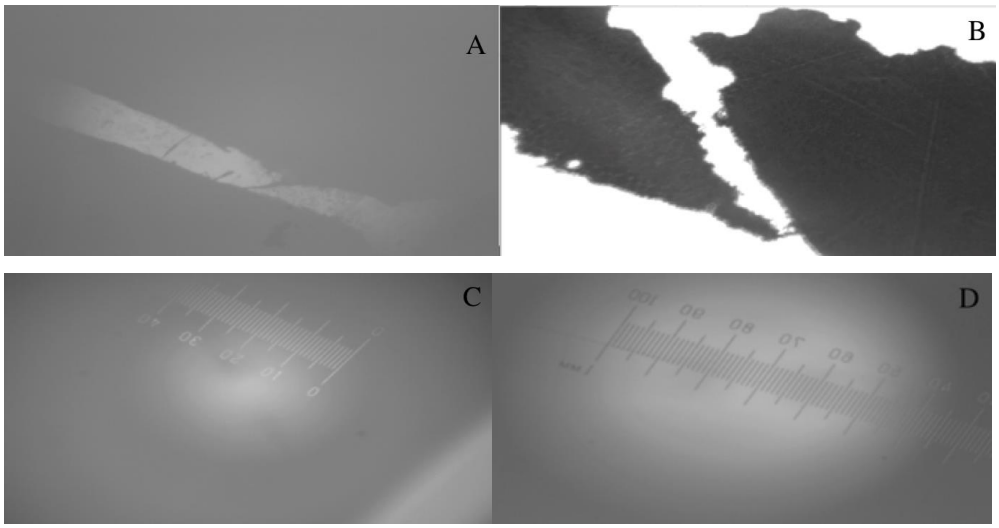


Figure 32. Pictures presented in this figure were taken using the dual objective lens combined OT-MPP setup. Picture A was taken using the polymerization 10X objective lens and image B was taken using the 100x trapping objective lens. Pictures c & D were taken simultaneously using two 10X objective lenses from both sides of a graticule.

A lower magnification objective lens with a larger spot size increased the field of view of one of the objective lenses and made it possible to focus on the same area on the sample using two objective lenses. The intensity gradient produced using an oil immersion objective lens is necessary for the generation of efficient OT but MPP setups with low magnification (20X) objective lenses have been reported in the literature [206]. Replacing a 100X objective lens with a 20X lens

could reduce the resolution of the setup but enables the combined setup to focus on the same area. To be able to overlay the imaging plane of the polymerization and imaging objective lens, the lens translation mount was used. Replacing the polymerization objective lens with a low magnification lens solved the lens alignment issue in X and Y. The camera software was used to monitor the amount of light that reaches the camera, and by moving the objective lens in the Z direction, it was tried to maximise the amount of light that reached the camera. Fine alignment of the system was done by fabricating simple structures using the polymerization lens and focusing on the fabricated structures using the trapping objective lens.

Unfortunately, the prefabrication steps for this system were very long and troublesome. Low accuracy and repeatability of the X-Y translation mounts and the lens translation-mount made it impossible to use this system efficiently.

The second combined setup was designed and assembled based on a single 100X objective lens for both trapping and polymerization. This system was built based on a microscope setup with backlight illumination. A Dichroic Beam Splitter (DBS) combined the trapping and polymerization beams into one optical pass. The DBS used in this experiment passed the trapping laser beam and efficiently reflected the polymerization laser beam.

In this design, both beams were combined at the multiphoton beam conditioner box output level and then reflected toward the objective lens back aperture using 3 IR mirrors. Common elements (3 IR mirrors) between the OT and MPP system made the system alignment and calibration challenging. Theoretically, both beams should follow the same path but because of imperfections in the system alignment and different laser sources used in the experiment the alignment procedure for the polymerization laser move the trapping laser away from the centre of the cage system. Beam quality for optical trapping is crucial, so the OT beam was aligned using the IR detector, and the MPP laser was left slightly misaligned. Having a misaligned MPP laser made the polymerization more challenging, but by increasing the laser power a high enough photon density

could be achieved for polymerization. The combined system assembled based on the microscope setup was not stable, and vibrations generated by the shutter and other external sources interfered with the operation of the system. In this setup, due to the chromatic aberration, the working distance of the objective lens was different for the polymerization, trapping and imaging beams. For instance, after fabrication, the stage was moved toward the objective lens for roughly 3 μm to be able to produce sharp images on the fabricated structures. The gap between the trapping and the polymerization areas was problematic for spot-welding the particles to the substrate. The particles crashed to the substrate before the polymerization area reaches the substrate surface. Although in some cases the trapped particle stayed on the surface, and it was possible to glue it to the substrate using the MPP laser, but this process was not repeatable for multi-tiered structures. Figure 33 shows the trapping process and transportation of particles above the substrate.

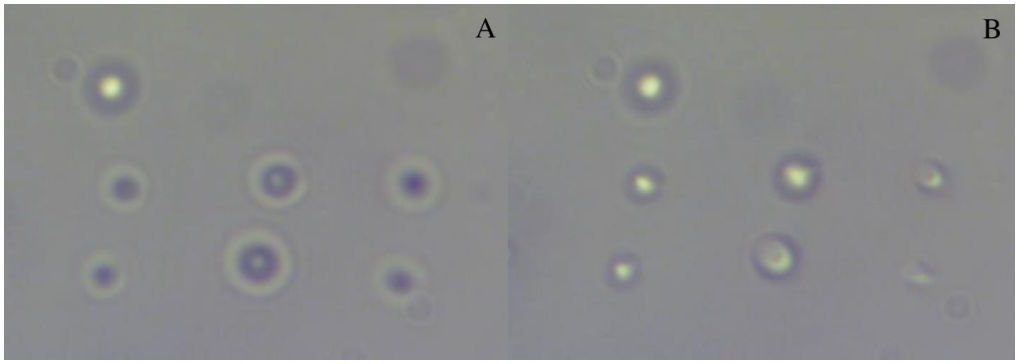


Figure 33. Two images demonstrate OT of a Soda-lime glass bead. The trapped particle in image A is placed above the substrate and particles on the substrate appears out of focus. As the stage moves towards the trapped particle, the immobilised beads become brighter in picture B.

This system was disassembled and changed to an inverted microscope setup with an afocal beam expander to enable the users to change the working distance of the objective lens for the trapping laser beam. The inverted microscope setup configuration increased the stability the system and reduced the number of common elements between the MPP and OT setups. By using the inverted microscope configuration, the majority of the optical components were assembled directly on the optical table, which reduced vibrational effects to the system. Figure 34 shows the schematic diagram of the combined setup that yielded the highest performance compared to its predecessor designs.

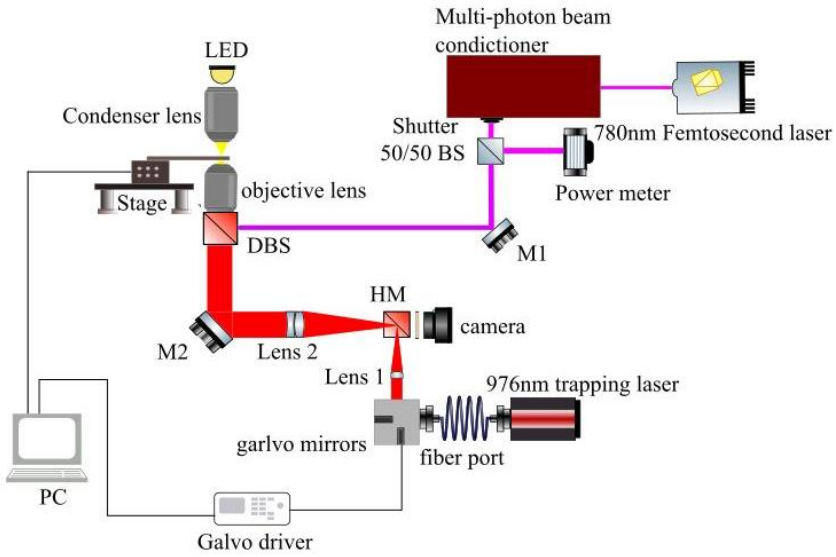


Figure 34. Schematic diagram of the combined setup that yielded the highest performance. This setup was the setup used to produce majority of the results in this work. The single objective lens inverted configuration of the setup made it the most stable setup. The trapping section of the setup remained unchanged comparing the upgraded OT setup presented in Figure 26.

The addition of an afocal beam expander was a major change in the final combined setup compared to its predecessor. The cage translation mount (CT1), which was used to mount one of the objective lenses in the double objective lens system, was used to mount the first lens (lens 1 in Figure 34) of the Keplerian beam expander.

The afocal beam expander decreases the objective lens focal distance for the trapping laser beam, which has a longer wavelength when compared to the polymerization beam. By changing the focal distance of the objective lens, the particle in the trap can move independently in the laser propagation direction (Z). Utilising the afocal beam expander and the GM system enables the user to overlay the focal volume of the objective lens for both trapping and polymerization laser beams in X,Y and Z directions.

The objective lens used in this experiment corrected the spherical aberration for Zeiss Number One coverslips (thickness of 170 μm). To use the inverted microscope setup with microscope slide holder, a custom coverslip adaptor was printed using the Objet Connex 260 3D printer.

Combining the OT setup with the MPP setup was one of the milestones in this PhD project and one of the most challenging objectives of this work was achieved after completing this section.

3.4 Imaging and diagnostic techniques:

Different imaging systems were used to characterise the structures built during this project. Bright Field Microscope (BFM) was one of the core instruments that provided images from samples in different stages. The imaging section of the setups was essentially a BFM that enables the user to monitor the build process while the sample is being fabricated. The built structures were checked after development using a commercial BFM microscope (Nikon Eclipse LV-100ND) and the position of the sample was marked on the coverslip using the silver pen. The MPP polymer is transparent in the visible frequency but the high refractive index particles appear brighter in the BFM, which makes particle identification relatively easy.

Confocal fluorescent microscopy is an advanced form of optical microscopy that has two major advantages when compared to normal BFM. The first major advantage of confocal fluorescent microscopy is its superior resolution. The pinhole inserted in the optical path eliminates the out of focus light rays and increases the optical resolution and contrast of the sample. Secondly, the confocal fluorescent microscope enables sample imaging and excite with a specific wavelength. Zeiss LSM880 was used to perform imaging of the fabricated samples. The argon laser mounted on the setup enables excitation of fluorescent beads inside the structure. This system was equipped with a piezoelectric stage, which enables sample slicing.

The maximum theoretical magnification attainable using bright field microscopes is 1000X. The resolution of the optical setups is limited by the diffraction limit of light. High NA objective lenses with short working distance should be used to achieve high resolution and magnification in the optical setup. Due to the limitations of the optical microscopy, researchers developed

techniques to replace the light source with an electron source. By using a high-energy electron source (electron gun), the electrons can be accelerated to 2-1000 keV and produce an electron beam with 0.62 to 0.00124 nm wavelength. The SEM is one of the most popular diagnostic techniques to investigate the specimens surface. Researchers use this method to gather information on the sample morphology, chemical composition, and crystallinity of the samples. High-energy electrons interact with the atoms in different manners and by using different detectors wide variety of information can be collected.

To produce SEM images using the electron beam, two sets of magnetic coils are being used to reflect the electron beam and raster scan the sample area. The deflection system controls the magnification of the SEM. Signals generated by the electron beam interaction with the sample are measured for each point. Based on the electron beam energy and the atomic mass of the sample the electron beam penetrate the sample in a teardrop shape. The interaction of electrons with the sample produce secondary, backscattered, Auger electrons and characteristic X-rays. Different sensors are being used to collect these signals.

Signals generated by the electron beam interaction with the sample are measured for each point. Based on the electron beam energy and the atomic mass of the sample the electron beam penetrate into the sample in a teardrop shape. The interaction of electrons with the sample produce secondary, backscattered, Auger electrons and characteristic X-rays. Different sensors are being used to collect these signals. High-quality images can be generated using secondary electrons. Secondary electron detectors composed of a collector, which is isolated from the rest of the SEM body and a scintillator. The collector is an Everhart-Thornley (E-T) electron detector with a positive charge. The positively charge E-T detector attract the secondary electrons and some of the backscattering electrons. Figure 35 shows the sites in which each signal is generated. Backscattered electrons can be efficiently collected using an overhead semiconductor detector.

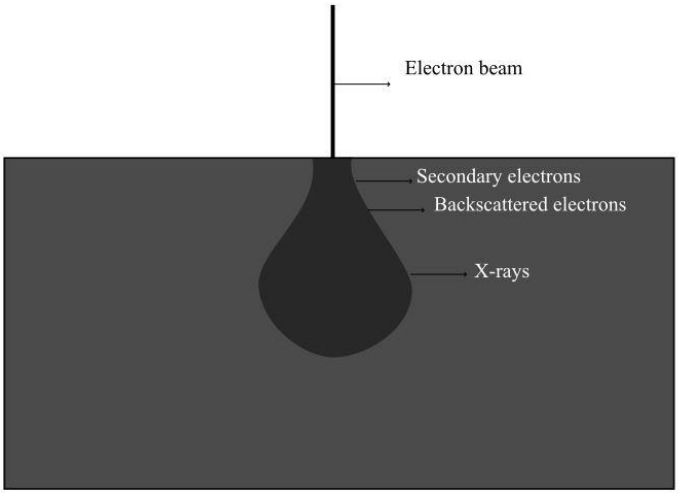


Figure 35 The electron beam penetration in a sample with different emitting signals and their sites.

Electron beam interaction with the sample can be classified into elastic and inelastic scattering. Elastic scattering occurs when the incident electron loses around 1 eV of its kinetic energy, which is not comparable with its primary energy (1keV). The other defining factor of elastic scattering is its high angle of reflection (2 to 180 degree).

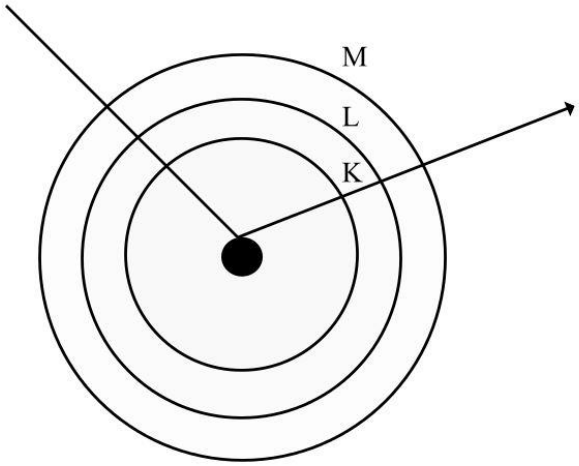


Figure 36 schematic diagrams of an atom and Elastic scattering of an electron with a high angle of reflection. The nucleus is placed at the centre, and different electron band is labelled M, L and K.

Inelastic scattering is the second general category of scattering. In contrast to elastic scattering the incident, electron deflects by less than 0.1 degrees, and it loses some of its kinetic energy. The absorbed energy can manifest itself in

different forms. One of the most common forms is phonon excitation. The electron beam oscillates the lattice structure of the sample and heat up the sample. For a conductive sample, the heat transfer can increase the sample temperature by few degrees but for a nonconductive sample, it can increase the sample temperature for several hundred degrees [207].

Secondary electrons are another example of inelastic scattering. The incident electron transfers some of its' kinetic energy to a loosely bounded electron and moves it from the valence band to the conduction band. The incident electrons with enough energy can exit the atom and produce secondary electrons.
The incident electrons can produce X-rays, and there are two sources for the generated X-ray signal. Ionized atom shells can produce bremsstrahlung X-rays, which is produced by electrons losing their energy also known as breaking X-ray and characteristic X-rays that generated when excited atom returns to its steady state. The incident electron can remove one of the tightly bounded electrons (inner-shell electrons) and leave the atom in an excited state. The excited atom fills the inner-shell vacancy by transferring one electron from outer-shell electrons to the inner-shell through series of permitted transitions. This transition, which happens in 1 ps, produces characteristic X-rays and because of its sharp and well-defined energy, it can be used to identify the element. Figure 36 shows a simplified diagram of an atom with 3 of its shells around the nucleus. Each shell is divided into a number of subshells that electrons in these subshells have similar energies. Each shell is marked with a principal quantum number (n), which defines the number of subshells for the particular shell. In X-ray terminology: n=1 corresponds to shell K, n=2 shell L and n=3 shell M. These shells have subshells numbered from 0 to n-1. Table 1 shows X-ray notation for shells and their subshells. It also displays the number of electrons that can occupy each shall. Each electron in the shell has unique energy and the quantum number $m_j$is defined that take the spin and angular momentum of the electrons in to account.

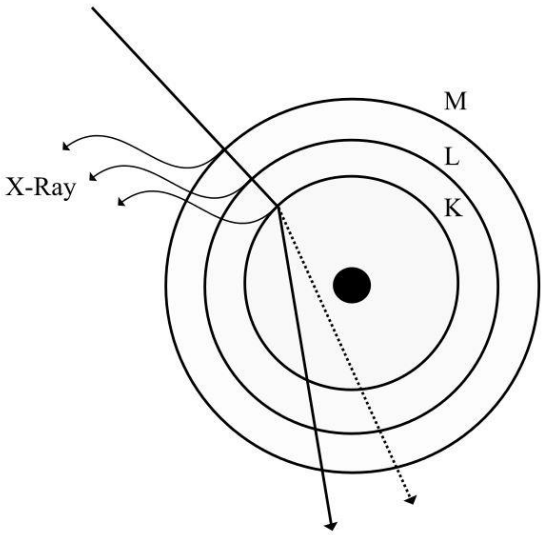


Figure 37 Schematic diagram of characteristic X-rays generation from the incident electron beam. The inelastic scattering of the electron (solid line) and possible Auger scattering (dotted line) is shown.

X-Ray notation	**Quantum numbers**			**Electrons**	**Subshell**
	n	l	m_j		
K	1	0	$\pm\frac{1}{2}$	2	1S
L_I	2	0	$\pm\frac{1}{2}$	2	2S
L_{II}	2	1	$\pm\frac{1}{2}$	2	2S
L_{III}	2	1	$\pm\frac{3}{2}\pm\frac{1}{2}$	4	2P
M_I	3	0	$\pm\frac{1}{2}$	2	3S
M_{II}	3	1	$\pm\frac{1}{2}$	2	3S
M_{III}	3	1	$\pm\frac{3}{2}\pm\frac{1}{2}$	4	3P
M_{IV}	3	2	$\pm\frac{3}{2}\pm\frac{1}{2}$	4	3P
M_V	3	2	$\pm\frac{5}{2}\pm\frac{3}{2}\pm\frac{1}{2}$	6	3D

Table 3 Shells and subshells of atom

EDX system in commercial SEM uses the characteristic X-ray signal energy and wavelength to identify the elements in the sample. The energy emitted by

electrons moving between above-mentioned shells produce a sharp X-ray peak. Although there is a small variation of electron energy in different subshells of a shell, but they are readily distinguishable from other shells. Each element can produce multiple X-ray peaks that represent electrons moving from K, L and M shells and by comparing the position of each peak (Peak energy) with the predefined table of electron energy, elements can be identified.

Three different SEM devices were used during this PhD project. A tabletop SEM Hitachi TM3000 was used to image the samples with low magnification and perform EDX analysis on uncoated specimens. The tabletop SEM produced high-resolution imaging with a maximum magnification of 3000. The charge reduction mode of this system enabled imaging of uncoated, nonconductive samples.

High magnification images were taken using a Philips XL30 FEG-ESEM and JEOL 6400 SEM. The field emission electron source in these microscopes produced smaller spot size and enabled high-resolution images with high magnification.

Time-Of-Flight Secondary Ion Mass Spectrometry (TOF-SIMS) was used to produce a depth profile of the fabricated structures. TOF-SIMS uses pulsed ion beam (Cesium, Argon or Gallium) to mill away the polymer layers and expose the inner structure of the fabricated parts. . The milling process remove molecules (secondary ions) which are accelerated toward the detector through the flight chamber. The flight time of each particle is measured with nanosecond accuracy. Based on the flight time, the particle mass will be calculated with 0.00× Atomic Mass Unit (AMU) resolution (i.e. one part in a thousand of the mass of a proton). Some of the TOF-SIMS key advantages are as follow:

- High mass resolution enables identification of molecules with same nominal mass.
- 0 to 10000 AMU mass range that can identify molecules, ions and compounds.
- Trace element can be detected with an accuracy of a part per million.

- The structures can be mapped with sub-micron resolution.
- The Ion beam can produce depth profiling by etching the sample with a typical rate of 1 A per minute.
- The data gathered from each pixel stores the elements in the pixel and it is possible to analysis the sample retrospectively. Therefore, it is possible to study the samples for different chemical compositions after completing the TOF-SIMS process.

In this project, TOF-SIMS IV (IONTOF GmbH) was used to analyse the samples. Using the Ion beam the structure was etched away and the material composition of each layer was tested to locate the particles. The data gathering process was optimised by using a 15 keV Ar_{17000} sputtering beam and 25 keV Bi_3 analysing beam

3.5 Materials

Different materials were tested and used during this PhD project. To test the custom-built setups, the commercial photoresist available in the market OrmoComp was used first. Afterwards, new photoresists were tested to produce the combined setup photoresist. In the combined setup photoresist, the refractive index of the resin must be as small as possible to increase the variety of particles that can be optically trapped. The photoresist viscosity was also very important. To enable the OT to transport particles adequate speed the viscosity of the photoresists must be as low as possible.

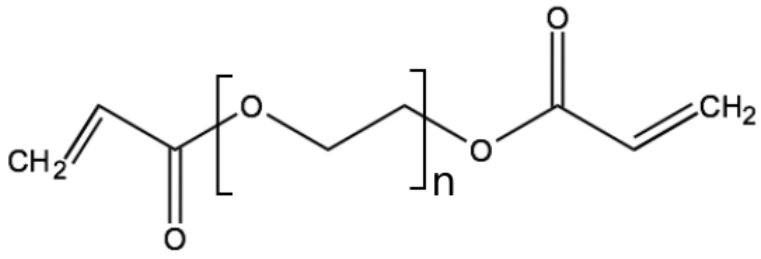
MPP mechanisms are currently being discussed in the scientific community, avalanche ionisation, and thermal polymerization has been suggested to be the polymerization source for photoresists such as SU-8 and the hybrid sol-gel SZ2080 [208], [209]. ORMOCOMP (Microresist, Germany) multiphoton photoresist was used in testing the MPP facility. This polymer has high thermal stability, low water absorption and little optical loss at communication wavelengths (0.2-0.3 dB/cm at 1320 nm, 0.5-0.6 dB/cm at 1550 nm) that makes it a suitable material for optical applications such as the fabrication of waveguides [210]. This material was used to test the resolution and the fabrication speed of the setup. Different structures fabricated using ORMOCOMP will be presented in Chapter 4. The developer agent (ORMODEV) must be used to develop the polymerised ORMOCOMP. Hard baking is necessary to enhance the mechanical properties of the manufactured structures; ORMOTHIN could be used to reduce the viscosity of ORMOCOMP.

For initial testing of the OT section, 2 µm silica beads suspended in deionized water were used. A µ-Slide with 100 µl capacity (Ibid µ-Slide I 0.1 Luer Uncoated) was used as the sample chamber for the optical trapping setup. The difference between the refractive indices of the silica beads and water ensured the stable trapping of particles. After calibration of the OT setup, stable 3D trapping of Silica beads suspended in deionized water was achieved. Besides the dielectric particles, 300 nm gold particles, 100 nm silver particles, carbon

nanotubes and soda lime glass particles suspended in deionized water were tested in the OT setup.

The combined setup photoresist must be a heterogeneous mixture of a low refractive index multiphoton photoresist and high refractive index particles. Choosing a low refractive index polymer as the host material increases the variety of particles that can be used in the combined setup. Another key property of the host polymer is the viscosity of the polymer. The viscous drag generated by the polymer is the main limiting factor in the particle transportation speed. Having highly viscous polymers makes the particle suspension, trapping, and transportation more challenging.

ORMOCOMP was not an ideal choice to be used as the host polymer for the photoresist due to its high refractive index and viscosity. Polyethene (Glycol) Diacrylate (PEGDA) with a refractive index of 1.47 nD20 (refractive index at 20°C taken at sodium D line) was used to prepare the photoresist for the combined setup. PEGDA is commercially available with different molecular weights (Mn) and viscosities. To produce the photoresist 1.1% w/v of a commercial photoinitiator (2-Benzyl-2-2(dimethylamino)-4-morpholinobutyrophenone) was added to PEGDA Mn 575. Figure 38 shows the molecular structure of PEGDA, Melamine resin particles, and the photoinitiator.



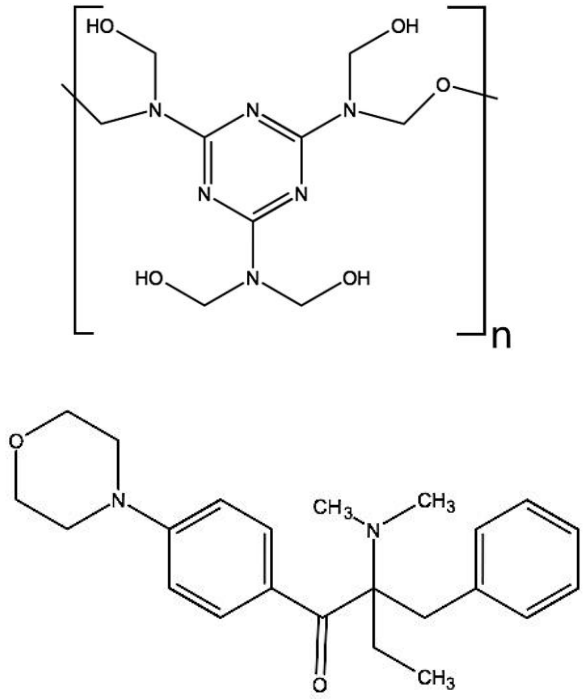


Figure 38. molecular structures of (a) PEGDA (Mn 575 g/mol), (b) melamine resin and (c) 2-benzyl-2-2(dimethylamino)-4-morpholinobutyrophenone (photoinitiator).

Compared to ORMOCOMP, this formulation had lower viscosity and refractive index at room temperature, and fewer post-processing steps were required. The excess polymer was washed away using deionized water to develop the polymerised structure.

Properties	PEGDA Mn575 g/mol [211]	ORMOCOMP [212]
Viscosity	0.057 Pa.s	5-8 Pa.s
Refractive index	1.467 (589.3 nm)	1.518 (635 nm)
Maximum fabrication speed	20 $\mu m s^{-1}$	600 $\mu m s^{-1}$
Achieved feature size	900 nm	700 nm
Absorption wavelength	<300 nm	<350 nm

Table 4 Comparison table of PEGDA Mn 575 g/mol and ORMOCOMP.

After successfully testing the custom photoresist (PEGDA+ PI) in the MPP section of the combined setup particles were introduced to the photoresist. Particles used in this experiment were high refractive index soda-lime

microspheres (Thermo Science 9000 series). The refractive index of these particles was 1.59 nD20, which is greater than the refractive index of PEGDA, and they have high mechanical and chemical stability. These particles were purchased in dry powder form, and different procedures were tested for suspending these particles in the photoresist.

To suspend the particles first, a slurry was created using isopropanol and then deionized water was added to the container. The mixture was sonicated in an open cap container for 20 minutes. The mixture was added to the photoresist and sonicated in a plastic amber container. This technique was not successful and shortly after removing the container from the ultrasonic bath, particles were agglomerated and sunk to the bottom of the container.

To reduce the particle agglomeration a surfactant (Triton X100) was used. To introduce the particles directly to PEGDA lower Mn PEGDA (Mn 250 g/mol) with lower viscosity was chosen. 1%v/v surfactant was added to PEGDA Mn250 g/mol and particles were introduced directly into the polymer. Due to the low wettability of the particles, it was critical to whisk the mixture vigorously before putting it in the ultrasonic bath. Higher Mn PEGDA and photoinitiator were added to the mixture in the last step of polymer preparation. Adding higher Mn PEGDA increases the viscosity of the mixture and helps the mixture to be more stable.

In the prepared photoresist the ratio of refractive index of the particle over its surrounding medium was 1.08, which has been reported to be sufficient for production of stable trapping forces [112]. Suspending soda lime glass particles in the polymer solution was not satisfactory, and stable solutions were not achieved. Due to the extended sonication process, the glass particles were damaged during the process and contaminated the samples. To decrease the contamination the mixture was placed in an amber plastic container during the sonication process. The image in Figure 39 is taken using the imaging section of the combined setup. Clusters and contaminations produced by the glass beads can be seen in this image.

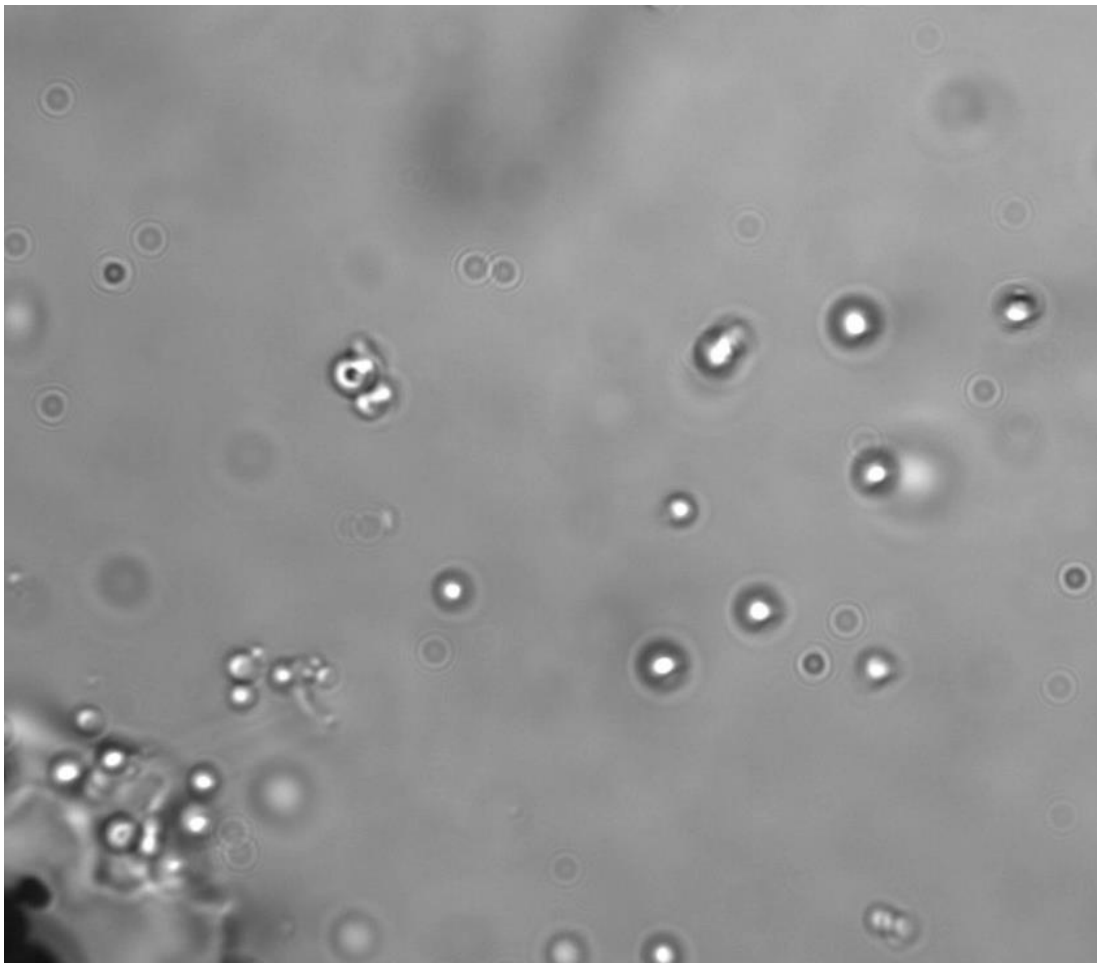


Figure 39. Pictures taken from the combined setup imaging camera. The photoresist produced using Soda-lime glass beads suspended in the photoresist. The particle aggregation and small contaminations produced by particle breakage are visible in the image.

To improve the stability of the combined system photoresist soda lime glass particles were replaced by Melamine resin based particles. 3 μm melamine resin based, FITC marked micro particles suspended in deionized water (Sigma Aldrich) were purchased and directly mixed with the prepared photoresist. These fluorescent beads had a refractive index of 1.67 n20/D. Having higher refractive index compared to soda lime glass beads enabled efficient trapping of these particles with lower laser power. Also, structures fabricated with fluorescent beads embedded in them can be investigated by confocal fluorescent microscopy. By exciting the fluorescent beads and performing imaging using the fluorescent beads emission wavelength it is possible to detect the position of the particles inside the structure.

The photoresist that produced the best results was prepared with a mixture of PEGDA Mn575 g/mol (1 mL), PEGDA Mn250 g/mol (1 mL), 5.6 mg of photoinitiator (2-benzyl-2-2(dimethylamino)-4-morpholinobutyrophenone and 10 μL of micro particles based on Melamine resin suspended in deionized water (Sigma Aldrich). The mixture was prepared under yellow light in an amber glass vial. To dissolve the photoinitiator and evenly distribute the particles in the photoresist, the mixture was mixed for 2 minutes and then sonicated for 15 minutes. After sonication it is important to check the vial and make sure that the mixture is not cloudy and the photoinitiator is completely dissolved. Figure 40 shows the viscosity of the combined setup photoresist.

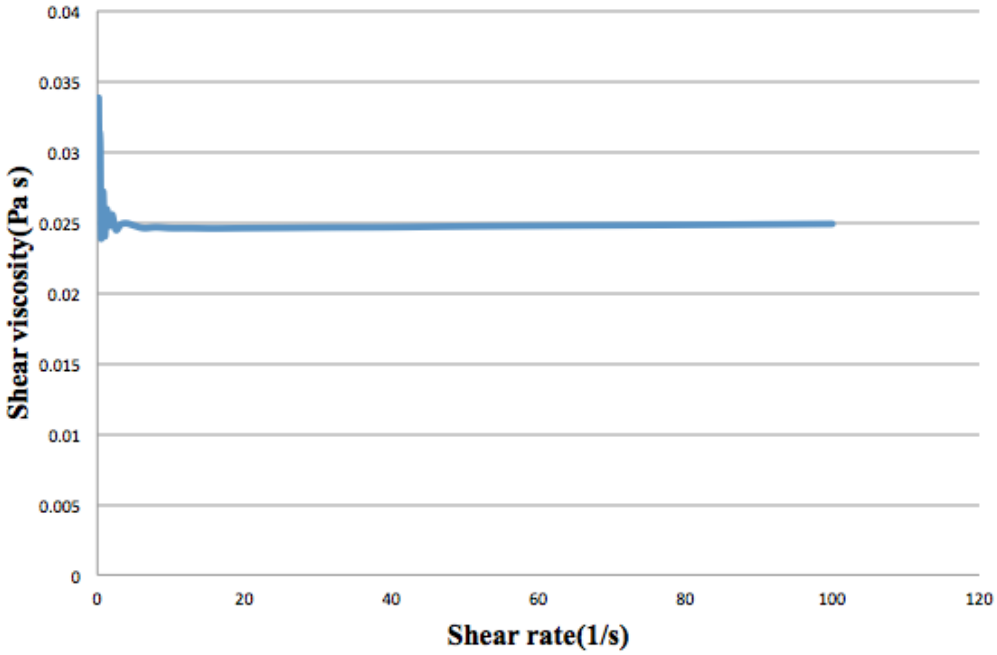


Figure 40. The viscosity of the equal mixture of PEGDA Mn575 g/mol and Mn250 g/mol at 20^{o}c over 20 minutes. After few minutes the system becomes stable, and the viscosity of the mixture becomes constant as the shear rate increases.

CHAPTER 4: PRELIMINARY EXPERIMENTS AND RESULTS.

One of the objectives of this project was to combine the MPP setup with an OT rig. The combined setup was envisioned to be able to manipulate and transport particles with different properties using the OT into the MPP vat to produce microstructures using a mixture of the particles and the polymer.

Before being able to combine the OT and MPP setups, the setups were assembled and tested independently. The testing procedure of the individual setups and the combined setup is presented in this chapter. Each section of this chapter presents the results and findings that were achieved by completing one of the projects' milestones and correlate directly with the objectives set at the beginning of the Thesis.

Assembling the MPP setup was the first objective of this PhD project. In the methodology chapter section 3.1, the design, assembly and alignment process of the MPP setup was explained. In the first section of this chapter (section 4.1), the structures fabricated using MPP will be presented, and the MPP operation procedure explained. The structures presented in section 4.1 were fabricated to test the capabilities of the MPP setup and its driver software.

The second section of this chapter (section 4.2) is dedicated to the OT testing and simulations. The trapping results for different particles tested in the OT rig are also presented in this section. Alongside the OT experimental results, simulation results for a variety of particles suspended in different photoresists will be presented in this chapter.

Experiments done using the combined setup are divided into two sections. The first section of the experiments, which were focused on the commissioning of the combined setup, will be presented in the last part of the chapter (section 4.3) and more advanced experiments will be presented in chapter 5.

4.1 MPP setup fabrication

The first step in using the MPP setup was to make sure that the MPP setup could use an IR femtosecond laser to solidify the photoresist. The MPPs' SOP included (a) safety information regarding the usage of the class four laser, (b) sample preparation, (c) sample alignment procedure, (d) the fabrication procedure and (e) post-fabrication processing.

After defining the SOP, system benchmarking started. During the system benchmarking, minimum laser power, minimum exposure time and the resolution of the setup was tested. The resolution of the setup is defined by the system voxel size that depends on the laser power, exposure time and the photoresist itself. To test the polymerization capability of the MPP setup, the multiphoton photoresist ORMOCOMP was used.

Table 5, gives an overview of different steps involved in the MPP setup sample preparation, fabrication and post-fabrication processing for ORMOCOMP.

A) A Zeiss number one coverslip (170 μm thick) was marked using a diamond-head pen. The scratch marks on the substrate serve as a reference for placing the focal volume of the objective lens on the substrate.
B) A droplet of ORMOCER was placed in the marked area.
C) The polymer was baked for 5 minutes at 80˚C.
D) A 150 μm spacer (printed using Connex Objet260 3D printer) was placed on top of the substrate and the polymer was sandwiched using a second coverslip. Figure 41 shows different steps of sample preparation.
E) The sandwich was placed inside a custom-designed mount and fixed to the piezoelectric stage using four gauge number three screws.
F) Using the imaging system and the 5X microscope objective lens (CFI LU Plan Fluor 5X objective lens), the mark on the coverslip was found. By employing the mechanical stage (Thorlabs RBL13D/M) and the piezoelectric stage, the scratches on the substrate was moved to the centre of the camera feed.

G) A droplet of immersion oil was placed on the coverslip and the 100X objective lens was brought close to the sample by utilising the objective lens turret. Using the microscope bod's fine adjustment on the scratch marks on the substrate were brought into the imaging plane of the objective lens.

H) The last step of the polymerization starts by setting the laser parameters and checking all the safety requirements. Before starting the laser, the enclosure door must be closed. The Femtosecond laser used in the MPP setup is a class-4 laser and based on the health and safety regulations, an interlocked enclosure must protect the users from accidental exposure to the laser beam. The interlock system shuts down the laser if the enclosure door is opened. Before opening the laser shutter, the appropriate polymerization beam must be selected. For the first experiment the polymerization wavelength was set to 800 nm and the laser beam was expanded by 3X using the beam conditioner GUI. For the first experiment the beam attenuator GUI amplitude of 680 (output power of 54 mW) was chosen for the first fabrication.

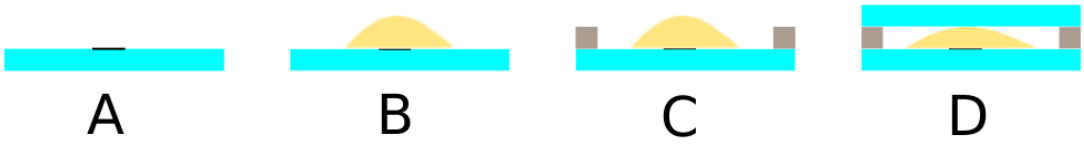


Figure 41. Different stages of sample preparation are shown in this figure. (A) Marked coverslip, (B) A droplet of the photoresist placed on the marked coverslip, (C) The spacer was placed on the coverslip, and (D) the polymer is sandwiched with a second coverslip.



Table 5. Flowchart of sample fabrication steps.

The beam attenuator GUI amplitude of 680 (output power of 54 mW) was chosen for the first fabrication. Initially, even with opening the laser shutter and the Thorlabs shutter, polymerization didn't commence. The objective lens working distance for the polymerization wavelength (800 nm) was longer than its working distance for visible light. Using the imaging system to focus on the substrate placed the polymerization area (the focal volume of the objective lens for the polymerization beam with a wavelength of 800 nm) inside the substrate. The sample was moved away from the objective lens using the piezoelectric stage until the polymerised areas were brought into the focal plane of the objective lens. By placing a portion of the objective lens focus volume inside the substrate higher polymer adhesion was achieved and stable lines were fabricated. The polymerised ORMOCOMP had a higher refractive index and using the MPP imaging system; it is possible to follow the polymerization, but the polymerised areas appear out of focus.

One of the most important steps in benchmarking the MPP setup was measuring the voxel size (minimum feature size) of the setup. The voxel size of the MPP setup depends on three sets of parameters: device configuration, photoresist, and

operational parameters. The most important device parameter that affects the minimum feature size of the setup was the objective lens. Using a high NA / magnification oil immersion objective lens focused the laser beam into a tight spot and increased the resolution of the setup. The shutter speed and stage resolution are two other defining factors in the minimum feature size attainable with the setup. Operational parameters like the exposure time and laser intensity are the user-controlled parameters that can affect the resolution of the setup.

The first step in defining the voxel size was to focus as close as possible to the substrate. The pullout method was used to place the polymerization area on the substrate. First, the piezoelectric stage was used to move the sample towards the objective lens and place the focal volume of the objective lens inside the coverslip. Second, while the objective lens was focused inside the substrate, the laser was turned on, and gradually the stage was moved away from the objective lens. As the objective lens focal volume moves out of the substrate, the photoresist close to the substrate solidifies, and the exact position of the coverslip could be defined.

Figure 42 (left) demonstrates an array of voxels fabricated using different exposure times. By increasing the exposure time the voxel size increased. The increase in voxel size was predominantly in the axial direction. Figure 42 (right) shows high magnification images of two voxels fabricated in the MPP setup to test the position of the focal volume of the objective lens. The elliptical shape of the voxels shows good alignment in the system. These voxels were fabricated with an exposure time of 300 ms and power of 33.5 mW. After completing the fabrication process, the sample must be developed before being ready further processing.

The sample development process is as follows:

1. The sample holder was unscrewed from the stage and the polymer sandwich was removed from the sample holder.
2. The upper coverslip that holds the immersion oil and the spacer were removed from the coverslip.

3. The coverslip was placed on a hot plate to bake the sample at 130°C for 10 minutes.
4. The baked sample was immersed into ORMODEV (the developer material supplied by Microresist Germany) for 5 minutes. ORMODEV dissolves and removes the unsolidified ORMOCER from the sample.
5. Using acetone the excess ORMODEV was washed from the sample.
6. Dry nitrogen gas (clean dry compressed air) was used to remove the acetone from the coverslip surface and blow-dry the sample.
7. The last step in the sample development process is hard baking the sample for 3 hours at 150°C.

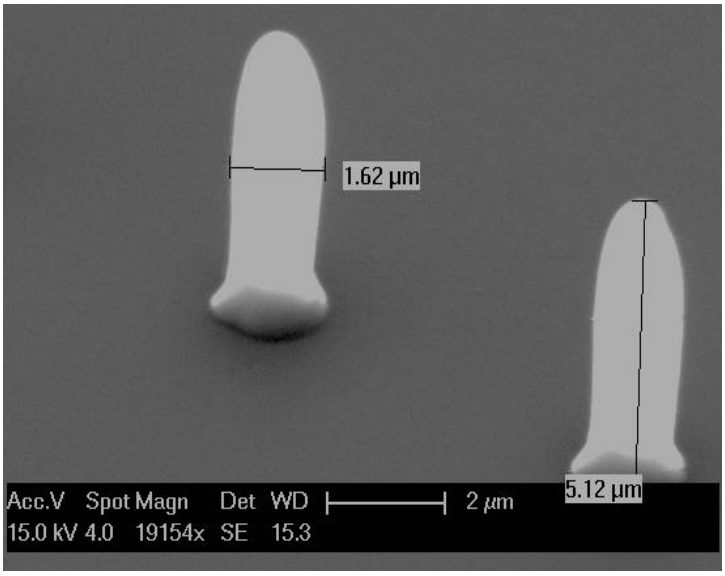


Figure 42. High magnification images of voxels fabricated using an exposure time of 300 ms and laser power of 33.5 mW.

The operational parameters like exposure time, stage travel speed and laser intensity are the user-controlled parameters that can affect the resolution of the setup. The mechanical properties of the photoresist and multiphoton absorption efficiency of the photoresist are other factors that can limit the minimum feature size of the system.

The first step in defining the voxel size was to focus as close as possible to the substrate. To define the exact position of the coverslip the piezoelectric stage was used to move the sample towards the objective lens and place the entire focal volume of the objective lens inside the coverslip. Subsequently, the laser was turned on, and gradually the stage was moved away from the objective lens.

As the objective lens focal volume exits the substrate, the photoresist close to the substrate solidifies and the exact position of the coverslip could be defined. To demonstrate the effect of exposure time on the voxel size, an array of voxels in Figure 43 was fabricated using fixed laser power and varying exposure. By increasing the exposure time the voxel size increased. The increase in voxel size was predominantly in the axial direction. The smallest voxels were fabricated using 20 ms exposure time. The voxels in lower left corner of the Figure 43 are delaminated from the substrate. Voxel delamination was caused by substrate imperfections, vibration in the system, the high aspect ratio of voxels and lower polymer adhesion. These issues are some of the practical factors that limited the operational voxel size of the setup. Therefore, to ensure the successful development of the samples, it was not possible to use the lowest feature size attainable using the setup. A more comprehensive MPP benchmarking was performed once the system was combined with the OT setup and it will be presented in chapter 5.

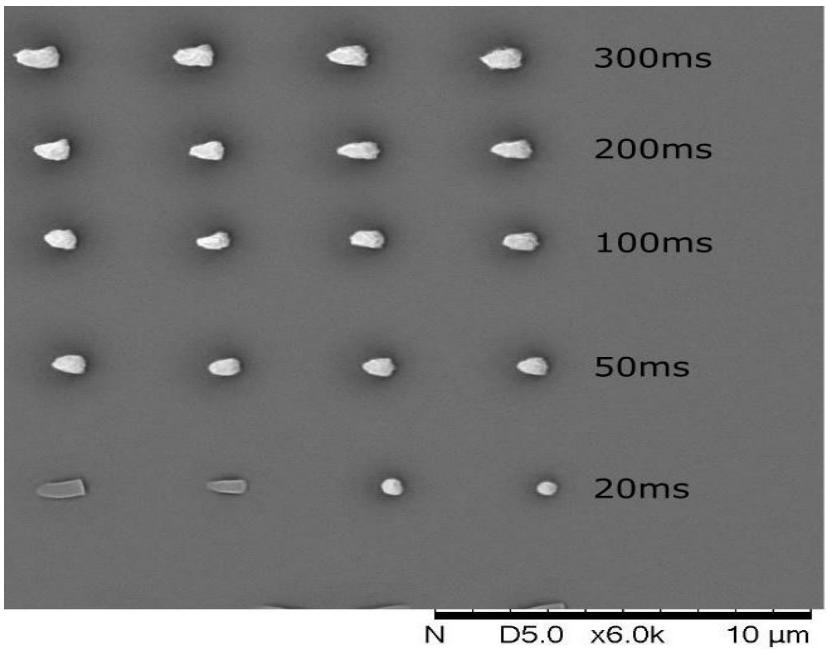


Figure 43. An array of voxels fabricated using different exposure time. All voxels fabricated using identical laser power and voxels in each row had similar exposure time. By increasing the exposure time the voxel length increases faster than the voxel diameter. The fallen voxels in the lower left corner can be used to measure the voxel length. The voxels measured was 0.96 µm and 1.26 µm.

The fabrication parameters for the MPP setup was defined experimentally. The Mechanical shutter speed limited the minimum exposure time to 20 ms and the minimum laser power was set to 11.56 mW. These numbers produced the highest resolution in the system but using the system with the lowest laser power and the shortest exposure time was made the system unreliable. Freestanding structures fabricated using the above-mentioned laser intensity and exposure time often collapsed or washed away during the post-fabrication development process. Using 14.55 mW greatly improved the reliability of the system with increasing the system minimum feature size and reducing the aspect ratio of voxels. After testing the MPP setup and developing the SOP, simple structures were fabricated using the piezoelectric stage driver software. Figure 44 shows a zigzag structure fabricated using the stage driver software with laser power of 14.55 mW and stage scanning speed of 20 $\mu m/s$.

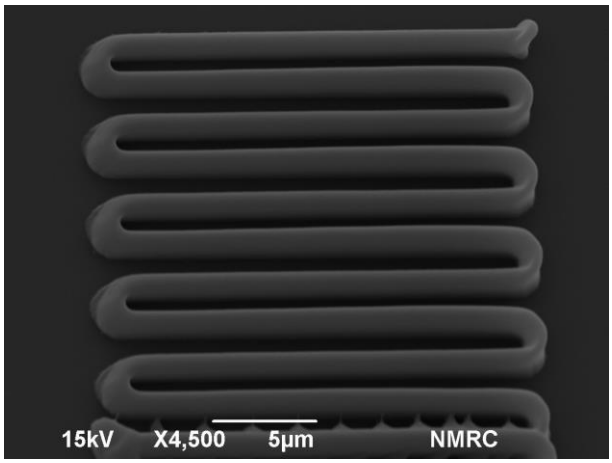


Figure 44. Zigzag structures fabricated using the piezoelectric stage driver software with different step size in X and Y (0.5 μm and 2 μm). The stage speed, step size and the laser power defines the feature sizes produced by the system.

The stage driver software had limited functionality with respect to raster scanning the travel range of the stage. The user could control the stage speed and step size but the system was unable to construct complex 3D forms. However, the developed Labview code was used to fabricate complex structures. Figure 45 shows a low magnification SEM image of one of the first structures successfully fabricated using the LabVIEW code using the MPP setup.

The fabrication process started by mounting the sample on the stage and placing the objective lens focus close to the substrate. Voxels fabricated to check the objective lens focus position can be seen on the right-hand side of the SEM picture in Figure 45. After finding the substrate surface and placing a portion of the focal volume of the objective lens inside the substrate, the stage driver software was closed, and the LabVIEW driver software started to build the structure. Before running the software, the position of the bitmap file and the step sizes in X and Y was defined in the software front panel. By running the driver software, the imported bitmap file was built voxel by voxel.

A second bitmap file generated using Microsoft Paint software was imported into the driver software to check software reliability. Taking a closer look at Figure 45 shows some fabrication issues that affected the built structure. Figure 46 and Figure 47 shows a high magnification SEM image of the structure in Figure 45. Figure 46 demonstrates the effect of external vibration and the stage drift in the built structure. The dent in the fabricated structure (Figure 46) was due to the external vibration and stage malfunction. The stage recalibration was done using the auto-zero function of the stage and external vibration sources were identified and eliminated.

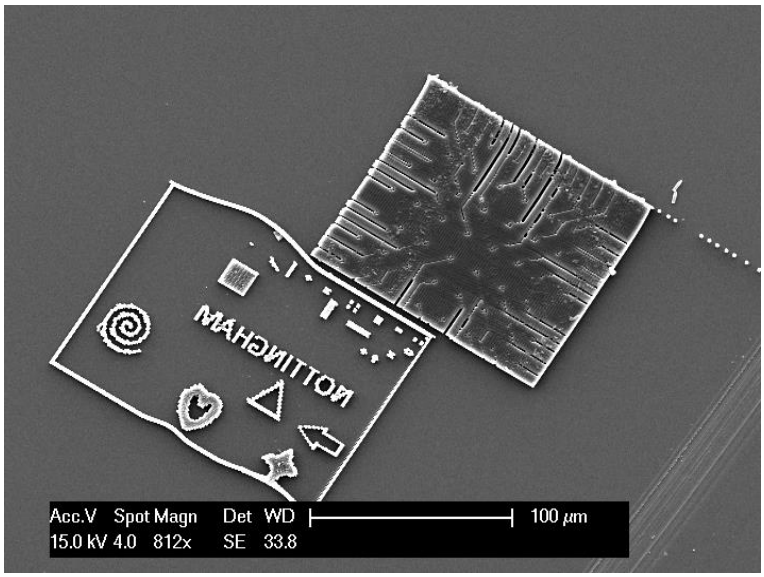


Figure 45. Two complex structures fabricated using the developed Labview code by importing bitmap files from the user-defined locations. The lower structure was fabricated to test the capabilities of the system to fabricate voxels close to each other.

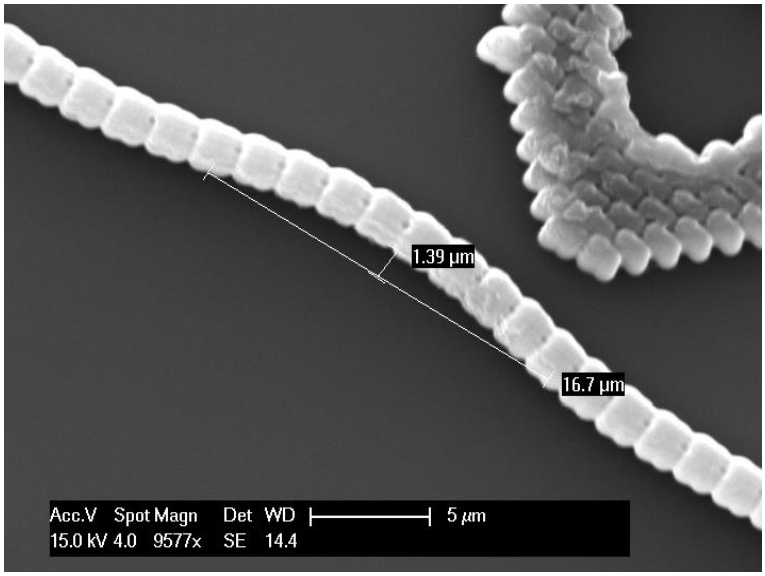


Figure 46**.** The effect of vibration on fabricating microstructure using MPP setup.

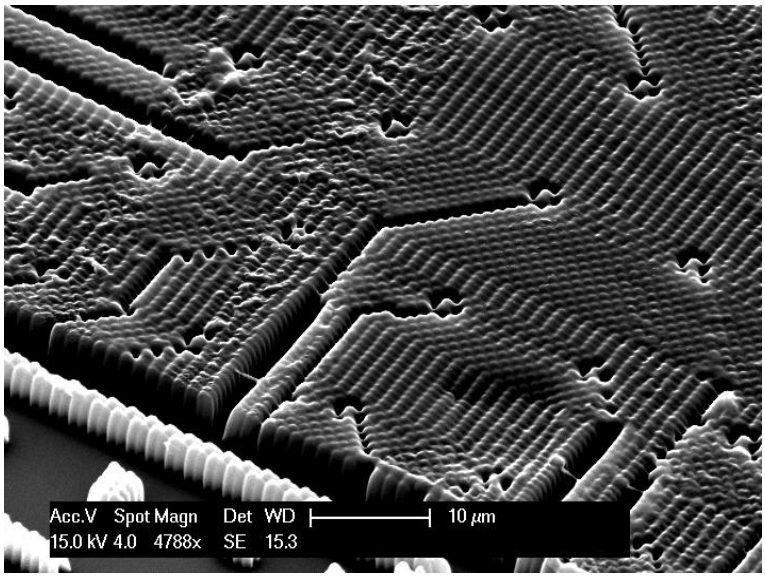


Figure 47. High magnification image of a structure fabricated using a bitmap file for a negative Printed Circuit Board (PCB). The metallic connections are left empty.

Figure 47 shows the surface of the sample fabricated using a printed circuit board bitmap file. On the left-hand side of the SEM picture, unwashed polymer distorted the structure, and some of the trenches are closed off due to polymer ingress. For this build the step sizes in the developed Labview code were set to 1 μm in X and Y. Based on the observation presented in Figure 43, this number is slightly smaller than the voxel size. The straight lines fabricated in Figure 47 show little distortion, but diagonal lines with small openings were partially closed off. Apart from some minor issues, the fabricated structures were the acceptable replica of the imported bitmap files. These structures demonstrate the ability of the software to import a bitmap file from the user-defined the location and replicate the structure in the MPP setup.

Figure 48 shows the surface profile of one of the fabricated structures with 37° tilt on an SEM stage. The developed Labview code uses raster scanning to build structures pixel by pixel and due to the elliptical shape of the MPP voxels (Figure 42) the sawtooth surface profile is unavoidable.

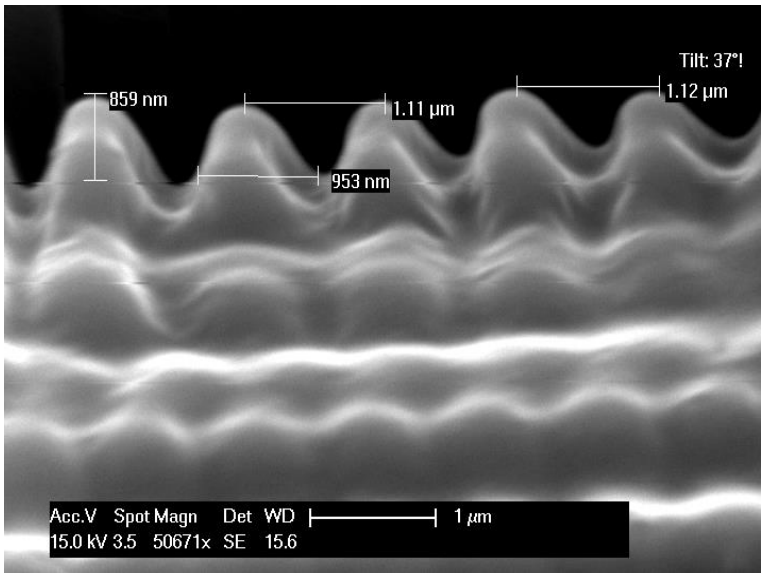


Figure 48. The sawtooth structure on the surface of the structure presented in Figure 49. Due to the point by point fabrication of the samples and the elliptical shape of the voxels this saw-tooth profile is produced.

After fabricating different single layered structures and debugging the software to replicate the imported bitmap file, the software was upgraded to be able to import multiple images one by one and fabricate true 3D structures layer by layer. In the previous software, the user used the front panel to select a bitmap file to be imported into the software but in the new software the user defines the path to the folder, which contains the bitmap files. The software constructs the new file names and imports them one by one. Another main change in the 3D software was Z movement. The Z movement function in the software utilises the absolute move function of the stage. The absolute move function moves the stage to a predefined position. To be able to stack layers on top of each other, a local variable was defined to store the stage position at the beginning of the build. Once the imported image was converted into a 2D array, the array size was also stored in another variable. Once the movements in X became equal to or an integer multiple of the 2D array size the Z movement function move the stage to the starting coordinate of the build and move down or up for one step. The software was originally designed for MPP setup assembled based on a microscope stage setup. To stack layers on top of each other, the stage must move away (down) from the objective lens. But in an inverted microscope setup in order to move away from the objective lens, the stage must move up.

Figure 49 shows one of the first 3D structures fabricated using the new software. Timing issues and stage movement in Z direction introduced new difficulties. Extra pixels were fabricated on the left-hand side of the structure, and the voxel size was not uniform throughout the structure. Delays were carefully introduced in different stages of the software to solve the fabrication issue by allowing the stage to move into a steady state before starting the next layer.

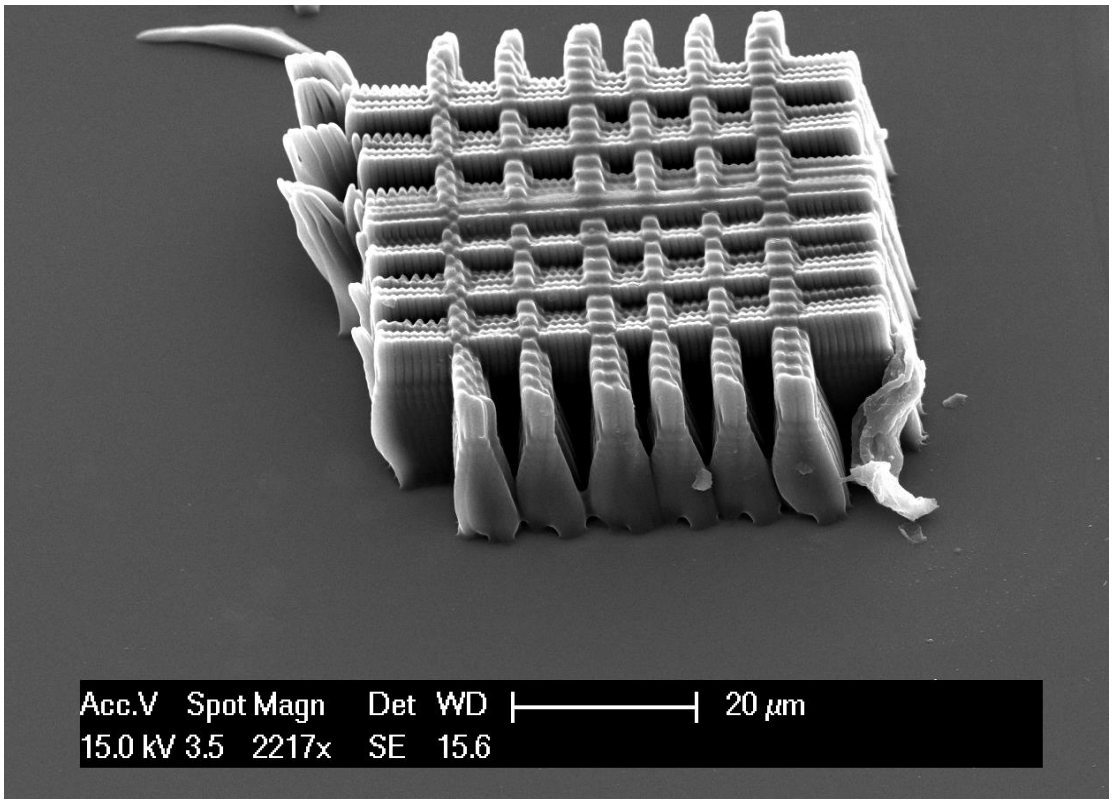


Figure 49. First 3D structures fabricated using the MPP rig.

Figure 50 shows one of the successful 3D structures fabricated using the MPP setup. In this figure, the 1-bit BMP files that were used in the fabrication of the structure are also presented for comparison.

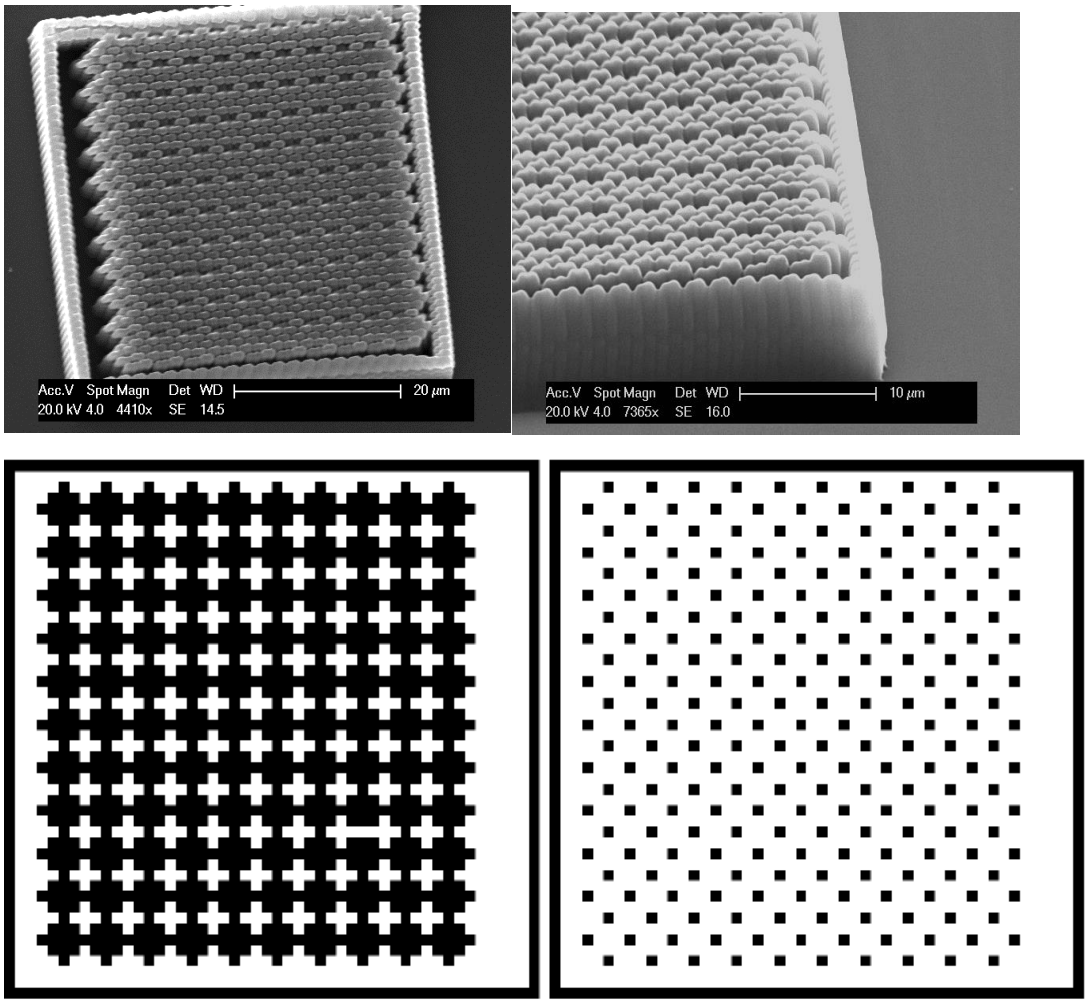
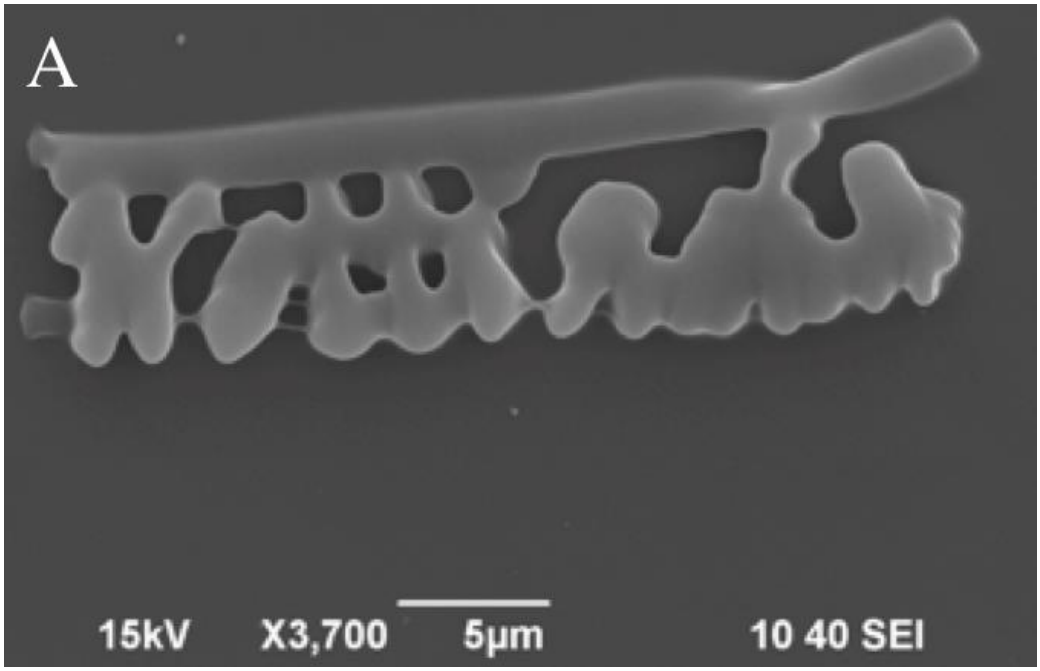
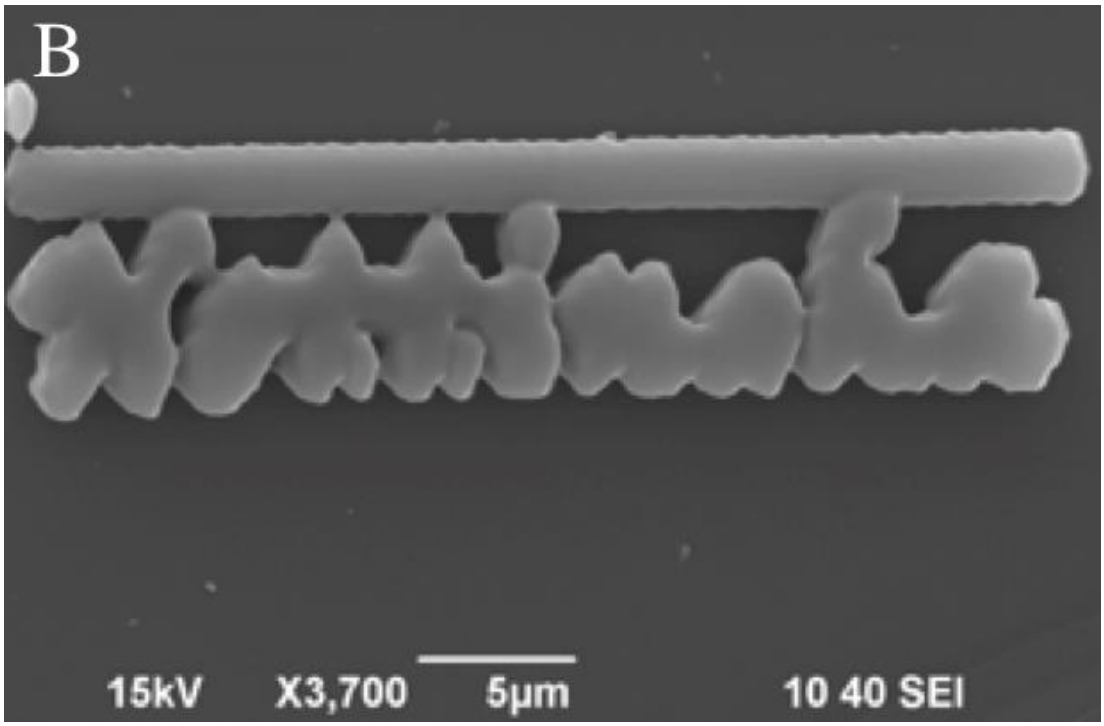


Figure 50. Multilayer structures fabricated with a laser wavelength of 800 nm and laser power of 14.55 mW and exposure time of 100 ms. (Left) the image shows the structure from the top. (Right) illustrates the structure with 37° tilt to demonstrate the layers stacked on top of each other.

To be able to use the Labview code with .STL files a further MATLAB code was developed to slice the 3D designs into a number of ".BMP" image files. In the MATLAB code, the user could control the picture size (X and Y) and the number of the layers (Z). By adding the new MATLAB code to the Labview driver, the MPP studio software was completed. The Labview software was changed to decrease the fabrication time. In the updated version of the Labview software (version 2.0), skipped the white pixels around the structure. In the original code, each pixel was tested and moved to the next stage, but in the new code, white pixels were stacked close to each other and the software skips directly to the first black pixel. By skipping the white pixels and reducing the delays, fabrication speed increased.

As explained before, having the right fabrication parameters are crucial to a successful build. To demonstrate the effect of the operation parameters on the final fabricated structure a complex structure was fabricated using different operating parameters. Figure 51 shows the *Nottingham* design fabricated with four different fabrication parameters. This figure was constructed from 1000 pixels (50 x 20) and the effect of step size in the shape and size of the structure is evident.





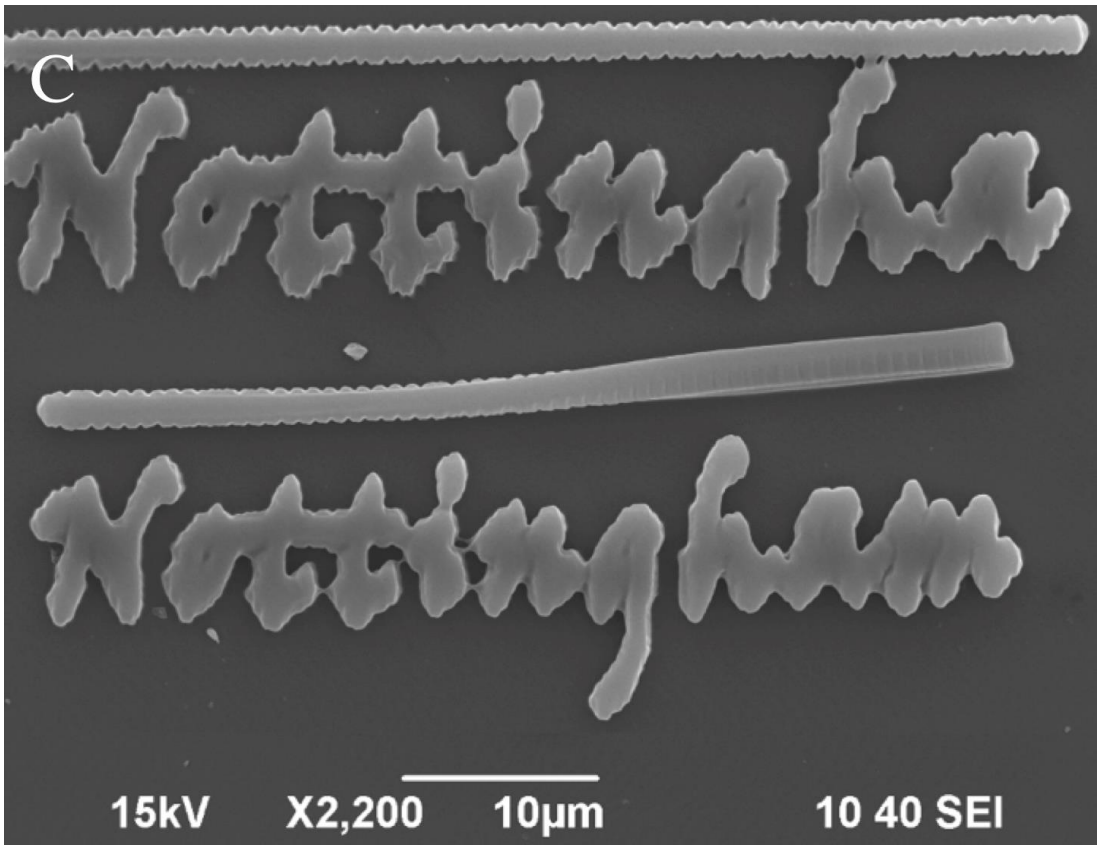


Figure 51. Nottingham design fabricated using different laser powers and step sizes. A) The structure in this figure fabricated with laser power of 9.62 mW and step size of 0.3 µm. Low laser power decreases the voxel length and the voxels was partially outside the substrate. B) This structure is fabricated using laser power of 14.55 mW and step size of 0.3 µm. The increase in the laser power improved the surface adhesion but the step size was smaller than the voxel dimension. Therefore, the small feature sizes were covered. C) The upper structures in figure C is fabricated with laser power of 14.55

mW and step size of 0.5 μm. Increasing the laser power and step size produced good structures but the saw-tooth surface profile is visible. The lower structure in figure C is fabricated with laser power of 11.65 mW and step size of 0.4 μm.

The first structures in Figure 51 is fabricated using laser power of 9.62 mW, the second and third structure is fabricated with laser power of 14.55 mW and the last stricture is fabricated using laser power of 11.65 mW. Using lower laser power decreases the voxel sizes. The step size in the first structure was 0.3 μm. Having a small voxel size (sub-micron) makes it more important that a portion of the fabrication volume stays inside the substrate throughout the fabrication process. In the structure in Figure 51a, the step size was smaller than the system voxel size and the letter counters are closed off. In Figure 51b the laser power increased to 14.55 mW and the step size was kept at 0.3 μm. In Figure 51b by increasing the laser power, bigger voxels fabricated and a portion of the voxel stayed in the substrate. The overlapping voxels destroyed the fine details of the structure. In Figure 51c two structures fabricated using laser power of 14.55 mW with the step size of 0.5 μm (top) and laser power of 11.65 mW with the step size of 0.4 μm (bottom). These parameters yield the best outcomes. In the structure fabricated with step size of 0.5 μm the sawtooth structure produced due to voxel separation can be seen but because of higher laser power the main body of voxels are connected to one another. Fine details like the counters in the letters o and a are more visible in the structure fabricated using bigger step size (0.5 μm).

4.2 Optical Trapping Testing and Simulation

In this chapter, trapping experiments done using the OT setup. After assembling and aligning the OT setup, different samples were used to test the capabilities of the OT setup.

The simulation results for multiple particles suspended in different immersion mediums will also be presented in the second section of this chapter. In these simulations, it was tried to demonstrate the effect of refractive index of particle and its surrounding on the trapping force.

4.2.1 Trapping Silica Bead suspended in deionized water

The first sample that was placed in the OT setup was 2 μm silica beads suspended in deionized water. These particles were supplied in high concentration. First, 10% v/v of the particle mixture was added to deionized water to dilute the mixture. Subsequently, an Ibidi micro chamber was filled with 100 µl of the diluted mixture and mounted to the OT stage. Using the stage, particles were brought into the focus of the objective lens.

The IR laser used in this experiment is not visible in the system and the position of the trap was unknown at the beginning. The first OT system was built based on a fixed beam system. Therefore, the sample was moved using the differential micrometres mounted on the stage to place a particle in the trap. Once a particle was placed close enough to the focal volume of the objective lens, it moved into the trap and became stationary as the stage moved. In this step it was confirmed that stable 3D trapping for single and multiple silica particles were achieved. The laser driving current of 100 mA (47 mW laser diode output) was chosen as the minimum trapping power for these particles. Reducing the laser power reduced the trapping capability of the setup specifically in the laser propagation direction.

After accomplishing stable 3D trapping using the basic OT setup for silica microspheres suspended in deionized water, the setup was upgraded with the GM unit. To install the GM unit the Galilean beam expander used in the OT setup was replaced with a Keplerian beam expander. The same particles were

tested in the system with the GM unit. The DAQ device connected to the GM motors controls the position of the laser beam. As mentioned before, the position of the trap was not visible and using GM to move the trap position made it more challenging to find the trap position. Labview software was developed to fully control the position of the trap using the GM and the imaging system. Using the Labview software, it was possible to trap single particle and transport it across the objective lens field of view. The position of the trapping laser while the GM operating voltage was zero was marked as the starting point of the trapping on the LabVIEW software front panel.

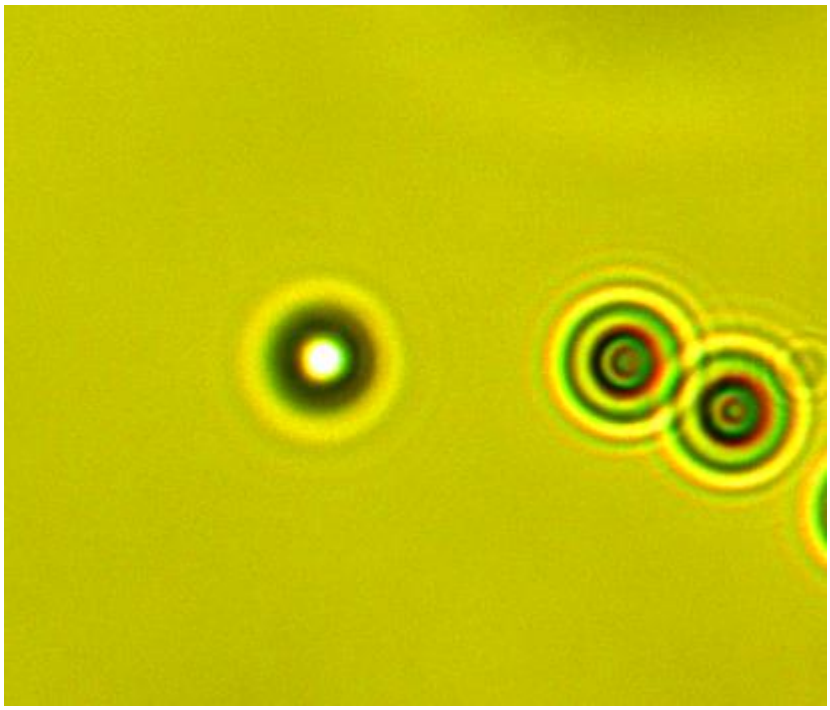


Figure 52 Single particle trapped using the laser beam. The particles outside the trap appear darker out of focus.

4.2.2 Testing Silver Nanoparticle in the OT

The second set of particles used in the trapping setup was 100 nm silver particles suspended in deionized water. These particles were initially designed to be utilised in the silver ink used in inkjet printers. After diluting the silver ink in deionized water 100 µl of the mixture was used to fill a microchannel sample (Ibidi µ-channel) and mounted to the stage. These particles were attracted towards the beam position, but stable trapping was not possible. The skin depth of silver nanoparticles for the trapping beam with a wavelength of 975 nm is 36

nm. Based on previous work by Hansen et al. the trapping laser beam partially polarises the particles that are bigger than the skin depth of the material [144]. Therefore, the gradient force produced by the polarisation of the particles decreases as the particle size increases beyond the particle skin depth. In contrast, the scattering forces that destabilise the trap increases with the particle size [143]. In this experiment particles that are attracted to the laser beam waist dislodge from the trap and stable trapping was not possible. By increasing the laser diode driving current the scattering force generated by the beam increases and particles were pushed out of the beam waist faster. Increasing the laser intensity also produced bubble formation around the particles, which was due to laser absorption by the metallic particles.

4.2.3 Trapping Gold Nanoparticle in OT

300 nm gold nanoparticles, suspended in deionized water (742082 Sigma-Aldrich), were the third set of particles that were used in the setup. Before using the solution in the OT setup, the solution was diluted using deionized water (1 part solution in 5 parts deionized water). 100 μl of the diluted solution was inserted in the sample chamber and tested in the OT setup. The first attempt to trap 300 nm gold nanoparticles was unsuccessful. After realigning the setup and improving the trapping beam quality, gold nanoparticles were tested in the OT setup for the second time. In this experiment the metallic nanoparticles were further diluted in 10 parts deionized water. Using a diluted solution reduced the number of particles in the vicinity of the trapping beam. By focusing on a single nanoparticles and changing the position of the beam waist, it was possible to trap 300 nm gold particles. In the literature Sato et al. suggested that by placing the focal plane of the objective lens at the bottom of the metallic particles, it is possible to produce attractive force towards the center of the trapping beam [147]. Trapping 300 nm gold nanoparticles was not easily reproducible and it was limited to the imaging plane (2D trapping).

4.2.4 Trapping CNT in OT

Another interesting material used in the optical trapping setup was carbon nanotubes (CNT). The sample employed in the OT setup was a mixture of single and multiwall carbon nanotubes with different chiralities. Having high

concentration of nanotubes, which were entangled with each other, made the trapping very challenging. Diluting the solution and selecting a single long carbon nanotube made it possible to trap carbon nanotubes. The trapping beam stretched the carbon nanotube in the laser propagation direction (vertical direction) and by turning the laser beam off the CNT moved back into horizontal view. Due to having a mixture of different types of CNTs in the solution it was not possible to determine which type of CNT was being trapped in our system but based on previous work by Marago et al., there is a high probability that trapped nanotubes were single wall CNT [213].

4.2.5 Optical Trapping Simulation

A simulation software developed at the University of Barcelona was used to simulate the trapping force exerted to the dielectric particles inside an optical trap [114]. The simulation software can examine the possibility of trapping dielectric particles suspended in different mediums. The effect of objective lens numerical aperture, beam filling factor and trapping laser wavelength can be seen in the output graph of the software.

4.2.5.1 OT simulation of Silica bead suspended in water

The first simulation was done to test the trapping force exerted to a 10 μm beads with refractive index of 1.49 suspended in water (refractive index of 1.33). The trapping objective lens was set to one of the predefined 100X objective lenses with NA=1.26 and the filling factor for the laser beam in this simulation was set to 100%. The radiation source of this simulation was set to 975 nm (similar to the laser diode in the experimental setup) with an output power of 50 mW. The ratio of the refractive index of the particle and medium was 1.12 and it produced a stable trap at the center of the force field.

Figure 53and Figure 54 shows forces applied to a particle that is positioned close and into the beam waist. Grey lines represent the trapping laser beam that converges rapidly after the objective lens and produces the optical trap. By removing the particle from the beam waist, the net force exerted to the particle forces the particle back to the centre of the beam waist. In Figure 53, the gradient force (blue), the scattering force (red) and the net force applied to the particle is in Orange. The scattering force pushes the particle in the laser propagation

direction but the larger gradient force produces negative pressure that pushes the particle toward the centre of the beam. The net force applied to the particle is towards the focal point of the objective lens. Figure 54 also shows the magnitude of the forces applied to the particle in X and Z directions.

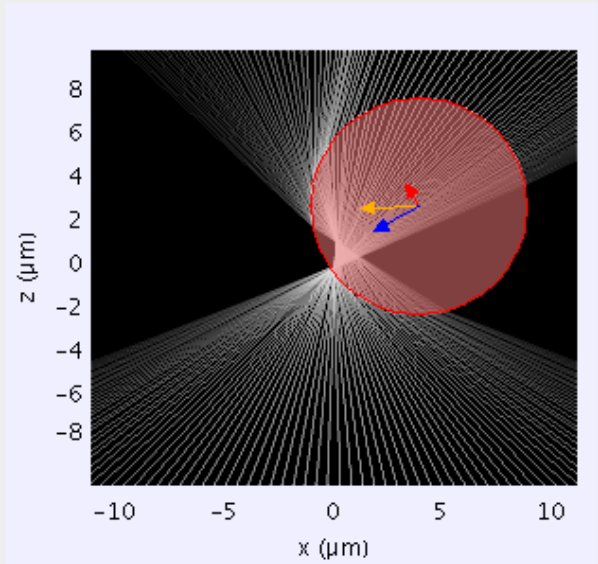


Figure 53. Forces applied to a particle placed close to the focal volume of the objective lens by the laser beam. The net force (orange arrow) is pointing towards the centre of

the beam, and stable trapping is possible if the gradient force is larger than the scattering force.

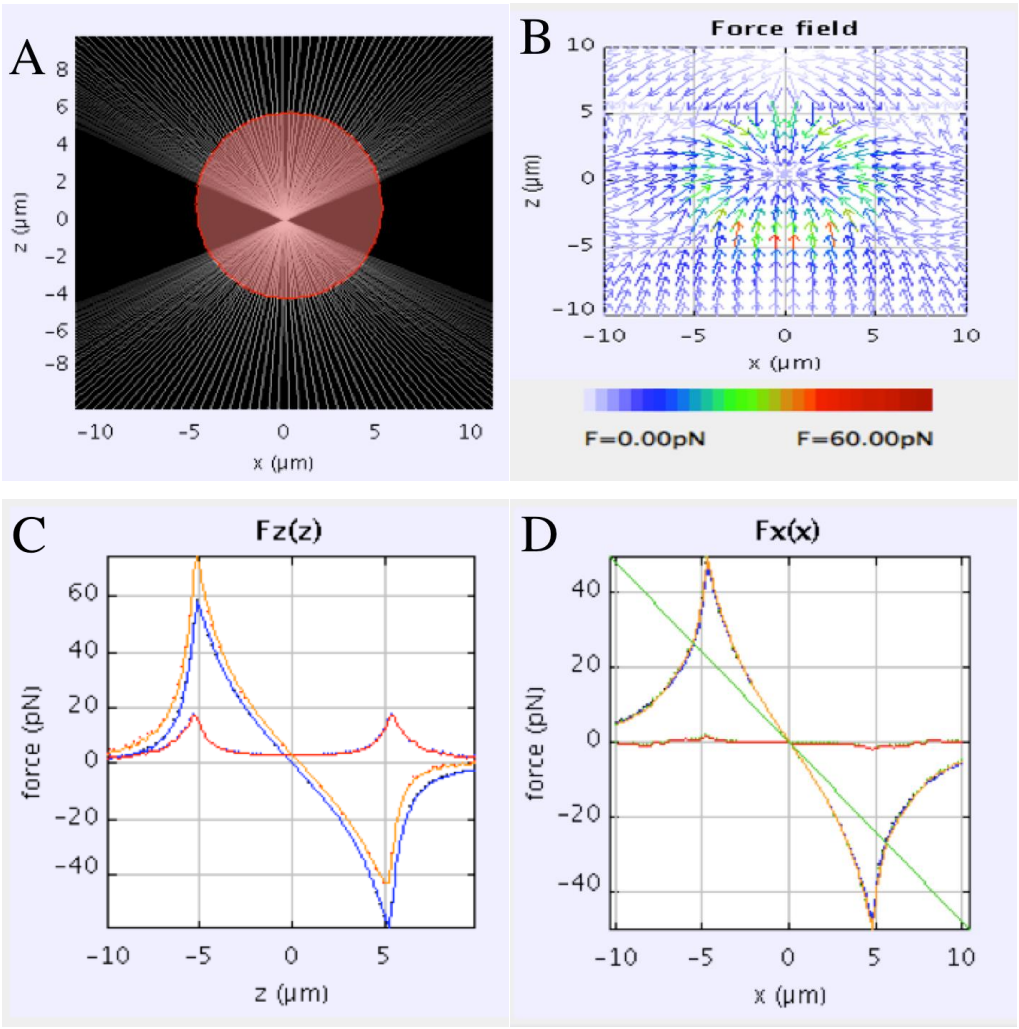


Figure 54. Trapping force excreted to 10 μm beads suspended in water. a) Illustration of the particle in the trap gray lines simulate the laser beam converges into the red particle using the objective lens. b) Force field diagram with the position of trap at the center of the field. C & D) forces applied to the particle in Z and X direction. The Orange line shows the net force; Blue is gradient force and red the scattering force.

4.2.5.2 OT Simulation for silica beads suspended in PEGDA

The second simulation was done to examine the trapping force exerted on identical particles suspended in a medium with higher refractive index and viscosity. PEGDA was chosen as the second immersion medium.

Figure 55 shows the simulation result of the particle in the previous simulation suspended in PEGDA (refractive index of 1.47). The refractive index of PEGDA

was close to the particles refractive index, and lower trapping force was generated. Figure 55b shows that it is possible to trap this particle at the centre of the force field. Due to the vibration in the system and imperfection in the optical path alignment, stable trapping for this particle suspended in PEGDA was not experimentally possible.

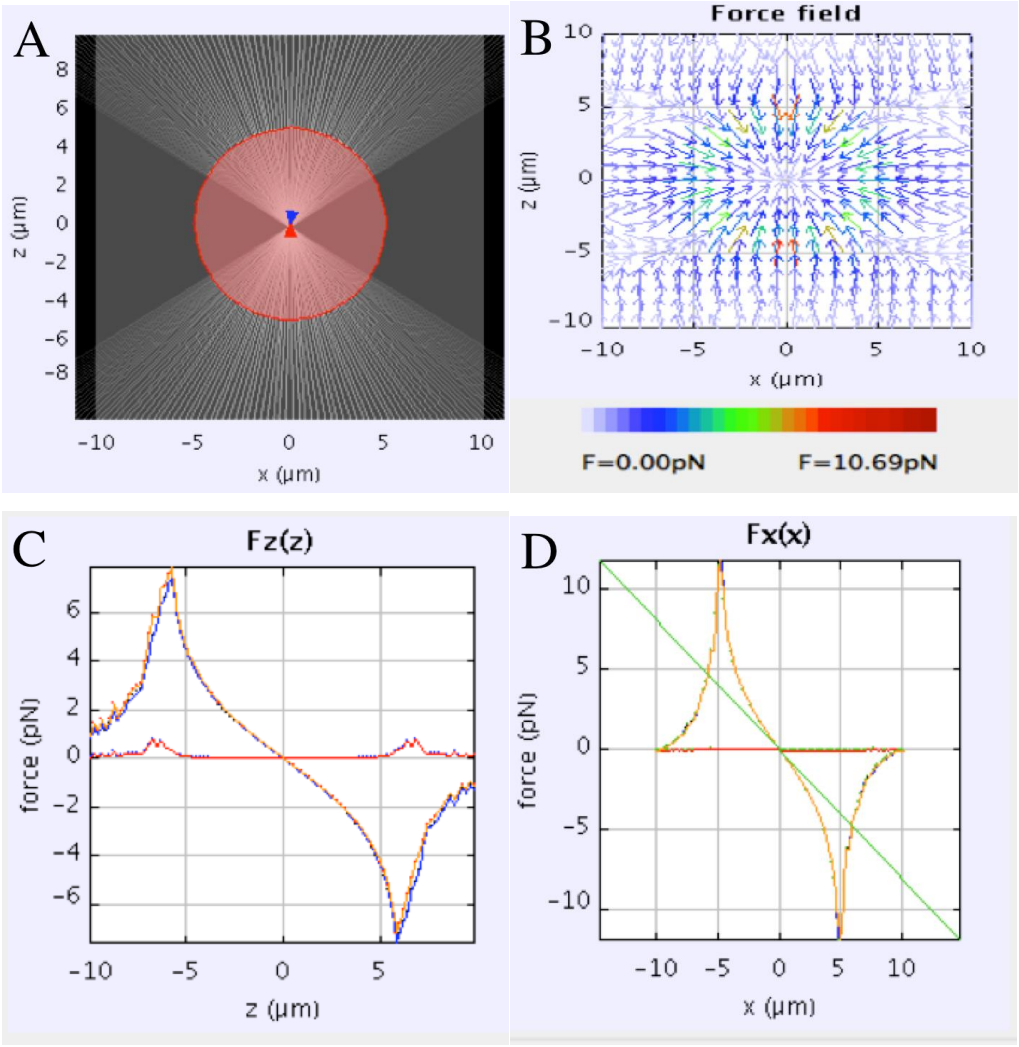


Figure 55. Trapping force excreted to 10 μm beads suspended in PEGDA. a) Illustration of the particle in the trap lines simulate the laser beam converges into the red particle using the objective lens. b) Force field diagram with the position of trap at the centre of the field. C & D) forces applied to the particle in Z and X direction. Orange line shows the net force; Blue gradient force and red scattering force.

Figure 55c & d shows forces applied to the particle due to the trapping laser beam. Comparatively, the trapping force for the particle suspended in PEGDA is 6 times smaller than the particles suspended in water (section 4.2.5.1), which makes it harder to trap these particles in PEGDA. Based on this simulation these particles are not suitable for the preparation of the combined setup photoresist.

In order to increase the trapping force generated by the OT, high refractive index soda lime glass beads (refractive index of 1.59) were substituted for the combined system photoresist. These particles have a higher refractive index and excellent chemical and mechanical stability.

4.2.5.3 Simulation of a particle suspended in the refractive index-matched medium

In the third simulation, the refractive index of the particles was changed to match the refractive index of the medium. Figure 56 shows the force field around the particle that resembles the previous two simulations but the force applied to the particle is much smaller than that previously used (Maximum force of 0.18 pN).

To be able to trap a particle and transport it in liquid, the trapping force must surpass the thermal energy of the particle, vibrations in the system and the Stokes drag generated by the fluid. Based on the simulation, the trapping force is insufficient for stable trapping of particles in the refractive index-matched medium.

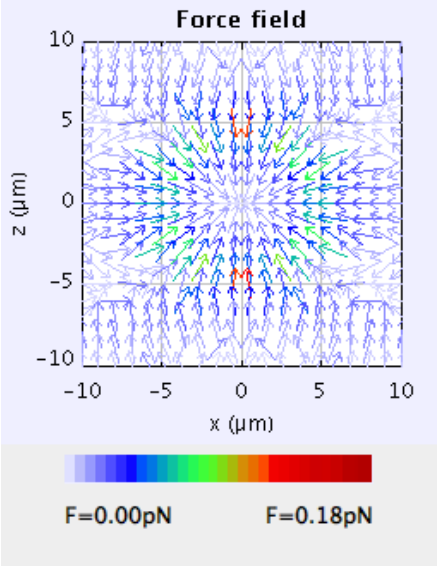


Figure 56. Force excreted to a particle suspended in the refractive index-matched medium by the trapping laser beam. The maximum applied force is 0.18 pN. The

direction of the force is toward the centre but the gradient force is very small and stable trapping cannot be achieved.

4.2.5.4 Simulation of particle suspended in a medium with higher refractive index

Figure 57 shows the fourth simulation with particle suspended in a medium with high refractive index. In this simulation, the force field shows no stable trap and the force generated by the particle is toward the edge of the field. In this case, the laser beam pushes the particle away from the beam waist.

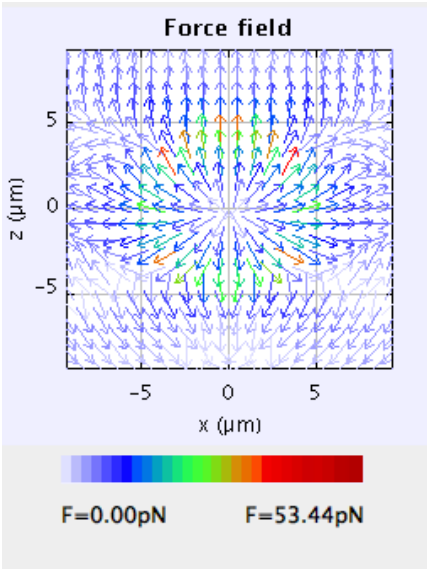


Figure 57. Force excreted to a high refractive index particle in a medium with lower refractive index. The direction of the force is toward the edge of the field and stable trapping cannot be achieved.

4.2.5.5 Particle monitoring

The Quad Photodiode Detector (QPD) mounted on the OT section of the combined setup can be used to monitor the existence and the number of particles in the trap. The sum voltage on the QPD LabVIEW front panel (Figure 29) demonstrates the amount of light that reaches the detector. The light level changes abruptly if a particle moves in or out of the trap. Figure 58 shows different events that the particle has moved in and out of the trap and the sum voltage after each transition. The trapped particles were packed closely and using the camera it was not possible to identify all the particles.

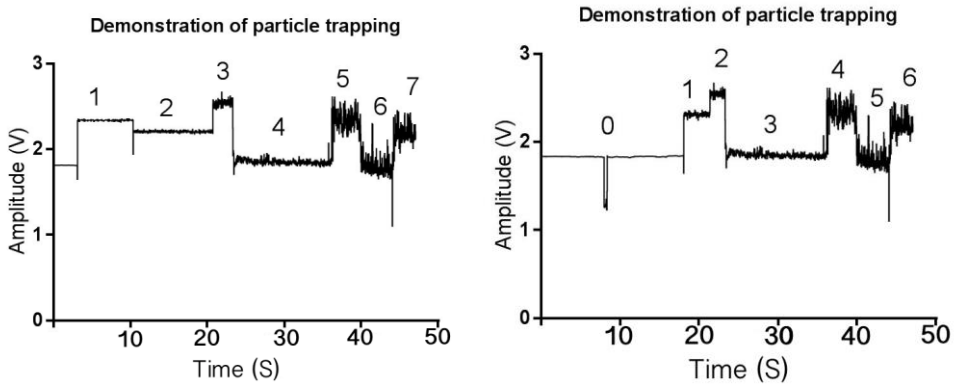


Figure 58. Demonstration of the QPD output voltage as the particles move in and out of the trap. The light level that reaches the QPD fluctuates as the number of particles in the trap changes. Therefore, the output voltage of the QPD changes abruptly. The numbers on the graph represent the events that a particle entered or exited the trap. Due to different arrangement that multiple particles can have in the trap, the light level can increase or decrease as the particle particles enter the trap.

Trapping metallic nanoparticles follow a different set of rules. Figure 59 shows the trapping phenomena for a combination of dielectric and metallic particles. As the metallic particle enters the trap, it blocks all the light, and the QPD sum voltage reduces to zero. Stable trapping of the metallic particle was not possible in this system, and the particle exits the trap soon after entering and the QPD sum voltage returned to the normal amplitude.

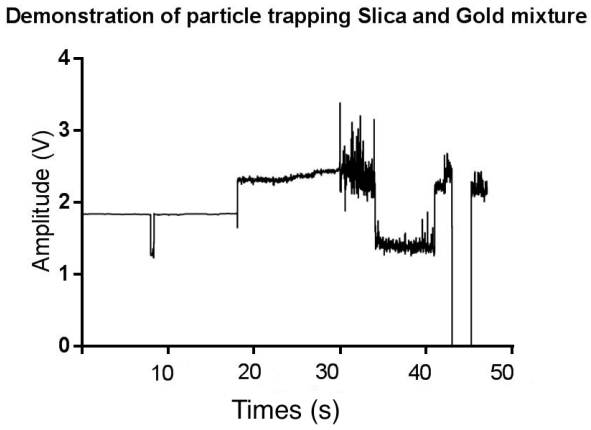


Figure 59. Trapping events for a combination of silica beads and metallic particles. As the metallic particle enters the trap the amount of light that reaches the QPD is reduced sharply. The 300 nm gold nanoparticle absorbs and reflects almost all the trapping beam and the QPD voltage reduces to zero.

The simulation software used during this experiment was a useful tool to examine if it is possible to trap dielectric particles with known refractive index in different immersion mediums. Although this software was unable to simulate metallic particles, it had a complete library for dielectric particles with different

sizes. This software offered various options for simulating dielectric particles in Mie and Rayleigh regions.

The simulation software functioned based on the assumption that 100% of the laser power will be delivered to the sample through the objective lens. Misalignment in the optical train and non-ideal optical elements reduces the amount of laser power focused onto the sample. The misalignment also changes the symmetrical shape of objective lens focal volume. Therefore, the trapping force measurement of the software should be considered with a margin of error.

4.3 The Combined Setup

OT can manipulate metallic and dielectric particles, DNA strands, biological samples and carbon nanotubes. Using OT to transport particles and prefabricated microstructures into the MPP vat can revolutionise the way that we employ OT as a scientific tool. In this chapter, the examination of different sections of the combined setup will be demonstrated and afterwards the core capabilities of the combined setup will be presented.

Manufacturing with the combined setup was more complicated than the individual setups. Before using the combined setup to transport particles into the MPP vat, each section of the combined setup was independently tested. To check the MPP section of the combined setup array of voxels fabricated using different laser powers and exposure times. The MPP section of the combined setup was assembled using mirrors fixed in the kinetic mounts with fine adjustment knobs. The adjustment knobs enabled precise alignment of the polymerization beam and increased the beam quality for the combined setup.

The first step in using the combined setup was to benchmark the polymerization section of the setup. The laser output was monitored and plotted against the attenuator GUI level. The graph in Figure 60 shows the polymerization laser output power before the objective lens in the combined setup.

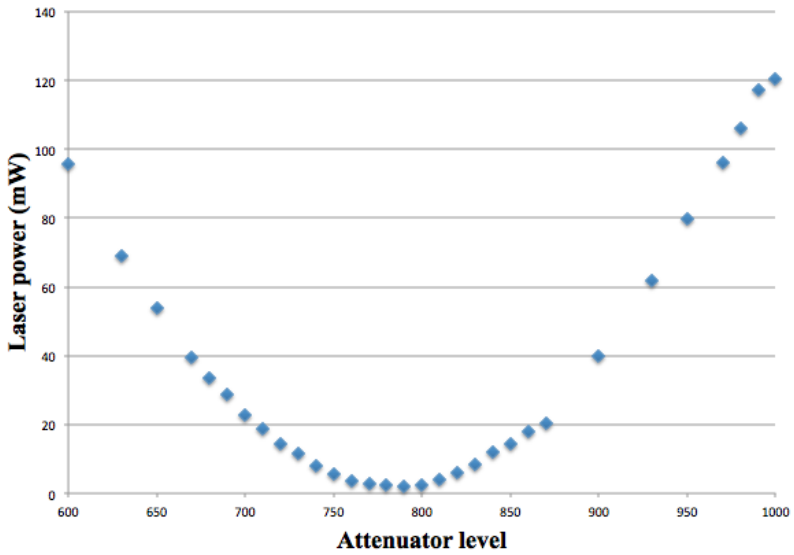


Figure 60. Laser power vs the attenuator level graph before the objective lens. As the attenuation level increases the laser power should decrease. Due to misalignment in the beam conditioner box, after 780, the laser power increases. This graph also presents loses in the optical chain.

Figure 61 shows an array of voxels fabricated using the same exposure time but different laser powers. In this figure, the attenuator GUI amplitude was increased from 700 to 750 in 5 intervals (the laser power decreased from 22.95 mW to 5.78 mW) and 3 voxels were fabricated using same laser power. In Figure 61 a change in voxel size is apparent. The second significant finding of this experiment was the threshold value of the ORMOCOMP in the experimental setup. Using 750 as the GUI amplitude (3.78 mW) no polymerization was observed regardless of exposure time. In this experiment, it was defined that the threshold value of ORMOCOMP in the combined setup is larger than 3.78 mW and smaller than 5.78 mW. This number did not specify the exact polymerization threshold due to other losses that were not considered during power measurement. The laser power was monitored before the objective lens, and it did not account for the losses in the objective lens and after it. Optical aberration also degraded the TEM_{00} beam profile of the MPP polymerization beam and spread the laser power over a larger area. The main source of aberration was the misalignment in the system that changed the shape of the focal volume of the objective lens and increased the objective lens spot size (decreased the power density). Due to aberration, a higher laser power was used to suppress the polymer threshold.

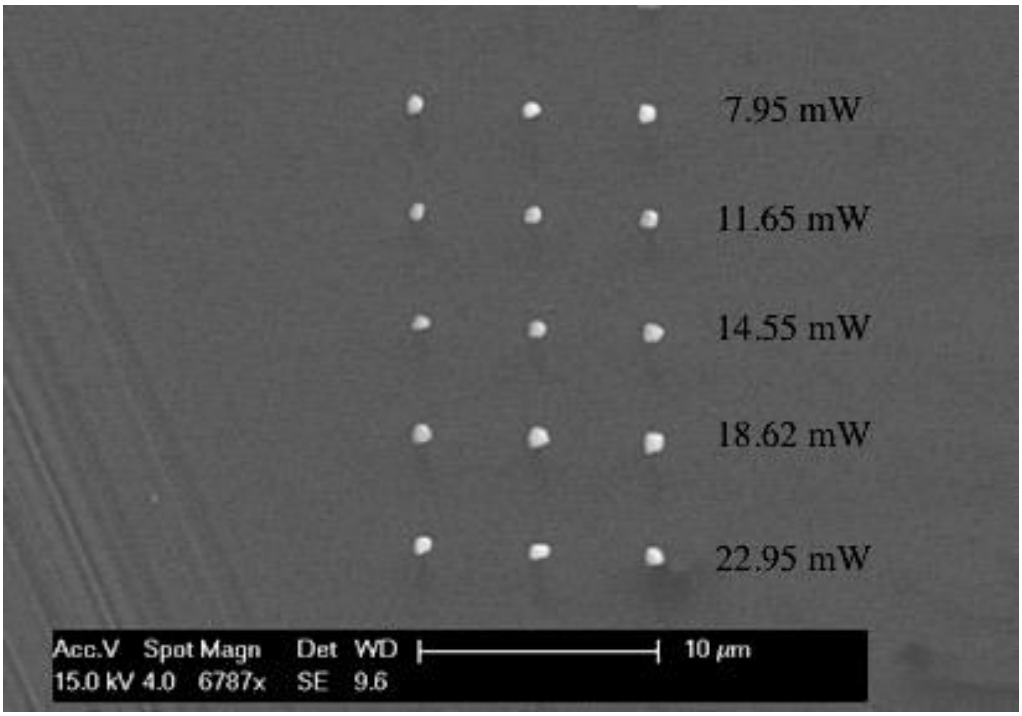


Figure 61. An array of voxels fabricated close to the focus mark on a coverslip using a fixed exposure time and varying laser power. The exposure time for this experiment was set to 100 ms and the laser power increased from top to bottom. No fabrication was achieved using laser power of 5.78 mW.

Figure 62 shows an array of voxels fabricated using different exposure times. In this experiment, the laser intensity was kept constant throughout the experiment for voxels fabricated in each row and the exposure time increased step by step. The voxel area in this experiment started from 1.092 μm^2 to 2.425 μm^2 (left to right). Due to imperfections in the coverslip and variation in the coverslip thickness the smallest voxels in the bottom left corner of the picture were not attached to the substrate completely, and during the development process these voxels collapsed into the substrate. The collapsed voxels show the lateral feature size of the system. The minimum exposure time used in this experiment was 30 ms and below this number, errors in shutter time increased significantly.

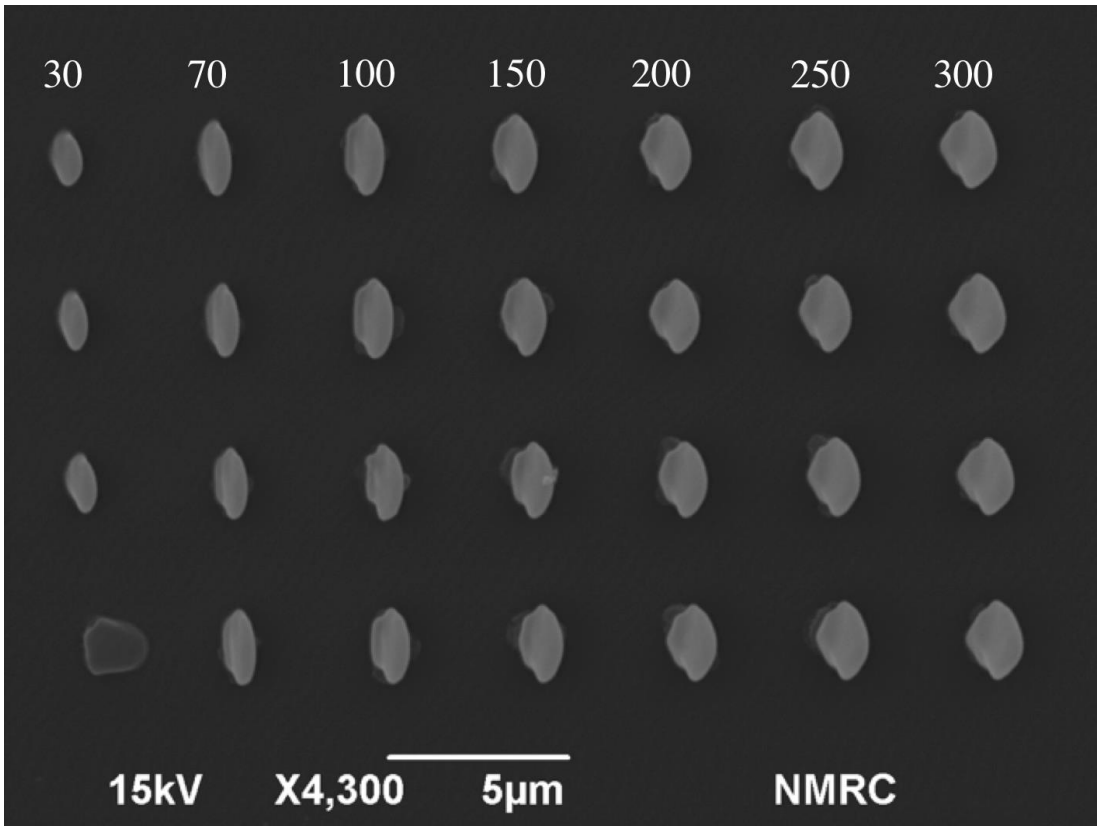


Figure 62. Left image: Array of voxels fabricated with different exposure times using the prepared photoresist. The voxels in each column fabricated with identical fabrication parameters. The exposure times increased from left to right (30 ms, 70 ms, 100 ms, 150 ms, 200 ms, 250 ms and 300 ms).

Because of the tilt in the coverslip and its imperfections, it was not possible to define what portion of the objective lens focal volume was inside the coverslip at any given time. Therefore, defining the exact minimum feature size of the MPP setup was not possible but the voxel in bottom left corner of the image is a representation of the system minimum feature size.

The processing window and fabrication parameters for the MPP section of the combined setup were different from the standalone MPP setup. The root cause of difference in laser power was improvement in system alignment and changes in the photoresist. Using the prepared PEGDA based photoresist with improved alignment, it was possible to fabricate voxels with laser power of 5.78 mW. In the combined setup, the mechanical shutter was installed on a separate mount and the vibrations produced by the shutter blade was minimized using dampers installed in the steel posts.

The OT section of the combined setup was tested using the silica beads suspended in deionized water. The trapping laser wavelength in this experiment was 975 nm, which is not visible to the naked eye. Samples with high particle density were used to find the position of the trap and test the OT section of the combined setup.

To prepare the sample for the combined setup a coverslip was marked at the centre using the diamond-head pen, and a droplet of the photoresist was placed in the middle of the coverslip. The coverslip was mounted and fixed to the microscope slide holder. Since the rig was assembled based on an inverted microscope setup, there was no need to sandwich the sample between two coverslips. The sample was moved in between the objective lens and condenser lens using the translation stage (Thorlabs TBB0606). Using the 3-axis roller block stage Z translation, the mark on the coverslip was brought into the focus of the objective lens. By following the procedure explained in the section 4.1, the position of the focal volume of the objective lens was placed on the substrate.

Different approaches were tested to overlay the trapping and polymerization area and the most efficient system for incorporating particles in the polymer matrix were based on using a fixed beam combined setup. Using the GM the position of the focal volume of the objective lens for the trapping beam positioned on top of the polymerization beam in X and Y axes. To overlay these two points in the Z direction the afocal beam expander was used. Using the polymerization beam a simple structure was fabricated on the substrate as the reference structure and the stage position was monitored during the fabrication. After finding the coverslip surface, the stage was used to trap and transport a particle suspended in the polymer to the previously polymerised area. The particle was trapped after the imaging plane of the objective lens, and it appeared out of focus (blurred) in the camera output. Using the afocal system, the trapped particle was moved in the laser propagation direction and placed close to the imaging plane (behind the polymerization area). Once the trapped particle was positioned before the polymerization area, it was possible to approach the

coverslip and align the polymerization area on the coverslip. By decreasing the gap between the beam expander lenses step by step, the trapped particle was moved toward the polymerization area and the coverslip. After each step, the position of the particle was tested in regard to the polymerization position by firing a single burst of the MPP laser. If the particles were positioned close to the polymerization area, the particle would be attached to the substrate using the polymerization beam, and it would not be possible to move using the OT. Different attempts were made to overlay the focal volume of the objective lens for the trapping and the polymerization beams in the Z direction. After each attempt, the positions of the lenses in the afocal beam expander were fixed, and a number of particles were trapped and fixed to the substrate. This step was taken to ensure the repeatability of the experiment.

The fabrication process using the combined setup always started by finding the substrate surface and noting the position of the stage (X,Y and Z coordinates). The combined setup used a fixed beam for trapping and polymerization, therefore, the stage could be used to track particles and place them in the OT. Once the particle moved into the trap, it was, transferred to the build area and brought close to the substrate for polymerization. In many cases, these particles were far from the substrate and having stable a 3D trap was crucial. During this experiment, it was found that due to the tilt in the stage, there was a high probability that the trapped particle would crash into the substrate during transportation. Figure 63 shows a 50 μm square Fishnet structure fabricated using the MPP section of the combined setup. It demonstrates the tilt and imperfections in the coverslip. At the upper left corner of the structure, the focal volume of the objective lens goes entirely inside the coverslip, and there is no visible polymerization. Due to the tilt and imperfections in the coverslip the trapped particles were moved a few µm above the substrate and then lowered to the substrate at their intended position. Moving the particles in Z direction must be done slowly due to lower trap stiffness in the laser propagation direction.

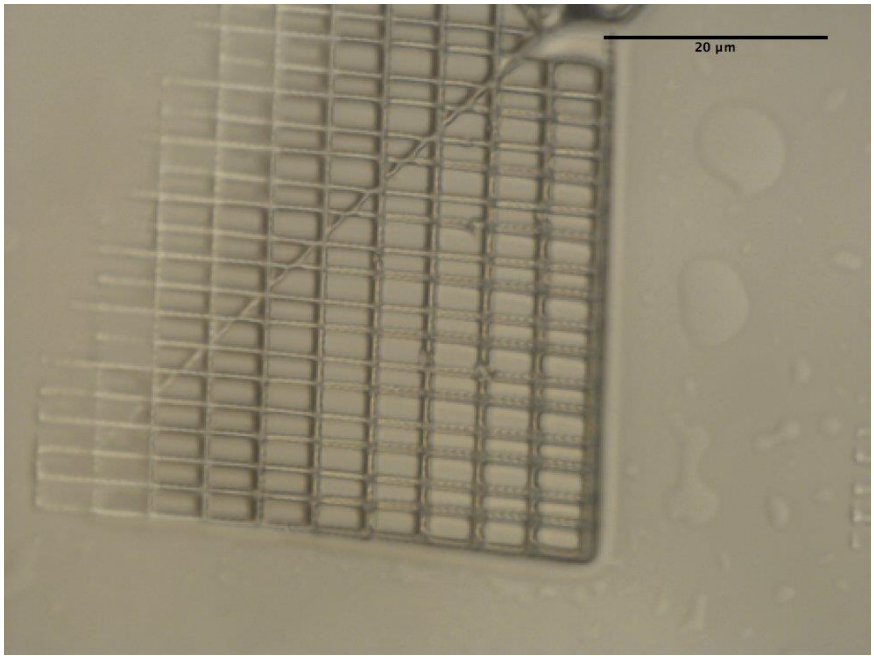


Figure 63. 50 μm square Fishnet structure fabricated using the MPP section of the combined setup. Change in the substrate thickens and tilt in the stage pushes the focal volume of the objective lens inside the substrate.

The core capability of the combined setup was based on transportation of particles into the MPP vat using the OT and immobilising the transported particles. In the first experiment performed using the combined setup this core capability was tested. Figure 64 shows particles carried by the OT section of the combined setup glued to the substrate using the MPP section of the combined setup.

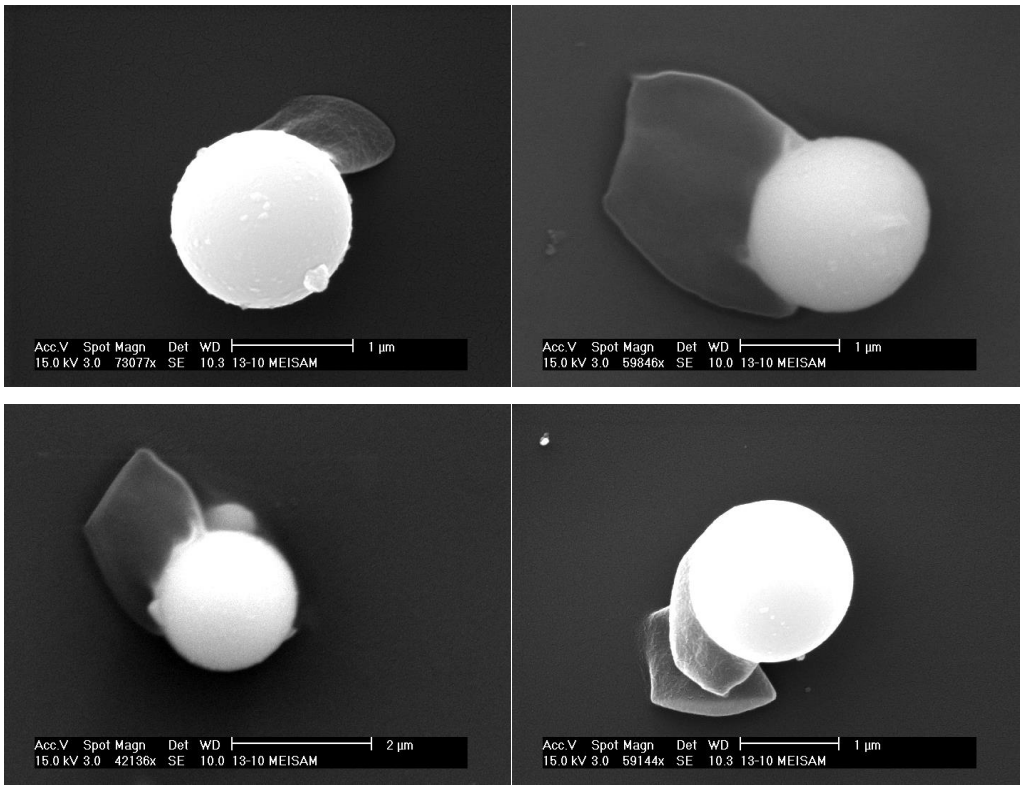


Figure 64. Single High refractive index soda lime particle immobilised by the polymer solidified using the MPP laser pulse. The minimum feature size of the MPP system is comparable with the particles and problems in particle suspension reduces the quality of the produced samples.

By repeating the procedure, multiple particles were trapped and fixed to the substrate using the MPP laser. The polymerization laser affected the particle inside the trap, and the trapping laser intensity was increased to make sure that the particle stayed within the trap. The form and size of the polymerization volume that attaches the particles to the substrate could be controlled, using the MPP laser intensity, exposure time and the position of the particle. The position of the particle in regards to the substrate and the polymerization volume can affect the polymer shape and size.

Table 6, shows the different steps involved in the fabrication of structures using the combined setup. The combined setup photoresist reduced the post-fabrication processing steps but introduced contaminations from the mobile particles on the substrate.

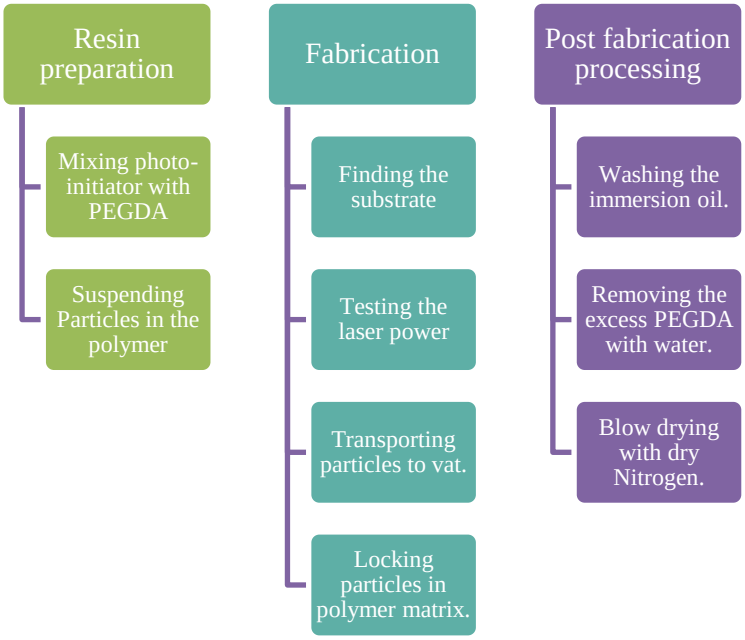


Table 6. Flowchart of sample fabrication steps using the combined setup.

Figure 65 shows a low magnification SEM image of a fabricated structure using the combined setup. The borders were fabricated to separate the fabrication area from the rest of the sample and to make it easier to find the immobilised particles in the SEM. Particles inside the borders are attached to the substrate using the MPP laser beam. The stage made it possible to align each particle to the previously immobilised particles and produce a line with particles locked inside the polymer.

It was a significant step to demonstrate the capabilities of the combined setup, and the shortcomings of the photoresist prepared for the combined setup. The particles attached to the substrate on or outside the borders are the unwanted particles left on the substrate after developing the sample. Due to the high particle concentration in the photoresist, some of the particles sunk to the bottom of the sample and adhered to the substrate during fabrication. These particles remained on the substrate after developing the sample using the deionized water and form clusters of particles. The ambient UV light solidifies the photoresist trapped between the particles and hardens the particle clusters. Decreasing the number of particles in the photoresist, washing the sample with acetone and blow-drying the sample using compressed air enabled the production of cleaner

samples. But this cleaning process might also affect the fabricated sample and delaminate it from the substrate.

Figure 66 shows a higher magnification image of the line fabricated using the combined setup. The solidified polymer pushes the particle away from the focal volume of the objective lens and moves the particle randomly. Due to the change in the final position of the particles, the straight line fabricated (Figure 66) had some errors. In-depth analysis of the fabrication error will be discussed in chapter 5.

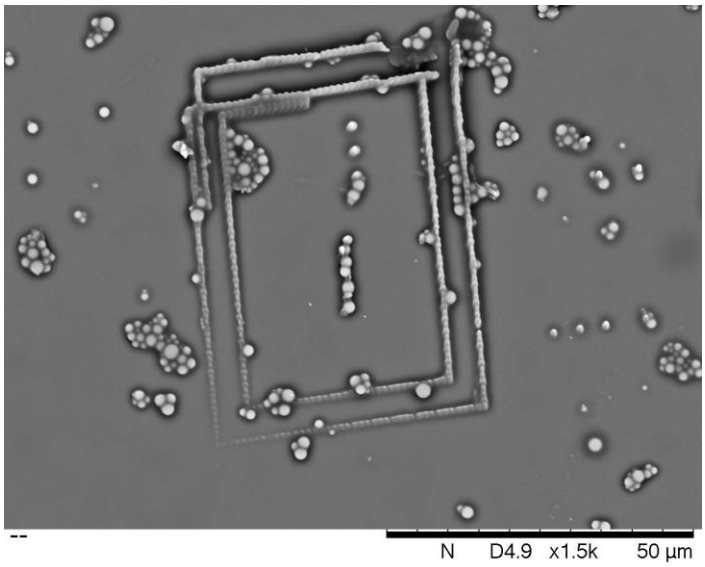


Figure 65. The fabricated structure using the soda-lime glass beads suspended in the photoresist. The combined setup was used to demonstrate the capability of the system to control the position particles and produce defined structures. Unwanted particles are scattered around the actual structure and contaminated the sample.

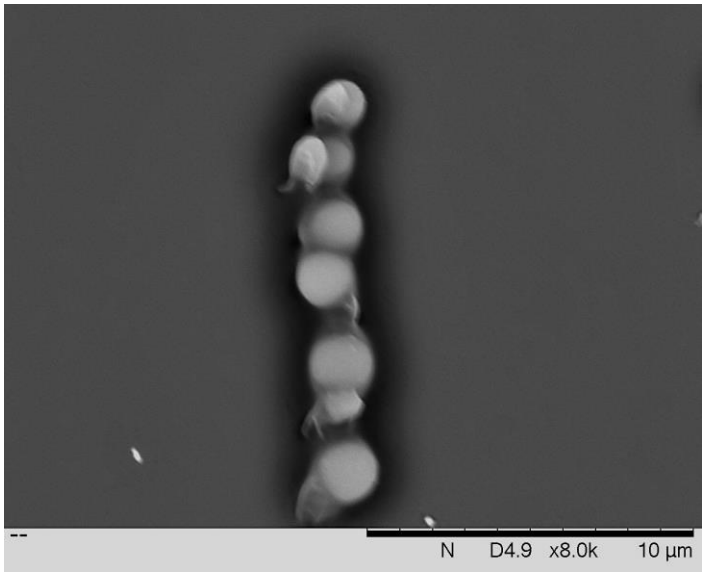


Figure 66. Using the combined setup the particles were placed one after another and arranged into a line. The particle breakage contaminated the combine setup photoresist and reduced the quality of fabricated structures.

One of the main issues in operating the combined setup was particle suspension. A stable suspension of glass beads in the prepared photoresist was not possible and due to low wettability of the particles; agglomeration was observed. Figure 67 shows a cluster of particles placed close to the scratch mark on the substrate.

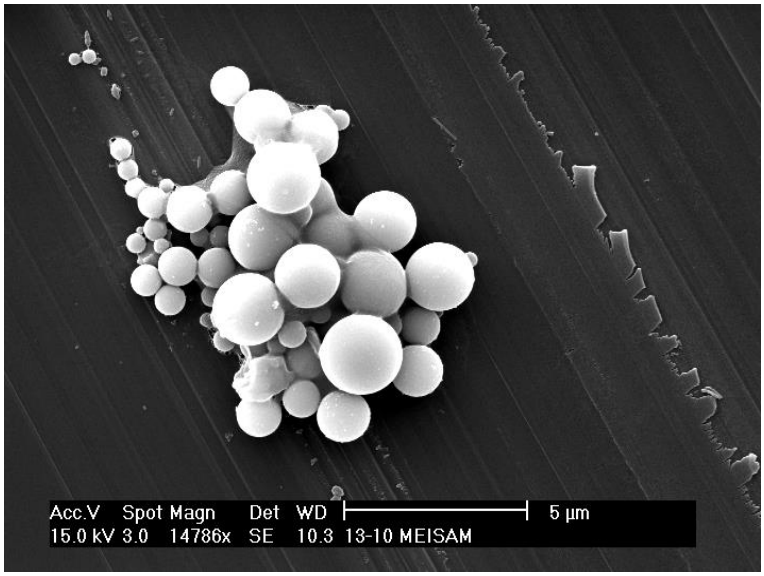


Figure 67. A cluster of particles left on the substrate after washing the sample with deionized water. The photoresist trapped between the particles solidifies with ambient UV radiation.

By replacing the glass beads with melamine resin based particles, it was possible to suspend particles in the photoresist for a longer period of time and reduce particle agglomeration.

4.4 Chapter Summary

In the first section of this chapter (Section 4.1) the structures fabricated using the MPP setup were presented alongside the system benchmarking. The 3D multilayered structures fabricated using the Labview software were also presented. Section 4.1, demonstrates that the assembled MPP setup has the capability to polymerise microstructures with high resolution and the Labview software is capable of transferring .BMP images to fabricated layers and stack these layers to build a 3D structure. The system benchmarking demonstrated the dependency of the system feature size on the polymerization laser power and exposure time.

By completing the MPP setup, the project focus was moved towards the OT setup. Assembling and aligning the OT setup was completed and stable 3D trapping for dielectric particles was achieved using the basic OT. The trapping system was then disassembled and upgraded with a GM system. Beside incorporation of a GM system, the beam expander section of the OT system was changed from a Galilean beam expander to a Keplerian beam expander. A number of Labview software routines were developed to calibrate the GM system in the OT and enable the user to precisely control the position of the trap on the camera live feed from the imaging section of the OT setup. During this project, 3D trapping of different dielectric particles was achieved. The dielectric particles were tested while suspended in deionized water and low refractive index photoresist. 2D trapping of gold nanoparticles and CNT were other achievements of this project that showed the limitation of the OT system in 3D manipulation on these particles.

In section 4.2.5, the simulation result for particles suspended in different immersion medium was presented. The simulations were in close agreement with the experimentally demonstrated results and produced a roadmap for choosing the appropriate particle / polymer for the preparation of the combined OT-MPP setup photoresist. The quad photodetector mounted after the condenser lens was used to monitor the position and number of particles in the trap.

Labview software was developed to export the light measurements from the photodetector and plot it on a time scale to show the change in light level as the particle enters or exits the trap.

In the third section of this chapter (section 4.3) the structures fabricated using the combined OT-MPP setup were presented. After completing the system design, assembly and alignment, each section of the setup (MPP and OT) were tested independently. MPP system benchmarking was performed again to define the best operating parameters for the MPP section of the combined OT-MPP setup. During benchmarking the developed software was used to clearly demonstrate the effect of operating parameters on the fabricated structure.

The OT and MPP section of the combined OT-MPP setup was used simultaneously to trap, transport and immobilise particles on the substrate. This was the core capability of the combined setup, which was made possible because of the utilisation of afocal beam expander. The afocal beam expander enabled precise overlaying of the trapped object with the polymerization area. Therefore, repeatable particle immobilisation was achieved using this system. These preliminary results demonstrated that the assembled setup has potential to trap the particles suspended in the prepared combined setup photoresist and immobilise them using MPP.

CHAPTER 5: COMBINED OT-MPP SETUP SAMPLE FABRICATION & EXAMINATION

In this chapter, further experiments undertaken using the combined OT-MPP setup will be presented, and fabricated structures will be examined using different diagnostic techniques. The experiments in Chapter 4 were designed to show the core capability of the combined setup to trap and polymerise around the particles using the combined setup photoresist. In this chapter further experiments were designed to demonstrate the accuracy of the combined setup and its capability to embed particles in specific areas/patterns inside 2D/3D MPP structures. The combined setup MPP photoresists used in this chapter were prepared using melamine resin based fluorescent particles and soda lime glass beads.

5.1 2D / 3D Hybrid Structures

The first experiment was designed to test the repeatability and accuracy of the combined system. Thirty particles were trapped and positioned at fixed distances from each other to produce a well-defined array of particles. Figure 68 shows a 5 by 6 array of particles immobilised on the substrate using the MPP laser. The combined setup was used to generate this sample; the trapping section of the combined setup was used to trap the particles individually and the polymerization section was used to immobilise the particles on the substrate. To produce a well-organized array of particles the stage was moved to the centre of its travel distance (X=200 µ, Y=200 µ and Z=150 µ) and the first particle was placed on the substrate. Subsequent particles were placed 5 µm apart from the previous particles. Therefore, an array of particles with 5 µm gaps was produced. Producing an array of particles with controlled distance is a stepping-stone towards fabrication of 3D photonic crystals.

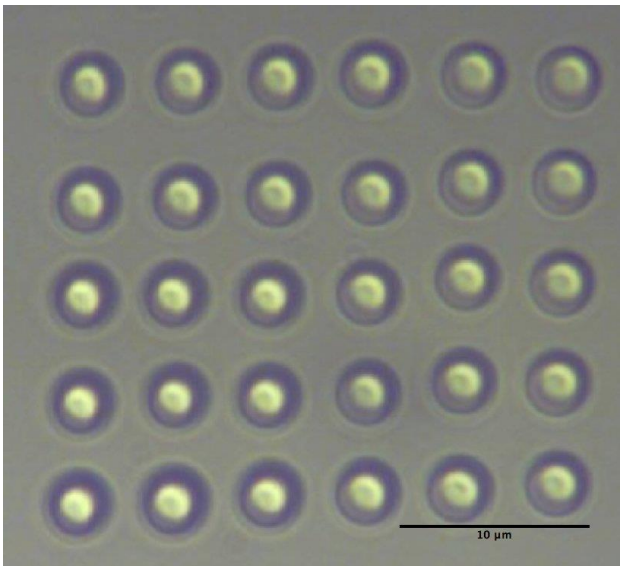


Figure 68. Bright field microscope image of 5 by 6 array of particles immobilised using the MPP laser. The distance between particles and the position of each particle was controlled using the piezoelectric stage. Drift in the stage and vibration in the system introduces inaccuracies in the particle array.

The second experiment that was carried out using the combined setup was based on incorporation of particles into a prefabricated structure. A fishnet structure was fabricated using the MPP section of the combined setup. After fabricating the fishnet structure, particles were trapped and transported into selected openings of the fishnet structure (Figure 69). In this experiment the glass particles suspended in PEGDA based photoresist was used. Due to reduced polymer adhesion, a significant portion of the polymerization volume was placed inside the coverslip to ensure connection to the substrate resulting in a thin polymer layer was solidified on the coverslip.

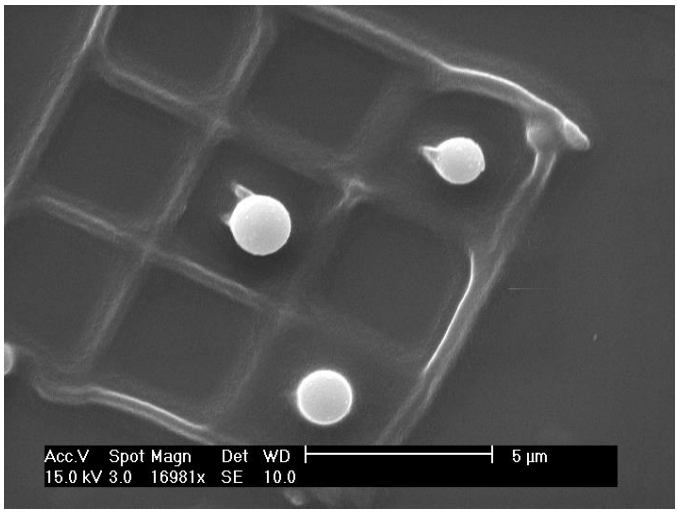


Figure 69. Soda-lime particles with different sizes arrange inside the fishnet structure fabricated using MPP laser.

Figure 70 shows a fishnet structure fabricated using PEGDA-Melamine photoresist. The low fabrication speed (20 μm/s) enabled fabrication of well-defined structure with good polymer adhesion. The thicker structure fabricated in this experiment could confine the particles. This system and material combination demonstrates a viable option to produce an array of particles inside a polymer matrix and avoids particle displacement due to external vibrations, laser pressure, and polymerization. After fabricating the fishnet, particles were transported to the structure individually and glued inside the openings using the MPP laser. The deposited polymer layer in Figure 70 is 1.1 μm. The structure height must be considered while transporting the particles into the openings. For this experiment particles were transported while being held 5 μm above the substrate and lowered down into the openings.

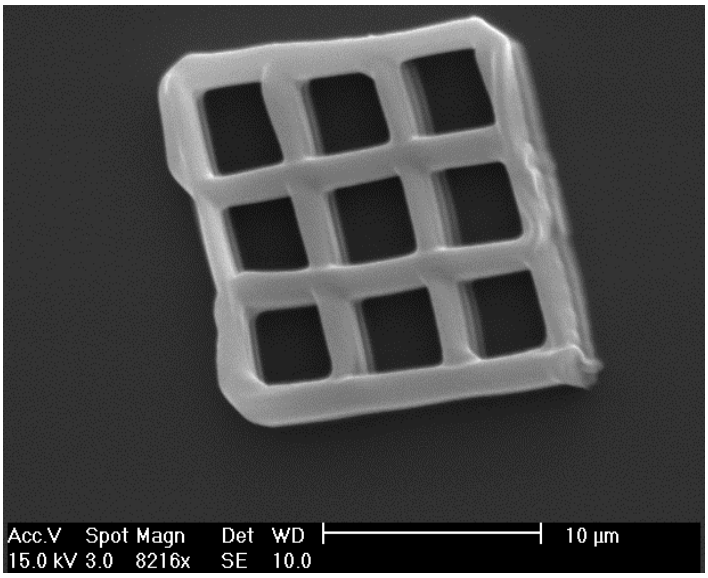


Figure 70. Fishnet structure fabricated using the MPP section of the combined MPP-OT setup to house particles. Openings are set to be 4 µm each. The structure was fabricated using the laser power of 14.55 mW and fabrication speed of 30 µm/s.

Figure 71 shows a structure fabricated using the MPP laser and filled with particles that were brought in by the trapping beam. The polymer attaching the particles to the substrate can be seen in the SEM picture. By decreasing the polymerization laser power and exposure time, less polymer will be used to glue the particles to the substrate.

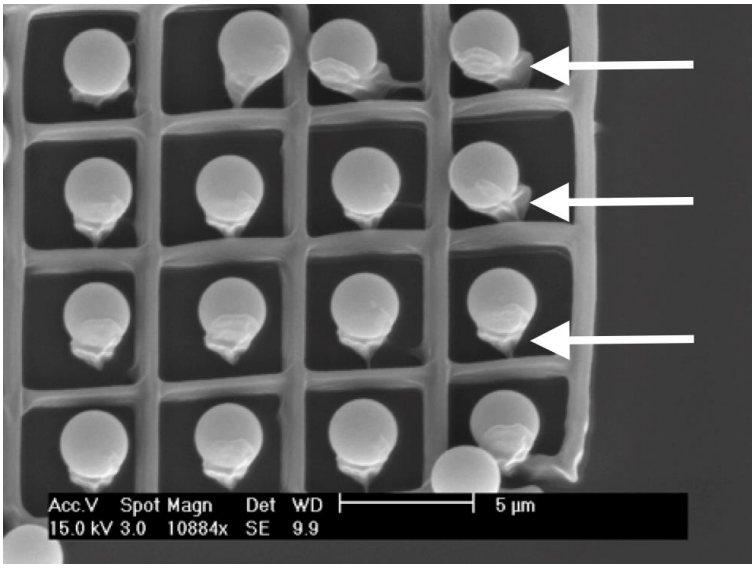


Figure 71. Image of 3 µm melamine resin based particles placed inside the fishnet structure fabricated with PEGDA. The fabrication speed of this sample was 20 µm/s

with laser power of 14.55 mW. The solidified polymers that glue the particles on the substrate can be seen in this image.

After successfully immobilising a 2D array of particles on the substrate the next step was to move toward multilayered (3D) structures with multiple particles embedded in different layers of the structure.

Moving toward multilayered structures made the structures more susceptible to delamination. Due to low surface adhesion between the polymer and the substrate some of the multilayered structures fabricated using the combined setup photoresist were washed away during the development process. To increase surface adhesion coverslips were placed in the plasma cleaner (Fischione 1020 plasma cleaner) and cleaned for 10 minutes. It was believed that the plasma cleaning reduced contamination from the coverslip and improved the surface adhesion.

In addition to the surface adhesion, tilt in the stage, which was demonstrated in Figure 63, made the fabrication process for large multilayered structures using the MPP driver software problematic. Figure 72 shows a structure fabricated using the MPP driver software and the bitmap file used for fabrication of this structure. As the polymerization beam moved towards the left-hand side of the image in Figure 72, the polymerization area moved away from the substrate. Therefore, the polymer adhesion for these regions was reduced, and the fabricated structures were washed away during the development process.

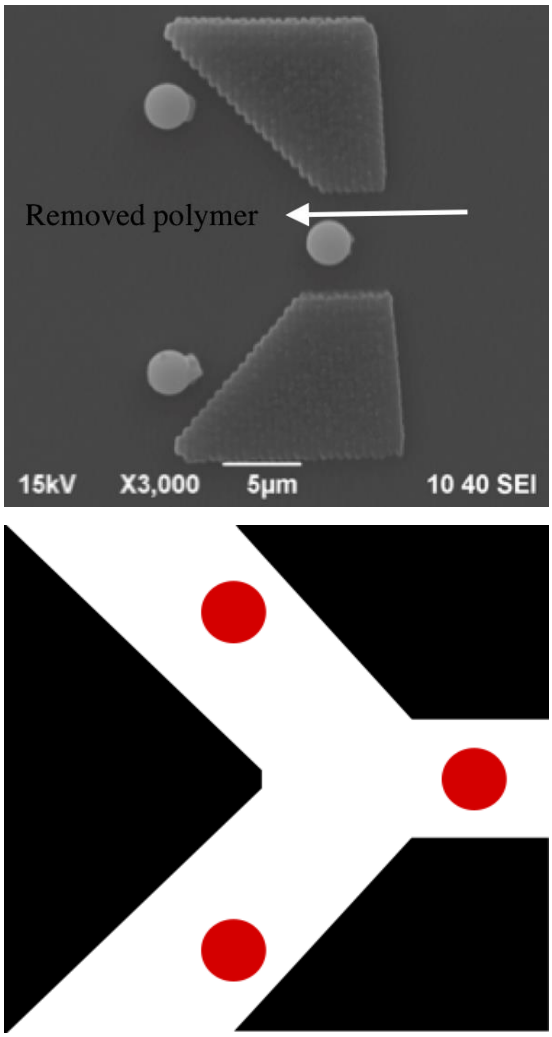


Figure 72. A structure fabricated using the MPP studio software. The bitmap file shows 3 particles inside a Y channel. But a portion of the structure has been washed away during the development process.

After improving the surface adhesion of the coverslip, the first successful multilayered structure was fabricated by incorporating 9 particles on a stepwise structure. The sample in Figure 73 was fabricated to demonstrate the ability of the system to embed particles in different layers of a fabricated structure. To fabricate this specimen a fishnet structure like Figure 71 was fabricated and the first layer of particles placed in the three openings on the left-hand side of the fishnet structure. Following the fixing of these 3 particles, the second layer of polymer was deposited using the MPP laser. The structure was fabricated using the laser power 14.55 mW and fabrication speed of 20 µm/s that produced 1.1 µm thick layers. After depositing the second tier, 3 particles were glued on the polymer layer. Using a shorter exposure time (50 ms) to reduce the amount of polymer used to fix the particles to the structure. The third layer of particles was

placed on top of the third layer of polymer. This structure was a successful attempt to fabricate 3D structure and fix particles on different layers of the structure.

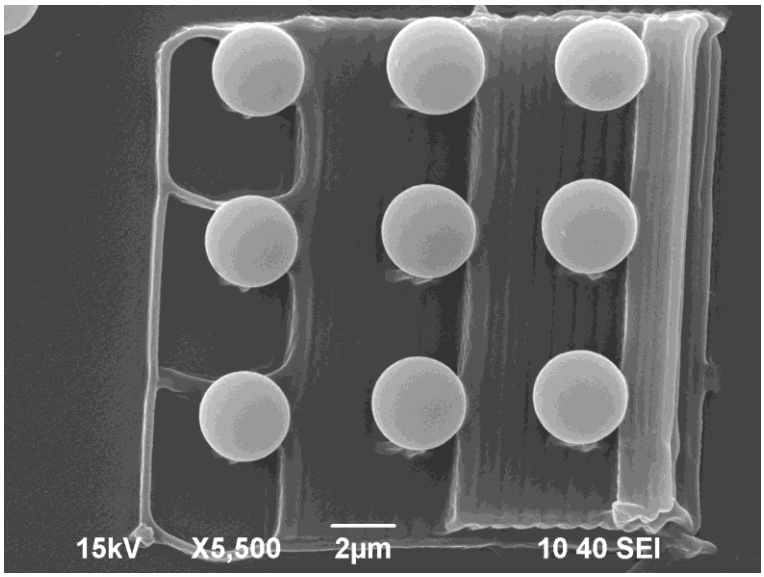


Figure 73. Step like structure with 3 particles adhered to each step. This picture demonstrates the ability of the structure to embed particles in deferent elevations and into 3D structures.

5.2 Particle Encapsulation

The next challenge was a fabrication of hybrid structures with an array of particles inside the polymer matrix. Figure 74 shows one of the first attempts to embed 8 particles within a polymer structure. In this structure, 4 particles were spot-welded to the substrate and covered with 3 layers of polymer. Because the polymerization beam goes through the particle, the interference caused by the particle in the polymerization path reduces the laser power near the particle edge. The deformation and lower polymerization rate make it possible to see the particles in the SEM picture presented in Figure 74. The second set of 4 particles spot-welded on the third polymer layer. The particles on the top of the structure were left exposed to be able to perform further characterization.

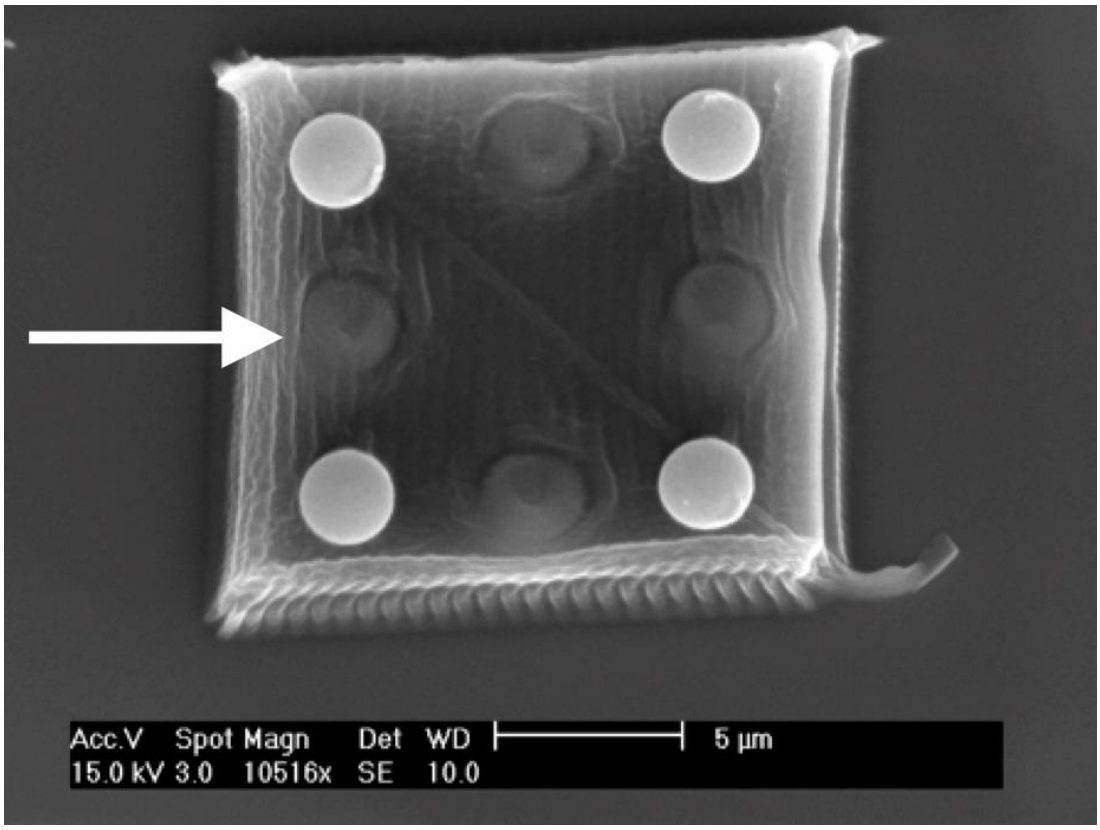


Figure 74. Multilayered structures fabricated using the combined setup. The arrow points out the position of a particle in the lower layer of the structure. The particles in the lower layer were partially covered with polymer and second set of particles embedded on top of the structure.

To utilise the combined setup, the CW trapping laser and the mode-locked polymerization laser should be utilised simultaneously. The accumulative energy of lasers can overheat the photoresist. The overheating is manifested by bubble formation in the photoresist, sample damage, and polymer dislocation. Figure 75 shows the effect of bubble formation on the fabricated structure. In this figure, the overheating occurred as the particle was being attached to the lower right section of the structure. The overheating broke the particle and removed a portion of the polymer structure. At this point, the fabrication stopped, and the sample was removed from the setup. Based on the observations made during the sample fabrication, contamination and debris in the sample increase the chance of bubble formation and overheating.

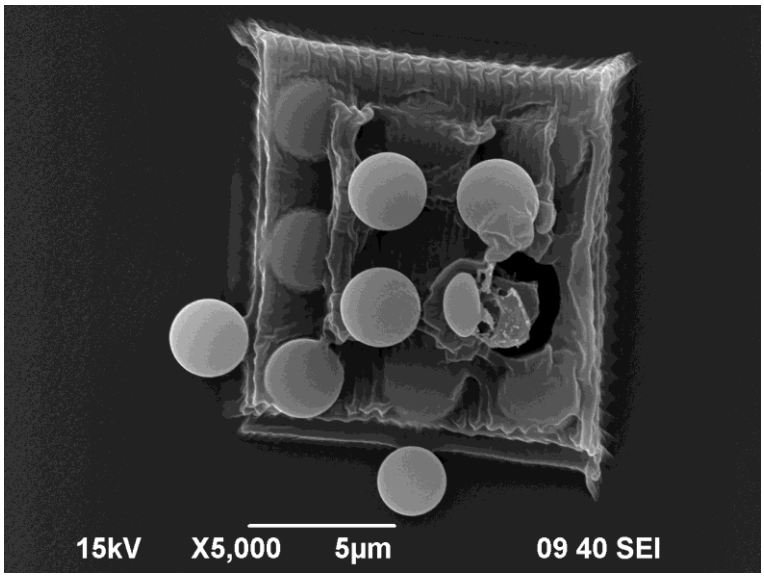


Figure 75. Multilayered structures fabricated in the combined setup. The first layer of structure has 9 particles in it. While immobilizing the particles in the second layer, the laser overheated the structure and damaged the particles.

5.3 BFM and EDX Sample examination

Different samples were fabricated in the combined setup by following the procedure explained in chapter 3.4. After developing the samples and washing away the excess the polymer samples were dried and examined using Bright Field Microscopy (BFM). Due to the difference between the refractive indices of the particles and the polymer, the particles are distinguishable in the bright field microscope images. High refractive index particles appeared brighter in the microscope.

The imaging section of the combined setup also provided images of structures while being fabricated. Figure 76 shows a structure fabricated in the combined setup. The solidified polymer is transparent to the visible light, and the bright spots represent high refractive index micro-beads. Although this is not an accurate technique to examine the fabricated structures but it can produce qualitative information about the fabricated structures before development.

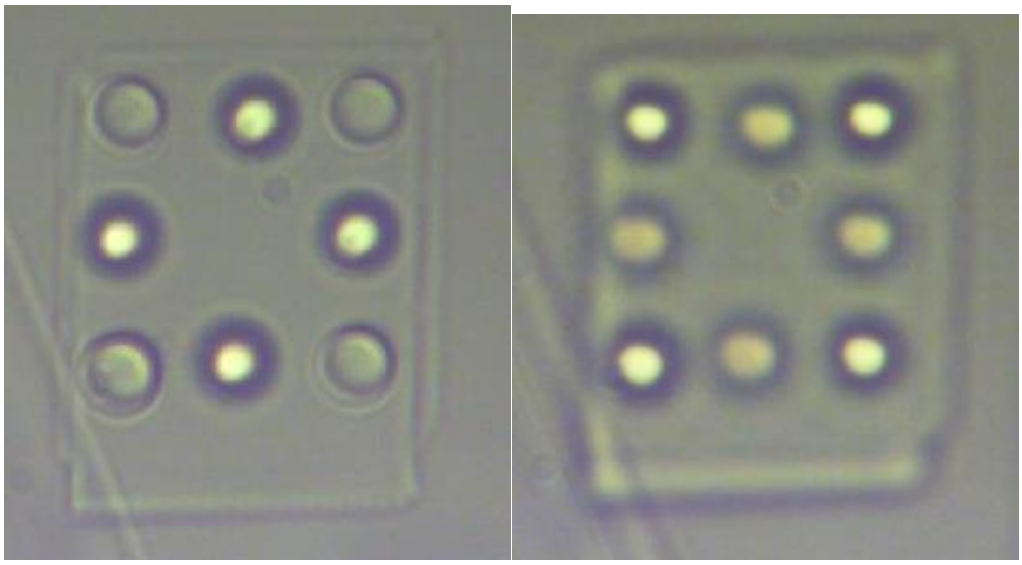


Figure 76. A multi-layered structure fabricated in the combined setup. Using a piezoelectric stage and the imaging section of the combined setup the structure is sliced into two layers. Left, the objective lens focus is close to the particles in the upper layer of the structure. Right, the imaging plane of the objective lens is placed close to the bottom layer of the structure and particles in the lower layer of the structure are in focus.

While examining the sample in the BFM, the position of the fabricated structure was marked on the coverslip using a silver pen. The silver pen leaves a thick layer of conductive ink on the substrate that can be easily distinguished during Scanning Electron Microscopy (SEM). SEM was used to produce higher resolution images of the samples. The SEM pictures were used to record information regarding the position of the particles and the polymer structures fabricated. To clearly differentiate the polymer structure from particles and produce more accurate information, EDX was used to check the elemental composition of the sample. Based on the molecular structure presented in Figure 38, only the melamine beads contained Nitrogen. Therefore, it made Nitrogen a useful marker for the particles. Figure 77 shows the Nitrogen-map of structure in Figure 74. The blue spots represent Nitrogen content in the structure and areas with higher density of blue spots are the particles. The particles inside the structure (first layer of the particles) are faintly distinguishable from their surrounding polymer.

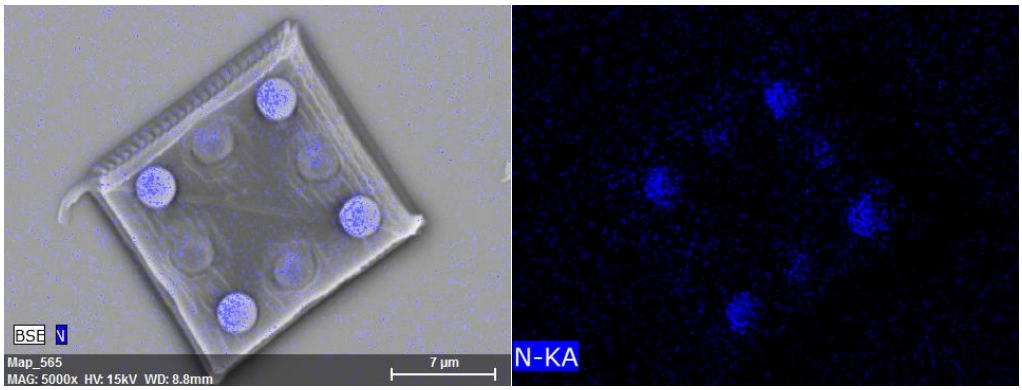


Figure 77. EDX elemental mapping of the structure fabricated using the combined setup. The high nitrogen content of the particles makes them distinguishable from the photoresist. In this picture the nitrogen content is demonstrated by accumulation of blue dots.

5.4 Confocal Fluorescent Microscopy Sample Examination

To build larger structures and increase the number of particles embedded in the structures, it was tried to reduce the fabrication time of the combined setup. To decrease the fabrication time, the stage travel speed was increased from 20 µm/s to 30 µm/s. By increasing the stage speed to 30 µm/s, the Stokes drag force generated increased beyond the trapping force generated by the trapping laser beam and the trapped particle was removed from the trap. In previous experiments, particles were brought to the fabrication site using a series of consecutive jumps. By moving the particle in a series of small jumps, it was possible to use a higher travel speed (20 µm/s). To enable the system to directly move the trapped particle from its original position to the polymerization site, the stage travel speed was reduced to 18 µm/s. using the reduced speed, it is possible to enter the final coordinates (X and Y position of the fabrication site) in the stage driver software and move the particles with one big jump.

The limiting factor for the combined system fabrication speed was finding, trapping and transporting the particles. To decrease the fabrication, time the particle concentration was therefore increased. To achieve this 12 µl of the purchased solution was mixed with 2 ml of the prepared photoresist. Increasing the number of particles in the sample increased the probability of finding particles close to the fabrication site, but it also had some drawbacks. Having high particle concentration increased the sample contamination. Developed

samples that had higher particle density were often contaminated with additional particles that adhered to the structure during the development process. Increasing the number of particles in the sample also increased particle agglomeration.

Figure 78 shows an array of 12 particles embedded inside the polymer structure. In the first layer, 8 particles placed 5 μm apart from each other (centre to centre). On the second layer, 4 particles were placed at the centre of a cubic structure. Four polymer layers (each layer 1.1 μm thick) were placed between the first and the second particle sets. The polymerization laser reflection and refraction that occurs in the presence of particles, attenuates the polymerization beam and produces the non-uniform surface structure in the layer just above the particles. To overcome this issue a higher number of polymer layers must be deposited after the particles. As the focal volume of the objective lens moves away from the particles, the effect of particles on the polymerization laser reduces and a more uniform polymer layer will be deposited.

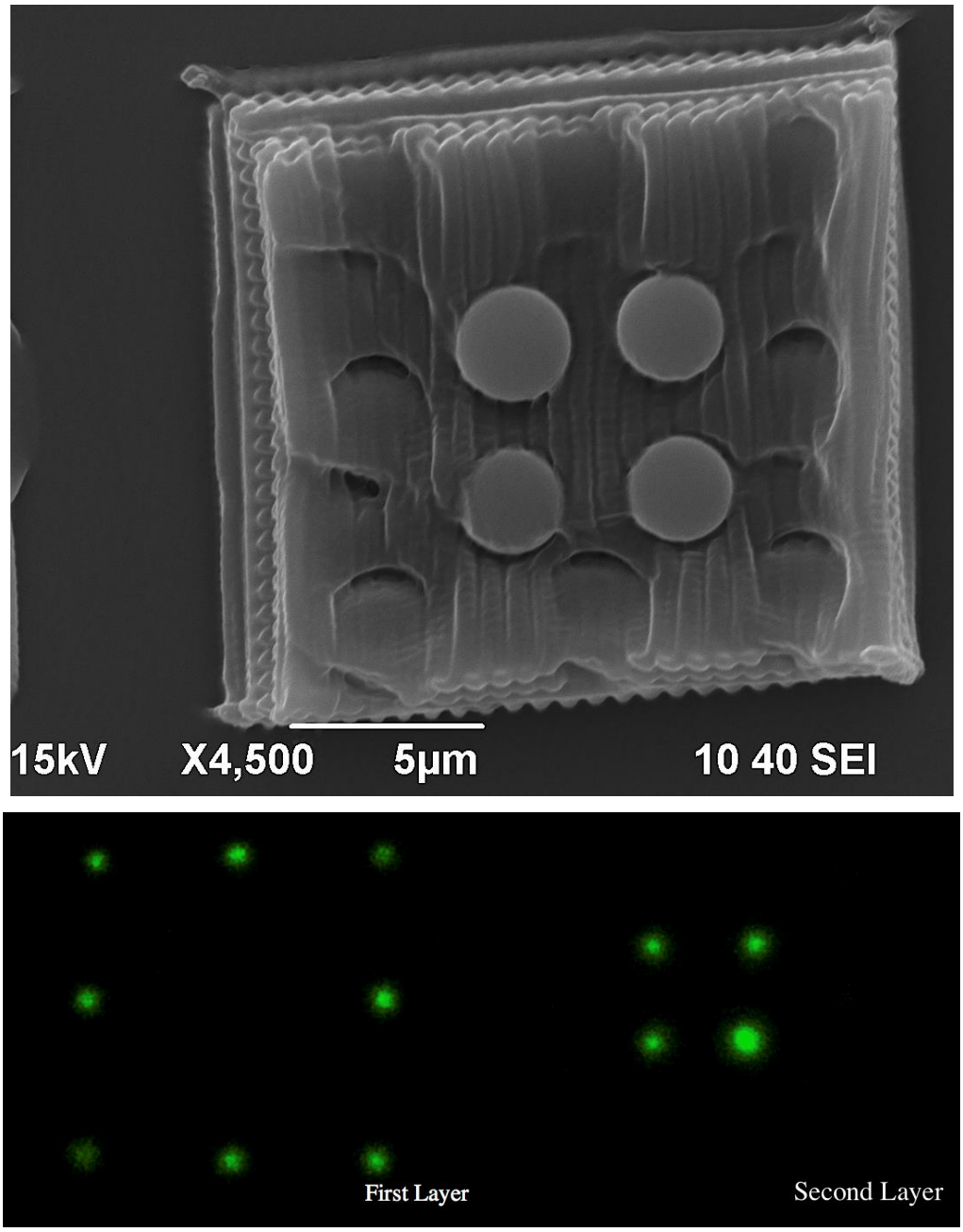


Figure 78. A structure fabricated using the combined setup with 12 particles in the first tier and 4 particles in the second tier. The Confocal fluorescent microscope was used to excite the particles with specific frequency and image them in their excitation wavelength. pictures clearly show the particle arrangements in both layers.

The confocal fluorescent microscope was used to study the internal structure of the fabricated samples. The fluorescent particles were excited with an argon laser with the wavelength of 490 nm, and they emitted fluorescent light with a wavelength of 525 nm. ZEN v2.3 (Blue edition) imaging software was then used to analyse the captured images. Using the 3D capabilities of this software the array of pictures taken during the experiment can be stacked on top of each other

and based on the step size of the piezoelectric stage 3D representation of the fabricated structure is reproduced.

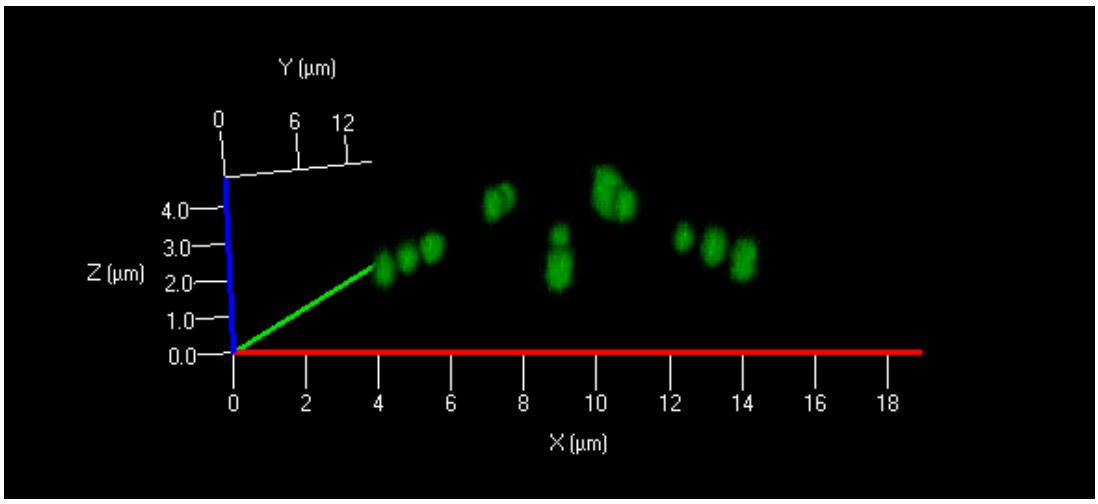


Figure 79. 3D reconstruction of the structure demonstrated in figure 67. By stacking the images taken from each layer, it is possible to produce 3D representation of the structure.

The spherical particles used during the experiment are slightly stretched in the 3D representation. Although the confocal setups are very efficient in eliminating the out of focus light, the emitted light from the fluorescent beads illuminated their surrounding polymer, and the particles are visible in larger number of the layers, which stretches the particles in Z direction once these pictures are stacked on top of each other. The Ar laser power was reduced to avoid bleaching the fluorescent particles and decrease the amount of light generated by the particles. Another solution was to increase the light threshold in ZEN v2.3 (Blue edition) lit software to reduce the light around the particles and therefore generate more accurate 3D structures, which is presented in Figure 79.

Figure 80 shows the images taken from another sample using the confocal fluorescent microscope with a 63X oil immersion objective lens. The piezoelectric stage step size of 400 nm was chosen for this experiment. Figure 80a is the phase contrast image taken using the visible illumination source that shows two sets of particles in the polymer matrix with mobile particles outside the structure. The Figure 80b& structure fabricated in the combined setup. The green spots represent the fluorescent particles in the structure. The particle arrangement can be seen in the Figure 80b&c.

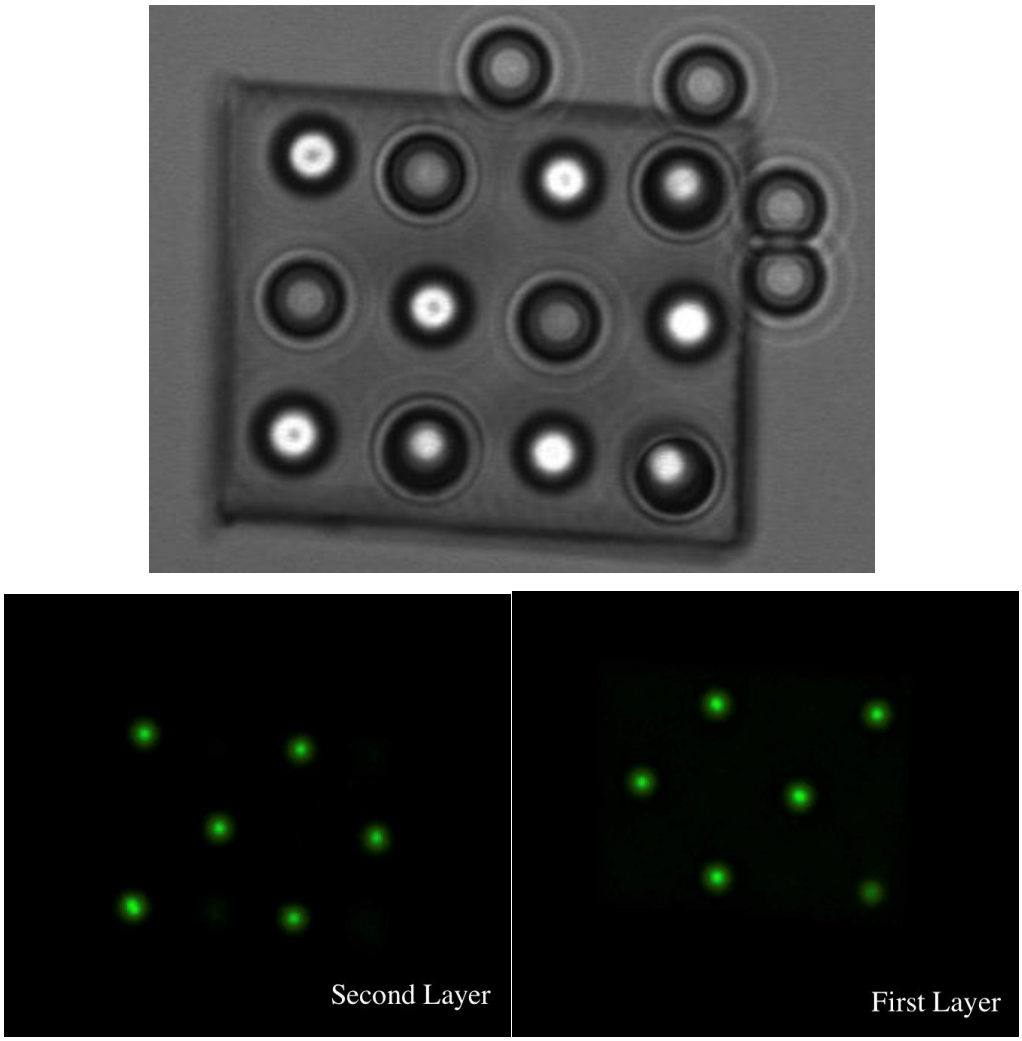


Figure 80. Confocal fluorescent image of the multilayered structure with fluorescent beads embedded in it.

Figure 81 is another example of successful structures fabricated using the combined setup. SEM was used to image the fabricated structures and produce high resolution / magnification pictures of the structures. To be able to observe the particles in both layers of the structure, the particles in the first layer were partially covered by the polymer and the second set of particles placed on top of the deposited polymer layers. In Figure 81, 16 particles were immobilised in the first tier. To partially cover the particles, two layers of polymer were deposited on the coverslip. The particles in the second layer of the structure were placed with different arrangments. Particles on the right-hand side of the structure placed between two particles from the previous layer, but particles on the left-hand side positioned in between 4 particles from the first tier (resembling BCC and FCC structures).

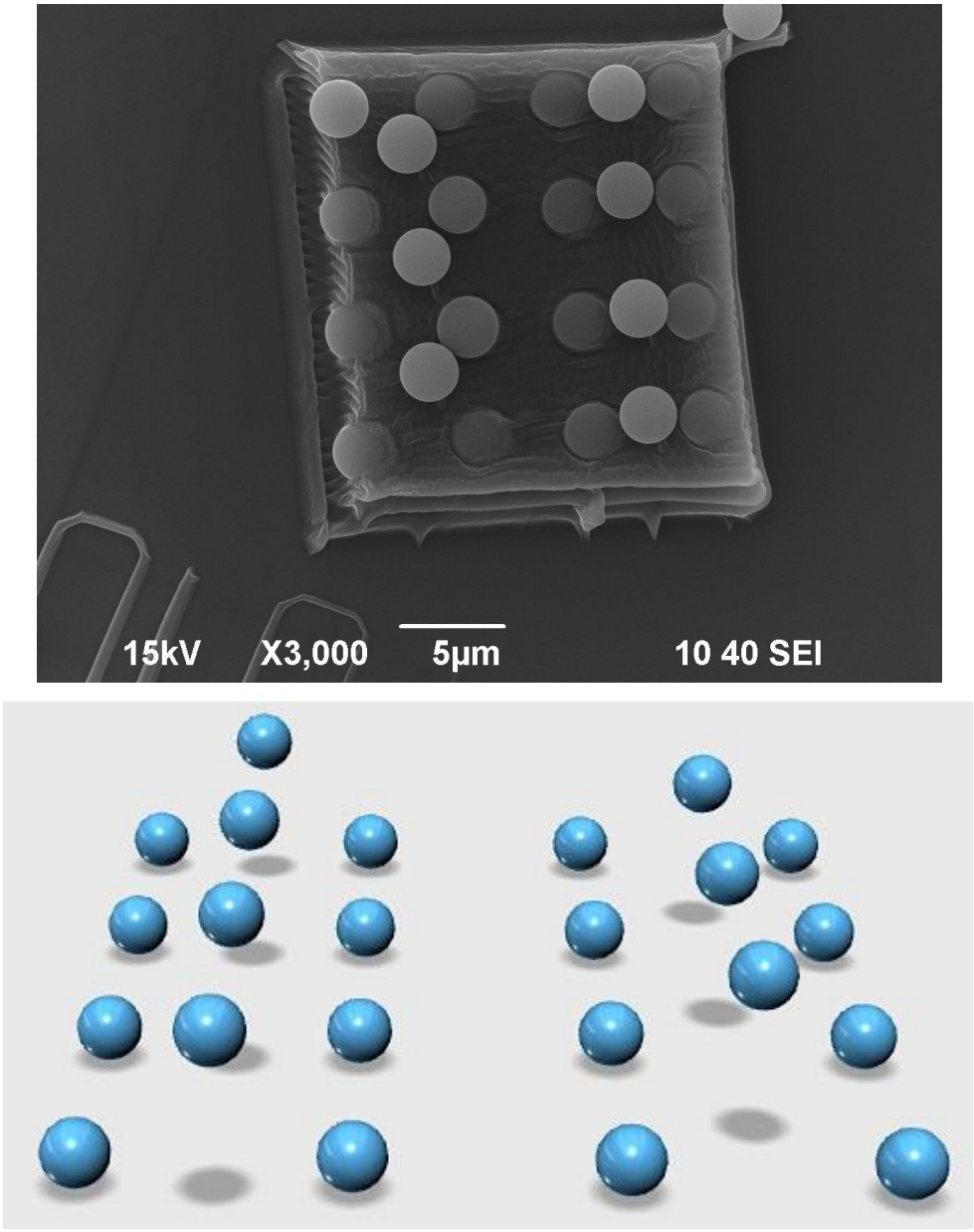


Figure 81. 20µm by 20µm structure fabricated that contains 23 particles in two layers and the 3D representation of particle arrangement.

5.5 System Accuracy

Particle placement accuracy was one of the concerns for this system. To be able to measure the system accuracy an array of particles were placed on the coverslip. Using ImageJ 1.49v software the particle edges were defined, and the position of the centre of each particle was found automatically. The intended distance between the particles (centre to centre) was 5 µm. Deviations from the targeted gap are due to inaccuracies in particle placement and polymerization.

The main source of error in particle placement is the sample drift. The combined setup was used as a fixed beam system and particle trapping, transportation and placement were done using the stage. While searching for a new particle to be trapped, the sample / stage drifted away from its original position. Recalibrating the stage for the new load and tightening the microscope slide holder screws that held the sample minimised the sample drift.

Polymerization often moved the particle from its intended position. Whilst the polymerization beam had minimal effect on the particles, the vibration caused by opening the mechanical shutter moved the particle as it was being adhered to the substrate. The solidified polymer also moved the particle away from the substrate and out of the focal volume of the OT setup. Misalignment between the OT position and MPP polymerization area was another key factor that changed the position of the particles. Figure 82, shows eight particles fixed to the substrate using the MPP laser and the position of the centre of each particle.

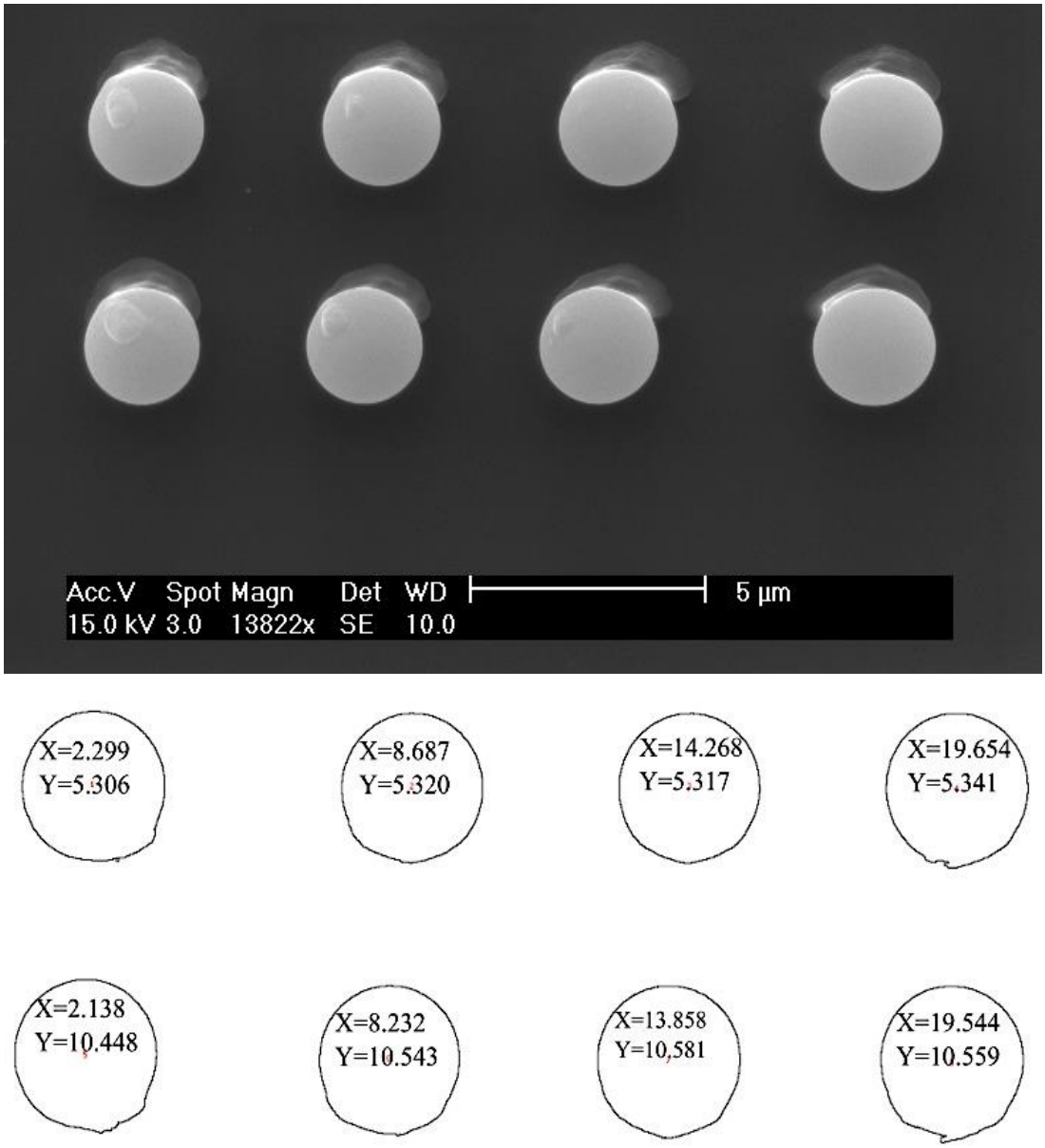


Figure 82. The first picture is an SEM image of a 2 by 4 array of particles immobilised using the MPP laser (exposure time of 150 ms and laser power GUI 700). The SEM image was processed using ImageJ 1.49v software, to define the particles borders and the coordinates for the centre of each particle are demonstrated in the picture.

The coordinates of the centre of each particle were used to calculate the gap between particles. The distance between the particles (centre to centre) in the X direction was 5.7±0.7 µm and in Y direction was 5.2±0.1 µm. In this sample particle placement error was larger in the X direction and lines produced with particles are relatively straight in the Y direction (the position of the centre of the particles are $Y_{line\ 1}$=5.32±0.02 µm and $Y_{line\ 2}$=10.5±0.1.

Different samples were fabricated and tested to increase the system accuracy. Using a shorter exposure time and smaller polymerization laser power, reduced the amount of polymer used for fixing the particles to the substrate.

Figure 83 shows an array of particle immobilised using the reduced MPP laser power and exposure time. For this experiment, the laser power of 14.55 mW and the laser exposure time reduced to 100 ms. Reducing the laser power and exposure time decreased the minimum feature size of the setup, and a smaller amount of polymer is observable underneath the particles. ImageJ v1.49 software was used to define the particle edges and to measure the gap between particles. Figure 83b illustrates the particles edges identified in ImageJ v1.49 and the position of the centre of each particle. The distance between particles in the X direction is reduced to 4.8±0.1 μm and in Y direction the gap is 5.75±0.05 μm.

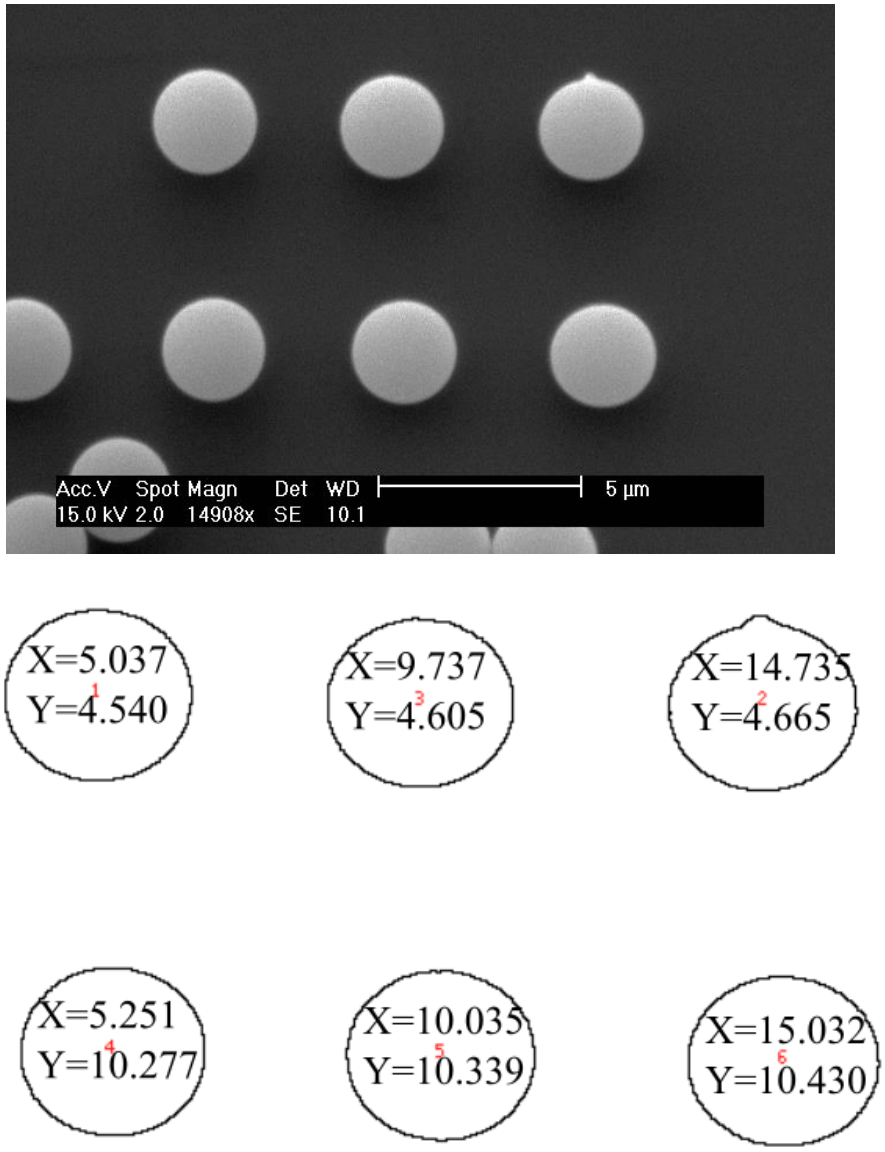


Figure 83. The first picture shows a SEM picture of an array of particles immobilised on the substrate using reduced laser power and exposure time. (b) Particle edge and the position of the centre of particles defined in the ImageJ 1.49 software.

5.6 TOF-SIMS Analysis of the Samples

To identify the particles inside the structure and produce depth profile of the samples, Time-Of-Flight Secondary Ion Mass Spectrometry (TOF-SIMS) was used. TOF-SIMS IV (IONTOF GmbH) was used to etch away the polymer and expose the particles in the samples. The data gathering process was optimised by using a 15 keV Ar_{17000} sputtering beam and 25 keV Bi_3 analysing beam. Using the ion beam the polymer structure was milled away and the composition

analysis was performed. The nitrogen content in the particles enabled the TOF-SIMS to differentiate particles from the polymer background. Figure 84 demonstrates different stages of TOF-SIMS analysis. Figure 84a shows 4 bright spots that represent particles in the upper layer of the structure. The second picture shows the top view of the structure after ion milling through the upper layers of the structure and exposing the second set of particles. Figure 84c shows the cross-section of the structure with two particles in the top layer and single particle in the lower layer.

Comparing the position of the particles in Figure 84a and b demonstrate a shift in the position of the particles. In TOF-SIMS sample analysis starts by focusing the ion and analysing beam on the upper layer of the structure. As the Argon beam etches away the polymer structure, the data gathering occurs out of the focus point of the analysing beam, and it shifts the position of features in the sample. The cross-section image in Figure 84c is the side view of the structure. Due to the change in the position of particles in the consecutive images taken by the analysing beam the particles cross section is distorted. Usually, there is a one to one ratio between the depth and shift in the features in the above-mentioned TOF-SIMS equipment.

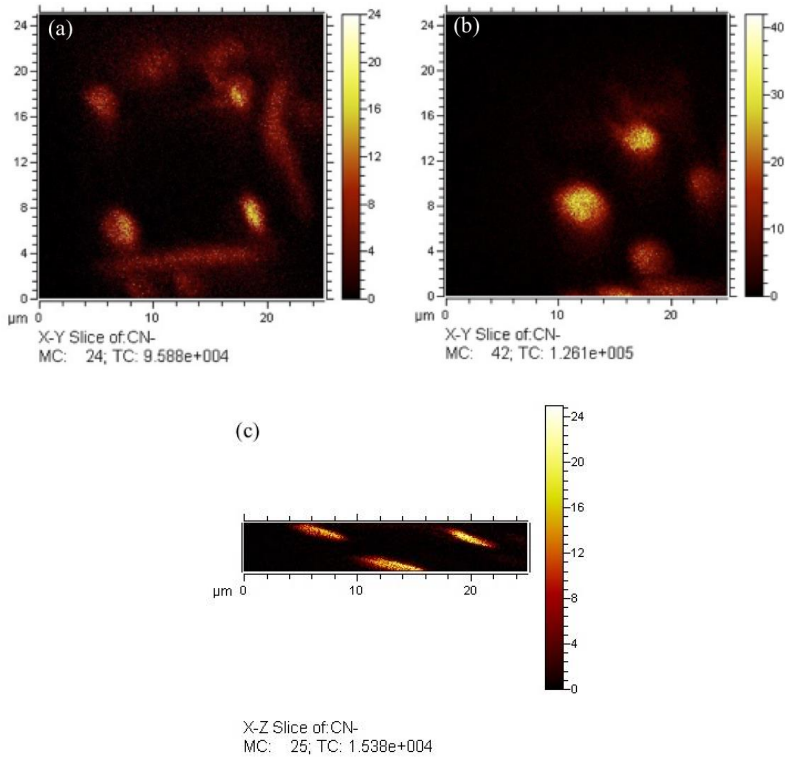


Figure 84. TOF-SIMS image of a structure fabricated using the combined MPP-OT setup. Images a / b demonstrate different layers of the structure. The bright spots show regions with higher Nitrogen content. Image c shows the cross-section view of the structure. The shift produced by the system in the position of the particles can be seen in image c.

5.7 Summary

In this chapter, the structures fabricated using the combined OT-MPP setup were presented and tested. The combined OT-MPP setup enables the user to transport micro-beads with high precision and immobilise them using the femtosecond laser.

To demonstrate the capabilities of the combined OT-MPP system an array of particles (up to 30 particles) was immobilised on the substrate to show the repeatability of the system. ImageJ v1.49 was used to analyse the fabricated structure and measure the distance between the particles. It was demonstrated that using lower exposure time and reducing the amount of polymer used to glue the particles to the substrate, reducing the gap between the polymerization and trapping area and placing the particle close to the substrate could potentially increase the system accuracy.
The combined OT-MPP setup was used to embed particles in the polymer matrix. These multilayered structures housed an array of particles with different arrangement were one of the key achievements of this project.

Different techniques were used to examine the particle arrangement after being encapsulated with the polymer. SEM pictures taken from the samples showed the particle arrangement on the upper layer of structures. The particles attenuated the polymerization beam and reduced the polymerization in areas close to the particle. Therefore, the particles in the upper layer were distinguishable in the SEM picture.

Confocal fluorescent microscopy was used to image the multilayered structures and detect the position of the particles. The photoresist used in the experiments was transparent to visible frequency and the fluorescent-marked melamine resin particles were imaged at their excitation wavelength. This technique enabled 3D reconstruction of the samples using the ZEN V2.3 (blue edition).

TOF-SIMS has used to further study and depth analysis the samples. Using the ion beam the polymer layers etched away and the underlying particles were

exposed. The Nitrogen content of provides enough contrast between the polymer and the particles to enables efficient particle detection.

The structures fabricated using the combined OT-MPP setup demonstrated the repeatability and accuracy of the system in transportation and immobilisation of both glass and melamine particles suspended in PEGDA photoresist. The repeatability of the system is largely due to utilisation of afocal beam expander, which enables precise overlapping of the trapping and polymerization area.

The system presented in this chapter was one of a kind combined optical trapping and multiphoton polymerization system. The key fact that set this system apart from the other systems was the capability of this system to transport trapped particles in 3D. The Polymerization and trapping process was done using a single objective lens but this system has the capability to move the trapping area independent of the polymerization site. This new capability enables the system to trap particles in different distances from the substrate. The 3D trapping capability of the system enables the system to function with different wavelengths and particle sizes and accurately place variety of particles close to the polymerization area to be fixed in their intended positions.

CHAPTER 6: DISCUSSION

One of the least developed areas of AM is the multimaterial microfabrication aspect of 3D printing. MPP is one of the AM techniques that have the capability of fabricating microstructures with high resolution. But there are few studies that demonstrate the ability to use multiphoton polymerization to fabricate composite structures [69]. In a search for a fabrication technique suitable for fabricating metamaterial structures, this thesis attempted to tackle the multimaterial microfabrication issue and to produce a versatile technique to build 3D composite microstructures. The proposed technique is based on simultaneous use of OT to transport particles with different properties and length scale into the MPP vat and incorporation of these particles in the polymer matrix. It is believed that the combined setup has the potential to tailor the mechanical, electrical and optical properties of the MPP photoresist by incorporating particles with specific properties in the polymer matrix. This technique can be a viable route for the production of functional multimaterial structures like photonic crystals and metamaterials.

The discussion chapter is divided into three major sections to examine different stages of the project. In the first section, the MPP setup will be examined in comparison to the setups assembled in different research groups. The second part of this chapter presents a discussion about the OT setup and the trappable particles. In the last part of the chapter the achievements and successes of the combined OT-MPP will be presented. Similar works done before completion of this project is also presented to highlight the differences and the engineering advancements made during this project.

6.1 The MPP setup

Constructing a modular MPP setup was the first prerequisite for building a versatile technique to fabricate metamaterials using additive manufacturing. The assembly process and parts used in building the MPP setup was presented in chapter 3 and structures fabricated using this system were presented in chapter 4.

MPP uses a tightly focused mode-lock femtosecond laser to initiate polymerization by absorption of more than one photon [23]. Due to the nature of multi-photon polymerization sub-diffraction limit resolution can be achieved using this technique [110]. In the literature, MPP setups with sub 100 nm resolution have been readily demonstrated [214]. The assembled setup demonstrated its capabilities in fabrication of 3D sub-diffraction limit structures.

The MPP setup assembled in this project followed the general designs for a basic MPP setup. The femtosecond laser was expanded and guided toward to objective lens using an optical chain. The objective lens mounted in a microscope body focused the laser beam into the sample chamber, which was mounted on a piezoelectric stage. The fixed beam MPP setup used a mechanical shutter to control the laser exposure time.

The assembled MPP setup was unable to fabricate submicron feature sizes and the polymerization threshold was higher than the expected values (4 to 8 mW [215]). After inspecting the setups beam alignment, it was defined that poor optical alignment between the laser head and the beam conditioner box deteriorated the beam conditioner box exiting beam quality. Further experiments and refinements were done to increase the polymerization beam quality and reduce the polymerization threshold of the system. The 45° fixed mirrors used in assembling the optical train made it impossible to realign the laser beam after each optical element. Consequently, the light that entered the objective lens was not at the centre of the back aperture. To decrease the MPP system minimum feature size, the fixed mirrors were replaced with 45° mounted mirrors with fine adjustment knobs. The poor alignment in the optical train also changed the PSF of the objective lens and spread the laser power into a larger area, therefore, reducing the photon density in the polymerization volume. Spreading the laser power over a larger area increased the polymerization area that should be restricted to the centre of the focal volume.

Based on the arrays of voxels fabricated and presented in Figure 42 and Figure 43 the voxels are stretched in the laser propagation direction. Consequently, the lateral resolution of the system is lower than its axial resolution. This phenomena can be explained by the defining the shape and size of the PSF of the system. By comparing equations Equation 24 and Equation 25 it is clear that the size of the high-intensity areas is larger (stretched) in the Z direction. Also due to the misalignment and aberration the PSF generated by the objective lens is further stretched in the laser propagation direction. Figure 85 shows the effect of negative and positive spherical aberration on the PSF of

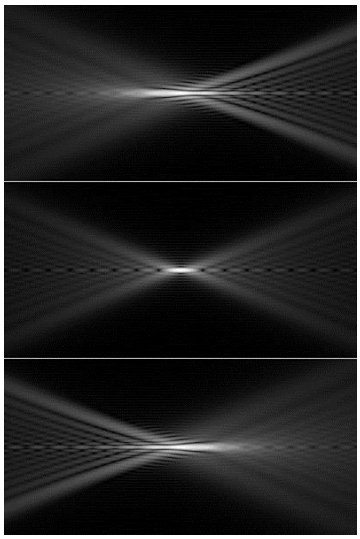


Figure 85 Longitudinal view of a focused beam with (top) negative, (centre) zero and (bottom) positive spherical aberration. The lens is placed at the left-hand side.

The diffraction patterns can be seen on the setup by focusing the laser beam on a reflective surface. The reflection of tightly focused laser beam acts similar to a point source and produce the diffraction patterns in the imaging side of the system. In the experimental setup, IR laser beam was used. Therefore, to visualize the diffraction pattern the IR filter, which was mounted to protect the camera, must be removed. It is also possible to use the piezoelectric stage to move the reflective sample in the Z direction and look at different slices of the hourglass-shaped cross-section.

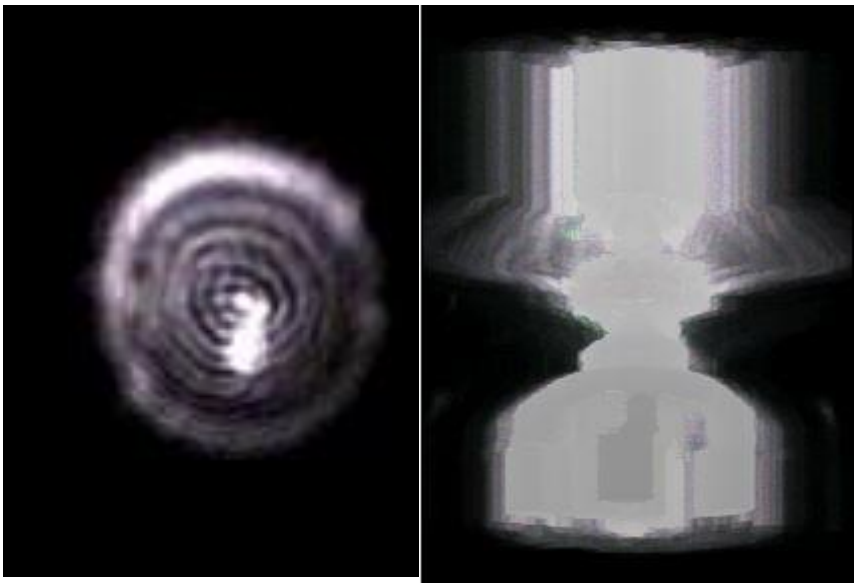


Figure 86 The polymerization laser is focused on a reflective surface. The focused light can be considered as a point source. The light collected by the objective lens produces diffraction patterns that can be seen by removing the IR filter from the imaging section of the system. Using the piezoelectric stage the reflective sample was moves in Z direction and a stack of images were captured. (left)Diffraction pattern produced by the focused laser beam in X-Y plane (right) Z projection of the stacked images produced using ImageJ v1.49.

Another limiting factor in the assembled setup was the mechanical shutter used in the setup. The low operating speed of the shutter increased the minimum exposure time and the mechanical blade movements introduced vibration in the optical chain. The minimum exposure time attainable using the SC10 mechanical shutter was 27 ms for a single voxel.

LabVIEW driver software was developed for fabrication of multilayered complex structures using .STL files. This software used raster scanning to build each layer of the structure layers voxel by voxel. Using the software to build the structures voxel by voxel increased the system minimum feature size dependency on the shutter operating speed.

Stage driver software was also used to fabricate simple structures. The driver software utilised continues movements to scan the build area with different step sizes. Using continuous movement can limit the exposure time and affect the minimum feature (resolution) of the setup. By increasing the stage travel speed it was possible to achieve sub-micron double line resolution and feature sizes.

6.2 OT achievements

By completing the MPP setup, the next objective of the project was undertaken, that was assembling and testing the OT unit. An OT system based on Thorlabs OT kit was assembled and tested with different particles suspended in deionized water and photoresist. This OT uses GM to trap and transport particles in the imaging plane. The piezoelectric stage can be used to move the sample in the Z direction. Therefore, examine the 3D trapping capability of the system.

During the experiments, stable 3D trapping of dielectric microparticles was achieved. Using the optical trapping setup 2D trapping of 300 nm gold nanoparticles and CNT's were also achieved. To understand the effect of the refractive index of particles and their surrounding medium, simulation software was used.

The experimental results were compared with the simulation results and the literature. The simulation software demonstrated the net force applied to the particles and the effect of decreasing the ratio of the refractive index particles to their immersion medium. Higher trapping forces were exerted to the particles with higher refractive index, and it was possible to displace these particles with higher velocity with less particle displacement. By introducing the same particles that were trappable in water to a photoresist with higher refractive index the ability of the OT to transport these particles deteriorated. Therefore, it was clear that a custom prepared photoresist is needed for the combined setup.

Based on the experiments done, PEGDA with a refractive index of 1.47 at 589.3 nm was selected. The simulation software was used to test the trapping force applied to different particles which were commercially available. High refractive index soda lime particles with a refractive index of 1.59 n20/D were purchased in dry powder form to be used in the combined setup photoresist.

Stable 3D trapping of soda-lime glass beads suspended in PEGDA was achieved but producing a stable solution of soda-lime glass particles in PEGDA was challenging. The dry powder had very low wettability and different techniques

were used to suspend these particles. Particle breakage and aggregation contaminated the photoresist and stopped the combined setup photoresist to viable for more than few minutes. To be able to produce more stable combined setup photoresist, melamine resin based microbeads was tested in the PEGDA. These particles were purchased in suspended form, and it was easier to suspend in PEGDA. The particle breakage that happens for glass beads in the ultrasonic bath was stopped using the melamine resin based fluorescent particles.

6.3 Fabrication of composite structures

Klein et al. for the first time demonstrated the Multi-component MPP polymer scaffolds. In their paper, they used two polymers with different polymer binding properties to build a cell scaffold [18]. Composite structure with three different polymers has also been demonstrated by a group in Vilnius University [19]. These papers demonstrated the potential of multimaterial MPP structure but they didn't deliver the multimaterial MPP system. The composite structures demonstrated in these two papers were fabricated by repeating the polymerization steps on top of previously solidified microstructures. Therefore, for each material, the user must remove the sample from the system, develop the polymer and remount the sample accurately on its original position for the next stage. This technique has a high probability of sample contamination and misalignment. Due to the high number of fabrication steps, this technique suffers from extremely low fabrication speed.

As it was mentioned in chapter 2, it is possible to use the mode-lock femtosecond laser to fabricate metallic structures. Liu et al for the first time reported utilisation of MPP to fabricate 3D structures using a combination of polymer and gold. In Liu et al approach they had limited control over the shape, size and position of gold clusters [216].

It is also possible to produce composite structures with particular properties, by introducing particles with specific properties into the polymer matrix fabricated using MPP. For instance, Ushiba et al distributed carbon nanotubes in the MPP resin and fabricated composite microstructures with enhanced mechanical

properties [217]. In their experiment, they produced a homogenous mixture of CNT and photoresist. Therefore, they had no control over CNT placement and they modified the properties of the whole structure. To be able to target specific areas of a design and tailor the material properties for these specific areas, there is a need for a technique that enables the researchers to control the existence / nonexistence of particles.

OT is a versatile, accurate and noninvasive technique that can manipulate a variety of materials. Tsai et al and Dawood et al have demonstrated the simultaneous application of MPP and OT [29][28]. Tsai et al. used the combined OT and MPP setup to fabricate nanostructures. In their work the trapped particle (3 μm polystyrene beads) performed as a microlens to further focus the polymerization beam. The near-field optical effect generated by the microlens enabled them to suppress the polymerization threshold of the polymer using lower laser power [29]. In this work, they used a single objective lens to perform polymerization and trapping. A dichroic mirror was used to combine the trapping laser beam (wavelength of 1064 nm) with the polymerization laser beam (wavelength of 780 nm to 800 nm). As Tsai et al. demonstrated in their paper, the trapped particle was placed above the substrate in front of the polymerization beam and focused the laser beam on the substrate to solidify sub-diffraction limit features. They simulated the effect of the spherical particle and concluded that using bigger particles the polymerization will occur further from the particle surface and reduce the chance that the particle gets stuck to the substrate [29]. In a follow-up paper published by the same group, they demonstrated that by placing the particle close to the substrate no polymerization could be observed [30].

Dawood et al. also demonstrated the simultaneous use of OT and MPP system. The OT system independently manipulates the particles and places them in the MPP vat. Using this technique they spot-weld 5 μm silica particles in specific arrangements on the substrate and on top of each other [28]. In their setup, the MPP laser beam (λ=740 nm) was combined with the OT beam (λ=800 nm)

before the objective lens and enabled them to trap 5 μm silica particles close to the polymerization site and spot-weld the particles in position.

These two papers are examples of simultaneous usage of OT and MPP. Similar setups (based on the single objective lens) were utilised in both papers, but the outcomes of the experiment were radically different. In the first paper published by Tsai et al. they tried to avoid particles being adhered to the substrate while Dawood et al. designed structures by spot-welding particles on the substrate. The key to the mode of operation of the combined setup is in the position of the trapped particle in regard to the polymerization area. If the trapped particle is placed close to the polymerization area, it is possible to spot-weld the particle onto the substrate. But by placing the particle further away from the polymerization area, it is feasible to use the particle as a microlens to enhance the resolution of the setup.

6.3.1 Combined OT-MPP Performance

After completing the OT system and achieving promising results for trapping particles suspended in a polymer, the combined setup development started. The combined setup was envisioned to be a parallel setup to the previously assembled MPP setup, which shared the mode-locked femtosecond laser.

During the experiments using the MPP system, the effect of chromatic aberration on the Working Distance (WD) of the objective lens was clear. The WD of the objective lens was longer for the polymerization beam (λ=800 nm) when compared to the visible light used for imaging. Therefore, to be able to image the fabricated structures, the build platform must move toward the objective lens. In this system the piezoelectric stage was used to move the sample for 3 μm toward the objective lens.

It was foreseen that the chromatic aberration would make it impossible to overlap the focal volume of the objective lens for the trapping (975 nm) and the polymerization (780 nm) lasers beams. Results demonstrated by Tsai et al. also showed the effect of wavelength on the position of the trapped particle in regard to the polymerization area [30].

On the first iteration of the setup, it was decided to use two different objective lenses to focus the trapping and the polymerization laser beams. The sample preparation and alignment process for this system was very lengthy and time-consuming. It was also very challenging to utilise two 100X oil immersion objective lenses with the field of view of 200 μm to perform polymerization and trapping in the same area. The mechanical translation mounts precision was not high enough. Therefore, the polymerization lens was replaced with a 10X objective lens. The 10X objective lens has bigger field of view and using a graticule, it was possible to focus both objective lenses on a same area (Figure 32). After performing different experiments, it was clear that, it is not possible to effectively overlay the objective lenses focal volumes using the double objective lens combined OT and MPP setup.

Poor performance, lengthy prefabrication steps and complicated alignment process steered us away from the double objective lens system. Using single objective lens for trapping and polymerization reduces the beam alignment difficulties. The trapping can be placed close to the polymerization are in the imaging plane using the 2D GM system. The polymerization and trapping occur in the focal volume of the objective lens. For parallel beams entering the back aperture of the objective lens, the working distance of the objective lens defines the position of the focal volume of the objective lens. The working distance of the objective lens depends on two sets of parameters, a) objective lens parameters and b) entering beam parameters. The shape, size, material and the number of optical elements in the objective lens are some of the objective lens parameters that define the objective lens working distance. Due to slight changes in the refractive index of the material for different colours (wavelengths), which is produced by the change in the light's speed in the medium, the working distance of the objective lenses are inherently different for different wavelengths. Some of the objective lenses are designed correct the chromatic aberration for specific wavelengths in the visible spectrum but they are ineffective in the IR range. . Consequently, the working distance of the objective lens is different for the trapping and the polymerization beams. This issue was clearly observed in the imaging section of the combined setup. The fabrication beam with a wavelength of 780 nm had longer working distance than the visible light used for imaging.

To control the position of the trapped particle in the laser propagation direction a 3D steerable trapping system was needed [169]. Afocal beam expanders can was used to control the position of the trapped particle by changing the parallel beams entering the objective lens back aperture. If diverging beams enter the objective lens, the working distance of the objective lens reduces and vice versa. Using this technique, it was possible to place the trapped particle close to the polymerization area. The new trapping system increased the potential application of the combined setup and relaxed the wavelength limitations of the combined setup. Researchers can use different wavelengths for the polymerization of a variety of photoresist without changing the trapping beam

wavelength. It is also possible to fix the polymerization wavelength and choose the most appropriate wavelength for trapping the objects suspended in the photoresist.

Therefore the setup was rebuilt to utilise single objective lens for both trapping and polymerization. The new combined system was assembled based on an inverted microscope setup. The inverted microscope setup reduced the vibration in the system and decreased the number of optical elements in the optical chain. The assembled system produced the best results comparing to the previous versions of the system but it still had some shortcoming that will be addressed in the section 7.1 (future work).

To be able to use the inverted setup custom coverslip mounts were designed and printed. The designed mounts allow the user to use the normal microscope slide mount supplied with the system with 170 µm Zeiss number 1 coverslips. Using the printed coverslip mount it was possible to sandwich the combined system photoresist between two coverslips and separate the sample from the room environment. This was particularly important because the fabrication process was undertaken in normal room environment.

Another advantage of the designed coverslip mount was the ease of access to the fabricated sample. Microfluid channels used for optical trapping experiments and sample holders produced using double sided sticky tape makes post-fabrication processing steps very risky and complicated. Often the coverslip (substrate) breaks before being removed from the sample.

After realigning and rebuilding the combined setup the performance of the setup was tested. In Figure 61, it was demonstrated that the minimum laser power that initiated polymerization was 5.78 mW with a repetition rate of 80 MHz and exposure time of 100 ms, 8×10^6 pulses were used to polymerise the smallest voxel in Figure 61. During this experiment, the laser pulse energy was$E_p = 0.0722\text{e} - 9$ J. The 100X oil-immersion objective lens used in this experiment produces a spot size of 732 nm for the radiation wavelength used in the experiment. The energy density used to polymerise the resin was 5.29 KJ/cm^2, which is in the expected range for MPP [79], [218], [219]. It is also possible to

control the exposure time using the stage travel speed. Two-dimensional patterns can be fabricated by moving the sample with a steady speed while the laser shutter is open. The structure in Figure 70 was fabricated using the scanning speed of 20 μm/s and laser power of 14.55 mW. The fabrication speed and laser power was experimentally optimized to produce best possible structure in the shortest fabrication time. The longitudinal feature sizes are usually larger than the transverse dimension of the voxels [10]. Figure 42 shows high-resolution SEM picture of these voxels. Using high scanning speed decreases the minimum feature size of the setup and increases the usual aspect ratio of 3:1 [10] to greater a number. Therefore, it is not possible to fabricate freestanding structures and the structures fall to the substrate. Figure 87 shows a fishnet structure fabricated using higher stage travel speed (30 μm/s and step size of 5 μm). It is possible to increase the laser power to compensate for the shorter exposure time but, it increases the chance of bubble formation. In the combined setup the Stokes' drag force generated by the particle movement in the resin is another limiting factor for the stage travel speed.

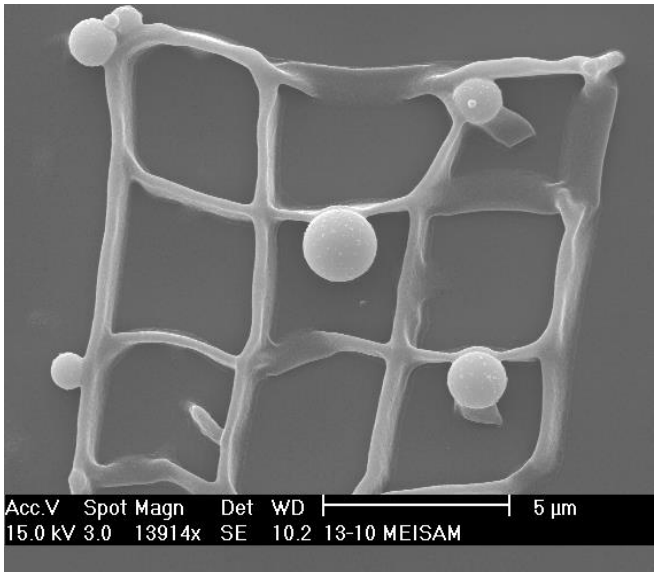


Figure 87. Fishnet structure fabricated using the stage scanning speed of 30 μm/s. Freestanding walls fabricated in this experiment collapsed under their own weight.

By defining the polymerization laser intensity and the stage scanning speed the combine, setup was used to fabricate composite structures and embed particles inside the polymer structure. 2D structures presented in the section 5.1 were fabricated by producing fishnet structures using the stage software and immobilizing the particles in the openings of the fabricated structure. The stage

speed defines the wall thickness for the fishnet structure and the transportation speed of the particles in the photoresist.

6.3.2 Fabrication of multilayered composite structures using Combined OT-MPP

One of the main objectives of this project was to combine an MPP setup with an OT to be able to manipulate particles in the polymerization vat and produce a composite structure. Figure 88 demonstrates an example of the composite structure that we envisioned to build. In Figure 88 an array of particles (Black) are embedded in a polymer structure (transparent). This prototype ($10 \times 10 \times 6cm$) was printed using Objet260 3D printer. During this project, it was tried to fabricate similar structure in micron length scale.

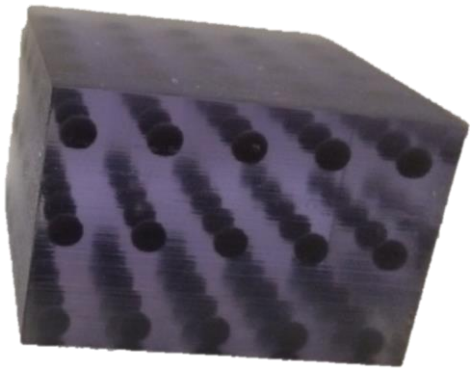


Figure 88. Multimaterial 3D printed cube printed using Objet 260 multimaterial printer. A 3D array of flexible black spheres was placed inside the rigid transparent plastic cube.

Based on the literature the particle properties and spacing between particles can potentially affect the optical, electrical and mechanical properties of the cube [199][220]. Figure 81 is one of the best examples of the samples produced during this PhD. In the SEM picture in Figure 81, 23 particles were embedded in / on the polymer solidified using MPP. These particles are placed in two tiers and represent two major crystal structures. On the left-hand side of the structure the particles follow a Body-Centered Cubic (BCC) crystal structure with one particle in the middle of 4 particles from the previous layer. On the right-hand

side, one particle is placed between two particles from the previous tier, which resembles the Face-Centered Cubic (FCC) crystal structure.

In the hybrid structures fabricated using the combined setup, 3 μm melamine resin based particles are placed 5 μm apart in the first layer. TOF-SIMS and fluorescent confocal microscopy were used to look inside the fabricated structures. The images taken using these techniques revealed that the particles inside the polymer retain their intended pattern.

Polymer adhesion is a complex phenomenon that depends on surface chemistry and free energy, polymer chemistry and molecular weight [221]. Different techniques were used to increase the polymer adhesion which was critical for larger structures.

The first approach was based on the fabrication of a fishnet pattern on a glass substrate underneath the structure. Based on the literature the polymer adhesion to the substrate can be increased by placing a layer of polymer on top of the glass substrate. Spin coating and UV curing have been used to coat the glass substrate with a thin layer of the polymer [210]. In this experiment the fabrication area was limited to tens of microns and the substrate surface morphology was crucial. An Inkjet printer was used to print a layer of PEGDA on the substrate. The high surface roughness of the inkjet printed layer made it an undesirable substrate. MPP was used to produce a base layer for the composite structures. The piezoelectric stage raster scanning function was used to generate a fishnet structure as a base for the composite structure. The fishnet structure increases the surface contact between the substrate and the composite structure. Figure 89 shows the fishnet structure fabricated before building the composite structure.

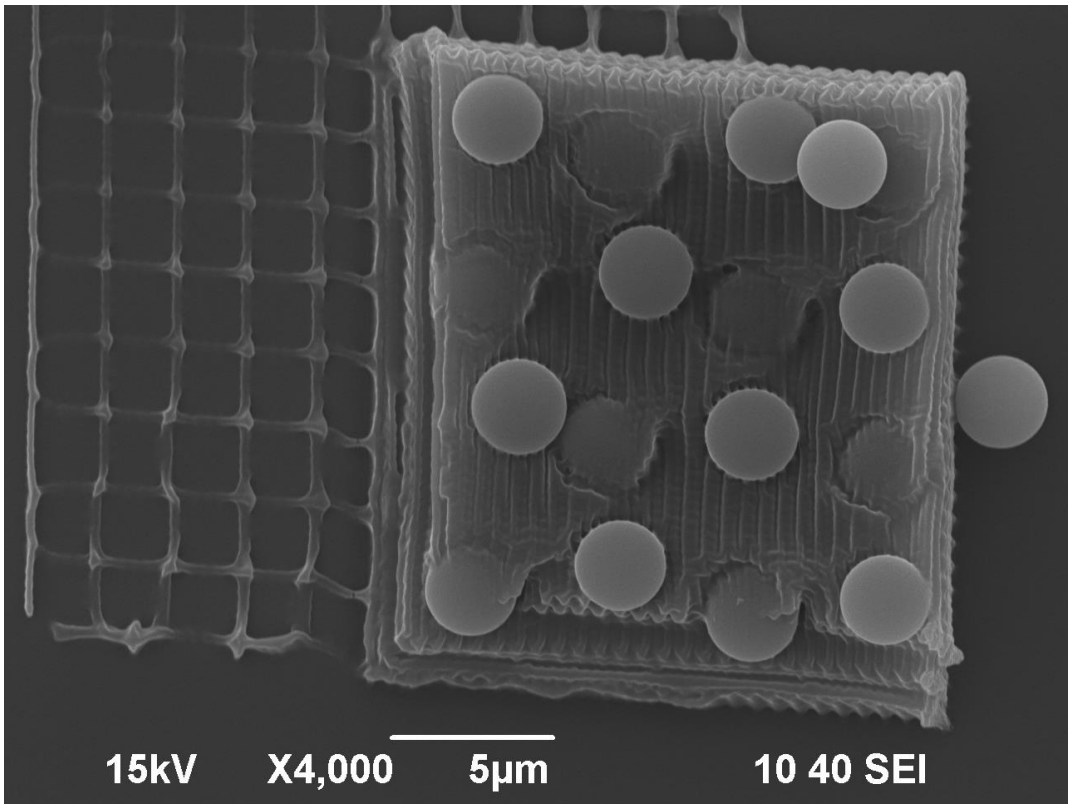


Figure 89. A composite structure fabricated on top of a fishnet structure. The fishnet structure was built to increase the surface adhesion of the samples.

Another approach to increasing the surface adhesion was to use plasma cleaning to clean the glass substrates. Oxidative cleaning of the coverslips can increase the polymer adhesion to the coverslips. There are different procedures like plasma cleaning or piranha that can be used. In this project plasma cleaning was used to clean the coverslips. Deposition technique (surface functionalization) is another approach that can increase the polymer adhesion. Adhesion performance of a polymer to the glass coverslip can be improved by deposition of suitable organosilane primer [222]. The protocol used for Silane deposition is as follow:

1) Coverslips were washed thoroughly and dried.
2) Plasma cleaner was used to clean the coverslips.
3) Cleaned coverslips immersed in 1 % silane in anhydrous toluene for 1 hour.
4) Coverslips removed from the solution, washed using isopropanol and blow dried using dry nitrogen
5) Coverslips were baked for 1 hour at 120ºC.

The above-mentioned protocol was followed for a small batch of samples. Comparing the results achieved by oxidative cleaning (10 minutes in plasma

cleaner) and the deposition technique brought us to the conclusion that the lengthy deposition technique is unnecessary.

As it was explained in the material section (Section 3.5), the combined setup photoresist was prepared using an equal volume of PEGDA Mn575 g/mol and PEGDA Mn200 g/mol. The lower molecular weight PEGDA reduces the viscosity of the prepared photoresist, and higher molecular weight PEGDA increases the surface adhesion of the polymer the effect of molecular weight of the adhesion strength [221]. Despite these efforts, some of the fabricated structures were washed away while removing the excess particles and liquid photoresist.

Multi-layered structures with more than 3 layers of particles were especially challenging. Larger (thicker) structures were more prone to delamination during the development, and in many cases, the fabricated structure was washed away during the development process. By increasing the number of layers, the interferences between the trapping laser beam and the fabricated composite structure reduced the trap quality. Therefore, it was not possible to accurately position the particles. The polymerization beam also attenuated while travelling through the fabricated structure. Hence, the polymerization beam intensity should be increased as the structure progresses to compensate for the losses in the structure. To solve this issue the microscope configuration can be used for the setup. In the microscope configuration, the polymerization and trapping beam will not go through the built structure, and the beam attenuation is minimum.

The excess particle and fabrication/trapping time are other issues that limit the practical application of the setup. The high resolution of MPP makes it a relatively slow technique to fabricate large structures. There are different approaches to increase the fabrication speed of the MPP setup. Using GM instead of the piezoelectric stage to position the polymerization beam and fabricate structures layer-by-layer can significantly increase the fabrication speed of the MPP setup. Another technique that can improve the fabrication

speed of MPP is the area sintering technique. Using Digital mirrors devices, spatial light modulators and microlenses expand the polymerization beam and solidify multiple points or an area at the same time.

In this experiment the stage speed is restricted by both polymerization and trapping. For the trapping section, the stage travel speed should be in a range that the Stock's drag force generated by the viscous photoresist, doesn't dislocate the trapped particle. On the polymerization side, the stage scanning speed affect the MPP feature sizes and by increasing the scanning speed smaller feature sizes with higher aspect ratio can be fabricated.

The excess particles in the photoresist are the main source of sample contamination. In this experiment, suspending the particles uniformly through the photoresist and trap particles close to the fabrication site to be encapsulated in the polymer matrix was attempted. This method is useful for small structures but going toward larger structures it increases the fabrication time of the composite structure. Using holographic optical tweezers can increase the fabrication speed of the combined setup. Labview Visualizer package can be used to automate the trapping process.

To decrease the trapping time, it is possible to produce resins with high particle density and use the optical trap to transport particles from these regions to the fabrication site. Practically the field of view of the objective lens was roughly 200 μm in this experiment and it doesn't give us enough room to have two separate regions. Another issue is particle agglomeration. High-density areas increase the chance of agglomeration, and the optical trapping cannot produce enough force to separate the particles, which formed a cluster.

During the experiments, it was desirable to have pockets of high-density particles suspended in water in the photoresist by introducing controlled number of particles directly to the photoresist. These packets were stable for short period, but it was not possible to remove the particles from the water bubbles. Therefore, uniform Suspensions of particles in the photoresist were the best

approach. Having a higher number of particles suspended in the photoresist ensures that enough particles can be found near the fabrication site and decreases the fabrication time by reducing the travel time. Decreasing the particle density in the photoresist reduces the chance of unwanted particles adhering to the fabricated structure. The particle density chosen and presented in this thesis was based on a balance between fabrication time and sample contamination. This balance was found by trying different concentration of particles in the photoresist.

Structures fabricated using the combined setup composed of polymerised PEGDA and particles (Melamine resin based or soda lime particles). Based on the Bruggeman effective material theory, spherical particles (inclusions) affect the properties of the composite structure [223]. Bruggeman theory is an effective approximation when the filling factor of the inclusion inside the polymer is high (f~ 0.4) [224]. In Figure 90, 3 μm melamine resin based particles with a refractive index of 1.68 were placed 5 μm apart from each other (centre to centre) inside a polymer cube. The cube is fabricated using PEGDA based photoresist with a refractive index of 1.47. Roughly 18.85% of the polymer cube volume has been occupied by the particles. The presence of the particle modifies the refractive index of the cube. Therefore, it increases the refractive index of the composite structure.

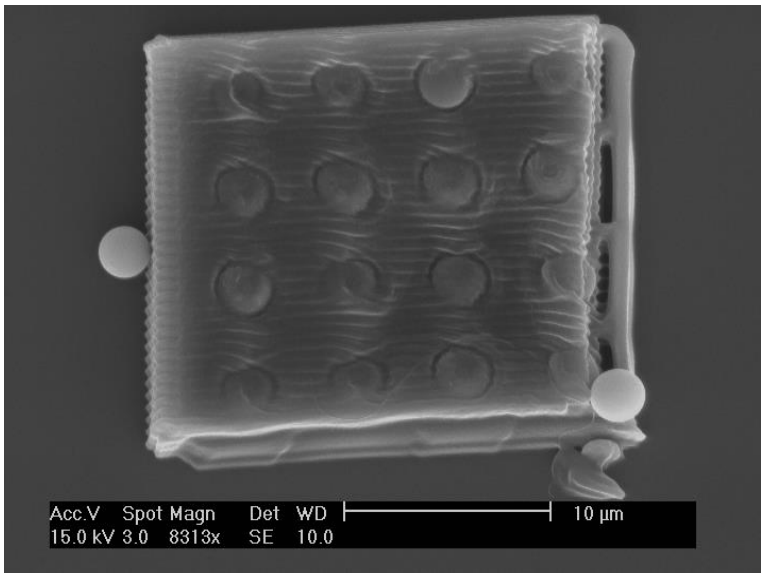


Figure 90. A 4 by 4 array of melamine resin based particles encapsulated in polymer cube.

By comparing the composite structures fabricated using the combined OT-MPP setup with previous multimaterial structures, which was mentioned in in section 6.3, it is clear, that utilising the combined setup reduces the fabrication process by eliminating the multiple rounds of sample preparation, fabrication, and development. Using this technique, it is possible to fabricate structures and place particles with properties or prefabricated structures in specific areas of the design.

The clear advantage of the assembled combine OT-MPP setup in comparison to the setups that were used in papers published by Tsai et al. and Dawood et al. is in the precise control that this system has on the position of the trapped particle. Having 3D steerable trap enables the system to place the trapped particle as close as possible to the polymerization area. This ability is critical to define the mode of operation the system. It also enables the system to use widely different wavelengths for trapping and polymerization and relaxes the limitation of the system. It is particularly important to be able to change the trapping and / or polymerization wavelengths because the polymerization efficiency and the trapping force is wavelength dependent [104], [205], [225]. The assembled combined OT-MPP setup enables the users to use to produce accurate and repeatable results regardless of the polymerization and trapping lasers wavelengths. Therefore, it is possible to use the combined OT-MPP setup with a wider verity of photoresists and particles.

The assembled combined OT-MPP setup, which has the capability of moving the trapped object in the laser propagation direction, opens the possibility of trapping and immobilisation of non-spherical objects too. The equilibrium positions of non-spherical particles are often away from the focal volume of the objective lens [226]. Therefore, the ability to move the trapped particle in Z direction can also be useful for trapping and immobilisation of the non-standard particles.

In this project the particle encapsulation in the polymer matrix was also demonstrated. The 3D multilayered composite structures fabricated in the combined OT-MPP system was tested to define the particle pattern after being encapsulated in the polymer matrix. The confocal fluorescent images presented in chapter 5 demonstrated that the particles are firmly immobilised and they hold their position during the polymerization and development.

CHAPTER 7: FUTURE STEPS & CONCLUSIONS

In this chapter future steps that can promote the combined MPP-OT setup to a commercial fabrication method for composite microstructures will be discussed. The conclusion section is the final part of this PhD thesis that briefly summarises the key findings of the project.

7.1 Future work:

To be able to increase the potential applications of the combined MPP and OT setup, a roadmap was defined to improve the combine system and the available materials used in this system.

1. Replacing the mechanical shutter of the MPP setup with an acousto-optic modulator can greatly decrease the exposure time and increase the stability of the system. Therefore, it can increase the resolution of the MPP setup.
2. Upgrading the OT system to a multi-beam trapping system using diffractive optical elements or SLM can greatly increase the trapping speed of the system and enable the system to immobilize multiple particles at the same time.
3. SLM can also be incorporated in the MPP setup to increase the polymerization speed of the MPP setup and enable the system to polymerise larger areas without reducing the resolution of the setup (area sintering using a high-resolution pattern).
4. System automation using NI Labview visualiser bundle can also increase the fabrication speed by automatically locating the particles in the photoresist and transporting them to the polymerization area.
5. Changing the trapping laser beam and the OT section of the combined setup can enable the system to trap a wider range of particles (metallic nanoparticles and carbon nanotubes).
6. Changing the configuration of the combined setup to microscope setup enable the system to fabricate on the substrate and minimize the aberration caused by the fabricated sample on the polymerization and trapping beams. This change enable the system to fabricate multi-layered

structures. During these experiments the photoresist is sandwiched between two Zeiss number 1 coverslips. The piezoelectric stage can also be replaced with a XYZ microscope stage that give us enough clearance to fabricate on the upper coverslip. In this technique after each layer the piezoelectric stage moves the sample further from the objective lens and the fabrication always occurs on the surface of the structure which is facing the objective lens. These two techniques can greatly increase the sample thickness that can be achieved using the combined setup.

7. Another critical step for the future of this project is the development of new combined setup photoresist. The photoresist developed during this project demonstrated the abilities of the system, but for practical applications, the gap between the refractive index of particles and the polymer must be wider.

One of the possible applications of this setup is in the fabrication of 3D photonic crystals. Photonic crystals are one of the attractive topics in optical communities. Photonic crystal works based on a consecutive change in the optical properties of the medium that the light is propagating through [199]. MPP has been used for fabrication of air gapped photonic crystals, but the refractive index of polymers are not adequate to produce the needed refractive index contrast for complete stop band [8]. Therefore, high refractive index materials are being incorporated into the polymer to increase the refractive index of the polymer [8][95]. It has been suggested that the needed contrast in the refractive index of solid vs air for generation of complete stop band is roughly 1.9 units [93][227]. In this approached the high refractive index material is mixed with the polymer, and there is no control on the placement of the high refractive index particle. Using optical tweezers enable the system to pick and place every single particle to produce a highly tailored array of optical potentials to interact with the propagating light. It is also possible to introduce defects in the system that can be used for system identification [228].

.

7.2 Conclusion

This thesis detailed the design and assembly process of OT and MPP setup was presented. The MPP setup was used to fabricate different structures using commercial and custom photoresists. The MPP fabricated structures were tested using BFM and SEM and optimum fabrication speed, exposure time and laser power were defined. LabVIEW driver software was developed to enable the MPP setup to fabricate multilayered complex structures using 3D objects designed digitally (CAD file). Completion of MPP setup and the LabVIEW software was one of the significant achievements of this project.

OT setup was the second system that was assembled and tested during this PhD project. The OT system was tested extensively using dielectric and metallic particles to establish the capabilities of the OT setup. The basic OT setup was upgraded with GM and the Galilean beam expander used in the OT was replaced with a Keplerian beam expander that facilitates the change in laser trajectory and 2D control of the trap in the objective lens field of view. A number of LabVIEW software were developed to fully utilise the capabilities of the OT system and produce a user interface for the OT setup to control the imaging and GM sections simultaneously.

After separately assembling and testing each setup, the combined OT-MPP setup was designed and assembled. Different iterations of the system were assembled and tested to achieve reliable and accurate system. The final iteration of the setup, which is unique setup that utilises afocal beam expander, enables incorporation of trapped particles in the MPP fabricated polymer matrix.

To test the combined OT-MPP setup array of particles (up to 30 particles) were transported and immobilised using the system in a predefined arrangement. 3D capabilities of the system were tested by fabricated a step structure and placing 3 particles on each step.

During this project, different particles were trapped and encapsulated in the polymer matrix. The particle placement and encapsulation for fabrication of 3D hybrid objects were done by simultaneous utilisation of MPP and OT section of the combined OT-MPP setup. Using the combined OT-MPP system accurate 3D particle placement was achieved for fabricated samples and particles with different properties were incorporated in various layers of the structures. Testing composite structures and defining the particle arrangement after developing the samples was done using confocal fluorescent microscopy and TOF-SIMS. Both techniques demonstrated the presence of particles inside the polymer structure. The qualitative data gathered from confocal fluorescent microscopy images demonstrated that the particles retain their original positions during encapsulation and development.

The aim of this project was to build metamaterial structures using AM. The meta-atoms, which are the building blocks of most metamaterials, are far smaller than the metamaterial operation frequency. To be able to fabricate metamaterial structures there was a need for a high-resolution multimaterial AM technique. Therefore, the efforts in this project were directed toward assembling the combined OT-MPP setup as a technique that has the potential to fabricate metamaterials. Photonic crystals are a class of metamaterials that have feature sizes comparable to their intended operating frequency. Consequently, the project attention was mainly focused on fabrication of photonic crystals.

The results presented in this work demonstrate the potential of the combined OT-MPP setup to fabricate complex composite microstructures. Combined OT-MPP could be a versatile technique that revolutionises the future of microfabrication. The ability to accurately pick and place particles and component and spot-weld them to the desired position can be beneficial in different disciplines.

The combined setup can be used in the fabrication of future optical communication and computation circuit boards. This technique can place active optical elements on the optical circuits and immobilise them in place. In a simple

term, MPP polymerization can be the equivalent of soldering but for optical circuits. Using this technique instead of using machinery to transport and handle sensitive optical components the OT section of the setup can transport these parts.

REFERENCES

[1] S. L. N. Ford, "Additive Manufacturing Technology : Potential Implications for U . S . Manufacturing Competitiveness," *J. Int. Commer. Econ.*, vol. 6, no. September, pp. 1–35, 2014.

[2] N. Hopkinson, *Rapid Manufacturing: An Industrial Revolution for the Digital Age*. John Wiley & Sons, 2006.

[3] R. F. Housholder, "Patent US4247508," 1979.

[4] T. Campbell, C. Williams, O. Ivanova, and B. Garret, "Could 3D Printing Change the World? Technologies, Potential, and Implications of Additive Manufacturing," *Technologies, Potential, and Implications of Additive Manufacturing*, p. 16, 2011.

[5] H. Wijshoff, "The dynamics of the piezo inkjet printhead operation," *Phys. Rep.*, vol. 491, no. 4–5, pp. 77–177, 2010.

[6] S. J. Leigh, R. J. Bradley, C. P. Purssell, D. R. Billson, and D. A. Hutchins, "A Simple, Low-Cost Conductive Composite Material for 3D Printing of Electronic Sensors," *PLoS One*, vol. 7, no. 11, p. e49365, Nov. 2012.

[7] M. Vaezi, H. Seitz, and S. Yang, "A review on 3D micro-additive manufacturing technologies," *Int. J. Adv. Manuf. Technol.*, vol. 67, no. 5–8, pp. 1721–1754, 2013.

[8] S. Maruo and J. T. Fourkas, "Recent progress in multiphoton microfabrication," *Laser Photonics Rev.*, vol. 2, no. 1–2, pp. 100–111, Apr. 2008.

[9] F. Jipa, M. Zamfirescu, A. Velea, M. Popescu, and R. Dabu, "Femtosecond Laser Lithography in Organic and Non- Organic Materials," *InTech*, 2013.

[10] L. Li and J. T. Fourkas, "Multiphoton polymerization," *Mater. Today*, vol. 10, no. 6, pp. 30–37, 2007.

[11] A. Boltasseva and V. M. Shalaev, "Fabrication of optical negative-index metamaterials: Recent advances and outlook," *Metamaterials*, vol. 2, no. 1, pp. 1–17, May 2008.

[12] T. Wohlers and T. Caffrey, *Additive manufacturing and 3D printing state of the industry annual worldwide progress report. 2014*. Wohlers Associates, 2013.

[13] M. Vaezi, S. Chianrabutra, B. Mellor, and S. Yang, "Multiple material additive manufacturing – Part 1: a review," *Virtual Phys. Prototyp.*, vol. 8, no. 1, pp. 19–50, 2013.

[14] L. R. Hart, S. Li, C. Sturgess, R. Wildman, J. R. Jones, and W. Hayes, "3D Printing of Biocompatible Supramolecular Polymers and their Composites," *ACS Appl. Mater. Interfaces*, vol. 8, no. 5, pp. 3115–3122, Feb. 2016.

[15] F. Zhang, C. Tuck, R. Hague, Y. He, E. Saleh, Y. Li, C. Sturgess, and R. Wildman, "Inkjet printing of polyimide insulators for the 3D printing of dielectric materials for microelectronic applications," *J. Appl. Polym. Sci.*, vol. 133, no. 18, pp. 43361–43372, 2016.

[16] C. Zhou, Y. Chen, Z. Yang, and B. Khoshnevis, "Development of a Multi-material Mask-Image-Projection-based Stereolithography for the Fabrication of Digital Materials," *Annu. Solid Free. Fabr. Symp.*, pp. 65–80, 2011.

[17] A. Inamdar, M. Magana, F. Medina, Y. Grajeda, and R. Wicker, "Development of an Automated Multiple Material Stereolithography Machine," *Proc. 17th Annu. Solid Free. Fabr. Symp. Austin, TX*, no. Lm, pp. 624–635, 2006.

[18] F. Klein, B. Richter, T. Striebel, C. M. Franz, G. Von Freymann, M. Wegener, and M. Bastmeyer, "Two-component polymer scaffolds for controlled three-dimensional cell culture," *Adv. Mater.*, vol. 23, no. 11, pp. 1341–1345, Mar. 2011.

[19] S. Rekštyte, E. Kaziulionyte, E. Balčiunas, D. Kaškelyte, and M.

Malinauskas, “Direct laser fabrication of composite material 3D microstructured scaffolds,” *J. Laser Micro Nanoeng.*, vol. 9, no. 1, pp. 25–30, 2014.

[20] E. Blasco, J. M??ller, P. M??ller, V. Trouillet, M. Sch??n, T. Scherer, C. Barner-Kowollik, and M. Wegener, “Fabrication of Conductive 3D Gold-Containing Microstructures via Direct Laser Writing,” *Adv. Mater.*, vol. 28, no. 18, pp. 3592–3595, 2016.

[21] A. Ishikawa, T. Tanaka, and S. Kawata, “Improvement in the reduction of silver ions in aqueous solution using two-photon sensitive dye,” *Appl. Phys. Lett.*, vol. 89, no. 11, pp. 79–82, 2006.

[22] T. Tanaka, A. Ishikawa, and S. Kawata, “Two-photon-induced reduction of metal ions for fabricating three-dimensional electrically conductive metallic microstructure,” *Appl. Phys. Lett.*, vol. 88, no. 8, p. 81107, 2006.

[23] C. N. LaFratta, J. T. Fourkas, T. Baldacchini, and R. A. Farrer, “Multiphoton fabrication,” *Angewandte Chemie - International Edition*, vol. 46, no. 33. WILEY- VCH Verlag, pp. 6238–6258, 20-Aug-2007.

[24] M. M. Hossain and M. Gu, “Fabrication methods of 3D periodic metallic nano/microstructures for photonics applications,” *Laser Photonics Rev.*, vol. 8, no. 2, pp. 233–249, 2014.

[25] G. A. Niklasson, C. G. Granqvist, and O. Hunderi, “Effective medium models for the optical properties of inhomogeneous materials,” *Appl. Opt.*, vol. 20, no. 1, p. 26, 1981.

[26] D. A. G. Bruggeman, “Berechnung verschiedener physikalischer Konstanten von heterogenen Substanzen. III. Die elastischen Konstanten der quasiisotropen Mischk??rper aus isotropen Substanzen,” *Ann. Phys.*, vol. 421, no. 2, pp. 160–178, 1937.

[27] J. C. M. Garnett, “Colours in Metal Glasses, in Metallic Films, and in Metallic Solutions. II,” *Philos. Trans. R. Soc. A Math. Phys. Eng. Sci.*, vol.

205, no. 387–401, pp. 237–288, Jan. 1906.

[28] F. Dawood, S. Qin, L. Li, E. Y. Lin, and J. T. Fourkas, "Simultaneous microscale optical manipulation, fabrication and immobilisation in aqueous media," *Chem. Sci.*, vol. 3, no. 8, p. 2449, 2012.

[29] Y. C. Tsai, K. H. Leitz, R. Fardel, M. Schmidt, and C. B. Arnold, "Generating Nanostructures with Multiphoton Absorption Polymerization using Optical Trap Assisted Nanopatterning," *Phys. Procedia*, vol. 39, pp. 669–673, Jan. 2012.

[30] K. H. Leitz, Y. C. Tsai, F. Flad, E. Schäffer, U. Quentin, I. Alexeev, R. Fardel, C. B. Arnold, and M. Schmidt, "Multiphoton polymerization using optical trap assisted nanopatterning," *Appl. Phys. Lett.*, vol. 102, no. 24, p. 243108, 2013.

[31] J. Thompson, "Microbead-based biosensing in microfluidic devices," Publicly accessible Penn Dissertation, 2011.

[32] S. Waheed, J. M. Cabot, N. P. Macdonald, T. Lewis, R. M. Guijt, B. Paull, and M. C. Breadmore, "3D printed microfluidic devices: enablers and barriers," *Lab Chip*, vol. 16, no. 11, pp. 1993–2013, 2016.

[33] E. W. Seelig, B. Tang, A. Yamilov, H. Cao, and R. P. H. Chang, "Self-assembled 3D photonic crystals from ZnO colloidal spheres," *Mater. Chem. Phys.*, vol. 80, no. 1, pp. 257–263, 2003.

[34] H. Nakamura, "Colloidal Crystals-Self-Assembly of Monodispersed Colloidal Particles," *Rev. Toyota CRDL*, vol. 39, no. 4, pp. 33–39, 2004.

[35] A. I. Barreda, H. Saleh, A. Litman, F. Gonzalez, J.-M. Geffrin, and F. Moreno, "Electromagnetic polarization controlled perfect switching effect with high refractive index dimers. the beam-splitter configuration," *Nat. Commun.*, pp. 1–28, 2016.

[36] B. L. V. Prasad, C. M. Sorensen, and K. J. Klabunde, "Gold nanoparticle superlattices," *Chem. Soc. Rev.*, vol. 37, no. 9, p. 1871, 2008.

[37] Gordon E. Moore, "Progress In Digital Integrated Electronics," *IEDM*

Tech. Digest, 1975. [Online]. Available: http://ww.w.lithoguru.com/scientist/CHE323/Moore1975.pdf. [Accessed: 29-Oct-2015].

[38] S.-H. Hsu, S.-P. Fang, I. H. Huang, B. S. Lin, and K.-C. Hung, "Extension of ArF Lithography for poly gate patterning of 65-nm generation and beyond," in *Microlithography 2004*, 2004, pp. 1214–1224.

[39] S. Peng, R. H. French, W. M. Qiu, R. C. Wheland, M. Yang, M. F. Lemon, and M. K. Crawford, "Second generation fluids for 193 nm immersion lithography," *Opt. Microlithogr. {XVIII}, Pts 1-3*, vol. 5754, pp. 427–434, 2005.

[40] W. Ehrfeld and H. Lehr, "Deep X-ray lithography for the production of three-dimensional microstructures from metals, polymers and ceramics," *Radiat. Phys. Chem.*, vol. 45, no. 3, pp. 349–365, Mar. 1995.

[41] A. N. Broers, A. C. F. Hoole Andrew C.F, and J. M. Ryan, "Electron beam lithography - Resolution limits," *Microelectron. Eng.*, vol. 32, no. 1–4 SPEC. ISS., pp. 131–142, Sep. 1996.

[42] K. Liu, P. Avouris, J. Bucchignano, R. Martel, S. Sun, and J. Michl, "Simple fabrication scheme for sub-10 nm electrode gaps using electron-beam lithography," *Appl. Phys. Lett.*, vol. 80, no. 5, pp. 865–867, Feb. 2002.

[43] Y.-T. Chen, T.-N. Lo, Y. S. Chu, J. Yi, C.-J. Liu, J.-Y. Wang, C.-L. Wang, C.-W. Chiu, T.-E. Hua, Y. Hwu, Q. Shen, G.-C. Yin, K. S. Liang, H.-M. Lin, J. H. Je, and G. Margaritondo, "Full-field hard x-ray microscopy below 30 nm: a challenging nanofabrication achievement.," *Nanotechnology*, vol. 19, no. 39, p. 395302, Oct. 2008.

[44] D. a Tichenor, G. D. Kubiak, M. E. Malinowski, R. H. Stulen, S. J. Haney, K. W. Berger, L. a Brown, R. R. Freeman, W. M. Mansfield, O. R. Wood Ii, D. M. Tennant, J. E. Bjorkholm, a a Macdowell, J. Bokor, T. E. Jewell, D. L. White, D. L. Windt, and W. K. Waskiewicz, "Diffraction-limited soft-x-ray projection imaging using a laser plasma source.," *Opt. Lett.*,

vol. 16, no. 20, pp. 1557–9, Oct. 1991.

[45] X. Zhou, Y. Hou, and J. Lin, "A review on the processing accuracy of two-photon polymerization," *AIP Adv.*, vol. 5, no. 3, 2015.

[46] K. Ikuta, K. Hirowatari, and T. Ogata, "Three dimensional micro integrated fluid systems (MIFS) fabricated\nby stereo lithography," *Proc. IEEE Micro Electro Mech. Syst. An Investig. Micro Struct. Sensors, Actuators, Mach. Robot. Syst.*, pp. 1–6, 1994.

[47] S. N. K. S. Shoji Satoru, "Photofabrication of a photonic crystal using interference of UV laser," in *Proceedings of SPIE - The International Society for Optical Engineering*, 1999, vol. 3740, pp. 541–544.

[48] J. Neumann, K. S. Wieking, and D. Kip, "Direct laser writing of surface reliefs in dry, self-developing photopolymer films.," *Appl. Opt.*, vol. 38, no. 25, pp. 5418–21, Sep. 1999.

[49] M. Thiel, J. Fischer, G. Von Freymann, and M. Wegener, "Direct laser writing of three-dimensional submicron structures using a continuous-wave laser at 532 nm," *Appl. Phys. Lett.*, vol. 97, no. 22, p. 221102, Nov. 2010.

[50] X. Zhang, X. N. Jiang, and C. Sun, "Micro-stereolithography of polymeric and ceramic microstructures," *Sensors Actuators, A Phys.*, vol. 77, no. 2, pp. 149–156, 1999.

[51] J. C. A. A. Bertsch, S. Zissi, J. Y. Jézéquel, S. Corbel, "Microstereophotolithography using a liquid crystal display as dynamic mask-generator," *Microsyst. Technol.*, vol. 3, no. 2, pp. 42–47, Feb. 1997.

[52] A. Bertsch, J. Y. Jézéquel, and J. C. André, "Study of the spatial resolution of a new 3D microfabrication process: the microstereophotolithography using a dynamic mask-generator technique," *J. Photochem. Photobiol. A Chem.*, vol. 107, no. 1–3, pp. 275–281, 1997.

[53] T. Takagi and N. Nakajima, "Photoforming applied to fine

machining," *[1993] Proc. IEEE Micro Electro Mech. Syst.*, pp. 173–178, 1993.

[54] L. Beluze, A. Bertsch, and P. Renaud, "Microstereolithography: a new process to build complex 3D objects," *Des. Test, Microfabr. Mems Moems, Pts 1 2*, vol. 3680, no. April, pp. 808–817, Mar. 1999.

[55] K. Subramanian, N. Vail, J. Barlow, and H. Marcus, "Selective laser sintering of alumina with polymer binders," *Rapid Prototyp. J.*, vol. 1, no. 2, pp. 24–35, Jun. 1995.

[56] P. Regenfuss, L. Hartwig, S. Klötzer, R. Ebert, and H. Exner, "Microparts by a Novel Modification of Selective Laser Sintering," *Rapid Prototyp. Manuf. Conf.*, pp. 1–7, 2003.

[57] I. Gibson, D. Rosen, and B. Stucker, "Direct Write Technologies," in *Additive Manufacturing Technologies*, New York, NY: Springer New York, 2015, pp. 269–291.

[58] J. Gaspar, P. J. Bartolo, and F. M. Duarte, "Cure and Rheological Analysis of Reinforced Resins for Stereolithography," in *Advanced Materials Forum Iv*, 2008, vol. 587–588, pp. 563–567.

[59] M. Hedges and A. B. Marin, "3D Aerosol Jet® Printing - Adding Electronics Functionality to RP/RM," in *WHITEPAPER - Optomec*, 2012, pp. 14–15.

[60] M. J. Renn, B. H. King, J. S. Leal, S. K. Pangrle, V. Circuits, and S. Valley, "Aerosol Jet ® Printing of High Density, 3-D Interconnects for Multi-Chip Packaging," *Wire*, pp. 3–6.

[61] OPTOMEC, "Aerosol Jet ® Printed Electronics Overview." [Online]. Available: http://www.optomec.com/wp-content/uploads/2014/04/AJ_Printed_Electronics_Overview_whitepaper.pdf. [Accessed: 08-Dec-2016].

[62] L. Hirt, S. Ihle, Z. Pan, L. Dorwling-Carter, A. Reiser, J. M. Wheeler, R. Spolenak, J. Vörös, and T. Zambelli, "Template-Free 3D Microprinting of Metals Using a Force-Controlled Nanopipette for

Layer-by-Layer Electrodeposition," *Adv. Mater.*, vol. 28, no. 12, pp. 2311–2315, 2016.

[63] M. Göppert-Mayer, "Elementary processes with two quantum transitions," *Ann. der Phys.*, vol. 18, no. 7–8, pp. 466–479, 2009.

[64] W. Kaiser and C. G. B. Garrett, "Two-photon excitation in CaF2: Eu2+," *Phys. Rev. Lett.*, vol. 7, no. 6, pp. 229–231, 1961.

[65] S. Maruo, O. Nakamura, and S. Kawata, "Three-dimensional microfabrication with two-photon-absorbed photopolymerization," *Opt. Lett.*, vol. 22, no. 2, p. 132, 1997.

[66] B. H. Cumpston, J. E. Ehrlich, S. M. Kuebler, M. Lipson, S. R. Marder, D. McCord-Maughon, J. W. Perry, H. Rockel, and M. Rumi, "Three-dimensional microfabrication using two-photon polymerization," *Mater. Device Charact. Micromach.*, vol. 3512, p. 168, 1998.

[67] K. S. Lee, D. Y. Yang, S. H. Park, and R. H. Kim, "Recent developments in the use of two-photon polymerization in precise 2D and 3D microfabrications," *Polym. Adv. Technol.*, vol. 17, no. 2, pp. 72–82, Feb. 2006.

[68] D. S., L. De, A. J. G. Otuka, V. Tribuzi, and C. R., "Two-Photon Polymerization Fabrication of Doped Microstructures," in *Polymerization*, A. D. S. Gomes, Ed. 2012.

[69] M. Farsari, M. Vamvakaki, and B. N. Chichkov, "Multiphoton polymerization of hybrid materials," *J. Opt.*, vol. 12, no. 12, p. 124001, 2010.

[70] K. S. Lee, R. H. Kim, D. Y. Yang, and S. H. Park, "Advances in 3D nano/microfabrication using two-photon initiated polymerization," *Prog. Polym. Sci.*, vol. 33, no. 6, pp. 631–681, Jun. 2008.

[71] L. Li, R. R. Gattass, E. Gershgoren, H. Hwang, and J. T. Fourkas, "Achieving /20 Resolution by One-Color Initiation and Deactivation of Polymerization," *Science (80-.).*, vol. 324, no. 5929, pp. 910–913, May 2009.

[72] S. Quabis, R. Dorn, M. Eberler, O. Gl??ckl, and G. Leuchs, "Focusing light to a tighter spot," *Opt. Commun.*, vol. 179, no. 1, pp. 1–7, 2000.

[73] S.-U. Hwang and Y.-G. Lee, "Simulation of an oil immersion objective lens: a simplified ray-optics model considering Abbe's sine condition.," *Opt. Express*, vol. 16, no. 26, pp. 21170–21183, 2008.

[74] A. Ovsianikov, "Investigation of Two-Photon Polymerization Technique for Applications in Photonics and Biomedicine," Göttingen, 2008.

[75] E. Käpylä, S. Turunen, J. Pelto, J. Viitanen, and M. Kellomäki, "Investigation of the optimal processing parameters for picosecond laser-induced microfabrication of a polymer–ceramic hybrid material," *J. Micromechanics Microengineering*, vol. 21, no. 6, p. 65033, Jun. 2011.

[76] S. Wu, J. Serbin, and M. Gu, "Two-photon polymerisation for three-dimensional micro-fabrication," *J. Photochem. Photobiol. A Chem.*, vol. 181, no. 1, pp. 1–11, Jul. 2006.

[77] L. L. Erskine, A. a Heikal, S. M. Kuebler, M. Rumi, X. Wu, S. R. Marder, and J. W. Perry, "Two-photon polymerization initiators for three-dimensional optical data storage and microfabrication," *Solid State Phys.*, vol. 398, no. March, pp. 51–54, Mar. 1999.

[78] S. A. Pruzinsky and P. V. Braun, "Fabrication and characterization of two-photon polymerized features in colloidal crystals," *Adv. Funct. Mater.*, vol. 15, no. 12, pp. 1995–2004, 2005.

[79] J. Serbin, A. Egbert, A. Ostendorf, B. N. Chichkov, R. Houbertz, G. Domann, J. Schulz, C. Cronauer, L. Fröhlich, and M. Popall, "Femtosecond laser-induced two-photon polymerization of inorganic organic hybrid materials for applications in photonics," *Opt. Lett.*, vol. 28, no. 5, pp. 301–303, Mar. 2003.

[80] J. B. Pawley, *Handbook of biological confocal microscopy*. Plenum Press, 1995.

[81] B. Tan, K. Venkatakrishnan, and A. Makaronets, "Effects of pulsewidth on two-photon polymerization," *Des. Monomers Polym.*, vol. 16, no. 2, pp. 145–150, 2013.

[82] S. H. Park, T. W. Lim, D.-Y. Yang, R. H. Kim, and K.-S. Lee, "Improvement of spatial resolution in nano-stereolithography using radical quencher," *Macromol. Res.*, vol. 14, no. 5, pp. 559–564, Oct. 2006.

[83] Z. Gan, Y. Cao, R. A. Evans, and M. Gu, "Three-dimensional deep sub-diffraction optical beam lithography with 9 nm feature size," *Nat. Commun.*, vol. 4, no. May, p. 2061, 2013.

[84] F. de C. P. Pires-de-Souza, B. Drubi Filho, L. A. Casemiro, L. da F. R. Garcia, and S. Consani, "Polymerization shrinkage stress of composites photoactivated by different light sources," *Braz. Dent. J.*, vol. 20, no. 4, pp. 319–324, 2009.

[85] J. Li, B. Jia, and M. Gu, "Engineering stop gaps of inorganic-organic polymeric 3D woodpile photonic crystals with post-thermal treatment," *Opt. Express*, vol. 16, no. 24, p. 20073, Nov. 2008.

[86] S. Maruo, K. Ikuta, and H. Korogi, "Submicron manipulation tools driven by light in a liquid," *Appl. Phys. Lett.*, vol. 82, no. 1, pp. 133–135, Dec. 2003.

[87] S. Maruo, K. Ikuta, and H. Korogi, "Force-controllable, optically driven micromachines fabricated by single-step two-photon microstereolithography," *J. Microelectromechanical Syst.*, vol. 12, no. 5, pp. 533–539, Oct. 2003.

[88] S. Maruo and H. Inoue, "Optically driven micropump produced by three-dimensional two-photon microfabrication," *Applied Physics Letters*, vol. 89, no. 14. American Institute of Physics, 02-Oct-2006.

[89] D. J. Shir, E. C. Nelson, D. Chanda, A. Brzezinski, P. V. Braun, J. A. Rogers, and P. Wiltzius, "Dual exposure, two-photon, conformal phase mask lithography for three dimensional silicon inverse

woodpile photonic crystals," *J. Vac. Sci. Technol. B, Nanotechnol. Microelectron. Mater. Process. Meas. Phenom.*, vol. 28, no. 4, pp. 783–788, Jul. 2010.

[90] T. Ergin, N. Stenger, P. Brenner, J. B. Pendry, and M. Wegener, "Three-Dimensional Invisibility Cloak at Optical Wavelengths," *Science (80-.).*, vol. 328, no. 5976, pp. 337–339, Apr. 2010.

[91] K. Kaneko, H. B. Sun, X. M. Duan, and S. Kawata, "Submicron diamond-lattice photonic crystals produced by two-photon laser nanofabrication," *Appl. Phys. Lett.*, vol. 83, no. 11, pp. 2091–2093, Sep. 2003.

[92] K. K. Seet, V. Mizeikis, S. Matsuo, S. Juodkazis, and H. Misawa, "Three-dimensional spiral-architecture photonic crystals obtained by direct laser writing," *Adv. Mater.*, vol. 17, no. 5, pp. 541–545, Mar. 2005.

[93] J. Serbin, A. Ovsianikov, and B. Chichkov, "Fabrication of woodpile structures by two-photon polymerization and investigation of their optical properties," *Opt. Express*, vol. 12, no. 21, p. 5221, 2004.

[94] Y. Murakami, C. A. Coenjarts, and C. K. Ober, "Preparation and Two-Photon Lithography of a Sulfur Containing Resin with High Refractive Index," *J. Photopolym. Sci. Technol.*, vol. 17, no. 1, pp. 115–118, Jan. 2004.

[95] X. M. Duan, H. B. Sun, K. Kaneko, and S. Kawata, "Two-photon polymerization of metal ions doped acrylate monomers and oligomers for three-dimensional structure fabrication," *Thin Solid Films*, vol. 453–454, pp. 518–521, 2004.

[96] M. Hermatschweiler, A. Ledermann, G. A. Ozin, M. Wegener, and G. Von Freymann, "Fabrication of silicon inverse woodpile photonic crystals," *Adv. Funct. Mater.*, vol. 17, no. 14, pp. 2273–2277, Sep. 2007.

[97] F. Formanek, N. Takeyasu, T. Tanaka, K. Chiyoda, A. Ishikawa, and S. Kawata, "Three-dimensional fabrication of metallic nanostructures

over large areas by two-photon polymerization," *Opt. Express*, vol. 14, no. 2, p. 800, 2006.

[98] N. Takeyasu, T. Tanaka, and S. Kawata, "Fabrication of 3D metal/polymer microstructures by site-selective metal coating," *Appl. Phys. A Mater. Sci. Process.*, vol. 90, no. 2, pp. 205–209, Oct. 2008.

[99] T. F. Scott, B. A. Kowalski, A. C. Sullivan, C. N. Bowman, and R. R. McLeod, "Two-Color Single-Photon Photoinitiation and Photoinhibition for Subdiffraction Photolithography," *Science*, vol. 324, no. 5929, pp. 913–917, 2009.

[100] S. Kawata, H.-B. Sun, T. Tanaka, and K. Takada, "Finer features for functional microdevices," *Nature*, vol. 412, no. 6848, pp. 697–698, Aug. 2001.

[101] D. Tan, Y. Li, F. Qi, H. Yang, Q. Gong, X. Dong, and X. Duan, "Reduction in feature size of two-photon polymerization using SCR500," *Appl. Phys. Lett.*, vol. 90, no. 7, p. 71106, 2007.

[102] X. Z. Dong, Z. S. Zhao, and X. M. Duan, "Improving spatial resolution and reducing aspect ratio in multiphoton polymerization nanofabrication," *Appl. Phys. Lett.*, vol. 92, no. 9, p. 91113, Mar. 2008.

[103] K. Takada, H. B. Sun, and S. Kawata, "Improved spatial resolution and surface roughness in photopolymerization- based laser nanowriting," *Appl. Phys. Lett.*, vol. 86, no. 7, pp. 1–3, Feb. 2005.

[104] J. F. Xing, X. Z. Dong, W. Q. Chen, X. M. Duan, N. Takeyasu, T. Tanaka, and S. Kawata, "Improving spatial resolution of two-photon microfabrication by using photoinitiator with high initiating efficiency," *Appl. Phys. Lett.*, vol. 90, no. 13, p. 131106, Mar. 2007.

[105] J. Fischer, G. von Freymann, and M. Wegener, "The Materials Challenge in Diffraction-Unlimited Direct-Laser-Writing Optical Lithography," *Adv. Mater.*, vol. 22, no. 32, pp. 3578–3582, Aug. 2010.

[106] Y. Cao, Z. Gan, B. Jia, R. A. Evans, and M. Gu, "High-photosensitive

resin for super-resolution direct-laser-writing based on photoinhibited polymerization," *Opt. Express*, vol. 19, no. 20, p. 19486, Sep. 2011.

[107] R. Wollhofen, J. Katzmann, C. Hrelescu, J. Jacak, and T. A. Klar, "120 nm resolution and 55 nm structure size in STED-lithography," *Opt. Express*, vol. 21, no. 9, p. 10831, May 2013.

[108] H. B. Sun, T. Suwa, K. Takada, R. P. Zaccaria, M. S. Kim, K. S. Lee, and S. Kawata, "Shape precompensation in two-photon laser nanowriting of photonic lattices," *Appl. Phys. Lett.*, vol. 85, no. 17, pp. 3708–3710, Oct. 2004.

[109] C. Y. Liao, M. Bouriauand, P. L. Baldeck, J. C. Ĺon, Ć. Masclet, and T. T. Chung, "Two-dimensional slicing method to speed up the fabrication of micro-objects based on two-photon polymerization," *Appl. Phys. Lett.*, vol. 91, no. 3, p. 33108, Jul. 2007.

[110] T. Tanaka, H. B. Sun, and S. Kawata, "Rapid sub-diffraction-limit laser micro/nanoprocessing in a threshold material system," *Appl. Phys. Lett.*, vol. 80, no. 2, pp. 312–314, Jan. 2002.

[111] E. R. Dufresne and D. G. Grier, "Optical tweezer arrays and optical substrates created with diffractive optics," *Rev. Sci. Instrum.*, vol. 69, no. 5, pp. 1974–1977, 1998.

[112] K. C. Neuman and S. M. Block, "Optical trapping," *Rev. Sci. Instrum.*, vol. 75, no. 9, pp. 2787–2809, Sep. 2004.

[113] S. P. Smith, S. R. Bhalotra, A. L. Brody, B. L. Brown, E. K. Boyda, and M. Prentiss, "Inexpensive optical tweezers for undergraduate laboratories," *Am. J. Phys.*, vol. 67, no. 1, pp. 26–35, 1999.

[114] J. Mas, A. Farré, J. Cuadros, I. Juvells, and A. Carnicer, "Understanding optical trapping phenomena: A simulation for undergraduates," *IEEE Trans. Educ.*, vol. 54, no. 1, pp. 133–140, 2011.

[115] A. Rohrbach and E. H. K. Stelzer, "Trapping forces, force constants,

and potential depths for dielectric spheres in the presence of spherical aberrations," *Appl. Opt.*, vol. 41, no. 13, p. 2494, May 2002.

[116] L. P. Ghislain, N. A. Switz, and W. W. Webb, "Measurement of small forces using an optical trap," *Rev. Sci. Instrum.*, vol. 65, no. 9, pp. 2762–2768, Sep. 1994.

[117] F. Gittes and C. F. Schmidt, "Signals and Noise in Micromechanical Measurements," in *Methods in Cell Biology*, vol. 55, 1997, pp. 129–156.

[118] F. Gittes and C. F. Schmidt, "Interference model for back-focal-plane displacement detection in optical tweezers," *Opt. Lett.*, vol. 23, no. 1, p. 7, Jan. 1998.

[119] A. Pralle, M. Prummer, E. L. Florin, E. H. K. Stelzer, and J. K. H. Hörber, "Three-dimensional high-resolution particle tracking for optical tweezers by forward scattered light," *Microsc. Res. Tech.*, vol. 44, no. 5, pp. 378–386, Mar. 1999.

[120] H. Zhang and K.-K. Liu, "Optical tweezers for single cells," *J. R. Soc. Interface*, vol. 5, no. 24, pp. 671–690, Jul. 2008.

[121] P. C. Ke and M. Gu, "Characterization of trapping force on metallic Mie particles," *Appl. Opt.*, vol. 38, no. 1, p. 160, Jan. 1999.

[122] K. Svoboda and S. M. Block, "Optical trapping of metallic Rayleigh particles," *Opt. Lett.*, vol. 19, no. 13, p. 930, Jul. 1994.

[123] A. Ashkin, "Acceleration and Trapping of Particles by Radiation Pressure," *Phys. Rev. Lett.*, vol. 24, no. 4, pp. 156–159, Jan. 1970.

[124] A. Ashkin and J. M. Dziedzic, "Optical levitation by radiation pressure," *Appl. Phys. Lett.*, vol. 19, no. 8, pp. 283–285, Oct. 1971.

[125] A. Ashkin, J. M. Dziedzic, J. E. Bjorkholm, and S. Chu, "Observation of a single-beam gradient force optical trap for dielectric particles," *Opt. Lett.*, vol. 11, no. 5, p. 288, 1986.

[126] K. Sengstock and W. Ertmer, "Laser Manipulation of Atoms," *Adv. At.*

Mol. Opt. Phys., vol. 35, no. C, pp. 1–44, Dec. 1995.

[127] A. Ashkin, J. M. Dziedzic, and T. Yamane, "Optical trapping and manipulation of single cells using infrared laser beams," *Nature*, vol. 330, no. 6150, pp. 769–771, Jan. 1987.

[128] A. Jurado, J. Kiggins, and P. Bggn, "Polystyrene Bead Size Behavior in Optical Trapping," *Spring*, 2010.

[129] C. Schmitz, J. Spatz, and J. Curtis, "High-precision steering of multiple holographic optical traps.," *Opt. Express*, vol. 13, no. 21, pp. 8678–8685, Oct. 2005.

[130] F. Hajizadeh and S. N. S.Reihani, "Optimized optical trapping of gold nanoparticles," *Opt. Express*, vol. 18, no. 2, p. 551, Jan. 2010.

[131] T. Li, "Fundamental Tests of Physics with Optically Trapped Microspheres," in *Fundamental Tests of Physics with Optically Trapped Microspheres*, Springer, 2013, pp. 9–21.

[132] G. Gouesbet, "Generalized lorenz-mie theory and applications," *Part. Part. Syst. Charact.*, vol. 11, no. 1, pp. 22–34, Feb. 1994.

[133] K. Ramser, "Applications of Raman spectroscopy to biology," in *IOS Press*, IOS Press, 2012, pp. 417–428.

[134] N. B. Simpson, L. Allen, and M. J. Padgett, "Optical tweezers and optical spanners with Laguerre–Gaussian modes," *J. Mod. Opt.*, vol. 43, no. 12, pp. 2485–2491, Dec. 1996.

[135] Daryl Preece, "Novel Uses of Spatial Light Modulators in Optical Tweezers," Glasgow, 2011.

[136] D. G. Grier, "A revolution in optical manipulation," *Nature*, vol. 424, no. 6950, pp. 810–816, 2003.

[137] L. Allen, M. J. Padgett, and M. Babiker, "The Orbital Angular Momentum Of Light," *Progress In Optics: Vol XXXIX 39*. ELSEVIER SCIENCE, pp. 291–372, 31-Aug-1999.

[138] Y. Seol, A. E. Carpenter, and T. T. Perkins, "Gold nanoparticles: enhanced optical trapping and sensitivity coupled with significant heating," *Opt. Lett.*, vol. 31, no. 16, p. 2429, 2006.

[139] L. Bosanac, T. Aabo, P. M. Bendix, and L. B. Oddershede, "Efficient optical trapping and visualization of silver nanoparticles," *Nano Lett.*, vol. 8, no. 5, pp. 1486–1491, 2008.

[140] A. Ashkin, "Applications of Laser Radiation Pressure," *Science (80-.).*, vol. 210, no. 4474, pp. 1081–1088, Dec. 1980.

[141] K. Sasaki, M. Koshioka, H. Misawa, N. Kitamura, and H. Masuhara, "Optical trapping of a metal particle and a water droplet by a scanning laser beam," *Appl. Phys. Lett.*, vol. 60, no. 7, pp. 807–809, 1992.

[142] H. Furukawa and I. Yamaguchi, "Optical trapping of metallic particles by a fixed Gaussian beam," *Opt. Lett.*, vol. 23, no. 3, p. 216, 1998.

[143] Q. Zhan, "Trapping metallic Rayleigh particles with radial polarization," *Opt. Express*, vol. 12, no. 15, p. 3377, 2004.

[144] P. M. Hansen, V. K. Bhatia, N. Harrit-, and L. Oddershede, "Expanding the optical trapping range of gold nanoparticles," *Nano Lett.*, vol. 5, no. 10, pp. 1937–1942, Oct. 2005.

[145] A. Van Der Horst and A. Van Der Horst, "High-refractive index particles in counter-propagating optical tweezers — manipulation and forces —," Utrecht University, 2006.

[146] A. van der Horst, A. I. Campbell, L. K. van Vugt, D. a Vanmaekelbergh, M. Dogterom, and A. van Blaaderen, "Manipulating metal-oxide nanowires using counter-propagating optical line tweezers.," *Opt. Express*, vol. 15, no. 18, pp. 11629–39, 2007.

[147] S. Sato, Y. Harada, and Y. Waseda, "Optical trapping of microscopic metal particles.," *Opt. Lett.*, vol. 19, no. 22, p. 1807, 1994.

[148] J. E. Curtis, B. B. A. Koss, and D. G. Grier, "Dynamic holographic optical

tweezers," *Opt. Commun.*, vol. 60637, no. June, pp. 169–175, 2002.

[149] K. B. Crozier, "Near-Field Optical Forces from Surface Plasmon Polaritons: Experiment and Theory," in *Trends in Nanophysics*, 2010, pp. 205–216.

[150] S. Bowman, "Design and Characterization fo an Optical tweezers system with adaptive optic control," Victoria, 2007.

[151] S. N. S. Reihani, M. a Charsooghi, H. R. Khalesifard, and R. Golestanian, "Efficient in-depth trapping with an oil-immersion objective lens.," *Opt. Lett.*, vol. 31, no. 6, pp. 766–8, 2006.

[152] J. Bhatt, S. Bhatt, S. Buch, R. P. Singh, S. Nisar, and A. Jaaffrey, "Variation of Trapping Strength with Size and Number of Particles in a Single Trap," *Opt. photonics J.*, vol. 3, no. June, pp. 178–183, 2013.

[153] D. G. Grier, "Optical tweezers in colloid and interface science," *Curr. Opin. Colloid Interface Sci.*, vol. 2, no. 3, pp. 264–270, 1997.

[154] P. Jordan, J. Cooper, G. McNay, F. T. Docherty, W. E. Smith, G. Sinclair, and M. J. Padgett, "Three-dimensional optical trapping of partially silvered silica microparticles.," *Opt. Lett.*, vol. 29, no. 21, pp. 2488–2490, 2004.

[155] M. C. Williams, "Optical Tweezers : Measuring Piconewton Forces," *Physics (College. Park. Md).*, no. 1, pp. 1–14, 2002.

[156] M. L. Juan, M. Righini, and R. Quidant, "Plasmon nano-optical tweezers," *Nat. Photonics*, vol. 5, no. 6, pp. 349–356, 2011.

[157] Y. Pang and R. Gordon, "Optical trapping of 12 nm dielectric spheres using double-nanoholes in a gold film," *Nano Lett.*, vol. 11, no. 9, pp. 3763–3767, 2011.

[158] A. Jamshidi, H. Y. Hsu, J. K. Valley, A. T. Ohta, S. Neale, and M. C. Wu, "Metallic nanoparticle manipulation using optoelectronic tweezers," *Proc. IEEE Int. Conf. Micro Electro Mech. Syst.*, pp. 579–582, Jan. 2009.

[159] A. Linnenberger, M. I. Bodine, C. Fiedler, J. J. Roberts, S. C. Skaalure, J. P. Quinn, S. J. Bryant, M. Cole, and R. R. McLeod, "Three dimensional live cell lithography," *Opt. Express*, vol. 21, no. 8, p. 10269, Apr. 2013.

[160] A. Farré, M. Shayegan, C. López-Quesada, G. A. Blab, M. Montes-Usategui, N. R. Forde, and E. Martín-Badosa, "Positional stability of holographic optical traps," *Opt. Express*, vol. 19, no. 22, p. 21370, Oct. 2011.

[161] K. K. Seet, V. Mizeikis, S. Juodkazis, and H. Misawa, "Three-dimensional horizontal circular spiral photonic crystals with stop gaps below 1 μm," *Appl. Phys. Lett.*, vol. 88, no. 22, p. 221101, May 2006.

[162] G. M. Gibson, R. W. Bowman, A. Linnenberger, M. Dienerowitz, D. B. Phillips, D. M. Carberry, M. J. Miles, and M. J. Padgett, "A compact holographic optical tweezers instrument," *Rev. Sci. Instrum.*, vol. 83, no. 11, pp. 1–7, 2012.

[163] D. R. Burnham, "Microscopic Applications of Holographic Beam Shaping and Studies of Optically Trapped Aerosols," St. Andrews, 2009.

[164] R. W. Bowman, G. M. Gibson, A. Linnenberger, D. B. Phillips, J. A. Grieve, D. M. Carberry, S. Serati, M. J. Miles, and M. J. Padgett, "Red tweezers: Fast, customisable hologram generation for optical tweezers," *Comput. Phys. Commun.*, vol. 185, no. 1, pp. 268–273, 2014.

[165] D. J. McKnight, D. G. Vass, and R. M. Sillitto, "Development of a spatial light modulator: a randomly addressed liquid-crystal-over-nMOS array.," *Appl. Opt.*, vol. 28, no. 22, pp. 4757–4762, Nov. 1989.

[166] U. Efron, J. Grinberg, P. O. Braatz, M. J. Little, P. G. Reif, and R. N. Schwartz, "The silicon liquid-crystal light valve," *J. Appl. Phys.*, vol. 57, no. 4, pp. 1356–1368, Feb. 1985.

[167] M. N. Ernstoff, A. M. Leupp, M. J. Little, and H. T. Peterson, "Liquid

crystal pictorial display," in *International Electron Devices Meeting*, 1973, vol. 19, pp. 548–551.

[168] M. Reicherter, T. Haist, E. U. Wagemann, and H. J. Tiziani, "Optical particle trapping with computer-generated holograms written on a liquid-crystal display," *Opt. Lett.*, vol. 24, no. 9, p. 608, 1999.

[169] E. Fällman and O. Axner, "Design for fully steerable dual-trap optical tweezers," *Appl. Opt.*, vol. 36, no. 10, p. 2107, 1997.

[170] "Metamorphose." [Online]. Available: http://www.metamorphose.org/. [Accessed: 11-Nov-2015].

[171] W. Cai and V. Shalaev, *Optical Metamaterials: Fundamentals and Applications*, vol. 23. Springer New York, 2009.

[172] J. Valentine, S. Zhang, T. Zentgraf, E. Ulin-Avila, D. A. Genov, G. Bartal, and X. Zhang, "Three-dimensional optical metamaterial with a negative refractive index," *Nature*, vol. 455, no. 7211, pp. 376–379, 2008.

[173] N. Engheta, R. W. Ziolkowski, R. W. Z. Nader Engheta, N. Engheta, and R. W. Ziolkowski, *Metamaterials: Physics and Engineering Explorations*. John Wiley & Sons, 2006.

[174] V. M. Shalaev, W. Cai, U. Chettiar, H.-K. Yuan, A. K. Sarychev, V. P. Drachev, and A. V. Kildishev, "Negative Index of Refraction in Optical Metamaterials," *Opt. Lett.*, vol. 30, no. 24, pp. 3356–3358, Dec. 2005.

[175] T. T. Mostyn clock, "British Museum - The Lycurgus Cup." [Online]. Available: http://www.britishmuseum.org/explore/highlights/highlight_objects/pe_mla/t/the_lycurgus_cup.aspx. [Accessed: 10-Nov-2015].

[176] V. V. Vorobev and A. V. Tyukhtin, "Nondivergent Cherenkov radiation in a wire metamaterial," *Phys. Rev. Lett.*, vol. 108, no. 18, 2012.

[177] D. R. Smith, W. J. Padilla, D. C. Vier, S. C. Nemat-Nasser, and S. Schultz, "Composite Medium with Simultaneously Negative Permeability and

Permittivity," *Phys. Rev. Lett.*, vol. 84, no. 18, pp. 4184–4187, May 2000.

[178] J. B. Pendry, "Negative refraction makes a perfect lens," *Phys. Rev. Lett.*, vol. 85, no. 18, pp. 3966–3969, 2000.

[179] J. Jiao, "The Simulation And Structure Design of Optical Metamaterials," Manchester, 2013.

[180] C. Caloz, "Metamaterial Antennas and Radiative Systems," in *Microstrip and Printed Antennas: New Trends, Techniques and Applications*, 1st ed., Y. M. . A. Debatosh Guha, Ed. Wiley & Sons Ltd, 2010, pp. 345–386.

[181] A. Di Falco, M. Ploschner, and T. F. Krauss, "Flexible metamaterials at visible wavelengths," *New J. Phys.*, vol. 12, no. 11, p. 113006, Nov. 2010.

[182] I. Staude, M. Thiel, S. Essig, C. Wolff, K. Busch, G. von Freymann, and M. Wegener, "Fabrication and characterization of silicon woodpile photonic crystals with a complete bandgap at telecom wavelengths.," *Opt. Lett.*, vol. 35, no. 7, pp. 1094–6, Apr. 2010.

[183] D. R. Smith, S. Schultz, P. Markoš, and C. M. Soukoulis, "Determination of effective permittivity and permeability of metamaterials from reflection and transmission coefficients," *Phys. Rev. B*, vol. 65, no. 19, p. 195104, 2002.

[184] A. A. Maradudin, *Structured surfaces as optical metamaterials*, 1st ed. Cambridge university press, 2011.

[185] G. Dolling, M. Wegener, C. M. Soukoulis, and S. Linden, "Negative-index metamaterial at 780 nm wavelength," *Opt. Lett.*, vol. 32, no. 1, pp. 53–55, Dec. 2006.

[186] R. W. Ziolkowski and E. Heyman, "Wave propagation in media having negative permittivity and permeability," *Phys. Rev. E - Stat. Nonlinear, Soft Matter Phys.*, vol. 64, no. 5 II, p. 056625/1-056625/15, 2001.

[187] S. Zhang, W. Fan, K. J. Malloy, S. R. J. Brueck, N. C. Panoiu, and R. M. Osgood, "Near-infrared double negative metamaterials," *Opt. Express*, vol. 13, no. 13, p. 4922, Jun. 2005.

[188] C. Rajni and A. Marwaha, "Analysis of magnetic resonance in Metamaterial structure," in *COMSOL conference*, 2011, pp. 187–190.

[189] M. Rill, C. Plet, M. Thiel, M. Wegener, G. Von Freymann, and S. Linden, "Photonic metamaterials by direct laser writing and silver chemical vapor deposition," *Conf. Quantum Electron. Laser Sci. - Tech. Dig. Ser.*, vol. 7, no. 7, pp. 543–546, Jul. 2008.

[190] C. Enkrich, F. Pérez-Willard, D. Gerthsen, J. Zhou, T. Koschny, C. M. Soukoulis, M. Wegener, and S. Linden, "Focused-ion-beam nanofabrication of near-infrared magnetic metamaterials," *Adv. Mater.*, vol. 17, no. 21, pp. 2547–2549, Nov. 2005.

[191] C. Enkrich, M. Wegener, S. Linden, S. Burger, L. Zschiedrich, F. Schmidt, J. F. Zhou, T. Koschny, and C. M. Soukoulis, "Magnetic metamaterials at telecommunication and visible frequencies," *Phys. Rev. Lett.*, vol. 95, no. 20, p. 203901, Nov. 2005.

[192] G. Dolling, C. Enkrich, M. Wegener, C. M. Soukoulis, and S. Linden, "Low-loss negative-index metamaterial at telecommunication wavelengths," *Opt. Lett.*, vol. 31, no. 12, p. 1800, Jun. 2006.

[193] U. K. Chettiar, A. V. Kildishev, H. K. Yuan, W. Cai, V. P. Drachev, and V. M. Shalaev, "Negative index metamaterial for two distinct polarizations: Double negative at 813 nm and single negative at 770 nm," *Conf. Lasers Electro-Optics, 2007, CLEO 2007*, vol. 32, no. 12, pp. 1671–3, 2007.

[194] P. U. Jepsen, B. M. Fischer, A. Thoman, H. Helm, J. Y. Suh, R. Lopez, and R. F. Haglund, "Metal-insulator phase transition in a VO2 thin film observed with terahertz spectroscopy," *Phys. Rev. B - Condens. Matter Mater. Phys.*, vol. 74, no. 20, p. 205103, 2006.

[195] R. Skomski and D. J. Sellmyer, "Multiscale Phenomena in

Bruggeman Composites," *MRS Proc.*, vol. 851, p. NN1.7, 2004.

[196] T. F. Krauss, "Slow light in photonic crystal waveguides," *J. Phys. D. Appl. Phys.*, vol. 40, no. 9, pp. 2666–2670, 2007.

[197] K. Inoue, H. Oda, N. Ikeda, and K. Asakawa, "Enhanced third-order nonlinear effects in slow-light photonic-crystal slab waveguides of line-defect," *Opt. Express*, vol. 17, no. 9, pp. 7206–7216, 2009.

[198] S. John, "Photonic band gap materials: a semiconductor for light," *Tech. Dig. CLEO/Pacific Rim 2001. 4th Pacific Rim Conf. Lasers Electro-Optics (Cat. No.01TH8557)*, vol. 1, pp. 1–23, 2001.

[199] J. J. D. Joannopoulos, S. Johnson, J. N. J. Winn, and R. R. D. Meade, *Photonic crystals: molding the flow of light*. Princeton University Press, 2008.

[200] E. Yablonovitch, "Photonic Crystals: Semiconductors of Light," *Sci. Am.*, vol. 285, no. 6, pp. 46–55, 2001.

[201] Y. Wan, K. Fu, C. Li, and M. Yun, "Improving slow light effect in photonic crystal line defect waveguide by using eye-shaped scatterers," *Opt. Commun.*, vol. 286, no. 1, pp. 192–196, 2013.

[202] H.-G. Park, "Electrically Driven Single-Cell Photonic Crystal Laser," *Science (80-.).*, vol. 305, no. 5689, pp. 1444–1447, Sep. 2004.

[203] S. Shukla, X. Vidal, E. P. Furlani, M. T. Swihart, K.-T. T. Kim, Y.-K. K. Yoon, A. Urbas, and P. N. Prasad, "Subwavelength direct laser patterning of conductive gold nanostructures by simultaneous photopolymerization and photoreduction," *ACS Nano*, vol. 5, no. 3, pp. 1947–1957, Mar. 2011.

[204] D. B. Burckel, J. R. Wendt, G. A. Ten Eyck, J. C. Ginn, A. R. Ellis, I. Brener, and M. B. Sinclair, "Micrometer-scale cubic unit cell 3D metamaterial layers," *Adv. Mater.*, vol. 22, no. 44, pp. 5053–5057, Nov. 2010.

[205] M. J. Kendrick, D. H. McIntyre, and O. Ostroverkhova, "Wavelength dependence of optical tweezer trapping forces on dye-doped

polystyrene microspheres," *J. Opt. Soc. Am. B*, vol. 26, no. 11, p. 2189, 2009.

[206] K. Stadlmann and K. Cicha, "Fabrication of Optical Interconnects with Two Photon Polymerization," *Proc. LPM2010 – 11th Int. Symp. Laser Precis. Microfabr.*, pp. 1–6, 2010.

[207] L. Reimer, "Electron diffraction methods in TEM, STEM and SEM," *Scanning*, vol. 2, no. 1, pp. 3–19, Oct. 1979.

[208] K. K. Seet, S. Juodkazis, V. Jarutis, and H. Misawa, "Feature-size reduction of photopolymerized structures by femtosecond optical curing of SU-8," *Appl. Phys. Lett.*, vol. 89, no. 2, p. 24106, Jul. 2006.

[209] M. Malinauskas, A. Žukauskas, G. Bičkauskaitė, R. Gadonas, and S. Juodkazis, "Mechanisms of three-dimensional structuring of photo-polymers by tightly focussed femtosecond laser pulses," *Opt. Express*, vol. 18, no. 10, p. 10209, May 2010.

[210] S. Uhlig, "Micro-Processing Applied to Optical Interconnects and High-Frequency Packaging," Linkopings University, 2006.

[211] Sigmaaldrich, "PEGDA Mn 575 Product specification," *Sigma-Aldrich*, 2015. [Online]. Available: http://www.sigmaaldrich.com/Graphics/COfAInfo/SigmaSAPQM/SPEC/43/437441/437441-BULK_____ALDRICH__.pdf. [Accessed: 12-Oct-2015].

[212] "Ormocomp — UV Curable Hybrid Polymer for Moulding ORMOCER ® for Microoptical Components Produced by UV moulding," *micro resist technology*, 2014. [Online]. Available: http://www.microchem.com/PDFs_MRT/Ormocomp Overview.pdf. [Accessed: 10-Sep-2015].

[213] O. M. Maragò, P. G. Gucciardi, F. Bonaccorso, G. Calogero, V. Scardaci, A. G. Rozhin, A. C. Ferrari, P. H. Jones, R. Saija, F. Borghese, P. Denti, and M. A. Iatì, "Optical trapping of carbon nanotubes," *Phys. E Low-Dimensional Syst. Nanostructures*, vol. 40,

no. 7, pp. 2347–2351, 2008.

[214] A. Selimis, V. Mironov, and M. Farsari, "Direct laser writing: Principles and materials for scaffold 3D printing," *Microelectron. Eng.*, vol. 132, pp. 83–89, 2014.

[215] M. T. Raimondi, S. M. Eaton, M. M. Nava, M. Laganà, G. Cerullo, and R. Osellame, "Two-photon laser polymerization: from fundamentals to biomedical application in tissue engineering and regenerative medicine," *J. Appl. Biomater. Biomech.*, vol. 10, no. 1, pp. 0–0, 2012.

[216] Y. Liu, Q. Hu, F. Zhang, C. Tuck, D. Irvine, R. Hague, Y. He, M. Simonelli, G. A. Rance, E. F. Smith, and R. D. Wildman, "Additive manufacture of three dimensional nanocomposite based objects through multiphoton fabrication," *Polymers (Basel).*, vol. 8, no. 9, p. 325, Sep. 2016.

[217] S. Ushiba, S. Shoji, K. Masui, P. Kuray, J. Kono, and S. Kawata, "3D microfabrication of single-wall carbon nanotube/polymer composites by two-photon polymerization lithography," *Carbon N. Y.*, vol. 59, pp. 283–288, Aug. 2013.

[218] T. Woggon, T. Kleiner, M. Punke, and U. Lemmer, "Nanostructuring of organic-inorganic hybrid materials for distributed feedback laser resonators by two-photon polymerization.," *Opt. Express*, vol. 17, no. 4, pp. 2500–2507, Feb. 2009.

[219] P. Kunwar, "Nanofabrication using Two-photon Polymerization and Direct Vectorial Writing," Tampere University of Technology, 2011.

[220] V. Mizeikis, S. Juodkazis, A. Marcinkevičius, S. Matsuo, and H. Misawa, "Tailoring and characterization of photonic crystals," *J. Photochem. Photobiol. C Photochem. Rev.*, vol. 2, no. 1, pp. 35–69, 2001.

[221] G. Y. Choi, W. Zurawsky, and A. Ulman, "Molecular weight effects in adhesion," *Langmuir*, vol. 15, no. 24, pp. 8447–8450, 1999.

[222] M. K. Chaudhury, T. M. Gentle, and E. P. Plueddemann, "Adhesion

mechanism of polyvinyl chloride to silane primed metal surfaces," *J. Adhes. Sci. Technol.*, vol. 1, no. 1, pp. 29–38, 1987.

[223] W. Zhou, B. B. Hinojosa, and J. C. Nino, "Applicability of the bruggeman equation for analyzing dielectric slurries containing ceramic powders with high permittivity," *J. Am. Ceram. Soc.*, vol. 95, no. 2, pp. 457–460, Feb. 2012.

[224] C. G. Granqvist, *Materials Science for Solar Energy Conversion Systems*. Pergamon, 2013.

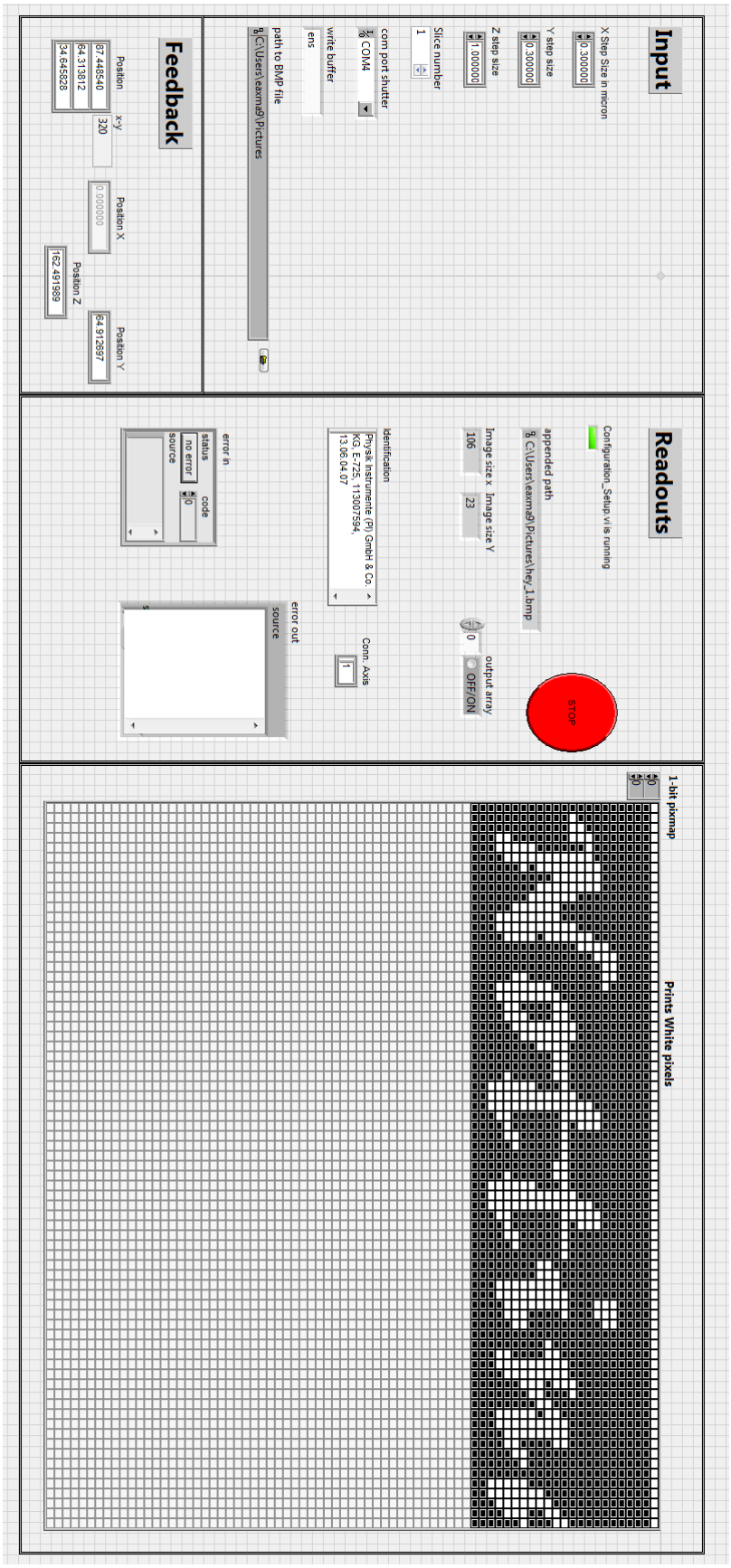
[225] B. Hester, G. K. Campbell, C. Lpez-Mariscal, C. L. Filgueira, R. Huschka, N. J. Halas, and K. Helmerson, "Tunable optical tweezers for wavelength-dependent measurements," *Rev. Sci. Instrum.*, vol. 83, no. 4, p. 43114, Apr. 2012.

[226] Y. Cao, A. B. Stilgoe, L. Chen, T. a Nieminen, and H. Rubinsztein-Dunlop, "Equilibrium orientations and positions of non-spherical particles in optical traps.," *Opt. Express*, vol. 20, no. 12, pp. 12987–96, Jun. 2012.

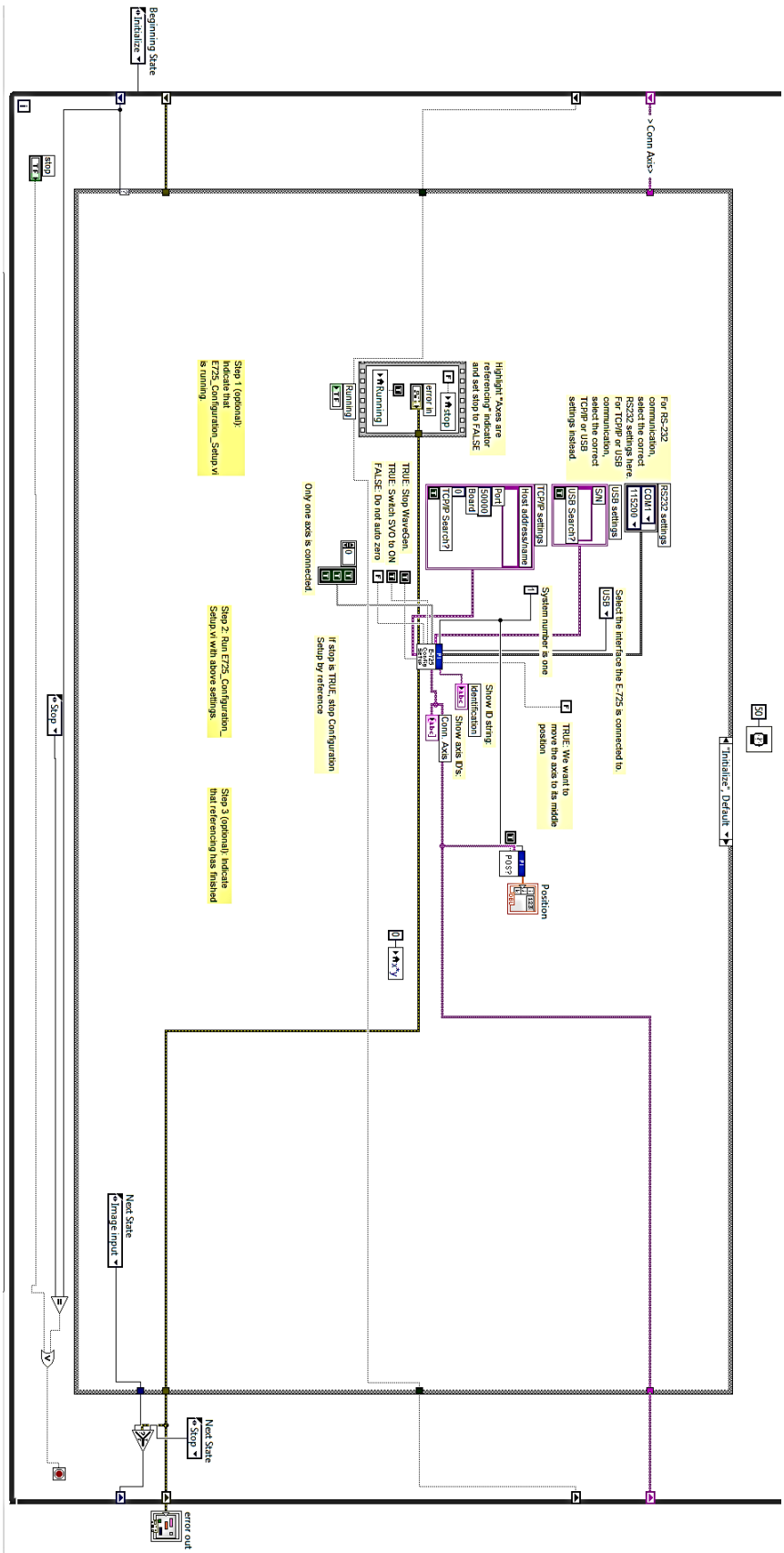
[227] S. Wong, M. Deubel, F. Perez-Willard, S. John, G. A. Ozin, M. Wegener, and G. Von Freymann, "Direct laser writing of three-dimensional photonic crystals with a complete photonic bandgap in chalcogenide glasses," *Adv. Mater.*, vol. 18, no. 3, pp. 265–269, 2006.

[228] J. Roberts, I. E. Bagci, M. A. M. Zawawi, J. Sexton, N. Hulbert, Y. J. Noori, C. S. Woodhead, M. Missous, M. A. Migliorato, U. Roedig, and R. J. Young, "Atomic-scale Authentication with Resonant Tunneling Diodes," *MRS Adv.*, pp. 1–5, Feb. 2016.

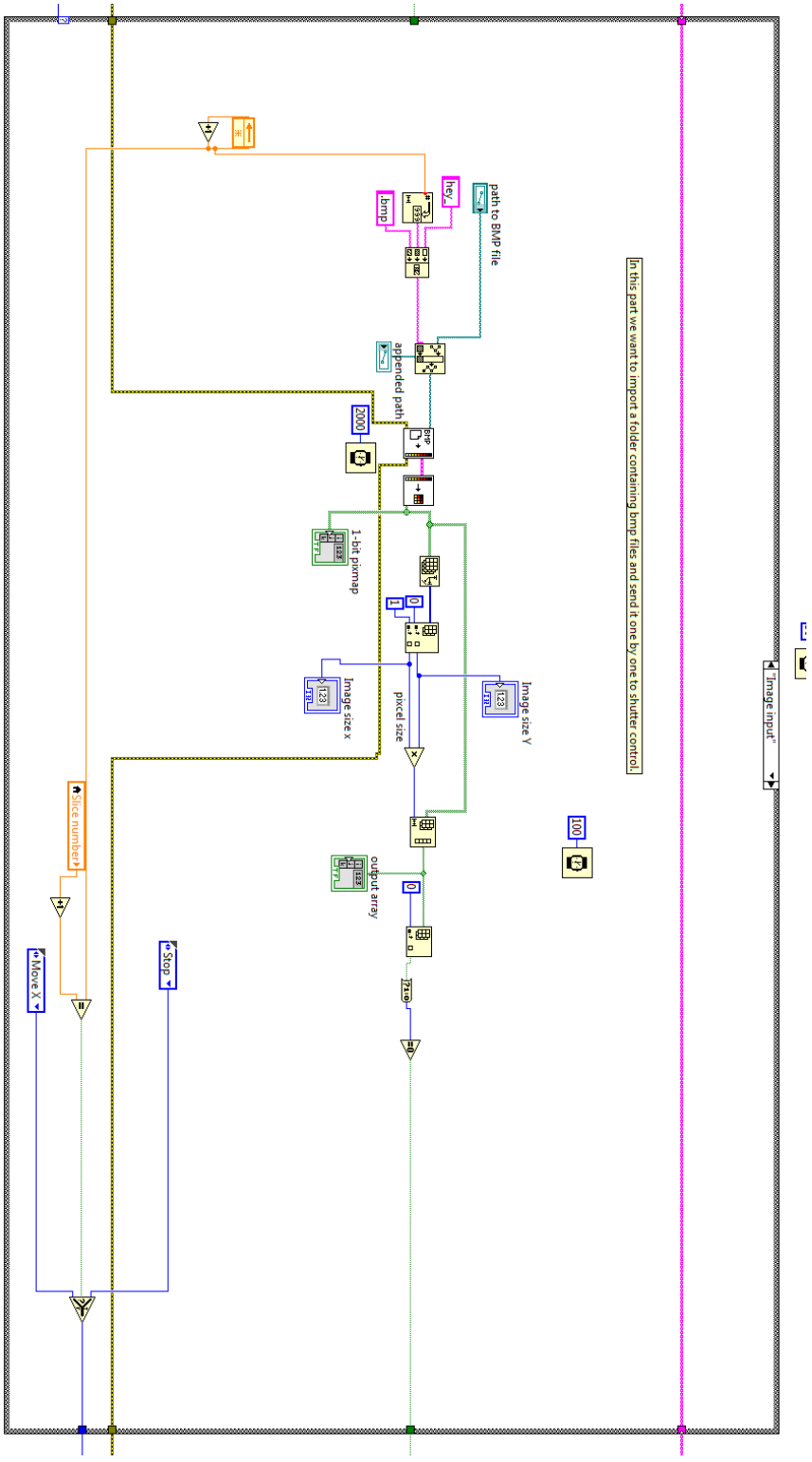
Appendix A: Developed LabVIEW software



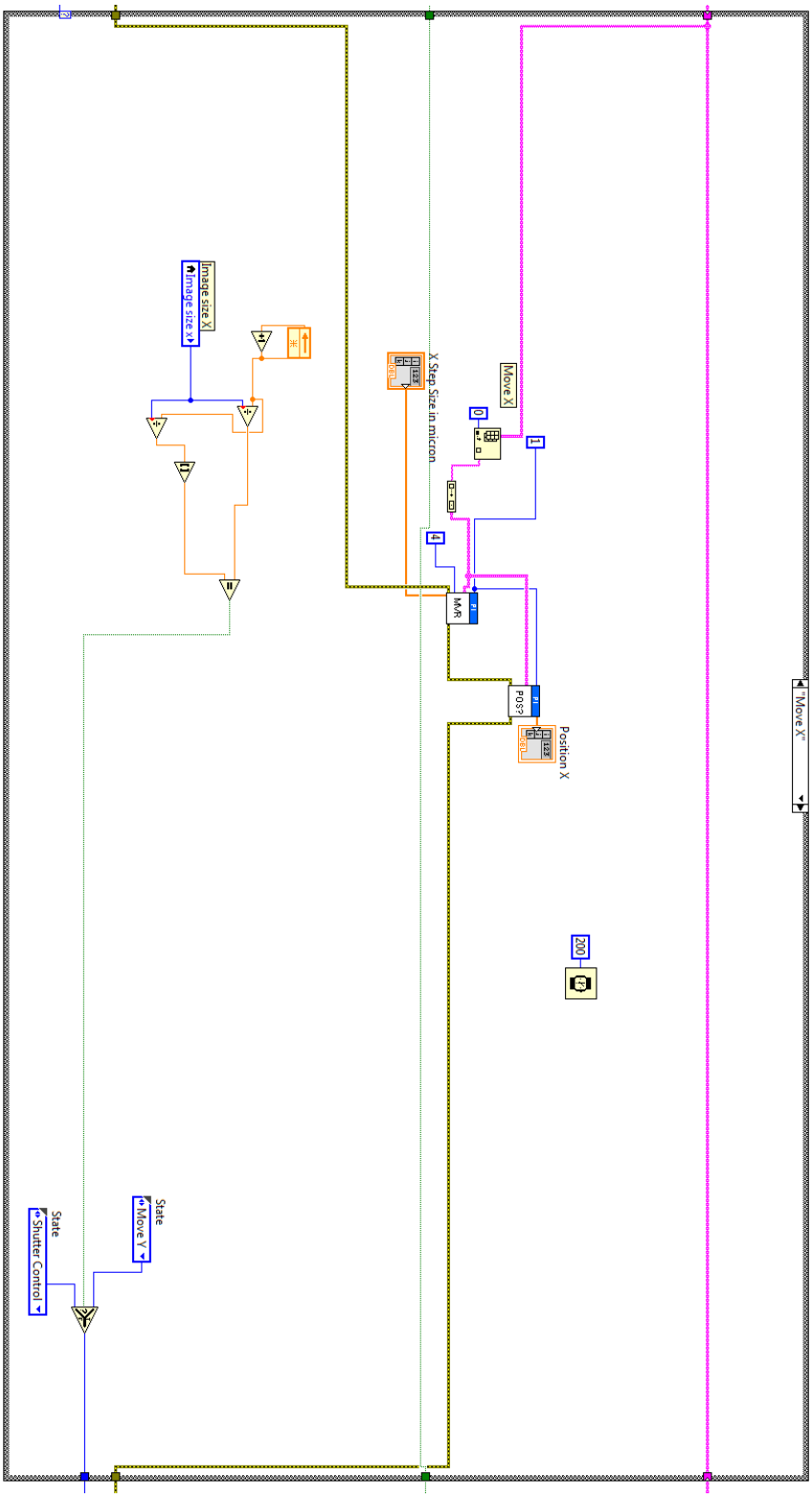
A 1 2PP studio software LabVIEW front panel.



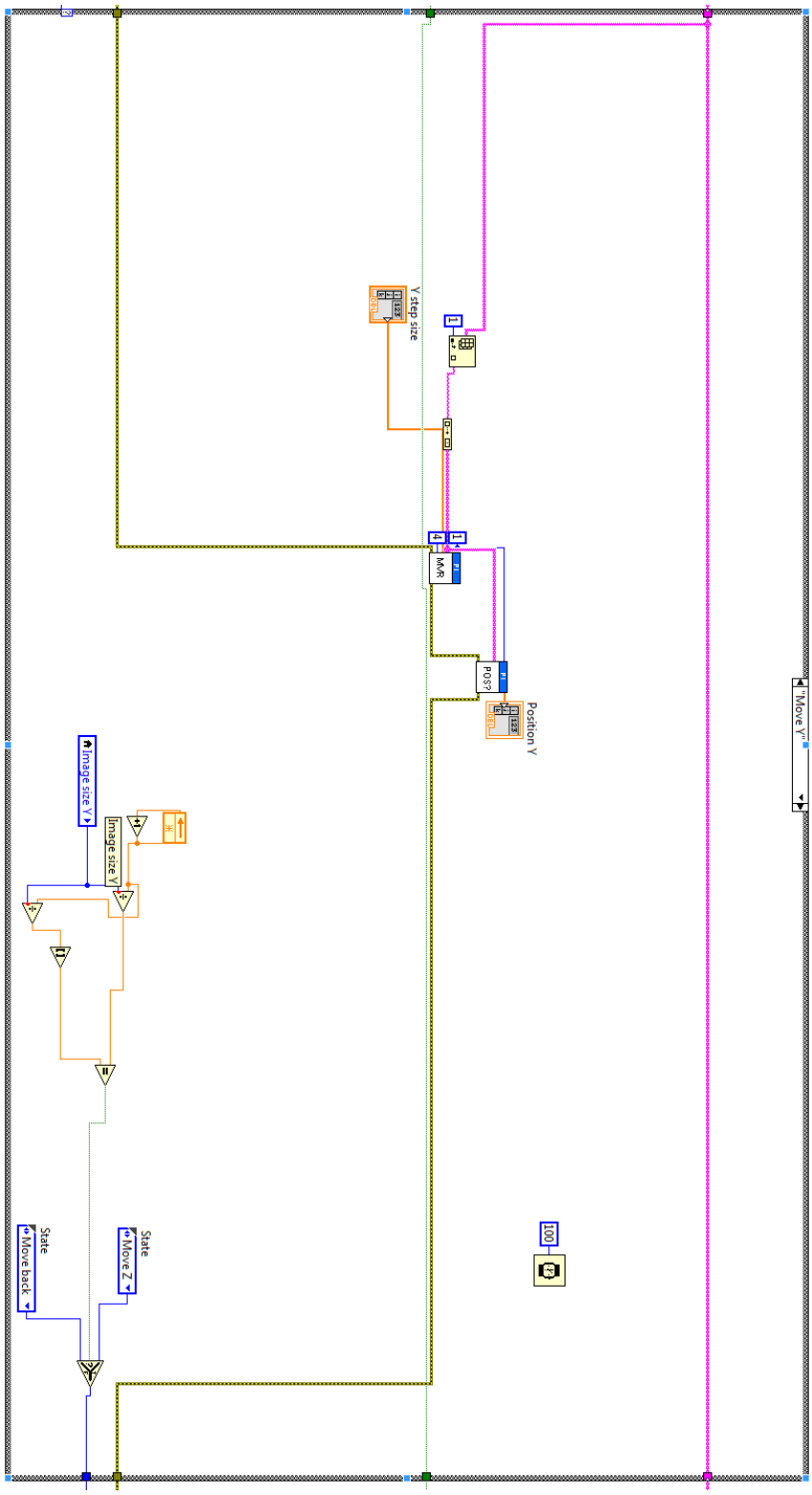
A 2 2PP studio stage initialization step.



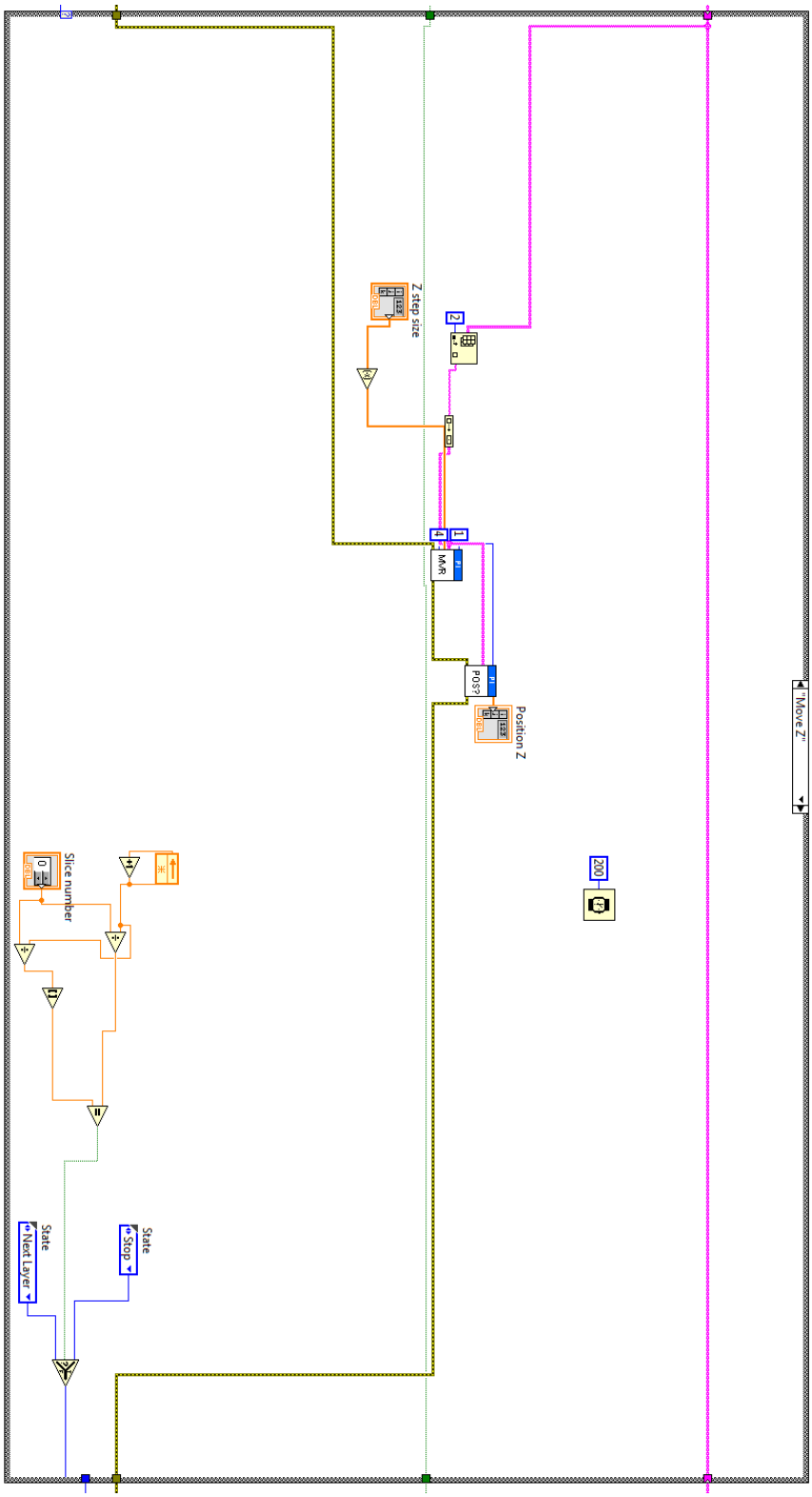
A 3 2PP studio image importing sequence.



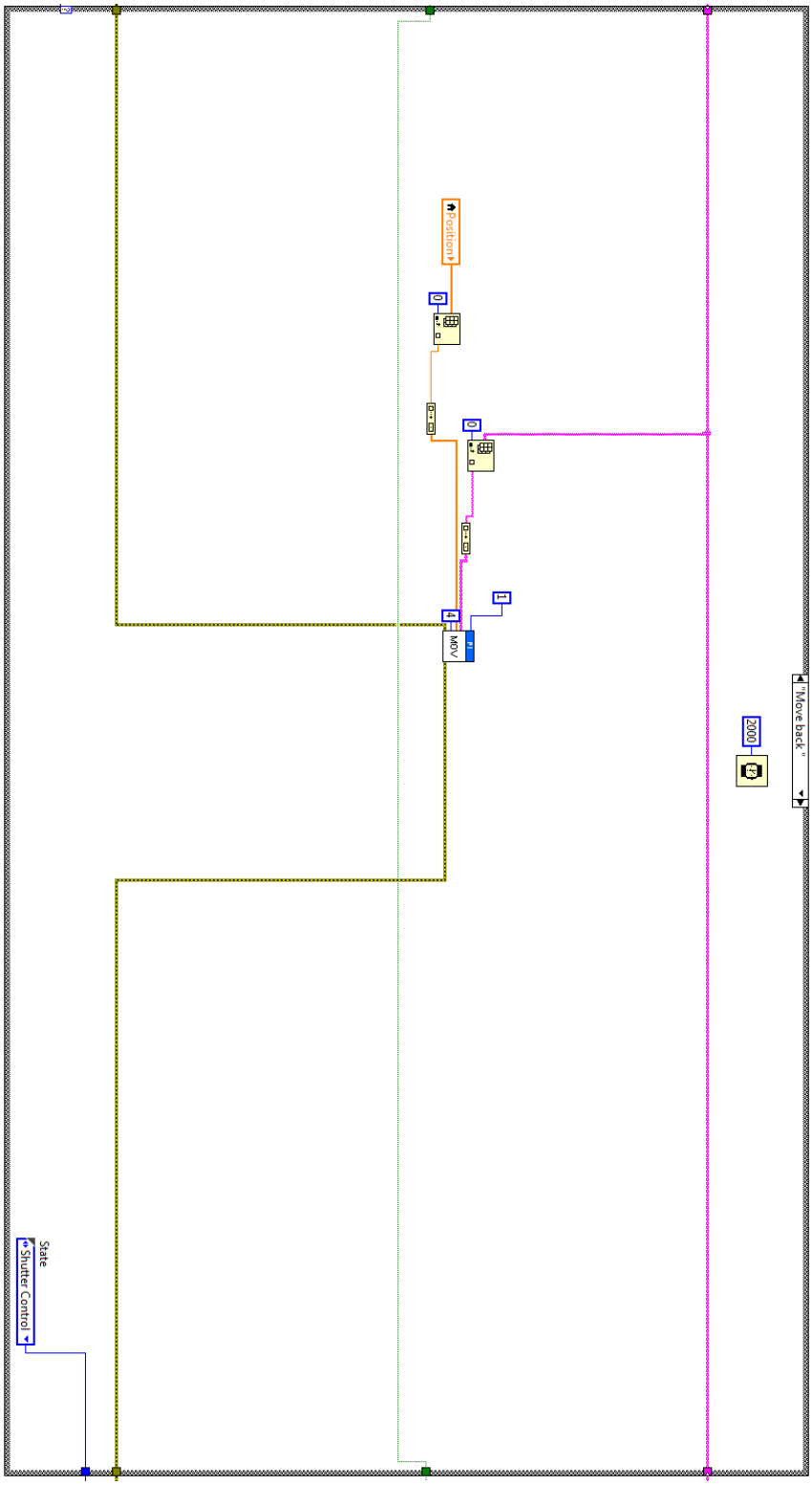
A 4 2PP studio stage relative move in X direction.



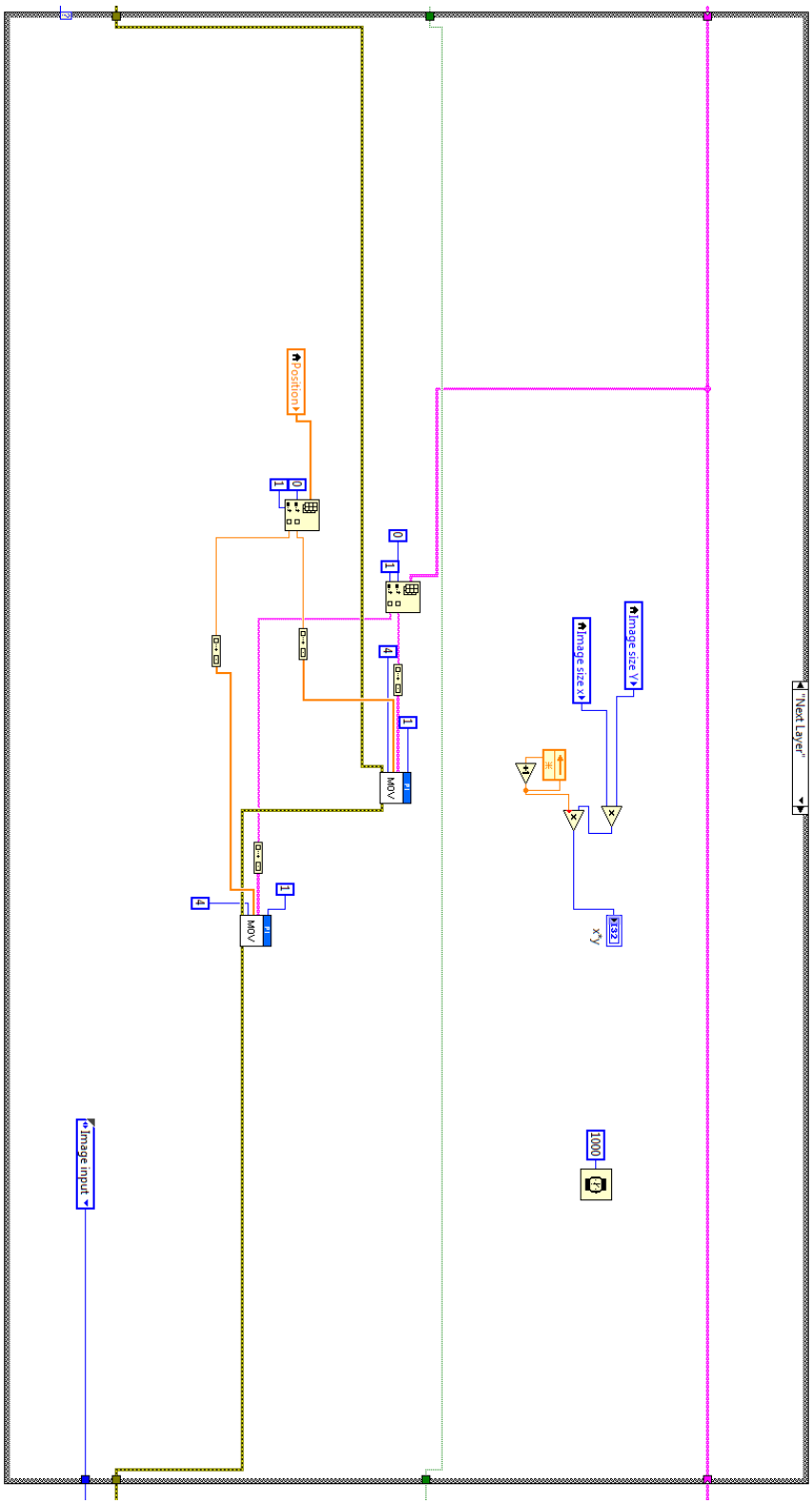
A 5 2PP studio stage relative move in Y direction.



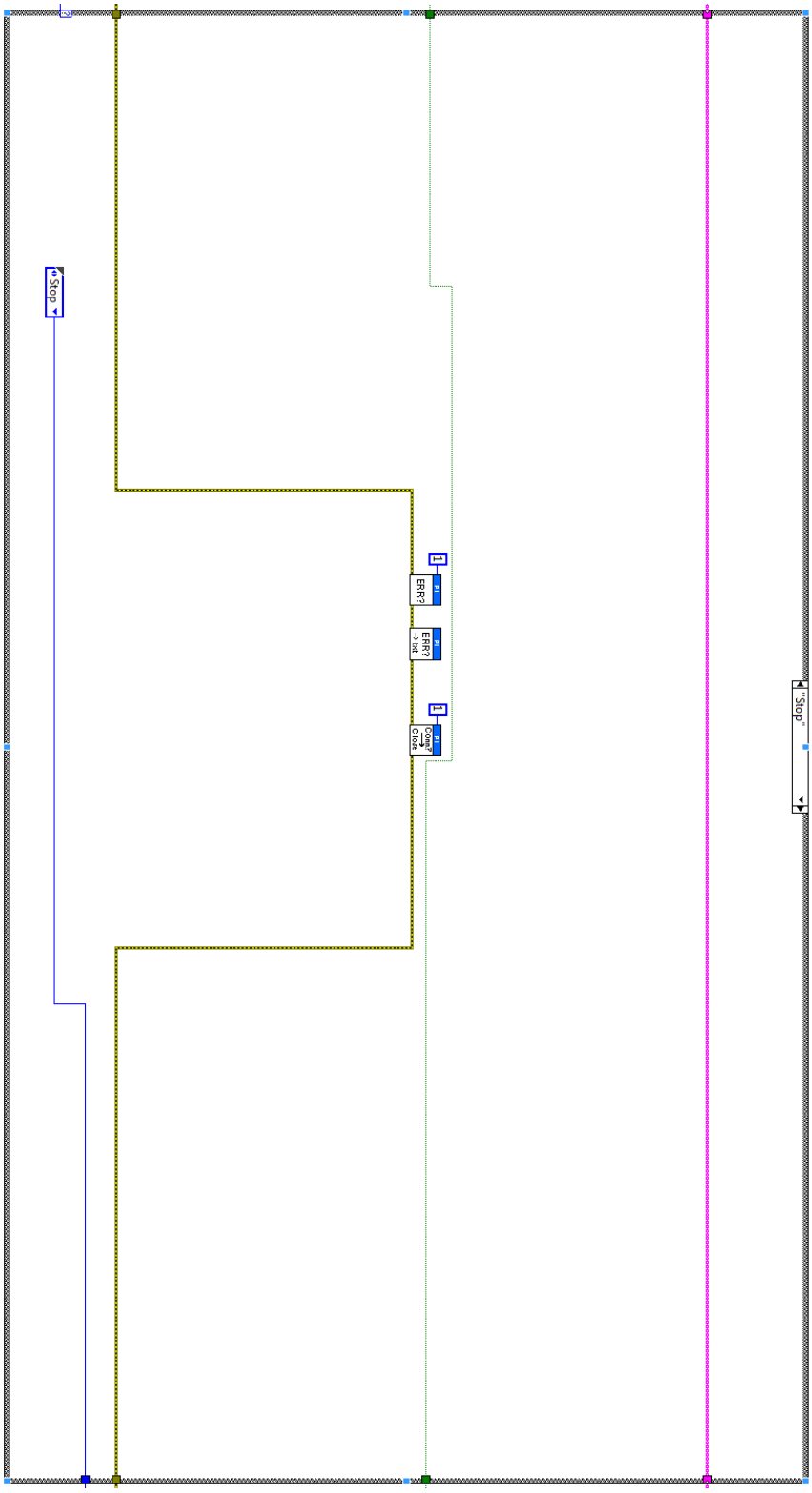
A 6 2PP studio stage relative move in Z direction.



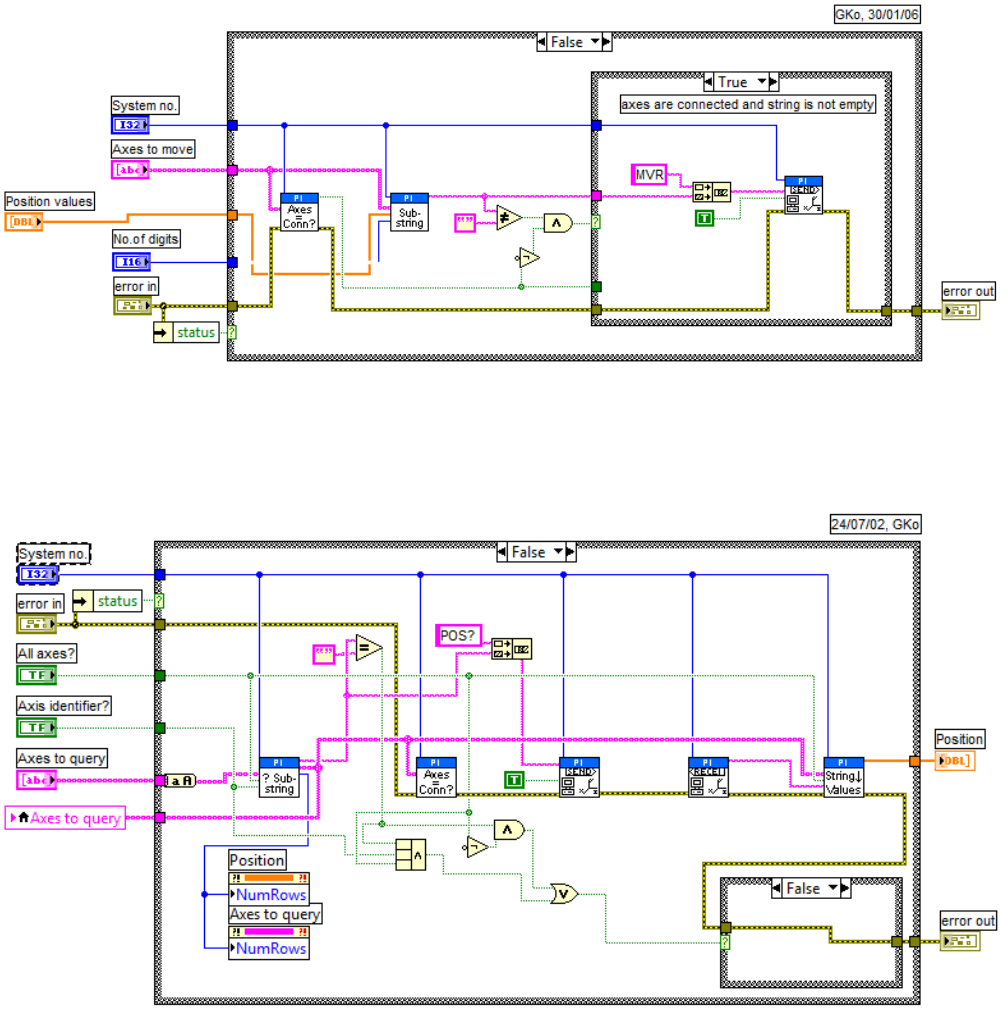
A 7 2PP studio stage absolute move to the starting position of the printed line.



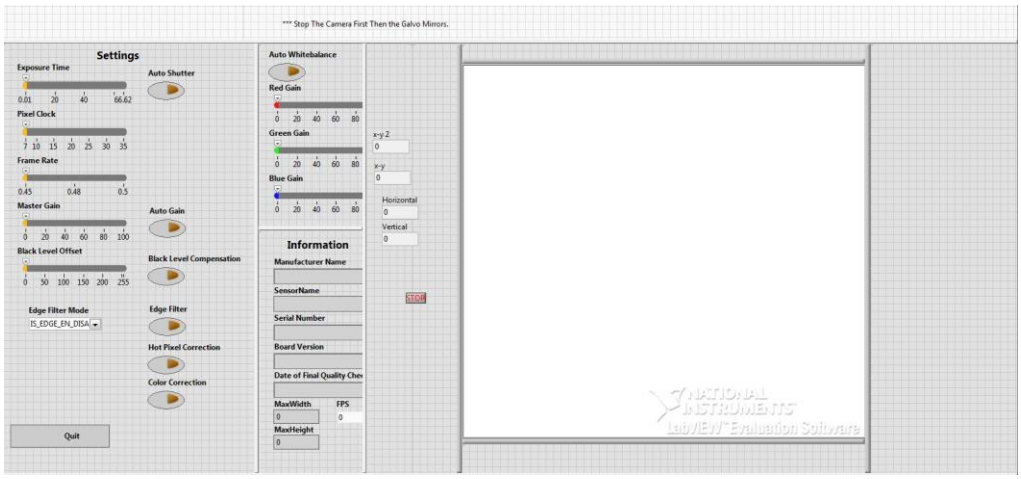
A 8 2PP studio stage absolute move to the starting position of the print and preparing for the stage for the next layer.



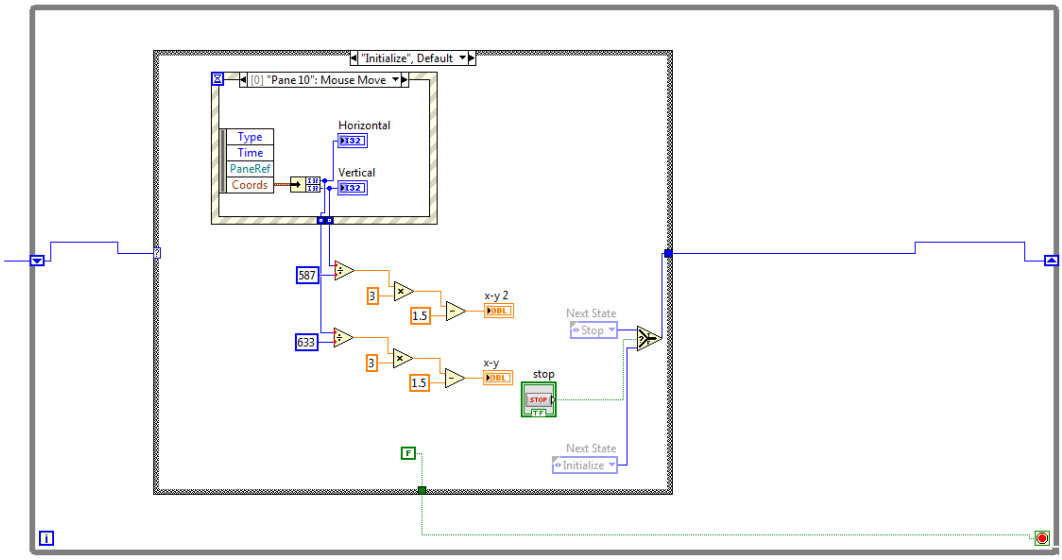
A 9 2PP studio stop and error check.

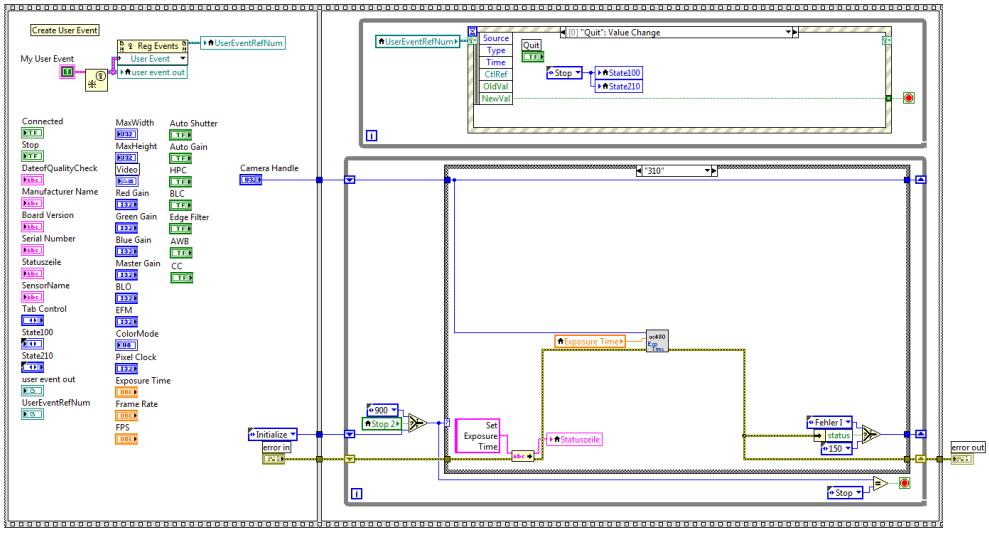


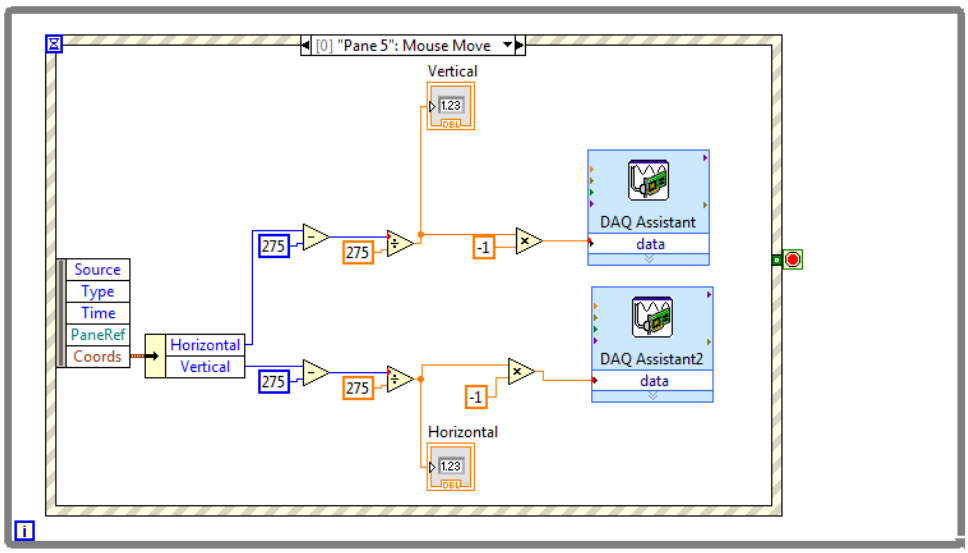
A 10 Absolute (top) and relative move VIs used in the software.



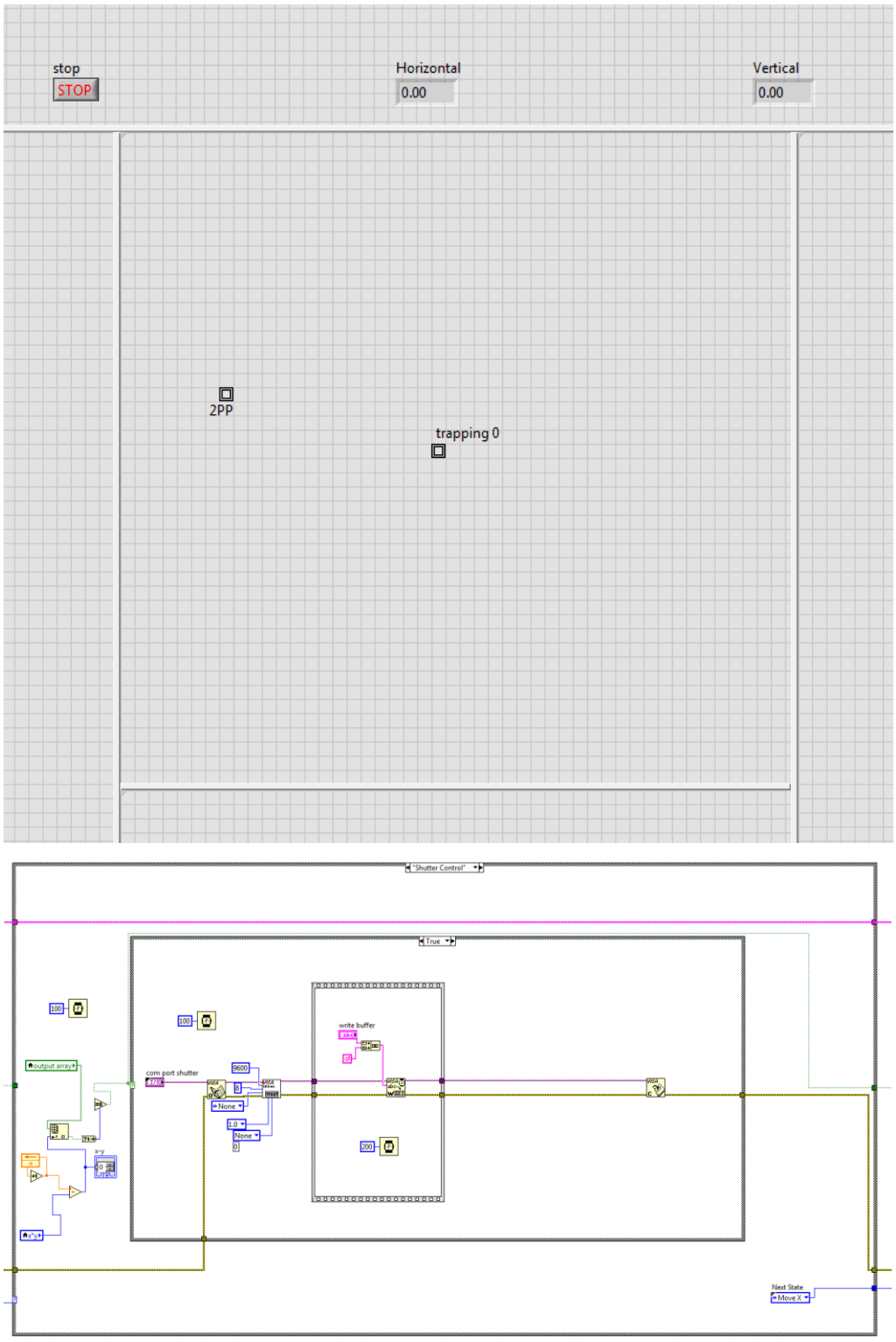
A 11 Galvo control software with live camera feed. Front panel.


"Initialize", Default
[0] "Pane 10": Mouse Move
Type
Time
PaneRef
Coords
Horizontal
Vertical
587
633
3
1.5
x-y 2
x-y
stop
Next State
Stop
Next State
Initialize


Create User Event
My User Event
Reg Events
User Event
user event out
UserEventRefNum
Connected
Stop
DateofQualityCheck
Manufacturer Name
Board Version
Serial Number
Statuszeile
SensorName
Tab Control
State100
State210
user event out
UserEventRefNum
MaxWidth
MaxHeight
Video
Red Gain
Green Gain
Blue Gain
Master Gain
BLO
EFM
ColorMode
Pixel Clock
Exposure Time
Frame Rate
FPS
Auto Shutter
Auto Gain
HPC
BLC
Edge Filter
AWB
CC
Camera Handle
Initialize
error in
[0] "Quit": Value Change
Source
Type
Time
CtlRef
OldVal
NewVal
Quit
Stop
State100
State210
"310"
Exposure Time
900
Stop 2
Set Exposure Time
Statuszeile
Fehler I
status
150
Stop
error out



A 12 The block diagram of galvo control software with live camera feed.



A 13 Galvo control VI front panel (top) and block diagram.